

Large-Scale X-ray Studies of Nearby Galaxy Clusters with eROSITA

Dissertation
zur
Erlangung des Doktorgrades (Dr. rer. nat.)
der
Mathematisch-Naturwissenschaftlichen Fakultät
der
Rheinischen Friedrich-Wilhelms-Universität Bonn

vorgelegt von
Angie Veronica
aus
Jakarta, Indonesien

Bonn, April 2024

Angefertigt mit Genehmigung der Mathematisch-Naturwissenschaftlichen Fakultät der Rheinischen
Friedrich-Wilhelms-Universität Bonn

Gutachter/Betreuer: Prof. Dr. Thomas H. Reiprich
Gutachter: PD Dr. Jürgen Kerp

Tag der Promotion: 20.12.2024
Erscheinungsjahr: 2025

Untuk Josef Hardi dan Henny Mulia

"Astronomy compels the soul to look upward, and leads us from this world to another."
— Plato, The Republic, 375 BC

Abstract

Galaxy clusters are the largest virialized objects in the Universe. They form in the intersections of the cosmic web and grow through mergers and accretion of smaller substructures transported by the cosmic web filaments. Thus, the outskirts of galaxy clusters are important for studying the signatures of the accretion processes, such as shocks, gas clumping, gas turbulence, and bulk motions. Additionally, these regions can be used to detect the elusive cosmic filaments. The filaments are known to be the key to solving the "missing" baryons problem. According to our census of matter in the local Universe, around 30-40% of the baryons predicted by cosmological studies, such as Big Bang Nucleosynthesis, are still unobserved. The cosmological hydrodynamical simulations predicted that they reside in the filamentary gas between galaxies, known as the warm-hot intergalactic medium (WHIM). Despite the importance, studying cluster outskirts is hindered by the lack of the soft X-ray energy sensitivity and field of view (FoV) of previous X-ray instruments. The extended ROentgen Survey with an Imaging Telescope Array (eROSITA), one of the primary instruments on board the Russian-German Spectrum-Roentgen-Gamma (SRG) mission, was launched in July 2019. Equipped with a large FoV and survey observation mode, as well as superior soft energy band sensitivity, eROSITA is an excellent instrument to target the faint cluster outskirts and the densest parts of the filaments.

In this dissertation, eROSITA data are employed to investigate the cluster outskirts of nearby galaxy clusters and characterize the gas properties of the detected filaments. The first two projects focus on the exploitation of eROSITA PV observations of the Abell 3391 and Abell 3395 galaxy cluster system, while the third project uses the eROSITA All-Sky Survey (eRASS) data of the Centaurus cluster field. Since the studied areas are faint and vast, meticulous steps were taken when reducing the data and correcting the images. The image corrections include the particle-induced background (PIB) subtraction and the correction of the inhomogeneous absorption in the FoV by Galactic material along the line of sight (LOS). The analyses performed in these projects consist of imaging analysis to trace and quantify surface brightness features from the corrected images, and spectral analysis to obtain the gas properties of the cluster and filament regions. Particular care of the cosmic X-ray background (CXB) was taken during the analyses.

The eROSITA A3991/95 PV data provide a snapshot of an ongoing large-scale structure (LSS) formation that has been predicted in simulations. The data reveal some infalling substructures/clumps that are connected to the main A3391/95 clusters by continuous warm-hot emission. The ~ 15 Mpc long emission spreads out in the FoV and connects at least five galaxy groups and clusters. In the first project, a comprehensive analysis of cluster outskirts of the Northern Clump cluster was carried out. The Northern Clump (MS 0620.6-5239) is a small galaxy cluster that is infalling toward the A3391 cluster along with the cosmic filament. Its X-ray morphology deviates from the common spherical or elliptical shape, suggesting an interaction with the intracluster medium (ICM) of the A3391 cluster, such as the ram-pressure stripped tail and the boxiness of the main body. The infalling head of the cluster is found to be hotter than the opposite region due to the compression heating. A similar system was found in the simulation and supported the findings. This study helps gain more insight into the LSS formation process.

The second project focuses on the gas properties of the cluster outskirts of the A3391/95 clusters and the detected filaments. The temperatures of the filament-facing cluster outskirts are found to be hotter than expected, which can be attributed to the faster thermalization induced by shocks from the accretion of matter by the filaments. Regarding the filament gas properties, their densities are within the predicted WHIM density range, however, the filaments are slightly hotter (~ 1 keV), but close to the

upper limit of the predicted WHIM temperature range (~ 0.9 keV). We also found that they are poorly enriched by metals ($\leq 10\%$ of solar metallicity). Concerning temperature enhancement, since these short filaments are found in a densely-populated galaxy cluster neighborhood, the A3391/95 filaments are likely experiencing stronger gravitational heating than their longer filaments counterpart. These findings are in agreement with the short filament properties from simulations, as well as other filament measurements that rely on stacking of numerous observations. More galaxy pairs and systems will be identified by eRASS and thus, will statistically increase the number of observational studies of the cluster outskirts and filaments. Furthermore, the high-resolution spectroscopy instrument onboard the newly launched XRISM mission (Resolve) and the future Athena mission (XIFU) will allow us to have better constraints on the metallicities.

In the last project, the outskirts of the Centaurus cluster are explored. The Centaurus (Abell 3526) cluster is one of the closest and brightest clusters in the sky. Early assessment of the LOS velocity distribution of the galaxies showed that the cluster is composed of two substructures: Cen 30, the main substructure located in the center, and Cen 45, about ~ 15 arcmin east of the center. Due to its relatively large extent in the sky, previous detailed X-ray studies were focused on the brightest part of the cluster (up to about 30 arcmin radial distance). Utilizing the combined five eRASS data (eRASS:5), we probed the Centaurus cluster out to ~ 180 arcmin in the imaging analysis and to ~ 90 arcmin in spectral analysis. At first sight, the cluster's X-ray emission appears undisturbed with a bright peak in the center and smooth elliptical morphology. Yet, in-depth studies of the core reveal a wealth of structures as the results of the active galactic nucleus (AGN) feedback hosted by the central galaxy and the merger interaction of the two substructures. In this work, we show that the excess emission along the Cen 45 direction extends out to about 60 arcmin (ram-pressure strip gas) and there are temperature enhancements around the area (shock-heated gas), caused by the ongoing merging with Cen 30. Surface brightness analysis indicates that there is a significant emission of 3.5σ at 90 arcmin and 2.9σ at 100 arcmin. However, supporting the apparent X-ray emission, no trail of galaxies is detected with good significance at larger radii, namely, no trace of a large-scale cosmic filament. This finding is reflected by the lack of excesses in the temperature profiles at the outskirt regime. The metallicities in the outskirts are also following the values of other galaxy cluster outskirts measurements. Hence, while the core is dynamically active, the outskirts of the Centaurus cluster are seemingly undisturbed due to the absence of influence from cosmic filaments.

List of Publications

Relevant First-Author Publications

The following is the list of the relevant first-author publications that are presented in this thesis, which includes two published publications and one submitted publication in the *Astronomy & Astrophysics* journal. In these publications, A.V. conducted the (*XMM-Newton* and *eROSITA*) data reduction, image correction, and scientific analyses. A.V. also contributed to most of the discussion of the results and wrote most of the manuscript.

1. **Veronica, A.**, Su, Y., Biffi, V., Reiprich, T. H., Pacaud, F., Nulsen, P. E. J., Kraft, R. P., Sanders, J. S., Bogdan, A., Kara, M., Dolag, K., Kerp, J., Koribalski, B. S., Erben, T., Bulbul, E., Gatuzz, E., Ghirardini, V., Hopkins, A. M., Liu, A., Migkas, K., Vernstrom. (2022), *The eROSITA view of the Abell 3391/95 field: The Northern Clump – The largest infalling structure in the longest known gas filament observed with eROSITA, XMM-Newton, and Chandra*, *Astronomy & Astrophysics*, **661**, A46 (DOI: [10.1051/0004-6361/202141415](https://doi.org/10.1051/0004-6361/202141415)).
2. **Veronica, A.**, Reiprich, T. H., Pacaud, F., Ota, N., Aschersleben, J., Biffi, V., Bulbul, E., Clerc, N., Dolag, K., Erben, T., Gatuzz, E., Ghirardini, V., Kerp, J., Klein, M., Liu, A., Liu, T., Migkas, K., Ramos-Ceja, M. E., Sanders, J., Spinelli, C. (2024), *The eROSITA view of the Abel 3391/95 field: Outskirts and Filaments*, *Astronomy & Astrophysics*, **681**, A108 (DOI: [10.1051/0004-6361/202347037](https://doi.org/10.1051/0004-6361/202347037)).
3. **Veronica, A.**, Reiprich, T. H., Pacaud, F., Sanders, J., Gatuzz, E., Yeung, M. C. H., Bulbul, E., Ghirardini, V., Liu, A., Mannes, C., Morelli, A., Ota, N. (2024), *The SRG/eROSITA All-Sky Survey: Large-scale view of Centaurus Cluster*, *accepted for publication in the Astronomy & Astrophysics journal on the 17th of December 2024* (DOI: [10.48550/arXiv.2404.04909](https://doi.org/10.48550/arXiv.2404.04909)).

Relevant Co-Authored Publications

1. McCall, H., Reiprich, T. H., **Veronica, A.**, Pacaud, F., Sanders, J., Edler, H. W., Brüggen, M., Bulbul, E., de Gasparin, F., Gatuzz, E., Liu, A., Merloni, A., Migkas, K., Zhang, X. (2024), *The SRG/eROSITA All-Sky Survey: View of the Virgo Cluster*, *Astronomy & Astrophysics journal*, **689**, A113 (DOI: [10.1051/0004-6361/202449391](https://doi.org/10.1051/0004-6361/202449391)).

Author's contribution: A.V. provided the *eROSITA* data reduction and image correction pipeline, and image manipulation scripts. A.V. also helped with technical and scientific supervision and gave feedback on the manuscript.

2. Dietl, J., Pacaud, F., Reiprich, T. H., **Veronica, A.**, Migkas, K., Spinelli, C., Dolag, K., Seidel, B. (2024), *Discovery of a >13 Mpc long X-ray filament between two galaxy*

clusters beyond three times their virial radii, *Astronomy & Astrophysics journal*, 691, A286 (DOI: [10.1051/0004-6361/202449354](https://doi.org/10.1051/0004-6361/202449354)).

Author's contribution: A.V. provided the eROSITA data reduction and image correction pipeline, and surface brightness analysis scripts. A.V. helped with technical and scientific supervision and gave feedback that helped improve the manuscript.

3. Migkas, K., Kox, D., Schellenberger, G., **Veronica, A.**, Pacaud, F., Reiprich, T. H., Bahar, Y. E., Balzer, F., Bulbul, E., Comparat, J., Dennerl, K., Freyberg, M., Garrel, C., Ghirardini, V., Grandis, S., Kluge, M., Liu, A., Ramos-Ceja, M. E., Sanders, J., Zhang, X. (2024), *The SRG/eROSITA All-Sky Survey: SRG/eROSITA cross-calibration with Chandra and XMM-Newton using galaxy cluster gas temperatures*, *Astronomy & Astrophysics journal*, 688, A107 (DOI: [10.1051/0004-6361/202349006](https://doi.org/10.1051/0004-6361/202349006)).

Author's contribution: A.V. provided the eROSITA data reduction and spectral analysis scripts to D.K., helped with the technical and scientific supervision of D.K., had discussions of the methods with K.M., as well as wrote a subsection of the manuscript.

4. Bulbul, E., Liu, A., Kluge, M., Zhang, X., Sanders, J. S., Bahar, Y. E., Ghirardini, V., Artis, E., Seppi, R., Garrel, C., Ramos-Ceja, M. E., Comparat, J., Balzer, F., Böckmann, K., Brüggén, M., Clerc, N., Dennerl, K., Dolag, K., Freyberg, M., Grandis, S., Gruen, D., Kleinebreil, F., Krippendorf, S., Lamer, G., Merloni, A., Migkas, K., Nandra, K., Pacaud, F., Predehl, P., Reiprich, T. H., Schrabback, T., **Veronica, A.**, Weller, J., Zelmer, S. (2024), *The SRG/eROSITA All-Sky Survey – The First Catalog of Galaxy Clusters and Groups in the Western Galactic Hemisphere*, *Astronomy & Astrophysics journal*, 685, A106 (DOI: [10.1051/0004-6361/202348264](https://doi.org/10.1051/0004-6361/202348264)).

Author's contribution: A.V. performed checks on the sub-sample of the preliminary galaxy cluster catalog. A.V. contributed comments that helped improve the manuscript.

5. Böckmann, K., Brüggén, M., Koribalski, B., **Veronica, A.**, Reiprich, T. H., Bulbul, E., Bahar, Y. E., Balzer, F., Comparat, J., Garrel, C., Ghirardini, V., Gürkan, G., Kluge, M., Leahy, D., Merloni, A., Liu, A., Ramos-Ceja, M. E., Salvato, M., Sanders, J., Shabala, S., Zhang, X. (2023), *Central radio galaxies in galaxy clusters: Joint surveys by eROSITA and ASKAP*, *Astronomy & Astrophysics*, 677, A188 (DOI: [10.1051/0004-6361/202346912](https://doi.org/10.1051/0004-6361/202346912)).

Author's contribution: A.V., K.B., T.R., and M.B., had several remote scientific discussions. A.V. helped with navigating the X-ray catalog and contributed comments that helped improve the manuscript.

6. Koribalski, B., **Veronica, A.**, Brüggén M., Reiprich, T. H., Dolag, K., Heywood, I., Andernach, H., Dettmar, R. J., Hoeft, M., Zhang, X., Bulbul, E., Józsa, G. I. G., English, J., Saponara, J. (2023), *MeerKAT discovery of a double radio relic and odd radio circle*, *Monthly Notices of the Royal Astronomical Society*, 531, 3 (DOI: [10.1093/mnras/stae1254](https://doi.org/10.1093/mnras/stae1254)).

Author's contribution: A.V. performed the eROSITA data reduction, image correction, and spectral analysis. Additionally, A.V. wrote some parts of the manuscript.

7. Spinelli, C., **Veronica, A.**, Pacaud, F., Reiprich, T. H., Migkas, K., Xu, W., Ramos-Ceja, M. E. (2023), *XMM-Newton follow-up of a sample of galaxy groups detected in the ROSAT All-Sky Survey*, subm. to the *Astronomy & Astrophysics journal*.

Author's contribution: A.V. provided the galaxy catalog filtering and spectral fitting scripts, conducted optical member galaxy identification, and edits that helped improve the manuscript. A.V. and C.S. had technical discussions about the *XMM-Newton* pipeline.

8. Whelan, B., **Veronica, A.**, Pacaud, F., Reiprich, T. H., Bulbul, E., Ramos-Ceja, M. E., Sanders, J. S., Aschersleben, J., Iljenkarevic, J., Migkas, K., Freyberg, M., Dennerl, K., Kara, M., Liu, A., Ghirardini, V., Ota, N. (2022), *X-ray studies of the Abell 3158 galaxy cluster with eROSITA*, *Astronomy & Astrophysics*, 663, A171 (DOI: DOI: [10.1051/0004-6361/202141621](https://doi.org/10.1051/0004-6361/202141621)).

Author's contribution: A.V. provided the eROSITA flare-filtering and surface brightness analysis scripts, helped to re-run the temperature map analysis, and generated surface brightness profiles.

Contents

1	Introduction	2
1.1	Motivation	2
1.2	Galaxy Clusters	3
1.3	Multiwavelength Views of Galaxy Clusters	4
1.3.1	Optical and Near Infrared	4
1.3.2	Millimeter	7
1.3.3	Radio	8
1.4	X-ray Observations of Galaxy Clusters	9
1.4.1	Emission Processes	10
1.4.2	Spatial Distribution of the ICM	13
1.5	X-ray Instruments	15
1.5.1	<i>ROSAT</i>	15
1.5.2	<i>Chandra</i>	16
1.5.3	<i>XMM-Newton</i>	16
1.5.4	<i>Suzaku</i>	16
1.5.5	eROSITA	17
1.6	Background Components of X-ray Observations	19
1.6.1	The Particle Induced Background	19
1.6.2	The Cosmic X-ray Background	20
1.7	Galaxy Cluster Outskirts	21
1.7.1	The Missing Baryon Problem	22
1.8	Cosmological Framework	23
1.8.1	Λ CDM Model	23
1.8.2	Cosmological Distances	24
2	Summary of the Projects	26
2.1	Methodology: eROSITA Data Reduction and Science Analysis Procedures	26
2.2	The eROSITA view of the Abell 3391/95 field: The Northern Clump	27
2.3	The eROSITA view of the Abell 3391/95 field: Cluster outskirts and filaments	28
2.4	The SRG/eROSITA All-Sky Survey: Large-scale view of the Centaurus cluster	30
3	Methodology: eROSITA Data Reduction and Science Analysis Procedures	33
3.1	Data and Software Availability	34
3.1.1	The A3391/95 Cluster System Projects: eROSITA-DE Early Data Release (EDR)	34
3.1.2	The Centaurus Cluster Project: eROSITA-DE Data Release 1 (DR1)	34
3.1.3	eROSITA Science Analysis Software System (eSASS)	34
3.2	Data Reduction	36

3.2.1	Event File Cleaning	37
3.2.2	Soft Proton Flare Filtering	37
3.2.3	Image Generations	37
3.3	Image Correction	39
3.3.1	PIB Subtraction	39
3.3.2	Relative Galactic Absorption Correction	40
3.3.3	Exposure Correction	42
3.4	Imaging Analysis	44
3.4.1	Wavelet Filtering and Source Catalog Generation	44
3.4.2	Imaging Processing Techniques	45
3.4.3	Surface Brightness Profile	47
3.5	Spectral Analysis	49
3.5.1	Components	49
3.5.2	Strategy	50
3.5.3	Gas Properties and the Derivative Quantities	51
4	The eROSITA view of the Abell 3391/95 field: The Northern Clump	
	<i>The largest infalling structure in the longest known gas filament observed with eROSITA, XMM-Newton, and Chandra</i>	54
4.1	The Northern Clump	56
4.2	Instrument Independent Surface Brightness Profiles	56
4.3	XMM-Newton Outer Spectral Profiles	57
4.4	Preliminary Assessment of the Northern Filament with eROSITA	59
4.5	Conclusions and Outlooks	60
5	The eROSITA view of the Abell 3391/95 field: Cluster outskirts and filaments	62
5.1	Configurations	63
5.1.1	Surface Brightness Analyses	63
5.1.2	Spectral Analyses	64
5.2	Surface Brightness Profiles	65
5.3	Spectral Analysis Results	65
5.3.1	Cluster Outskirts	67
5.3.2	Filaments	68
5.4	Summary and Conclusions	71
6	The SRG/eROSITA All-Sky Survey: Large-scale view of the Centaurus cluster	73
6.1	Configurations	74
6.1.1	The Cosmic X-ray Background	74
6.1.2	Surface Brightness and Spectral Analyses	75
6.2	Redshift Analysis	76
6.3	Imaging Analysis	78
6.3.1	GGM Images	78
6.3.2	Surface Brightness Analysis	79
6.4	Spectral Analysis	81
6.4.1	Core	83
6.4.2	Eastern Excess	84
6.4.3	$r > 0.5R_{500}$	84
6.5	Summary and Conclusions	85

Bibliography	88
A The eROSITA view of the Abell 3391/95 field: The Northern Clump	
<i>The largest infalling structure in the longest known gas filament observed with eROSITA, XMM-Newton, and Chandra</i>	98
B The eROSITA view of the Abell 3391/95 field: Cluster outskirts and filaments	123
C The SRG/eROSITA All-Sky Survey: Large-scale view of the Centaurus cluster	141
List of Figures	161
List of Tables	163

Chapter 1

Introduction

1.1 Motivation

Within the framework of the Λ CDM cosmological model, in which the Universe is dominated by dark energy and cold dark matter, structures are formed by a hierarchical process. Small structures form through gravitational instabilities and evolve into larger structures through mergers and accretion of sub-structures. Galaxy clusters, the largest virialized objects in the universe, are the culmination of this process. They represent the highest-density peaks of the cosmic web (e.g., [Bond et al., 1996](#)) and are connected by the cosmic filaments that transport matters into them, supporting their growth (e.g., [Springel et al., 2006](#)). At the outskirts of galaxy clusters, where the gravitational pull of the cluster intersects with the cosmic filaments, the imprints of these accretion processes (e.g., shocks, gas clumping, gas turbulence, and bulk motions) can be traced.

Furthermore, the outskirts of galaxy clusters are important for locating the cosmic filaments. It is known that there are discrepancies in the observed amount of the baryons with those predicted by Big Bang nucleosynthesis and the observations of the cosmic microwave background. The large-scale cosmological hydrodynamic simulations predicted that these "missing baryons" (about 30 – 40% of the total baryons in the local Universe) may reside in the warm-hot intergalactic medium (WHIM) in the cosmic filaments ([Cen & Ostriker, 1999](#); [Davé et al., 2001](#)). Due to its properties, electron densities in the range of $n_e \approx 10^{-6} - 10^{-4} \text{ cm}^{-3}$ and temperature in the range of $T = 10^5 - 10^7 \text{ K}$ that corresponds to $k_B T \approx 0.009 - 0.862 \text{ keV}$ ([Nicastro et al., 2017](#)), the WHIM is faint and detecting them is challenging. One method of detecting the WHIM is through absorption lines, however, it relies on the presence of a bright background source (e.g., a quasar or a gamma-ray burst) along the line of sight, thus, does not facilitate the spatially-resolved study of the WHIM ([Reiprich et al., 2021](#)). Since the X-ray emissivity is proportional to the square of the electron density, attempts to detect the filaments via X-ray emission should be directed at their densest parts, namely, between a pair of nearby galaxy clusters (e.g., [Kull & Böhringer, 1999](#); [Vazza et al., 2019](#)) and at the outskirts of a galaxy cluster (e.g., [Reiprich et al., 2013](#); [Nicastro et al., 2018](#)).

The extended ROentgen Survey with an Imaging Telescope Array (eROSITA; [Predehl et al., 2021](#)) is the X-ray instrument on board the Spectrum-Roentgen-Gamma (SRG) mission. It has a wide field of view (FoV) of 1.03 degrees and also operates in survey mode, such that, it can easily cover a cluster out to large radii. It has a superior soft X-ray sensitivity, namely, the effective area of the seven combined eROSITA telescope modules (TMs) in the 0.5 – 2.0 keV energy band is slightly higher than the combined *XMM-Newton* cameras ([Predehl et al., 2021](#)). The FoV-averaged PSF ($\sim 26 \text{ arcsec}$) is significantly better than that of the *Suzaku* satellite, allowing us to remove unrelated background sources to much lower flux levels. The energy resolution at soft energies is better than for any other operating X-ray satellite CCD,

which enables better characterization of the soft band emission lines. These specifications, therefore, make eROSITA an excellent instrument for studying the outskirts of galaxy clusters and tracing the cosmic filaments.

In this dissertation, explorations of galaxy cluster outskirts of two nearby systems using eROSITA data are presented. In the first two projects, the eROSITA Performance Verification observations on the interacting galaxy cluster system, Abell 3391 and Abell 3395 (A3391/95), were utilized. These observations reveal a view of an ongoing structure formation as predicted in simulations (Reiprich et al., 2021; Biffi et al., 2022) that includes discoveries of a continuous warm-hot emission (~ 15 Mpc) connecting at least five galaxy groups and clusters and some infalling clumps toward the A3391/95 system. In the A3391/95 projects, the characterization of the detected filaments and the infalling clumps were covered. In the third project, the eROSITA All-Sky Survey data (eRASS; Predehl et al., 2021; Merloni et al., 2024) were used for the analysis of the Centaurus cluster (Abell 3526). The Centaurus cluster is one of the closest and X-ray brightest clusters in the sky. Due to its proximity, the cluster has a relatively large spatial extent in the sky, and covering the cluster out to the outskirts with previous X-ray instruments will require numerous observations. Hence, previous X-ray studies focus mainly on the brighter part of the cluster. With eRASS data, we can see the large-scale view of the cluster. Extensive image correction and analysis, as well as galaxy distribution analysis to trace any large-scale structures connected to the cluster, were done. More importantly, we obtained ICM properties out to R_{200} in various directions, increasing the probed volume of the Centaurus cluster by a factor of almost 30.

This dissertation is outlined as follows: this chapter introduces the necessary theoretical background. In Chapter 3, all the technicalities are described, such as the used eROSITA data and software versions, the developed data reduction and image correction steps, and the science analysis strategies. Chapter 4 summarizes the contents of the first published paper (Veronica et al., 2022)¹. The paper is focused on the outskirts of the Northern Clump, which is the largest infalling structure in the filament in the A3391/95 system. The contents of the second publication (Veronica et al., 2024a)² are outlined in Chapter 5, where the characterization of the gas properties of the cluster outskirts and the detected filaments in the A3391/95 system is pursued. Last but not least, in Chapter 6 (Veronica et al., 2024b)³, the findings from the analyses of the Centaurus cluster are reported. Unless stated otherwise, the primary sources of reference in this first chapter are cosmology, astronomy, and astrophysics textbooks, as well as X-ray astronomy and galaxy cluster books and reviews by Sarazin (1988), Unsöld & Baschek (2001), Arnaud (2005), Arnaud et al. (2011), Ota (2012), Kravtsov & Borgani (2012), Bennett et al. (2013), Schneider (2015).

1.2 Galaxy Clusters

Clusters of galaxies are the largest virialized objects in the Universe. They consist of up to thousands of galaxies that are gravitationally bound together within a radius of between one and five million pc⁴. The total mass of a galaxy cluster typically ranges between 10^{14} and $10^{15} M_{\odot}$ ⁵. Even though galaxy clusters are optically represented by the agglomeration of galaxies, they only contribute a small fraction of the total mass ($\sim 2\%$; Lin et al., 2003). With the dawn of X-ray astronomy in the late 1960s, it was discovered that hot plasma permeates between the galaxies in clusters (Kellogg et al., 1971; Gursky et al., 1971).

¹Veronica, A., Su, Y., Biffi, V., et al. 2022, A&A, 661, A46

²Veronica, A., Reiprich, T. H., Pacaud, F., et al. 2024a, A&A, 681, A108

³Veronica, A., Reiprich, T. H., Pacaud, F., et al. 2024b, arXiv e-prints, arXiv:2404.04909 (submitted to A&A)

⁴1 parsec (pc) = 3.086×10^{18} cm.

⁵The mass is measured in the Sun mass unit. $1 M_{\odot} \approx 1.989 \times 10^{30}$ kg.

This so-called intracluster medium (ICM) has a temperature range of about 10^7 to 10^8 K (1 to 10 keV)⁶, a typical luminosity of $\sim 10^{43} - 10^{45}$ erg s⁻¹, and gas densities that rapidly fall from 10^{-2} cm⁻³ in the centers to 10^{-4} cm⁻³ in the outskirts (Markevitch & Vikhlinin, 2007). These properties make galaxy clusters among the brightest extragalactic X-ray sources. The X-ray emission from clusters is spatially extended and not time variable, implying that the emission is diffuse and does not originate from the galaxies (Elvis, 1976; Schneider, 2015). While the ICM is the most massive visible component of galaxy clusters, it only contributes to only about 15% of the total cluster mass. The depth of the gravitational potential well of galaxy clusters as inferred from the galaxy velocity dispersions or the gravitational lens effect of background sources (Schneider, 2015) suggests an additional component that dominates the cluster total mass ($\sim 80\%$), that is the dark matter (Zwicky, 1937). A tiny fraction of the cluster's total baryonic mass is embedded in a population of relativistic charged particles produced during the cluster mergers. In the presence of a magnetic field, these particles will be accelerated and generate synchrotron emissions that are observable in the radio band.

Galaxy clusters are powerful tools to probe cosmology and astrophysical processes. Their distributions in space, mass, and evolution allow us to probe the physics of structure formation and different cosmological models (e.g., Allen et al., 2011; Kravtsov & Borgani, 2012; Pratt et al., 2019). Being located at the intersections of the cosmic filaments, galaxy clusters are also good tracers of the large-scale structure (LSS) of the Universe (e.g., Springel et al., 2006; Reiprich et al., 2013; Walker et al., 2019). Moreover, in contrast to galaxies, galaxy clusters can retain their gas due to being in deeper gravitational wells. This enables us to trace the production means and distribution of metals⁷ in the Universe (e.g., Biffi et al., 2018a; Mernier et al., 2018). Galaxy cluster mergers, the second most energetic events in the Universe after the Big Bang, provide valuable opportunities to study hydrodynamical processes, such as shocks, contact discontinuities, gas sloshing, and turbulence (e.g., Buote, 2002; Sarazin, 2002; ZuHone & Su, 2022).

1.3 Multiwavelength Views of Galaxy Clusters

As hinted in the previous section, different components of a galaxy cluster can be traced in different wavelengths. This section will provide an overview of the various other observational methods used to study galaxy clusters.

1.3.1 Optical and Near Infrared

Optical Cluster Catalogs

In the optical and near-IR, galaxy clusters are seen as an over-density of galaxies (mostly ellipticals and lenticulars) and the emission is in the form of starlight (see Figure 1.1a). Starting from 1930, more systematic galaxy surveys were performed by H. Shapley, E. Hubble, and others. These surveys produced some of the first widely used optical galaxy cluster catalogs. For example, the Abell catalog of rich clusters of galaxies by George O. Abell with 4073 clusters listed (Abell, 1958; Abell et al., 1989) and the Catalogue of Galaxies and of Clusters of Galaxies by Fritz Zwicky (Zwicky et al., 1961) were compiled using the Palomar Observatory Sky Survey. The main observables of the optical galaxy cluster surveys are the richness (number of member galaxies within an aperture), galaxy magnitude/color, and luminosity. While optical observations have proved to be successful in detecting galaxy clusters, this

⁶In the studies of galaxy clusters, the temperature is commonly measured in the unit of energy, $k_B T$, where $k_B = 8.617 \times 10^{-3}$ eV K⁻¹ is the Boltzmann constant.)

⁷In astronomy, chemical elements that are heavier than helium are called metals.

method is susceptible to the projection effect from background and foreground galaxies, which results in false detections.

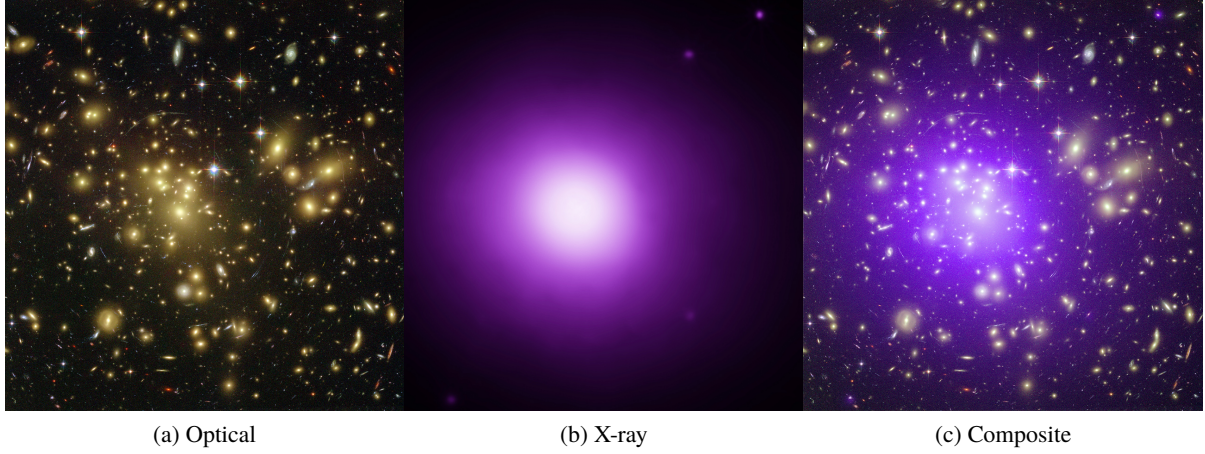


Figure 1.1: (a) Optical image of the Abell 1689 cluster (A1689) taken by the Hubble Space Telescope. The image is a composite of three optical images in different wavelength bands: 475 nm in blue, 625 nm in green, and 850 nm in red. The arc-shaped objects around the cluster are background galaxies whose lights are bent by the gravity (gravitational lensing) of the A1689. Credit: NASA; ESA; L. Bradley (Johns Hopkins University); R. Bouwens (University of California, Santa Cruz); H. Ford (Johns Hopkins University); and G. Illingworth (University of California, Santa Cruz). (b) X-ray image taken by the NASA’s *Chandra* X-ray Observatory, showing the ICM of the A1689 cluster. Credit: NASA/CXC/MIT/E.-H Peng et al. (c) Composite image of the optical and X-ray images. Credit: NASA/STScI.

Mapping Large-Scale Structures

Optical galaxy surveys have also revealed that galaxies are not randomly distributed in space. They spread out in chains and sheets, forming coherent large-scale structures. In the intersections of these sheets are the galaxy clusters, connected by the chains and grouped in superclusters. It was also discovered that between these structures are giant empty regions, almost spherical, which are called voids. Hubble’s discovery, that the Universe is expanding, is the basis of charting the distances of the objects in the Universe. The expansion is described by the Hubble’s law,

$$v = H_0 \times d, \quad (1.1)$$

where v is the velocity of a galaxy moving away from us (recession velocity), d is its distance, and H_0 is the so-called Hubble’s constant. The recession velocity can be inferred from the shift of the emission or absorption lines of the observed spectra of a galaxy, i.e., redshift z , that is,

$$z = \frac{\lambda_{\text{obs}} - \lambda_{\text{rest}}}{\lambda_{\text{rest}}}, \quad (1.2)$$

where λ_{obs} is the observed wavelength of the line and λ_{rest} is the wavelength of the line at rest (laboratory reference). For nearby galaxies ($z \ll 1$), the recession velocity is $v = cz$, where c is the speed of light.

In Figure 1.2, three-dimensional galaxy distribution from optical redshift surveys is shown. Each of

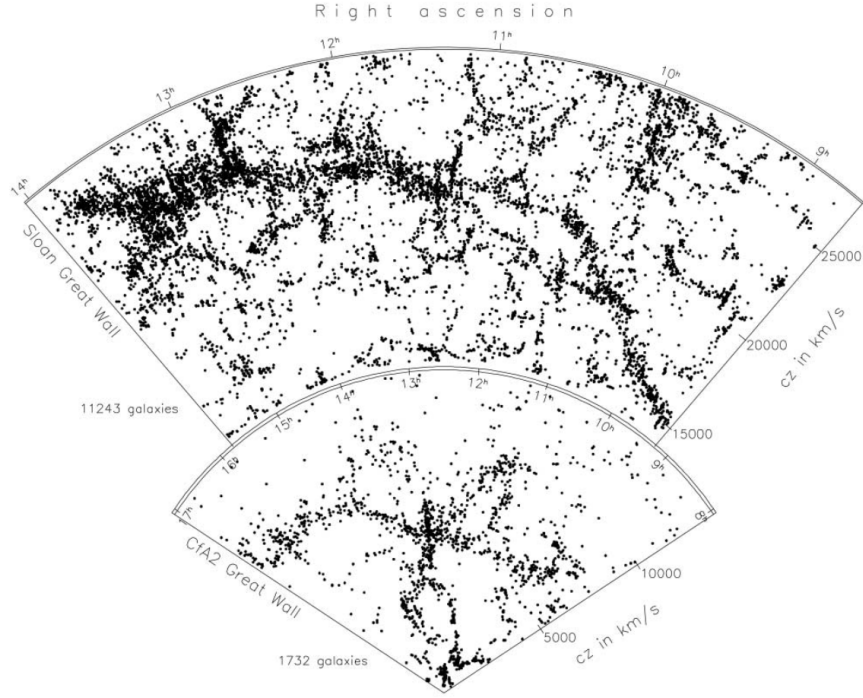


Figure 1.2: Distribution of galaxies in two slices of the Universe extending outward from the Milky Way Galaxy (bottom vertex). The bottom slice shows the CfA2 galaxy redshift survey and the upper slice shows the SDSS survey. Each dot represents a galaxy. Source: [Gott et al. \(2005\)](#).

the wedges is a slice of the Universe that stretches farther out from the Milky Way (bottom vortex) to greater distances. The galaxies are represented by the dots and placed at their measured redshift distances. The bottom wedge displays the galaxy redshift distribution from the second Center for Astrophysics (CfA2) redshift survey started by John Huchra and Margaret Geller in 1985 at the Smithsonian Astrophysical Observatory ([Geller & Huchra, 1989](#)). The CfA2 map reveals a structure stretching between 8^{h} and 17^{h} in Right Ascension (RA) and between 5,000 km/s and 10,000 km/s, named the CfA2 Great Wall. The second wedge shows the galaxy redshift distribution from the Sloan Digital Sky Survey (SDSS), showing a great structure, called the Sloan Great Wall, that extends between 9^{h} and 14^{h} in RA ([Gott et al., 2005](#)).

Total Masses

For individual optical observations, one of the main objectives is to estimate the total masses of galaxy clusters, and hence more involved parameters are acquired, such as the galaxy number density and their velocities. The total masses of galaxy clusters were first calculated using the velocity dispersion of the member galaxies by [Zwicky \(1933\)](#) (Coma cluster) and [Smith \(1936\)](#) (Virgo cluster). With the assumption that galaxy clusters are gravitationally bound systems, we can apply the virial theorem that states that the total kinetic energy of the system is equal to half of its potential energy,

$$2E_{\text{kin}} + E_{\text{pot}} = 0. \quad (1.3)$$

From Equation 1.3, the total mass of a cluster, M_{tot} , can be calculated as follows,

$$M_{\text{tot}} = \frac{r_{\text{Grav}} \sigma^2}{G} \quad (1.4)$$

where r_{Grav} is the gravitational radius, σ is the mass-weighted velocity dispersion of the member galaxies, and G is the gravitational constant. Using this method, Zwicky found greater masses than implied by the optical luminosities of galaxy clusters and hence concluded that visible mass from stars in galaxies is not the main contributor to the total mass of the objects.

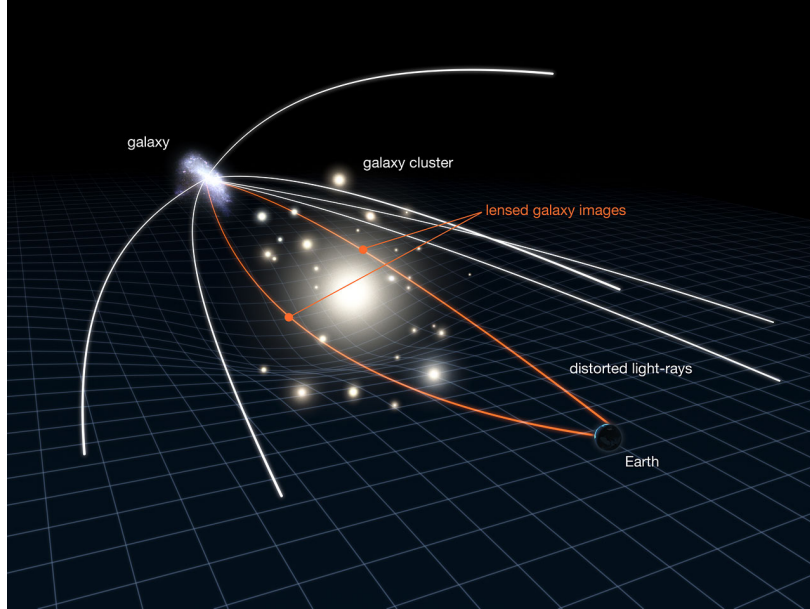


Figure 1.3: Illustration of gravitational lensing of a background galaxy by a galaxy cluster. Credit: NASA, ESA & L. Calçada.

Another method of measuring galaxy cluster masses is by using the gravitational lensing phenomenon (e.g., [Schneider et al., 1992](#); [Bartelmann, 2010](#)). According to Einstein's general theory of relativity, the gravity of a massive object can act as a lens that distorts the light rays passing nearby. This phenomenon is illustrated in Figure 1.3, where the light from a background galaxy is bent as it passes near the gravitational well of a galaxy cluster. This generates distortions (arc shape) and multiple images of the background sources. In Figure 1.1a, we can see multiple blue arcs around the cluster. By studying the degree of the distortions seen in the images, the masses of the lenses, e.g., galaxy clusters, can be inferred. However, interpreting the lensing analysis is limited not only by the number of available background galaxies with good shape measurements but also by the knowledge of their distance distribution inferred through their redshifts.

1.3.2 Millimeter

The detection of galaxy clusters can also be done at the millimeter wavelengths through the Sunyaev-Zel'dovich effect ([Sunyaev & Zeldovich, 1972](#)) on the cosmic microwave background (CMB) photon (e.g., [Carlstrom et al., 2002](#), for a review). The CMB is the remnant radiation when the Universe was about 380,000 years old, the epoch of recombination ($z_{\text{rec}} = 1100$). During this time, due to the expansion, the Universe had cooled down to a temperature of about 3000 K, allowing nuclei and electrons to recombine to form neutral atoms. As most of the electrons were bound into atoms, the Universe became transparent for photons to travel freely. The CMB radiation should exhibit a black-body spectrum with a peak wavelength at ~ 1000 nm. However, due to the expansion of the Universe, the wavelengths of these photons have been shifted by a factor of 1100, into the millimeter regime. Today, the CMB radiation has a temperature of 2.72548 K ([Fixsen, 2009](#)).

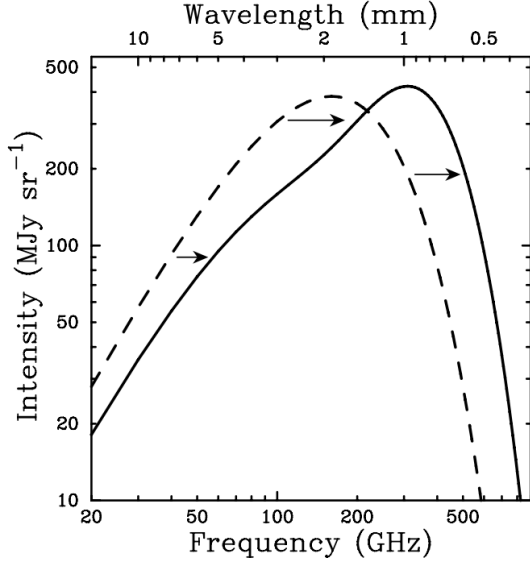


Figure 1.4: The undistorted and distorted CMB spectrum by the Sunyaev-Zel'dovich effect is shown by the dashed and solid lines, respectively. The magnitude of the effect has been exaggerated to show the small effect. Source: [Carlstrom et al. \(2002\)](#).

All-sky survey maps of the CMB, e.g., by the COBE satellite ([Smoot et al., 1992](#); [Bennett et al., 1996](#)), the WMAP ([Bennett et al., 2003](#)), more recently by the Planck observatory (e.g., [Planck Collaboration et al., 2016, 2020b](#)), consistently reveal tiny CMB temperature fluctuations in the order of 10^{-5} , showing the inhomogeneities (anisotropy) at the early Universe

A small fraction of the CMB photons that pass through a galaxy cluster will get scattered off by the high-energy electrons of the ICM via the inverse Compton process. The energy of the CMB photon is boosted by $\sim k_B T / m_e c^2$ causing a small distortion ($\lesssim 1$ mK) in the CMB spectrum. Figure 1.4 shows the CMB spectral distortion by the SZ effect, where the magnitude has been exaggerated to illustrate the small effect. The SZ effect is visible as an intensity decrease below 218 GHz and an increase above the cut. The SZ effect can be formulated as a temperature change as,

$$\frac{\Delta T_{SZ}}{T_{CMB}} = f(x) \cdot y = f(x) \int n_e \frac{k_B T_e}{m_e c^2} \sigma_T dl, \quad (1.5)$$

where $x \equiv h\nu / k_B T_{CMB}$ is the dimensionless frequency, n_e and T_e are the electron number density and temperature, respectively, y is the Compton y -parameter, and σ_T is the Thomson cross-section for electron scattering defined as,

$$\sigma_T = \frac{8\pi}{3} \left(\frac{e^2}{m_e c^2} \right)^2. \quad (1.6)$$

The Compton y -parameter is proportional to the gas temperature or the integral of the gas pressure along the LOS of the cluster, $P = nk_B T$, and can be used for estimating the cluster masses. Since the SZ effect is independent of redshift, it is also ideal for detecting high-redshift cluster (e.g., [Bleem et al., 2015](#); [Huang et al., 2020](#)).

1.3.3 Radio

Radio emission in galaxy clusters can generally be divided into extended diffuse radio emission and diffuse source from individual galaxies (see, e.g., [Mills, 1960](#); [Willson, 1970](#); [Feretti & Giovannini, 2008](#); [van Weeren et al., 2019](#); [Hlavacek-Larrondo et al., 2022](#); [O'Dea & Baum, 2023](#), and the references therein). The presence of these radio sources shows that the ICM contains relativistic particles and magnetic fields. The relativistic particles gyrate around the magnetic field lines and generate synchrotron emission.

The first type of extended radio emission can be categorized into three main classes: First, the radio halos, which are large-scale diffused radio emissions that are about a few Mpc in size. They are located in the center of a merging cluster and do not correspond to any individual sources, such as a galaxy or an active galactic nucleus (AGN). A sub-class of this source is mini-halos, which are smaller in size and

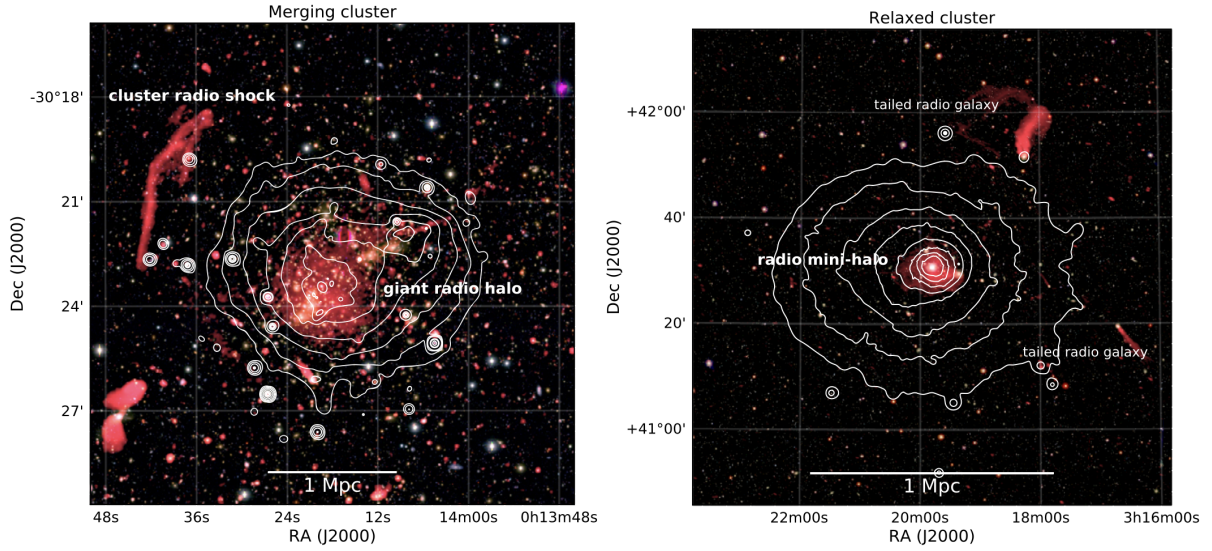


Figure 1.5: *Left*: Radio image in 1 – 4 GHz of the merging cluster A2744 taken by the VLA radio telescope. The white contours are generated from the *Chandra* X-ray image. *Right*: Radio image in 230 – 470 MHz of the relaxed, cool-core Perseus cluster. The white contours are generated from the *XMM-Newton* X-ray image. The radio structures are labeled on both panels. Source: [van Weeren et al. \(2019\)](#).

located in the centers of relaxed clusters. The two types of radio halos can be observed in the centers of two galaxy clusters displayed in Figure 1.5 (in red). Second, the radio relics/shocks, which are extended radio emissions ($\gtrsim 1$ Mpc) found in the periphery of merging galaxy clusters. The structures trace the locations of shock fronts where the particles are (re-)accelerated. A radio relic is shown in the left panel of Figure 1.5. Third, radio phoenixes. They are the AGN fossil radio plasmas that are re-energized by merger processes in the ICM.

Another type of diffuse radio emission in galaxy clusters is associated with the AGN hosted in radio galaxies. They extend between a few kpc and about 1 Mpc, and thus, their structures can be affected by ICM and vice versa. For instance, their jets and lobes can be bent/distorted showing their movements relative to ICM, resulting in the tailed radio sources that can be narrow-angle tail (NAT) or wide-angle tail (WAT) radio sources (right panel of Figure 1.5). The interaction of powerful radio sources in the center of cool-core clusters can generate radio-bubble-filled X-ray cavities. This so-called AGN feedback has been known to be a reliable source of heating that balances the radiative losses in the cores of clusters with central temperature drops, preventing catastrophic cooling (e.g., [McNamara & Nulsen, 2007](#)). In Figure 1.6, the galaxy cluster MS0735.6+7421 in three wavelengths is displayed. The diffuse X-ray emission from *Chandra* is shown in blue, and it shows a pair of X-ray cavities that anti-correlate with the radio lobes shown in red (taken by the Very Large Array radio telescope). The optical image from the HST is displayed in yellow and it shows that the radio emission originated from the AGN hosted in the cluster's brightest cluster galaxy (BCG).

1.4 X-ray Observations of Galaxy Clusters

The most massive baryonic component of galaxy clusters is the hot, diffused, collisionally ionized, and optically thin plasma, known as the intracluster medium (ICM). Since only gas retained in the deepest

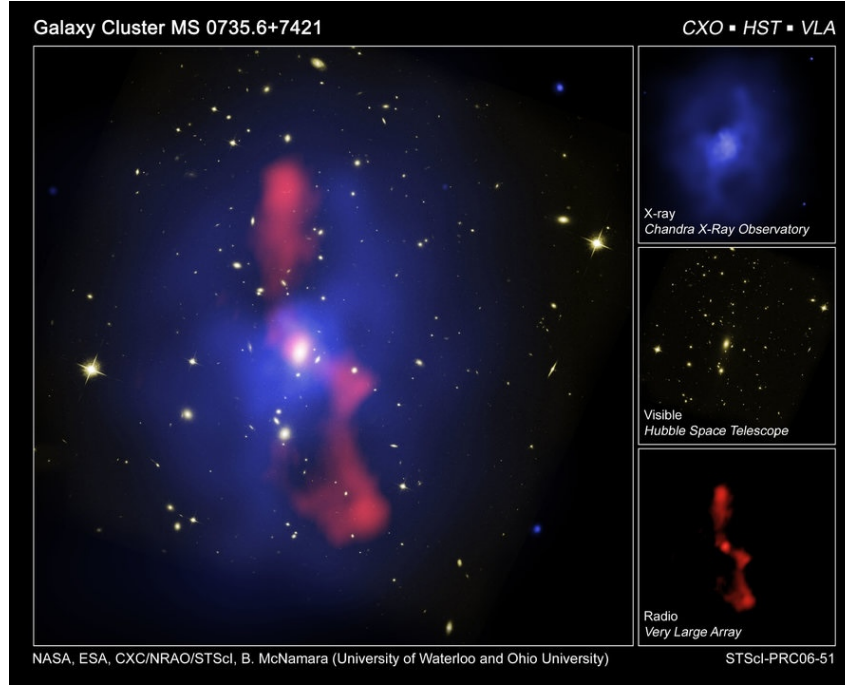


Figure 1.6: Composite image of the galaxy cluster MS0735.6+7421. The diffuse X-ray emission from *Chandra* is shown in blue, and it shows a pair of X-ray cavities that anti-correlate with the radio lobes shown in red (taken by the VLA telescope). The optical image from the HST in yellow shows that the radio emission originated from the AGN hosted in the cluster’s BCG. Credit: Hubble and Chandra Image: NASA, ESA, CXC, STScI, and B. McNamara (University of Waterloo); Very Large Array Telescope Image: NRAO, and L. Birzan and team (Ohio University).

gravitational potential can be heated up to X-ray emitting temperatures, then if extended hot gas is present, there must likely be a galaxy cluster, i.e., X-ray observations of galaxy clusters are not affected by a strong projection effect. Moreover, the ICM preserves the imprints of hydrodynamical processes and metal enrichments, making it an ideal tool to probe the physics involving these processes.

1.4.1 Emission Processes

While various processes occur in the ICM, the primary emission processes that shape the X-ray spectra of galaxy clusters are bremsstrahlung (continuum emission) and line emissions.

Thermal Bremsstrahlung

The thermal bremsstrahlung (free-free emission) is the result of the acceleration of electrons in the presence of the Coulomb field of protons and atomic nuclei. It is the dominant process for ICM with a temperature $k_B T \gtrsim 2$ keV and metallicities range between 0.1 and one times the solar value (Z_\odot). The emissivity at a given frequency ν is formulated as

$$\epsilon_\nu^{ff} = \frac{2^5 \pi e^6}{3 m_e c^3} \left(\frac{2\pi}{3 m_e k_B} \right)^{\frac{1}{2}} Z^2 n_e n_i g_{ff}(Z, T_e, \nu) T_e^{-\frac{1}{2}} e^{-\frac{h\nu}{k_B T_e}}, \quad (1.7)$$

where n_e and T_e are the electron number density and temperature, respectively, n_i stands for the ion number density, Z is the ion charge in the plasma, and g_{ff} is the Gaunt factor to correct for quantum mechanical effects, that is of order unity ($g_{ff} \approx 0.9(h\nu/k_B T)^{-0.3}$). When integrating over all frequencies, the total bremsstrahlung emissivity is approximately

$$\epsilon^{ff} = \frac{2^5 \pi e^6}{3 h m_e c^3} \left(\frac{2 \pi k_B}{3 m_e} \right)^{\frac{1}{2}} Z^2 n_e n_i g_B(Z, T_e) T_e^{\frac{1}{2}} \quad (1.8)$$

$$\propto T_e^{\frac{1}{2}} n_e^2,$$

where $g_B \approx 1.2$ is the average of g_{ff} over all frequencies.

Two fundamental ICM properties, the gas temperature, and the emission measure, can be readily obtained from the continuum emission. The first quantity is derived from the exponential cut-off marking the transition from a power-law regime at lower energies to an exponential drop at higher energies. The exponential drops at higher energies of ICM with different temperatures (1 keV in black, 3 keV in red, and 9 keV in green) are compared in the left panel of Figure 1.7. The latter quantity is defined as

$$EM = \int_V n_e n_H dV. \quad (1.9)$$

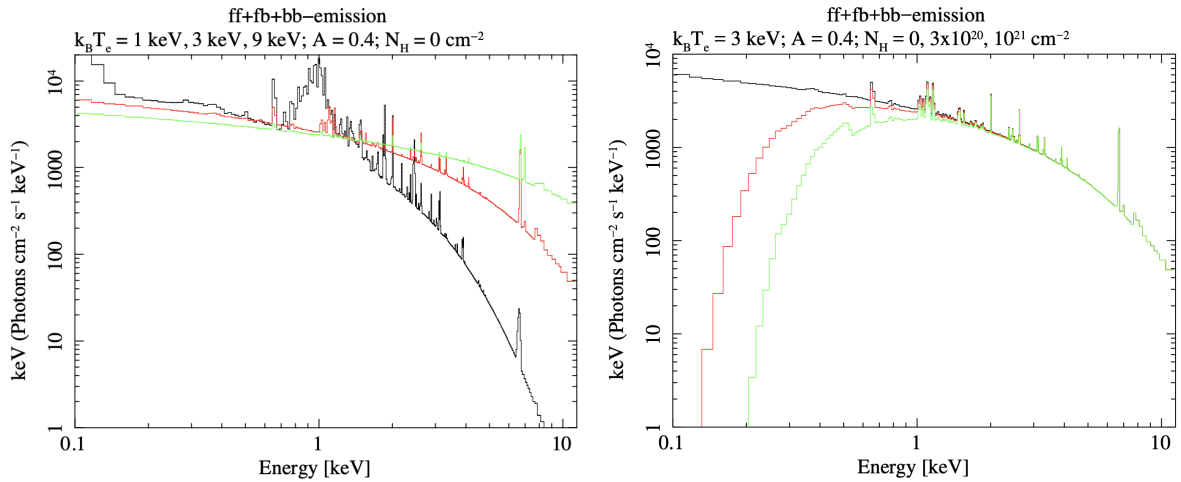


Figure 1.7: The simulated X-ray spectra of the ICM. The free-free (ff), free-bound (fb), and bound-bound (bb) emissions are included in each spectrum. *Left*: The metallicity, A , and the photoelectric absorption by the Galactic hydrogen column density, N_H , are fixed at $0.4Z_\odot$ and 0 atoms cm^{-2} , respectively. The Fe-L ($\sim 1 \text{ keV}$) and Fe-K ($\sim 6.7 \text{ keV}$) shell line complexes become more prominent as the gas temperature decreases. *Right*: N_H is varied, while the gas temperature is fixed at 3 keV and the metallicity at $0.4Z_\odot$. Cut-offs due to Galactic absorption are apparent at lower energies. Source: [Reiprich et al. \(2013\)](#).

Line Emission

The ICM also contains heavier elements. The line emission (bound-bound) process occurs when a bound electron falls to a lower energy state and radiates a photon with an energy corresponding to the difference between the two states. While the H and He are completely ionized, depending on the temperature, the heavier elements are only partially ionized. The electron density is independent of the ionization state

and is given by $n_e \approx 1.2n_H$, where n_H is the hydrogen density. The intensities of the emission lines in the spectrum depend on the ICM temperatures, namely, the hotter it is, the more ionized the plasma, thus the weaker the emission lines. This temperature dependency is demonstrated in the left panel of Figure 1.7. In the same figure, it can also be observed that the most prominent emission lines are contributed by iron (Fe), namely, the Fe-K and Fe-L shell line complexes at around 6.7 keV and around 1 keV. The line emission can be the dominant process in the low-temperature regime ($k_B T_e \lesssim 2$ keV) and the total emissivity is given as

$$\epsilon \propto T_e^{-0.6} n_e^2. \quad (1.10)$$

In contrary to the bremsstrahlung emission, the emissivity of the line emission increases with decreasing T_e .

Absorption Processes

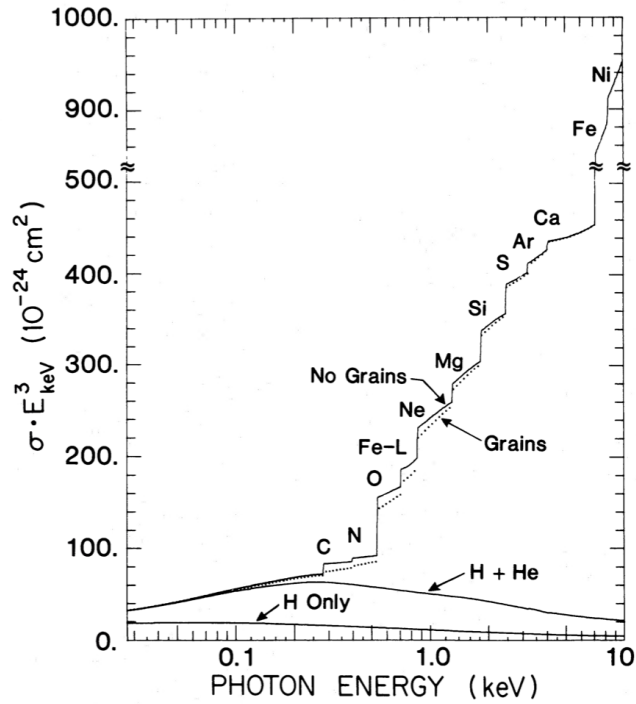


Figure 1.8: The effective photoelectric absorption cross-section as a function of energy, scaled by E^3 . Source: [Morrison & McCammon \(1983\)](#).

The low energy X-ray photons are heavily absorbed by the interstellar medium (ISM) material of the Milky Way along the LOS via the photoelectric absorption process (e.g., [Morrison & McCammon, 1983](#); [Wilms et al., 2000](#); [Willingale et al., 2013](#)). The effect of this absorption can be seen as the low energy cut-offs in the right panel of Figure 1.7. To understand the soft X-ray spectra of the sources, this effect needs to be accounted for and it requires information on the column density of the absorbing material along the LOS. Moreover, the X-ray absorption in the ISM is highly dependent on the total photoionization cross-section σ_{ISM} , which is the sum of three phases

$$\sigma_{\text{ISM}} = \sigma_{\text{gas}} + \sigma_{\text{molecules}} + \sigma_{\text{dust}}. \quad (1.11)$$

At $E \gtrsim 0.28$ keV, the photoelectric absorption is contributed by the heavier elements produced by the stars. The photoelectric absorption cross-section as a function of photon energy normalized by one hydrogen atom is displayed in Figure 1.8. The figure shows that hydrogen and helium contribute to the absorption in the soft X-ray energies at $E \lesssim 0.28$ keV, while heavier elements dominate above this energy threshold. Due to the correlation between the densities of hydrogen and the other elements, it is common practice to approximate the absorbing particles by using the hydrogen column density together with the assumption of solar metal abundance ratios (Reiprich et al., 2021). Thus, for the observed X-ray spectrum at a given energy, $I(E)$, is given as

$$I(E) = e^{-\sigma_{ISM}(E)N_{\text{Htot}}} I_0(E), \quad (1.12)$$

where $I_0(E)$ stands for the emitted X-ray spectrum by the source and N_{Htot} is the total hydrogen column density measured in atoms cm^{-2} and given as,

$$N_{\text{Htot}} = N_{\text{H}} + 2N_{\text{H}_2}. \quad (1.13)$$

The Galactic neutral hydrogen column density, N_{H} , can be measured through the 21-cm radio observations as done by, for example, the Leiden/Argentine/Bonn (LAB) survey (Kalberla et al., 2005) and the HI4PI survey (HI4PI Collaboration et al., 2016). On the other hand, determining the molecular hydrogen density N_{H_2} in all directions is challenging. However, the dust extinction in the infrared wavelengths can be used to infer this component (e.g., Willingale et al., 2013; Reiprich et al., 2021).

1.4.2 Spatial Distribution of the ICM

Total Mass

The ICM/gas densities in cluster vary from about 10^{-2} cm^{-3} in the center to 10^{-4} cm^{-3} in the outskirts. To infer the gas properties and the mass of a cluster, the gas distribution is to be modeled with some assumptions. Firstly, since the collision time scales for ions and electrons in the ICM are significantly shorter compared to the time scales of heating and cooling, the gas can be regarded as a fluid. Then, the time for a sound wave traveling of a given speed c_s across the ICM of a radius R is given by

$$t_{\text{sc}} \approx \frac{2R}{c_s} \sim 2 \text{ Gyr} \left(\frac{R}{1 \text{ Mpc}} \right) \left(\frac{c_s}{1000 \text{ km s}^{-1}} \right). \quad (1.14)$$

If we consider $c_s \sim 1000 \text{ km s}^{-1}$ and take a typical cluster radius of 1 Mpc, the sound-crossing time t_{sc} is shorter than the lifetime of the cluster itself or the Hubble time, $t_{\text{H}} = H_0^{-1} \sim 14 \text{ Gyr}$, thus the gas can be considered to be in hydrostatic equilibrium. Assuming that the cluster is spherically symmetric, the following hydrostatic equation holds

$$\frac{1}{\rho_g} \frac{dP}{dr} = -\frac{d\Phi}{dr} = -\frac{GM_{\text{tot}}(< r)}{r^2}, \quad (1.15)$$

where $M_{\text{tot}}(< r)$ is the total enclosed mass (including dark matter and galaxies) within the radius r , P denotes the gas thermal pressure, and ρ_g is the gas density. The thermal pressure of the gas following the ideal gas equation reads

$$P = nk_{\text{B}}T = \frac{k_{\text{B}}}{\mu m_{\text{p}}} \rho_g T, \quad (1.16)$$

where m_{p} is the proton mass and μ is the mean molecular weight in units of proton mass. With the assumptions of fully ionized hydrogen and the ICM containing helium and heavier elements, then

$\mu \sim 0.6$. Substituting Equation 1.16 into Equation 1.15 gives

$$M_{\text{tot}}(< r) = -\frac{k_B T r}{G \mu m_p} \left(\frac{d \ln \rho_g}{d \ln r} + \frac{d \ln T}{d \ln r} \right). \quad (1.17)$$

The above equation is referred to as the hydrostatic equation. It holds significant importance in the X-ray studies of galaxy clusters which demonstrate that the total gravitational mass of a galaxy cluster within a given radius can be derived from the radial profiles of the observables, such as gas density and temperature.

The β -model

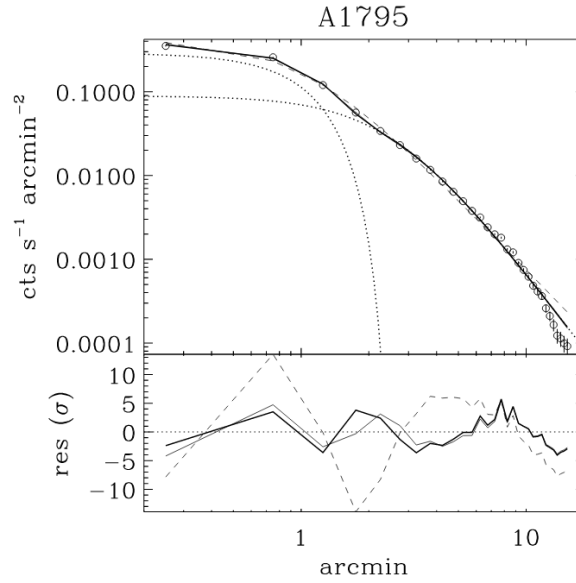


Figure 1.9: *Top*: Surface brightness profile of A1795 fitted with a single β -model (dashed line) and a double β -model (solid line; the constituent single β -models are shown by dotted line). Note the steepening at larger radii is not well-fitted by a single β -model. *Bottom*: Residuals in unit of σ . Source: [Ettori \(2000\)](#).

Another assumption for the gas is the isothermal distribution. It is based on the premise that the velocity distribution of massive particles within a cluster (both galaxies and dark matter particles) adheres with the Maxwellian distribution, namely they are in thermal equilibrium. Then,

$$\frac{d \ln \rho_g}{dr} = -\frac{\mu m_p}{k_B T} \frac{d\Phi}{dr}, \quad (1.18)$$

and for the galaxies in clusters, similarly,

$$\frac{d \ln \rho_G}{dr} = -\frac{1}{\sigma^2} \frac{d\Phi}{dr}, \quad (1.19)$$

where σ is the galaxy LOS velocity dispersion. Together with Equation 1.15, we can compare Equation 1.18 and 1.19,

$$\rho_g \propto \rho_G^\beta, \quad \text{with} \quad \beta \equiv \frac{\mu m_p \sigma^2}{k_B T}. \quad (1.20)$$

This implies that the gas density distribution is directly proportional to the total density to the power of β . With the King's approximation (King, 1962), we obtain β -model (Cavaliere & Fusco-Femiano, 1976)

$$\rho_g(r) = \rho_g(0) \left(1 + \frac{r^2}{r_c^2}\right)^{-\frac{3}{2}\beta}, \quad (1.21)$$

where $\rho_g(0)$ denotes the central gas density and r_c is the core radius within which the density is roughly constant.

Now, the X-ray surface brightness along the LOS is defined as

$$S_X = \frac{1}{4\pi(1+z)^4} \int_{-\infty}^{\infty} \epsilon dl. \quad (1.22)$$

Since the total emissivity is approximately $\epsilon \propto n_e^2 \propto \rho_g^2$, hence, the X-ray surface brightness at the projected distance R from the cluster center is

$$S_X(R) = S_X(0) \left(1 + \frac{R^2}{r_c^2}\right)^{-3\beta + \frac{1}{2}}. \quad (1.23)$$

The surface brightness profile is shaped by r_c and β . From measurements of 39 galaxy clusters, Vikhlinin et al. (1999) found $\beta = 0.65 - 0.85$. In most cases, Equation 1.23 can describe the measured surface brightness profile reasonably well, especially in the intermediate radial range between $\sim r_c$ and $\sim 3r_c$ (Voit, 2005). However, since the gas in clusters is not exactly isothermal, some discrepancies exist: the model often underestimates the cores of cool-core clusters and overestimates the values in the outskirts. In that case, a second model can be added to fit these regions (a double β -model). Figure 1.9 shows the measured surface brightness profile of the A1795 cluster (empty circles) fitted with a single β -model (dashed line) and a double β -model (solid line) that is the sum of two single β -models (dotted lines). At larger radii ($r \gtrsim 10$ arcmin), we observe a steepening that is not well fitted by the single β -model.

1.5 X-ray Instruments

Although the projects rely heavily on X-ray data obtained through the eROSITA telescope, there are other missions worth mentioning that are relevant to the research. In this section, along with eROSITA, we will provide a brief overview of these missions.

1.5.1 ROSAT

The *Röntgensatellit*, *ROSAT*, was a collaboration effort between Germany, the United States, and the United Kingdom, with Germany leading its design and operation (Briel et al., 1996; Arnaud et al., 2011). Launched on the 1st of June 1990 by the United States, *ROSAT* remained operational until the 12th of February 1999⁸. During the first six months of its operation (August 1990 to January 1991), *ROSAT* carried out an all-sky survey in the 0.1 – 2.4 keV energy band, known as the *ROSAT* All-Sky Survey (RASS; Voges, 1993). About 135,000 X-ray sources were cataloged into the second *ROSAT* all-sky survey (2RXS; Boller et al., 2016) and *ROSAT* cluster catalogs, namely, the main cluster catalog for

⁸<https://heasarc.gsfc.nasa.gov/docs/rosat/rosat3.html>

the northern sky is NORAS (Böhringer et al., 2000) and the southern sky is REFLEX (Böhringer et al., 2001). The survey also produced RASS diffuse background maps (Snowden et al., 1997).

1.5.2 *Chandra*

NASA's *Chandra* X-ray observatory was launched on the 23rd of July 1999 (Weisskopf et al., 2000) into the elliptical high-Earth orbit (HEO). Along with the High Resolution Mirror Assembly (HRMA), *Chandra* carries four science instruments: the High Resolution Camera (HRC) composed of two micro-channel plates, the Advanced CCD Imaging Spectrometer (ACIS), and two transmission gratings for high-resolution spectroscopy, namely, the High Energy Transmission Grating Spectrometer (HETGS) and the Low Energy Transmission Grating Spectrometer (LETGS). The HRMA focuses the incoming X-ray photons onto either HRC or ACIS at a given time. The ACIS instrument is commonly used for X-ray imaging and spectroscopy of galaxy clusters. The ACIS-I for imaging has a FoV of $16 \text{ arcmin} \times 16 \text{ arcmin}$ with an energy resolution of 130 eV at 1.49 keV⁹, while ACIS-S is optimized as a readout of HETG. To date, *Chandra* has an unrivaled on-axis spatial resolution of $\sim 0.5 \text{ arcsec}$.

1.5.3 *XMM-Newton*

The X-ray Multi-Mirror Mission (*XMM-Newton*) was launched by the European Space Agency (ESA) on the 10th of December 1999 (Jansen et al., 2001; ESA: *XMM-Newton* SOC, 2023b) into the HEO. It comprises three Wolter type-I X-ray telescopes and a 30 cm optical/UV telescope. Equipped with European Photon Imaging Camera Metal Oxide Semi-conductor (EPIC MOS) detectors and EPIC pn detector, the X-ray telescopes observe in the energy range of 0.15 to 12 keV. Each of the EPIC MOS detectors comprises seven CCDs, one of which is centered on the optical axes. On the other hand, the EPIC pn CCD array, slightly offset from the optical axis, consists of twelve chips. The FoV of EPIC cameras is about 30 arcmin in diameter. The 58 gold-coated mirror shells nested in each of the X-ray telescopes enable *XMM-Newton* to achieve the largest soft-band effective area of any available X-ray telescope, while simultaneously providing a good angular resolution. The on-axis Point-Spread Function (PSF)¹⁰, defined by the Half Energy Width (HEW), is about 17 arcsec at 1.5 keV. The spectral resolution for EPIC MOS and pn are $\sim 70 \text{ eV}$ and $\sim 80 \text{ eV}$ at 1 keV, respectively.

Each of these cameras is equipped with a filter wheel system with different setups for observing different targets, such as thin, thick, medium, closed, and open. The filter wheel has a circular aperture with a 30 arcmin diameter, hence, the area outside the aperture is always unexposed to the sky. During the Filter Wheel Closed (FWC) observations, i.e., when the filter setting is closed, there is no emission from the sky received, leaving the signal dominated by the instrumental background. The FWC data are useful for modeling and subtracting the instrumental background from the observations¹¹.

1.5.4 *Suzaku*

Suzaku was the fifth Japanese X-ray mission (Mitsuda et al., 2007; Pottschmidt, 2015). It was developed by the Institute of Space and Astronautical Science (part of the Japan Aerospace Exploration Agency, ISAS/JAXA) in collaboration with NASA's Goddard Space Flight Center (NASA/GSFC). Launched on the 10th of July 2005, *Suzaku* completed its mission in 2015. *Suzaku* was equipped with three main instruments: the X-Ray Spectrometer (XRS) with a spectral resolution of 6–7 eV was designed to perform high-resolution spectroscopy. However, it was only operational for a few weeks due to a malfunction in

⁹<https://cxc.harvard.edu/cal/Acis/index.html>

¹⁰It characterizes the focusing ability of the telescope.

¹¹<https://www.cosmos.esa.int/web/xmm-newton/filter-closed>

its cooling system. The X-ray Imaging Spectrometer (XIS) has a FoV of $17.8 \text{ arcmin} \times 17.8 \text{ arcmin}$ and consists of four X-ray-sensitive imaging CCD cameras. It operates in the energy range of $0.2 - 12 \text{ keV}$, which is comparable to the energy bands of the other X-ray instruments discussed here. Due to its soft X-ray sensitivity and low background, the XIS cameras were ideal for studying the diffuse soft X-ray sources with low surface brightness, such as cluster outskirts (e.g., [Reiprich et al., 2009](#); [Simionescu et al., 2013](#); [Walker et al., 2013b](#); [Hattori et al., 2017](#); [Alvarez et al., 2022](#)). *Suzaku* also carried a Hard X-ray Detector (HXD) that covered a higher energy range of $10 - 600 \text{ keV}$.

1.5.5 eROSITA

The extended ROentgen Survey with an Imaging Telescope Array (eROSITA) is the primary X-ray instrument on board the Russian-German Spektrum-Roentgen-Gamma (SRG) mission ([Merloni et al., 2012](#); [Predehl et al., 2021](#); [Merloni et al., 2024](#)). The mission was launched on the 13th of July 2019 from Baikonur and placed in a halo orbit around the second Lagrange point (L2). The primary scientific goals of eROSITA include detecting about 100,000 galaxy clusters and groups and hot gas in filaments between clusters to study cosmic structure evolution, sampling a few million AGNs, and studying the physics of galactic X-ray sources populations, such as the pre-main sequence stars, supernova remnants, and X-ray binaries.

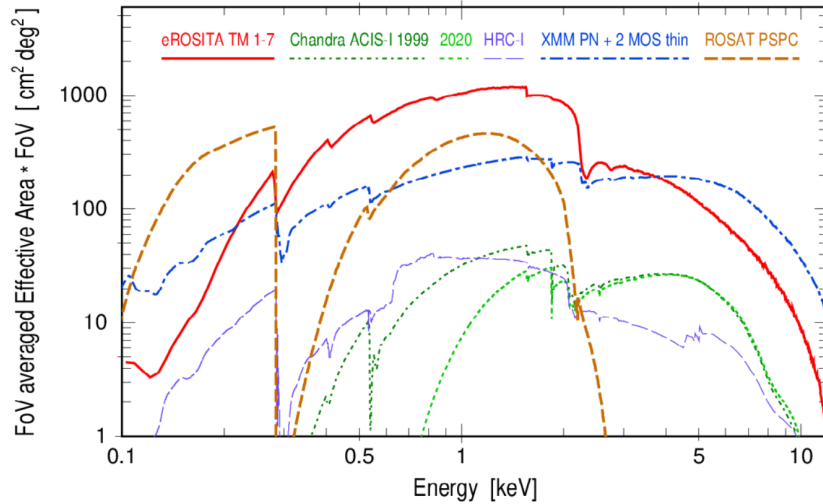


Figure 1.10: The on-axis effective areas as a function of energy for various X-ray instruments: eROSITA (red), *XMM-Newton* (blue), *Chandra* ACIS-I from 1999 (dark green) and from 2020 (light green), *Chandra* HRC-I (purple), and *ROSAT* (brown). Source: [Predehl et al. \(2021\)](#).

The eROSITA data distribution follows an inter-agency agreement, split along the Galactic longitude (l) and latitude (b) marked by the Galactic poles $(l, b) = (0^\circ, +90^\circ); (0^\circ, -90^\circ)$ and the Galactic Center Sgr A* $(l, b) = (359.9442^\circ, -0.04616^\circ)$. For instance, the data with $-0.05576^\circ < l < 179.9442^\circ$ (eastern Galactic hemisphere) belong to the Russian consortium and data with $359.9442^\circ > l > 179.9442^\circ$ (western Galactic hemisphere) belong to the German eROSITA consortium (eROSITA-DE). eROSITA operates in the energy range of $0.2 - 10 \text{ keV}$, as such it is the first to perform an all-sky imaging survey in the hard X-ray band of $2.3 - 8 \text{ keV}$. In the soft energy band ($0.5 - 2.0 \text{ keV}$), eROSITA was designed to be about 25 times more sensitive than its predecessor, RASS (see Section 1.5.1).

The eROSITA mirror system consists of seven identical mirror modules, referred to as Telescope Modules (TMs). Each of the TMs consists of 54 co-aligned mirror shells and a 1.6 meters focal length.

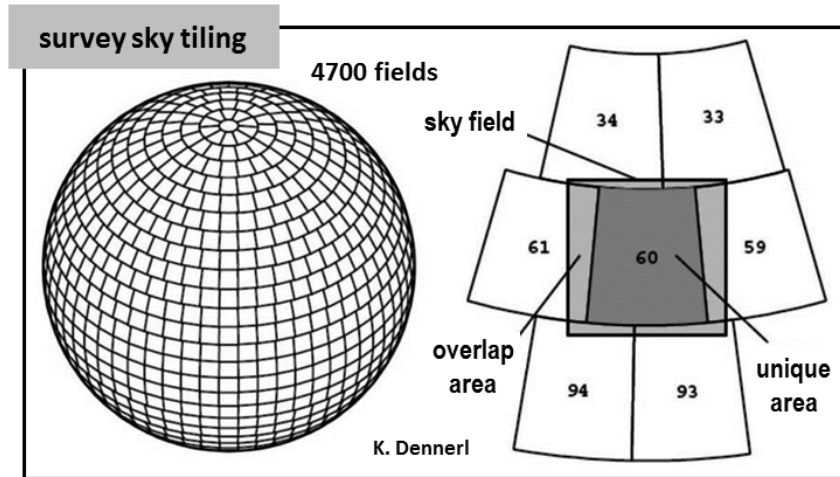


Figure 1.11: An illustration of eRASS sky division. The eRASS sky is divided into 4700 non-overlapping unique areas, called sky tiles (dark grey area). Each sky tile is embedded in a $3.6^\circ \times 3.6^\circ$ overlapping sky field (light grey box). Credit: eROSITA-DE, MPE, Konrad Dennerl.

The optical axes of the TMs are also co-aligned, resulting in an identical FoV of 1.03° in diameter. The grasp (product of FoV and effective area¹²) of eROSITA between ~ 0.3 keV and ~ 3.5 keV surpasses other X-ray instruments (Figure 1.10). The average on-axis spatial resolution of the seven TMs is 16.1 arcsec HEW at 1.5 keV. Five of the TMs (TM1, 2, 3, 4, 6)¹³ are equipped with an aluminum on-chip optical light filter. Meanwhile, since they were planned for low-energy spectroscopy, TM5 and TM7¹⁴ are not equipped with the filter. However, during the commissioning phase, it was discovered that the bottom part of these TMs were contaminated by optical light. To reduce the registration of the light leak contamination, the primary telemetry threshold of these TMs was increased and consequently, it decreased the low-energy coverage and spectroscopic capabilities.

Between mid-September and mid-December 2019, the SRG mission was in the Calibration and Performance Verification (Cal-PV) phase. During this period, eROSITA carried out over one hundred pointing and field scan observations. Afterward, the all-sky survey was started on the 12th of December 2019. Each eROSITA all-sky survey (eRASS; Merloni et al., 2024) was completed in about six months. The eRASS sky is divided into 4700 non-overlapping unique areas, called sky tiles (dark grey area in Figure 1.11)¹⁵. Each sky tile is embedded in a $3.6^\circ \times 3.6^\circ$ overlapping sky field (light grey box). On the 31st of January 2024, the first six months of the eROSITA all-sky survey (eRASS1; see Figure 1.12) data belonging to the eROSITA-DE were released to the public through the eROSITA-DE Data Release 1 (DR1) site¹⁶. The main eRASS1 X-ray catalog (including point sources and extended sources) in the 0.2 – 2.3 keV band was published in Merloni et al. (2024). It lists $\sim 930,000$ sources, expanding the number of known X-ray sources in the existing literature by more than 60%.

¹²The capability of the mirror to collect photons of different energies.

¹³The combination of these TMs is referred to as TM8.

¹⁴Both combined is referred to as TM9.

¹⁵https://erosita.mpe.mpg.de/dr1/AllSkySurveyData_dr1/

¹⁶<https://erosita.mpe.mpg.de/dr1/>

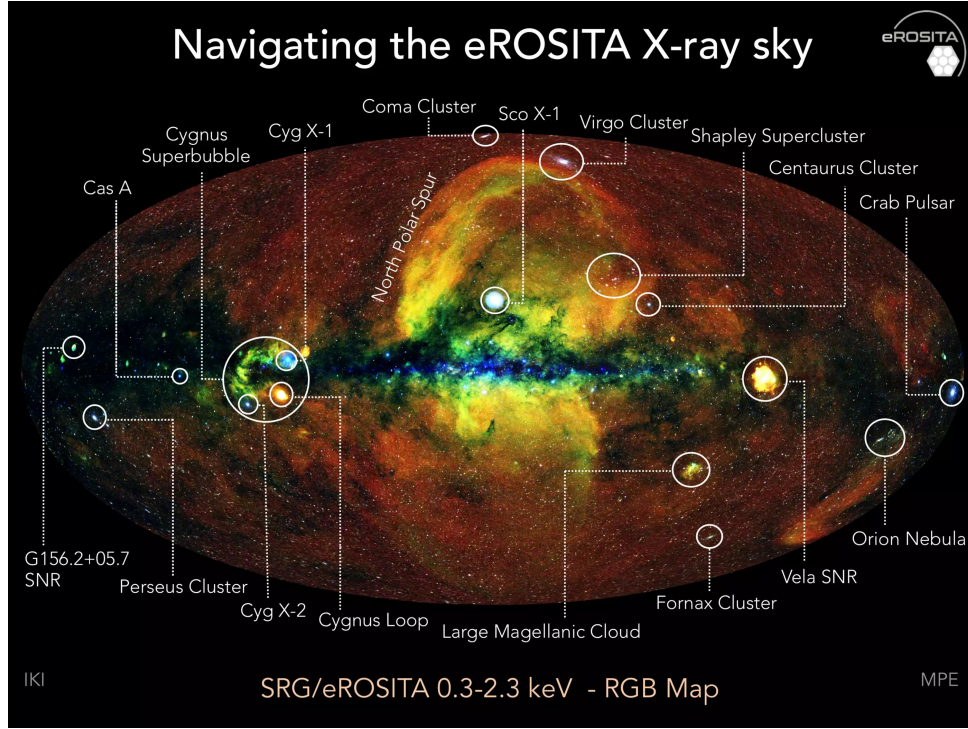


Figure 1.12: Composite image of the entire eRASS1 sky. Photons of different energies are divided into three color channels: 0.3 – 0.6 keV in red, 0.6 – 1.0 keV in green, and 1.0 – 2.3 keV in blue. Labeled are some prominent X-ray sources, such as galaxy clusters, supernova remnants (SNR), nebulae, and bright point sources. Credit: Jeremy Sanders, Hermann Brunner, Andrea Merloni, and the eSASS team (MPE); Eugene Churazov, Marat Gilfanov (on behalf of IKI).

1.6 Background Components of X-ray Observations

When observing the sky, the received photons not only originated from the target but also photons from other unrelated sources; resolved and unresolved, point sources or diffused emissions that might even fill the entire FoV. Detailed X-ray background analyses are provided in, e.g., [Lumb et al. \(2002\)](#); [Snowden et al. \(2008\)](#); [Kuntz & Snowden \(2008\)](#) for *XMM-Newton* and, e.g., [Freyberg et al. \(2020\)](#) for eROSITA.

Based on the origin, the X-ray background can be grouped into two: the Particle-Induced Background (PIB) and the cosmic X-ray background (CXB). They will be discussed in the following subsections.

1.6.1 The Particle Induced Background

When energetic particles interact with the detectors (or the materials surrounding them), they generate secondary X-ray photons that get detected by the detectors, known as the instrumental background or the Particle-Induced Background (PIB). Studying the behavior of the PIB is done by utilizing the FWC observations. This will enable us to treat this background component, either model or subtract it during the science analyses. The PIB consists of several components:

- quiescent particle background (QPB): this background component is generated through the interaction between highly energetic particles with the detectors. The QPB contributes as the

continuum component of the FWC spectra and dominates at high ($\gtrsim 2$ keV) and low ($\lesssim 1.2$ keV) energies,

- fluorescent X-ray (FX) background: the interaction between energetic particles and various materials around the detector, for example, detector housing and filter wheels, produces the fluorescent X-ray (FX) emission. For eROSITA, some noticeable FX lines include Al- K_α at 1.486 keV and Fe- K_α at 6.391 keV, and weaker FX lines are Ti- K_α at 4.504 keV Co- K_α at 6.915, Ni- K_α at 7.46 keV, Cu- K_α at 8.027 keV, and Zn- K_α at 8.615 keV (Figure 1.13),
- soft proton flares (SPFs): this background component is caused by low-energy protons with energies (\lesssim a few hundred keV) that can partially bounce on X-ray mirrors and funnel through the telescopes. The SPFs are variable and have been thought to originate from proton clouds that reside in the Earth's magnetosphere (ESA: XMM-Newton SOC, 2023b).

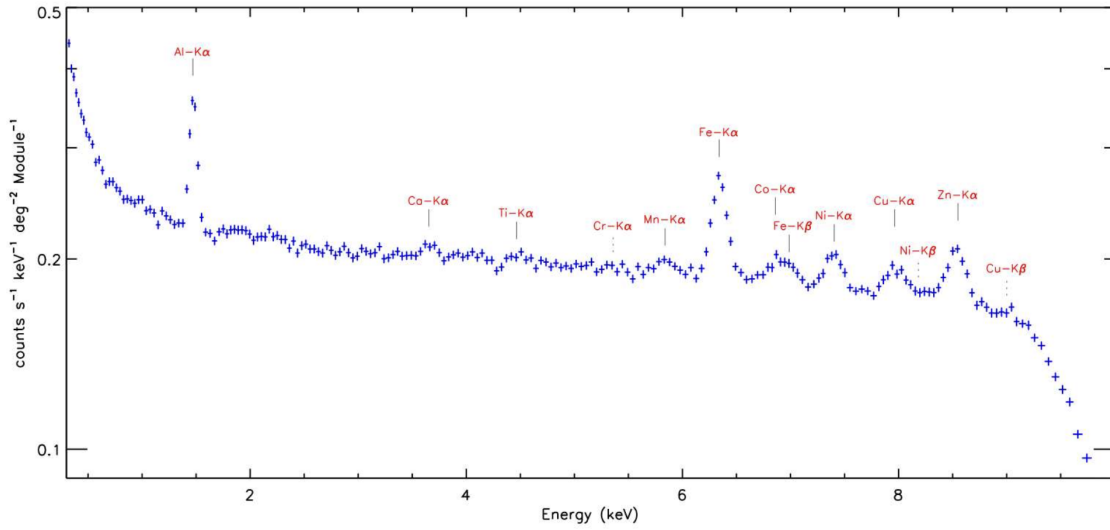


Figure 1.13: eROSITA PIB spectrum from the FWC data. The fluorescent X-ray lines are labeled. Source: Freyberg et al. (2020).

1.6.2 The Cosmic X-ray Background

The cosmic X-ray background (CXB) originates from cosmic sources within and outside our Galaxy, which include:

- the unresolved background sources: are mostly from unresolved AGNs. The contribution of this component in the observed galaxy cluster spectra can be described by a power law,
- Local Hot Bubble (LHB): diffused thermal emissions filling the entire FoV. The LHB is an irregular cavity of hot plasma ($T \sim 10^6$ K) surrounding the Solar System (e.g., Liu et al., 2017a). The radius of LHB is approximately 100 – 200 pc,
- Milky Way Halo (MWH): thermal emission from the Galactic halo with a temperature range of $1 - 3 \times 10^6$ K. Unlike the LHB emission, the MWH emission is absorbed by the Galactic material along the LOS,

- **eROSITA Bubbles:** ROSAT All-Sky Survey (RASS) discovered a soft X-ray emission that is a part of the North Polar Spur (see Figure 1.12) and Loop I (Egger & Aschenbach, 1995). The eRASS1 image further reveals a huge structure in the southern sky analogous to the northern structure (Predehl et al., 2020). Termed as the "eROSITA Bubbles", these X-ray structures appear as annuli or shells centered about the Galactic center, extending approximately 80° in longitude and 85° in latitude. The eROSITA Bubbles morphology resembles those of the Galactic gamma-ray structure, "Fermi Bubbles" (Su et al., 2010), hence, thought to share a common origin, i.e., large energy injections from the Galactic center,
- **solar wind charge exchange (SWCX):** arises from either the interaction between a highly-ionized ion in the solar wind and the neutral ISM in our Solar System (the heliospheric emission) or the neutral gas in the Earth's exosphere (the geocoronal emission) (Arnaud et al., 2011). During this process, highly ionized ions with large cross-sections capture electrons from neutral gas. Upon decay to the ground state, the excited ions release either soft X-ray or Extreme-UltraViolet (EUV) photons. SWCX emission varies depending on solar wind properties, observing direction, and observatory location at a given time. Moreover, due to its smooth distribution across the FoV, distinguishing and removing the SWCX emission from observations of diffuse emission (e.g., LHB, MWH, WHIM, galaxy clusters, nearby galaxies, SNRs, and super bubbles) are challenging (Kuntz et al., 2015).

1.7 Galaxy Cluster Outskirts

Galaxy clusters are the highest-density peaks of the matter distribution in the Universe in the cosmic web (Bond et al., 1996). As illustrated in Figure 1.14, galaxy clusters sit at the junction of cosmic web filaments. They form hierarchically through mergers and gravitational infall of material from the surrounding large-scale structures (e.g., Springel et al., 2006). Imprints of these accretion processes are embedded in the cluster outskirts, such as caustics in the dark matter density profile, inhomogeneous/clumpy gas density distribution, gas bulk, and turbulent motions, and non-equilibrium states (e.g., Reiprich et al., 2013; Walker et al., 2019, for reviews on cluster outskirts).

Clumpy Gas Density Distribution

In the cluster outskirts, inhomogeneous gas density distribution due to random density fluctuations is expected. The inhomogeneity or clumpiness in the ICM can be quantified by the mean-mass-weighted clumping factor

$$C \equiv \frac{\langle \rho_g^2 \rangle}{\langle \rho_g \rangle^2}. \quad (1.24)$$

The impact of gas clumpiness in the cluster interior is modest, i.e., a mass bias of $\leq 10\%$, while in the cluster outskirts, it could cause a significant systematic bias in the X-ray measured ICM profiles, e.g., overestimation of gas density and underestimation of entropy¹⁷ profiles (Mathiesen et al., 1999; Nagai & Lau, 2011; Roncarelli et al., 2013).

Gas Temperatures

Accretion of mass into galaxy clusters through the cosmic filaments occasionally renders internal shocks of the ICM, which convert a considerable amount of the kinetic energy into thermal energy, heating the

¹⁷ $K \equiv k_B T / n_e^{2/3}$

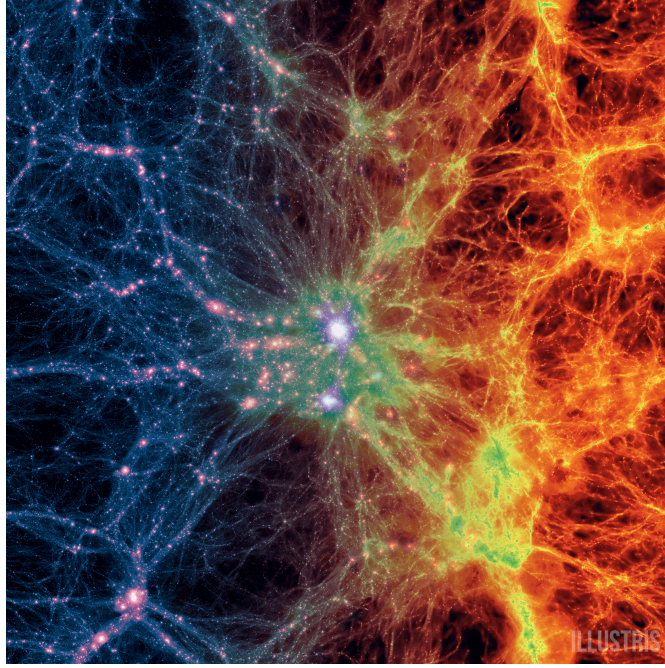


Figure 1.14: Cosmic web from Illustris simulation taken at $z = 0$, centered on the most massive cluster. The image shows the transition from dark matter density (left) to gas density (right). Credit: [Illustris Collaboration](#).

ICM. [Kawaharada et al. \(2010\)](#) measured the outskirts temperatures of the A1689 cluster with deep *Suzaku* observations. They reported a higher temperature by a factor of three in the cluster outskirts connected to the large-scale filament than in the outskirts that are bordered by the voids (see Section 1.3.1).

1.7.1 The Missing Baryon Problem

Comparing to the epoch of recombination ($z \approx 1100$; see Section 1.3.2) and when the Universe was 2 – 3 billion years ($z = 3$), about 30 – 40% of the total number of baryons in the local Universe are still not yet observed ([Shull et al., 2012](#); [Nicastro et al., 2017, 2018](#)). The large-scale cosmological simulations of a standard Λ CDM model ([Cen & Ostriker, 1999](#); [Davé et al., 2001](#)) predicted that starting at $z \approx 2$, as the structures continuously form, these “missing” baryons condensed into filamentary web with electron densities $n_e \approx 10^{-6} - 10^{-4} \text{ cm}^{-3}$ and temperatures $T \approx 10^5 - 10^7 \text{ K}$, known as the Warm-Hot Intergalactic Medium (WHIM). The WHIM is classified into three phases ([Nicastro et al., 2018](#)): 1) warm phase ($T \approx 10^5 - 10^{5.7} \text{ K}$ or $k_B T \approx 0.009 - 0.043 \text{ keV}$), 2) hot phase ($T \approx 10^{5.7} - 10^{6.3} \text{ K}$ or $k_B T \approx 0.043 - 0.172 \text{ keV}$), and 3) hotter phase ($T \approx 10^{6.3} - 10^7 \text{ K}$ or $k_B T \approx 0.172 - 0.862 \text{ keV}$).

Due to its properties, the detection of the WHIM is challenging. One method of detecting the WHIM is through absorption lines in the spectrum of a bright background source, such as a quasar or gamma-ray burst. For instance, the first clear WHIM detection was made by the absorption of ionized oxygen lines (O VI) in ultraviolet spectra of background quasar (e.g., [Tripp et al., 2006](#)). However, the O VI lines trace the fraction of the WHIM at lower temperatures, whereas most of the WHIM is present at higher temperatures and hence, observable in X-rays ([Davé et al., 2001](#)). The hot phases of the WHIM can be traced via X-ray absorption of the O VII lines (e.g., [Nicastro et al., 2005](#); [Buote et al., 2009](#); [Nicastro et al., 2018](#)). Nevertheless, the absorption method relies on the presence of a bright background source along the line of sight and does not facilitate the spatially-resolved study of the WHIM ([Reiprich](#)

et al., 2021).

Since the X-ray emissivity scales with the square of the electron density (Section 1.4.1), direct attempts to detect the filaments via X-ray emission should be aimed at their densest parts, namely, between a pair of nearby galaxy clusters (e.g., Kull & Böhringer, 1999; Vazza et al., 2019) and at the outskirts of a galaxy cluster (e.g., Reiprich et al., 2013; Nicastro et al., 2018). Some examples of the WHIM studies in these locations are, for instance, between the Abell 222 and 223 cluster pair (Werner et al., 2008b), the Abell 399 and 401 system (e.g., Fujita et al., 2008; Akamatsu et al., 2017; Bonjean et al., 2018), the Abell 98N/S system (Sarkar et al., 2022; Alvarez et al., 2022), the outskirts of the Coma cluster (Bonamente et al., 2009, 2022), the Abell 2744 cluster (Eckert et al., 2015a; Hattori et al., 2017), and the Abell 1750 cluster (Bulbul et al., 2016). Studies using previous X-ray instruments are limited by their FoVs, such that they require multiple observations to cover some fractions of the area of interest (see example for the A3391/95 cluster system and the Centaurus cluster in Figure 1.15).

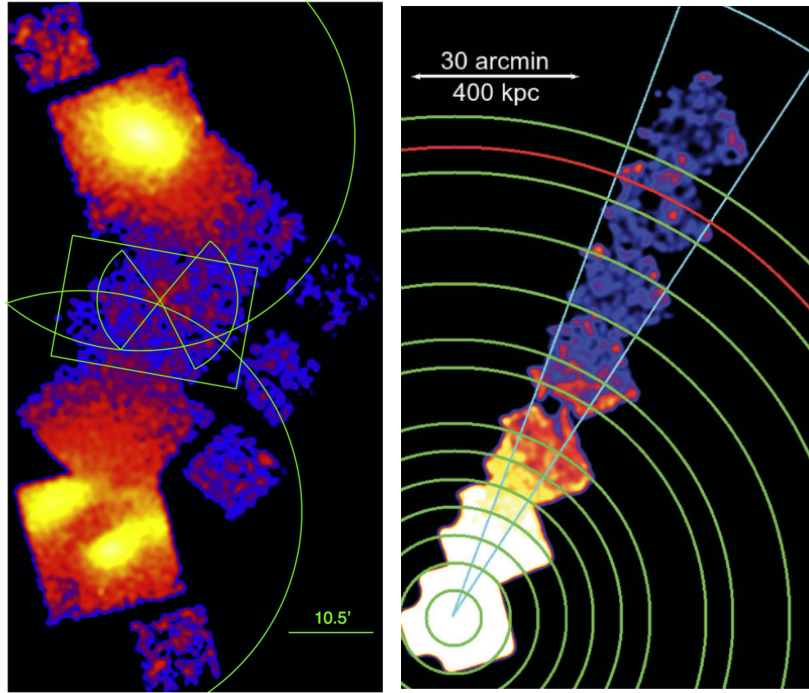


Figure 1.15: *Left*: Five *Chandra* observations covering the A3391 cluster (north), A3395S/N cluster (south), and the emission between them. Source: Alvarez et al. (2018). *Right*: Seven *Suzaku* observations of the Centaurus cluster covering from its core out to $0.95R_{200}$. Source: Walker et al. (2013b).

1.8 Cosmological Framework

1.8.1 Λ CDM Model

The Λ CDM is the widely-accepted concordance model of cosmology, that includes the cosmological constant Λ , associated with the dark energy that explains the accelerating expansion of the Universe, and the cold dark matter (CDM) that is dark matter particles that travel with non-relativistic velocities. In the Λ CDM model, the Universe is composed of three major components: dark energy (70%), CDM(25%), and baryonic matter (5%). There are six base parameters shaping the Λ CDM model, which are determined from observations or experiments (e.g., CMB, supernovae), including baryon density, CDM density, an

approximation to the observed angular size of the sound horizon at recombination, the reionization optical depth, the initial super-horizon amplitude of curvature perturbations, and the primordial spectral index. From these base parameters, other quantities can be derived. Some of the relevant Λ CDM parameters to this work from the Planck CMB observations (Planck Collaboration et al., 2020b) are listed in Table 1.1.

Parameter	Description	Value
$\Omega_b h^2$	baryon density	0.0224 ± 0.0001
$\Omega_c h^2$	CDM density	0.120 ± 0.001
t_0	age of the Universe	13.8 ± 0.02 Gyr
H_0	Hubble constant	67.4 ± 0.5 km s ⁻¹ Mpc ⁻¹
Ω_Λ	dark energy density	0.685 ± 0.007
Ω_m	matter density	0.315 ± 0.007
The dimensionless Hubble parameter is given by $h = H_0/(100 \text{ km s}^{-1} \text{ Mpc}^{-1})$.		

Table 1.1: The Λ CDM parameters relevant to this work from the Planck CMB observations (Planck Collaboration et al., 2020b)

1.8.2 Cosmological Distances

When measuring the distances and the sizes of the studied objects, the expansion of the Universe must be considered. First, let us define the comoving distance, which is the distance between two objects where the expansion of space over time is taken into account. It is given by

$$r(z) = \int_0^z \frac{dz'}{H(z')} = \int_0^z \frac{1}{H_0 E(z')} dz', \quad (1.25)$$

where $E(z) = \sqrt{\Omega_r(1+z)^4 + \Omega_m(1+z)^3 + \Omega_k(1+z)^2 + \Omega_\Lambda}$. The two most important definitions of distance are the angular-diameter distance D_A and the luminosity distance D_L . Given an object of a size x and an angular size θ , then

$$D_A(z) = \frac{x}{\theta} = \frac{r(z)}{(1+z)}, \quad (1.26)$$

and given an object with bolometric luminosity L and flux S , then

$$D_L(z) = \sqrt{\frac{L}{4\pi S}} = (1+z)r(z), \quad (1.27)$$

such that the two distance measures are correlated by $D_L(z) = (1+z)^2 D_A(z)$, and for small redshifts ($z \ll 1$), they agree with each other.

Chapter 2

Summary of the Projects

This chapter provides a summary of the projects included in the dissertation, along with their context and results. The dissertation is composed of a methodology for cleaning and procuring products employed in the science analyses and three chapters based on the investigation of galaxy cluster outskirts and cosmic filaments. The data used for this research were obtained from the eROSITA X-ray instrument onboard the SRG mission.

2.1 Methodology: eROSITA Data Reduction and Science Analysis Procedures

Chapter 3 describes all the technicalities, including the used eROSITA data and software versions, as well as the steps leading up to the science analyses. The first step upon retrieving the data is to check and clean it of any contaminations, such as bad pixels and soft proton flares (SPFs; see Section 1.6.1). From the cleaned data, the standard eROSITA Science Analysis Software System (eSASS; Brunner et al., 2022) already allows the extraction of spectral products together with dedicated instrument responses. Meanwhile, for imaging analysis, additional corrections are required to rectify the inhomogeneity in the FoV due to instrumental effects and background components. The corrections consist of modeling and subtracting particle-induced background (PIB; Section 1.6.1) from the photon image employing information from the filter-wheel-closed (FWC) data (Section 1.5.3), correcting the effect of the absorption by the Galactic material, and correcting the inhomogeneity in the exposure maps caused by the different response of the eROSITA telescope modules (TMs) and different lower energy bounds due to the light-leak in a couple of the TMs. The image correction steps were first developed and applied to the A3391/95 eROSITA PV field for Reiprich et al. (2021). Over the course of this Ph.D., the data reduction and image correction procedure was developed further and is now wrapped in a pipeline for full automatization for any eROSITA processing versions. Visual inspection, image enhancements, and surface brightness analysis were performed using the fully-corrected image products. Their methods are also described in the corresponding chapter.

Moreover, spectral analyses were carried out to determine the ICM and filament properties, such as gas temperature, metallicity, and density. The spectral analysis requires intricate treatments, in particular for faint regimes. In general, the full model is composed of the sky fore-/background (cosmic X-ray background/CXB; Section 1.6.2), the PIB, and the source component (ICM/filament). The modeling of PIB, similar to the image correction steps, is done with the help of the available FWC analysis results. The treatments of the CXB component, on the other hand, might vary slightly depending on the position of the field relative to the Galactic latitudinal axis. In most cases, modeling the Local Hot Bubble (LHB),

Milky Way Halo (MWH), and unresolved background sources is enough, as was done for the A3391/95 projects. However, if the studied field is close to the Galactic axis, contamination by Galactic sources, for example, the eROSITA Bubbles, is expected. It means an additional foreground component is necessary, which is the case for the Centaurus cluster project. The details on the spectral fitting components and strategy are presented in this chapter.

2.2 The eROSITA view of the Abell 3391/95 field: The Northern Clump

The Abell 3391 and 3395 (A3391/95) system is a complex galaxy cluster system that is composed of two closely interacting clusters: the A3391 cluster in the north and the A3395 cluster in the south that consists of two subcomponents, i.e., A3395S and A3395N. Additionally, the system is relatively nearby ($z = 0.05$), and hence, it is a good target for researching filamentary structures. With this purpose, the A3391/95 system has been extensively observed by various instruments in different wavelengths, including in X-rays. Naturally, the searches were focused on the region between the two clusters (bridge), where a small galaxy group (ESO 161-IG 006) resides. Earlier studies using the data taken by the 1990's X-ray satellites, *ROSAT* and *ASCA*, showed the gas in the bridge is consistent with filamentary emission (Tittley & Henriksen, 2001). Meanwhile, recent studies using more modern X-ray instruments (*XMM-Newton*, *Chandra*, and *Suzaku*) report that the properties of the gas in this bridge region are more typical of tidally-stripped ICM gas from the clusters resulting from the early phase of a merger (Sugawara et al., 2017; Alvarez et al., 2018). A significant excess of signal between these clusters is observed in the residual thermal Sunyaev-Zel'dovich (tSZ) map taken by the *Planck* instrument (Planck Collaboration et al., 2013), which signifies the presence of hotter gas rather than warmer WHIM gas.

The latest dedicated X-ray observation of the A3391/95 system was carried out by eROSITA in October 2019 during the calibration and performance verification (Cal-PV) phase. Three raster-scan and one pointed observations were performed. These observations cover an area of about 15 degree^2 and they represent the deepest large-scale X-ray view of the system to date. From the bridge region, eROSITA detected the hot ICM gas, but also hints of warm filamentary gas connecting the clusters (Reiprich et al., 2021). Moreover, soft emission extending northward of the A3391 cluster and southward of the A3395 cluster was also discovered, revealing a continuous large-scale structure with a projected length of $\sim 15 \text{ Mpc}$. This continuous warm-hot emission appears to connect at least five galaxy groups and clusters in the field, including, from the north to the south, the Northern Clump, the A3391 cluster, the ESO 161-IG 006 group, the A3395 cluster, and the Little Southern Clump. In the south of the FoV, the outskirts emission of the MCXC J0631.3-5610 cluster is apparent. Given that this cluster is located at the same distance as the other galaxy groups and clusters, its connection with the Southern Filament is likely. The eROSITA A3391/95 PV observations show a snapshot of large-scale structure formation with a great resemblance to the analog system found in the Magneticum simulation (Biffi et al., 2022).

In Chapter 4, we summarize the contents of the first published paper (Veronica et al., 2022) that are included in this dissertation. The focus of the study is the Northern Clump (NC; also known as the MCXC J0621.7-5242 cluster, Piffaretti et al., 2011; or MS 0620.6-5239 cluster, De Grandi et al., 1999; Tittley & Henriksen, 2001), the largest infalling structure in the filament in this field. The NC is a small galaxy cluster located at a similar redshift to the main system, $z = 0.0511$. It has entered the atmosphere of the A3391 cluster and its X-ray emission deviates from the typical spherical or elliptical shape. The main body is boxy with a sharp edge in the south, namely, the A3391 direction. The trail of X-ray emission is also apparent in the north. The ASKAP/EMU radio data (Norris et al., 2021) reveals a bright wide-angle tail (WAT) radio emission in the center of the cluster originated from the radio source PKS 0620-52 (Morganti et al., 1993; Trussoni et al., 1999; Venturi et al., 2000), that is hosted by the brightest cluster galaxy (BCG), 2MASX J06214330-5241333 (Brüggen et al., 2021). The opening angle

of the asymmetric lobes of the WAT radio source indicates its movement relative to the ICM toward the south. Utilizing the eROSITA A3391/95 PV observations and *XMM-Newton* follow-up observation of the Northern Clump, outskirts surface brightness and spectral analyses were carried out. In this work, we aimed to answer the following main questions:

Science Questions:

- What causes the unique ICM morphology of the Northern Clump?
- How does the ICM of the Northern Clump look like at large radii?
- How are the gas properties of the Northern Filament?

To answer these questions, imaging and spectral analyses on the X-ray data were carried out with the methods described in Chapter 3. From the results, we concluded that the Northern Clump is dynamically non-relaxed. The temperature in the south is hotter than in the north. This temperature elevation is in alignment with the gas being shock- or compression-heated due to its movement toward the south. In the north, the tail-like trail of X-ray emission is confirmed by significant emission measure excess in this direction. The tail-like features are often observed in merging systems. They are the gas that was ram pressure stripped from the smaller substructures as they enter the ICM of the bigger structures. These observed X-ray features of the Northern Clump are greatly similar to those found in the infalling substructures from other observations (e.g., M86 and M49 in the Virgo cluster; [Randall et al., 2008](#); [Su et al., 2019](#)). Moreover, a small substructure resembling the Northern Clump is also found in the analog A3391/95 system found in the Magneticum Simulation ([Biffi et al., 2022](#)). The findings from the simulations further support the hypothesis that the unique X-ray morphology of the Northern Clump was shaped by the interaction with the atmosphere of the A3391 cluster (ram-pressure stripping and shock-/compression heating), hinting its movement along the Northern Filament.

Additionally, thanks to the large coverage by eROSITA, the X-ray surface brightness profile of the Northern Clump could be constructed out to large radii. In the regime where the sky background starts to dominate ($R_{500} < r < R_{200}$)¹, the surface brightness profile appears flat instead of gradually falling. This suggests that there is still some source emission that could originate either from the ICM, filament, or both. To characterize the gas in the Northern Filament², preliminary spectral analyses were also conducted, namely, with a single temperature from the thermal emission model (1T) and a two-temperature model (2T). We compared the results with the WHIM properties from simulations (e.g., [Shull et al., 2012](#); [Nicastrò et al., 2018](#)). The 1T model shows that the gas in the Northern Filament is hotter than the expected WHIM temperature, while the electron density of the gas falls within the range of the WHIM density range. Using the 2T model we identified the presence of a cooler component whose temperature and density are consistent with WHIM properties. The implications of the warm-hot filament gas and the 2T model spectral fitting are further investigated in the next paper.

2.3 The eROSITA view of the Abell 3391/95 field: Cluster outskirts and filaments

In Chapter 5, we discuss the second publication ([Veronica et al., 2024a](#)), which focuses on the gas properties of the cluster outskirts and the detected filaments in the A3391/95 system using the eROSITA PV data. The detected filaments are the Northern Filament that connects the A3391 cluster and the

¹The R_X is the radius within which the density is X times the critical density of the Universe at the given redshift.

²We assume the filament emission to be inter-cluster emission at $r > R_{200}$.

Northern Clump and the Southern Filament that extends southward to the A3395 cluster and is potentially connected to another cluster outside the FoV, the MCXC J0631.3-5610 cluster. The filaments consist of not only diffuse gas but also matter clumps (e.g., [Angelinelli et al., 2021](#)). It has been shown in the simulations and observations that the presence of the clumps in the cluster outskirts significantly biases the measurement of gas density and entropy profiles ([Nagai & Lau, 2011](#); [Eckert et al., 2015b](#)). Yet, similar to the filaments, these clumps are difficult to resolve due to the low X-ray emissivity. Owing to the superior soft energy response and observing strategy of eROSITA, a small extended clump is discovered within the periphery of the A3395 cluster ($\sim 1.5R_{200}$), residing in the Southern Filament. The clump is named the Little Southern Clump (LSC; [Reiprich et al., 2021](#)). Its characteristic properties and its impact on the Southern Filament are also assessed in this work. Since we are studying the faint emission of the cluster outskirts and the filaments, we took particular care of the foreground. The following is the list of the main science questions of this paper:

Science Questions:

- How do the surface brightness profiles along the filament ($r > R_{200}$) directions compare to the off-filament directions?
- How do the ICM properties in the filament-facing outskirts ($R_{500} < r < R_{200}$) differ from other outskirts measurements?
- How are the gas properties of the detected Northern and Southern Filaments?
- How are the measured filament properties compared to the WHIM predictions and other filament measurements?
- What is the impact of the LSC on the Southern Filament?

The surface brightness profile is an essential diagnostic to identify fluctuations, such as excesses or deficits, in the gas distribution in different directions. Hence, we constructed surface brightness profiles in different directions (sectors) from the center of the A3391 and A3395S clusters out to $2R_{200}$. From the profiles, we find that the filament-facing outskirts sectors are brighter than the off-filament sectors. From spectral analysis, we also observe that the outskirts temperatures in these filament directions are higher than the temperature profile obtained from a fit of other cluster outskirts measurements ([Reiprich et al., 2013](#)). Previous studies (e.g., [Kawaharada et al., 2010](#)) have reported temperature excesses in regions of the cluster outskirts that are connected with cosmic web filaments, which could be due to the heating caused by the accretion of matter.

Through spectral fitting, we constrained the gas properties of the filaments, including temperature, metallicity, and density. While the gas density of both Northern and Southern Filaments classify the gas within as WHIM, their temperatures, however, are slightly hotter than the predicted WHIM temperature range. The acquired temperatures for these filaments are ~ 1 keV, which is close to the upper WHIM range of 0.9 keV. Since these filaments are found in a dense large-scale environment and thus, located in a deeper gravitational well than the longer filaments that make up the skeletons of the Universe, the temperature enhancements are likely the result of stronger gravitational heating ([Galárraga-Espinosa et al., 2020, 2021, 2022](#); [Vurm et al., 2023](#)). Moreover, the Northern and Southern Filaments are metal-poor, which is expected as the filaments are located away from metal production sites, such as star-forming regions ([Biffi et al., 2022](#)). Nevertheless, the estimated values are within the predicted filament metallicity range from the simulations.

Based on the obtained X-ray properties, the LSC is classified as a small galaxy group. This is also

supported by the galaxy overdensity that coincides with the X-ray emission. Furthermore, no significant changes in temperature and metallicity are observed after excluding the LSC from the spectral analysis of Southern Filament. However, a 30% decrease in the gas density is identified, which demonstrates the level of bias and the importance of accounting for the clumps for the outskirts and filament studies (Nagai & Lau, 2011; Eckert et al., 2015b; Mirakhor & Walker, 2021).

Additional spectral fittings were performed to test whether the filaments, despite the good alignment with the galaxy clusters and the surface brightness enhancement, could actually be fortuitous and originating from Galactic foregrounds, as well as to investigate the multi-component gas (2T model). The results of the first test type confirm that the filaments are not from our Galaxy, and in comparison to the 1T model, we find that the 2T model does not significantly improve the fit. The test results further substantiate the robustness of our main findings.

2.4 The SRG/eROSITA All-Sky Survey: Large-scale view of the Centaurus cluster

As one of the closest and X-ray brightest galaxy clusters in the sky, the Centaurus cluster (Abell 3526) is an ideal target to conduct astrophysical studies. The brighter, central part of the cluster has been extensively observed by most X-ray instruments (e.g., ASCA, Churazov et al., 1999; Dupke & Bregman, 2001; Furusho et al., 2001; ROSAT, Allen & Fabian, 1994; Churazov et al., 1999; Ikebe et al., 1999; Suzaku Ota et al., 2007; Walker et al., 2013b; Ota & Yoshida, 2016; XMM-Newton, Walker et al., 2013a; Fukushima et al., 2022; Gatuzz et al., 2022, 2023; Chandra, Sanders & Fabian, 2002; Sanders et al., 2016b; Lakhchaura et al., 2019). The distribution of the redshifts of the galaxies within the proximity shows that the cluster is composed of two substructures, namely, the Cen 30 and the Cen 45 (Lucey et al., 1986a,b). The Cen 30 is located in the center of the cluster and centered at the NGC 4696 galaxy that hosts a low-power radio source, PKS 1246 – 410 (Taylor et al., 2002, 2006). The Cen 45 is centered at the NGC 4709 galaxy, about 15 arcmin eastward to the cluster center. This substructure is currently being accreted toward Cen 30. The multi-wavelength studies of the core of the Centaurus cluster reveal numerous astrophysical features (e.g., cold fronts, shocks, X-ray cavities, etc.) that are the results of AGN feedback and merger-induced sloshing.

Due to its close proximity, the Centaurus cluster has a large apparent size ($R_{500} \approx 59.0$ arcmin). The FoV limitation of previous instruments has restricted the coverage of the clusters to the brightest part of the cluster ($r \lesssim 30$ arcmin). A small fraction of the outskirts, however, was observed by a mosaic of six *Suzaku*³ observations along the northwestern direction out to $0.95R_{200}$ (Walker et al., 2013b). In this work (Chapter 6), we employed the eROSITA All-Sky Survey (eRASS; Predehl et al., 2021; Merloni et al., 2024; Bulbul et al., 2024) data to probe the ICM properties of the Centaurus cluster out to R_{200} . The comprehensive surface brightness and spectral analyses are carried out in four directions. We, therefore, increase the probed volume of the Centaurus cluster by a factor of almost 30. The main goal of this work is to address the following questions:

Science Questions:

- How are the ICM morphology and properties of the Centaurus cluster at $r > 0.5R_{500}$?
- Is there any hint of emission from large-scale structures at $r > R_{200}$?

Galaxy clusters can be traced by the agglomeration of galaxies. Hence, they can be detected by

³The FoV of the *Suzaku* XIS instrument is 19 arcmin \times 19 arcmin (NASA's HEASARC, 2006).

assessing the spatial density of galaxies in the plane of the sky and in redshift space. The redshifts of the galaxies belonging to the same system should lie around a certain value and the dispersion can be approximated by a Gaussian distribution. Furthermore, large-scale filaments can also be traced by trails of gas clumps and galaxies (e.g., [Malavasi et al., 2020](#); [Tuominen et al., 2021](#); [Angelinelli et al., 2021](#)). Therefore, we utilized the publicly available database, NED⁴, to compile the optical redshift catalog of the galaxies in the FoV. The results include, first, the identification of the galaxy members of the two substructures (Cen 30 and Cen 45) within the proximity of the Centaurus cluster. Second, a detection of a low significant trail of galaxies stretching westward of the cluster out to $1.5R_{2500}$. This structure is known as the "Western Branch" ([Lucey et al., 1986a,b](#)) and it is composed of galaxies with their redshift values within the ranges of those of Cen 30 or Cen 45. Although the direction of this structure is aligned with the elongation of the cluster, there is no X-ray emission correlated with it. Additionally, due to a large separation between the peak concentration of the Cen 45 in the east and the Western Branch location, it is unlikely that the galaxies with similar redshifts are associated with the substructure. This decreases further the significance of the Western Branch.

We note that the X-ray emission of the Centaurus cluster is measured with good significance up to large radii. At 90 arcmin (R_{200}), the surface brightness value is at 3.5σ above the CXB level, then at $\sim 1.1R_{200}$, it goes down to 2.9σ . In agreement with visual inspections and optical redshift analysis, no apparent large-scale structures seem to be connected with the cluster.

Regarding the ICM properties from the spectral analysis, overall, the profiles in various directions show a similar trend: low temperature and high metallicity in the core, peak temperature in the intermediate range, and then decreasing temperature and metallicity outward. Some deviations are present, however. The most prominent feature is the eastern excess along the Cen 45 direction. This excess is also seen in the residual images generated using the *ROSAT* PSPC ([Churazov et al., 1999](#)) and *XMM-Newton* ([Walker et al., 2013a](#)), but they are limited to ~ 30 arcmin ($0.5R_{500}$). The full extension of the eastern excess out to R_{500} is traced in this work. Based on previous ICM velocity (redshift) measurements ([Gatuzz et al., 2022](#)), the excess behind Cen 45 is likely the ram-pressure-stripped gas from this substructure. Around the location of Cen 45, temperature elevations are measured which are likely caused by shock-heating due to the interaction of Cen 30 and Cen 45. The locations of the temperature enhancements are congruent with other works ([Churazov et al., 1999](#); [Furusho et al., 2001](#); [Walker et al., 2013a](#)).

We compared the eROSITA temperature profiles at large radii with the temperature profiles derived from simulations ([Burns et al., 2010](#)) and fit from *Suzaku* outskirts measurements ([Reiprich et al., 2013](#)). The measured temperature profiles are in good agreement with the compared profiles. We attribute the absence of temperature deviations, such as excess, in the outskirts ($R_{500} < r < R_{200}$) of the Centaurus cluster to the lack of large-scale filaments connected to the cluster. Metallicity asymmetry is observed in the eastern and western directions (0.07 and $0.21Z_{\odot}$) with the northern and southern directions (0.003 and $0.08Z_{\odot}$). Higher metallicity in the east-west direction might be related to the merger direction. Regardless, the metallicity values in this radial range, $0.003/Z_{\odot} < Z < 0.21/Z_{\odot}$, are also in accordance and within the scatters of other cluster outskirts measurements (e.g., the A2204 cluster, [Reiprich et al., 2009](#); Perseus cluster [Simionescu et al., 2011](#); [Werner et al., 2013](#)).

⁴The NASA/IPAC Extragalactic Database (NED) is funded by the National Aeronautics and Space Administration and operated by the California Institute of Technology.

Chapter 3

Methodology: eROSITA Data Reduction and Science Analysis Procedures

During the early phase of the Ph.D., I developed the eROSITA pipeline that enables automatization of data reduction and image corrections, as well as most of the imaging and spectral analyses, under the supervision of Prof. Thomas H. Reiprich and Dr. Florian Pacaud. Some parts of the procedures have been summarized and used in some of the eROSITA galaxy cluster publications (e.g., [Koribalski et al., 2023](#); [Dietl et al., 2024](#); [McCall et al., 2024](#)). The eROSITA workflow is illustrated in Figure 3.1.

The data reduction and image correction steps were realized by HEASoft and the extended Science Analysis Software System (eSASS; [Brunner et al., 2022](#)). HEASoft version 6.25 (6.29) and eSASS version eSASSusers_201009 (eSASSusers_211214) were used for the A3391/91 projects (Centaurus project). For wavelet filtering and source detection steps, wavelet pipeline developed by Dr. Florian Pacaud ([Pacaud et al., 2006](#)) was utilized.

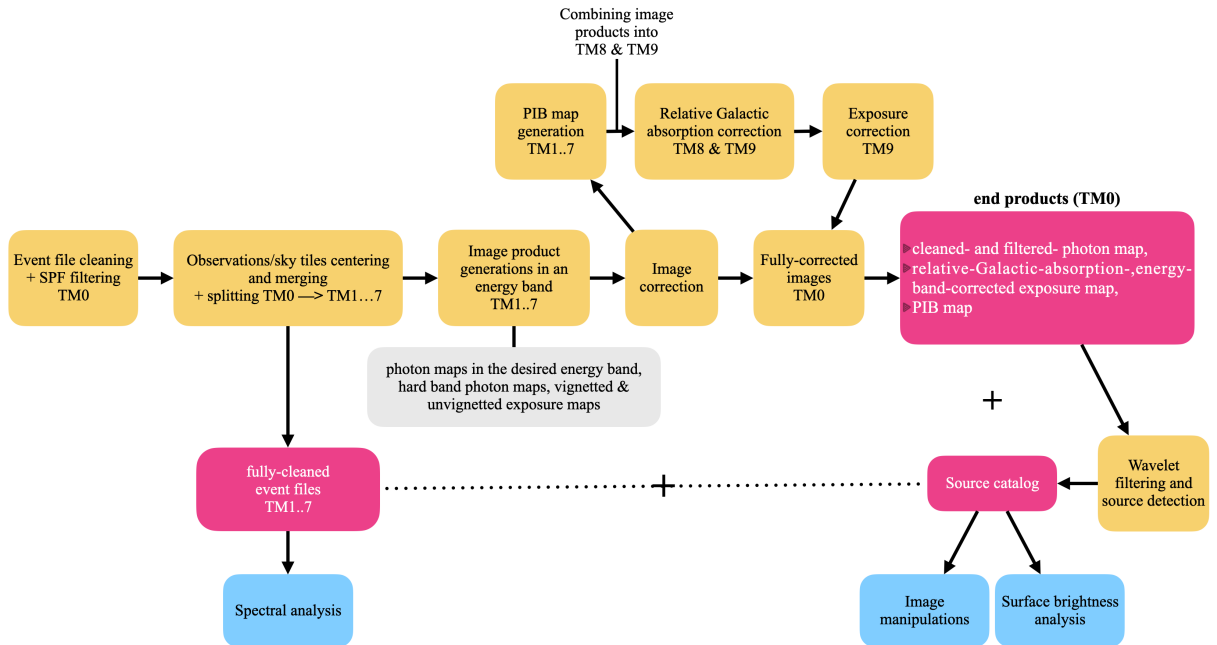


Figure 3.1: The eROSITA data reduction and science analysis workflow.

3.1 Data and Software Availability

3.1.1 The A3391/95 Cluster System Projects: eROSITA-DE Early Data Release (EDR)

The A3391/95 system was observed as an eROSITA Performance Verification (PV) target (see Section 1.5.5), resulting in three scan and one pointing observations. Out of these A3391/95 PV observations, only the third scan (300016) was performed with all TMs being operated. We listed the information of the A3391/95 PV observations used in the first and second projects in Table 3.1. To indicate the footprints of the different observations, we display all-TM-combined photon images of the individual observations in Figure 3.2.

The eROSITA-DE released the German-led Cal-PV observations to the public on 28 June 2021 through the Early Data Release (EDR) site¹. The released EDR data were processed with the eSASS version `users_201009`, which is called the data processing version c001.

Observing Date	ObsID (mode)	TM	Exposure* [ks]
October 2019	300005 (scan)	5-7	55
October 2019	300006 (scan)	5-7	54
October 2019	300016 (scan)	1-7	58
October 2019	300014 (pointed)	5-7	35

*The exposure times listed are the average filtered on-axis exposure time across the available TMs of each observation.

Table 3.1: The information of eROSITA A3391/95 PV observations used in the first and second projects. There are 16 datasets in total among the observations. The datasets were processed with the c001 (EDR) processing version.

3.1.2 The Centaurus Cluster Project: eROSITA-DE Data Release 1 (DR1)

At the start of the Centaurus cluster project (Spring 2023), newer processed eROSITA-DE eRASS data became available, namely the c020 version (internally released). Thus, the project made use of this processing version, together with the eSASS4DR1. We utilized the first five eRASS data (eRASS:5) and chose nine sky tiles that cover about $\sim 11.5^\circ \times 11.5^\circ$ area and include the $3 \times R_{200}$ radius of the cluster. The sky tiles ID are 188129, 188132, 188135, 191129, 192132, 192135, 195129, 196132, and 197135. Their configurations are shown in Figure 3.3, which was taken from the X-ray sky viewer of the eROSITA-DE DR1 site² and as can be seen, the Centaurus cluster is mainly located at sky tile 192132.

3.1.3 eROSITA Science Analysis Software System (eSASS)

The eROSITA Science Analysis Software System (eSASS) is the official software to handle eROSITA data products (Predehl et al., 2021; Brunner et al., 2022). The software was developed based on the experience from previous ESA X-ray observatories, *ROSAT* and *XMM-Newton*. It provides various tasks, scripts, and libraries that enable the users to calibrate the eROSITA event files, carry out data analysis tasks, as well as to derive some scientific products, such as images, exposure maps, spectra, and response files. The data products received by the users, e.g., event files, have already been calibrated with the eROSITA Calibration Database (CALDB) using the eSASS pipeline at the Max-Planck Institute for the

¹<https://erosita.mpe.mpg.de/edr/>

²<https://erosita.mpe.mpg.de/dr1/erodat/skyview/sky/>

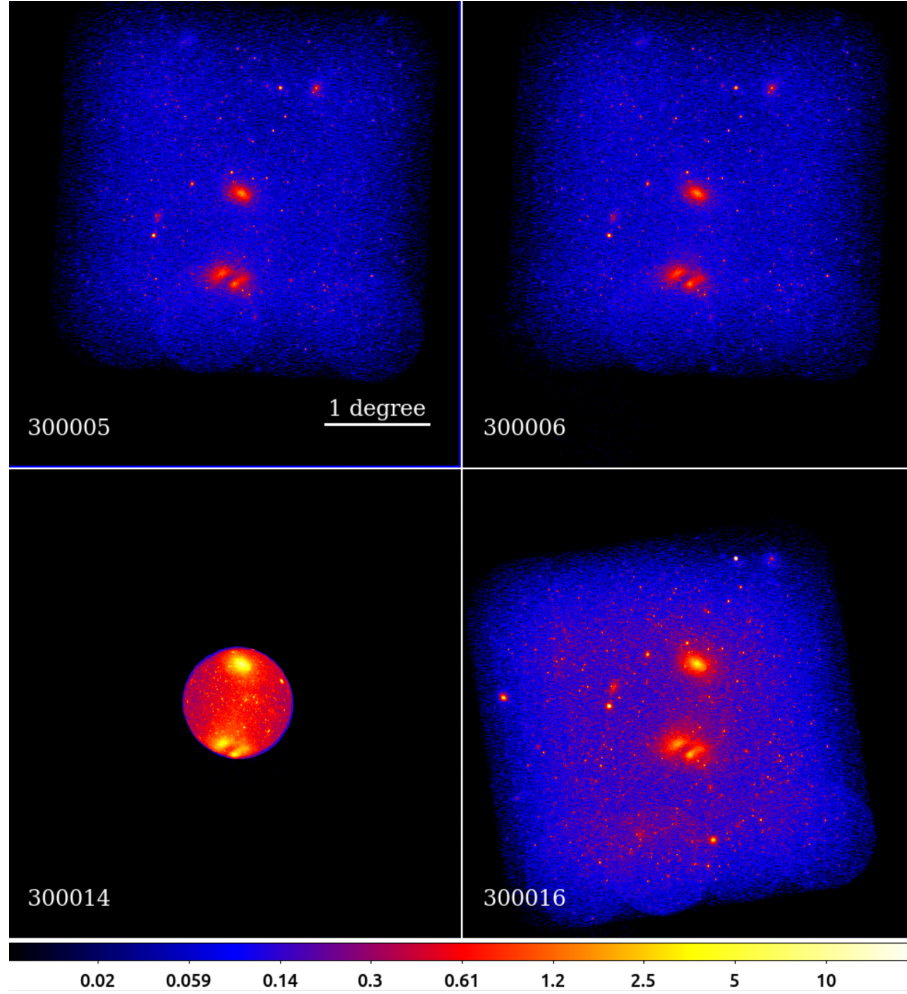


Figure 3.2: Photon images of the A3391/95 PV observations in the 0.2 – 10.0 keV energy band. The colorbar is in the units of counts.

Extraterrestrial Physics (MPE). Such calibrated eROSITA products are labeled with a processing version to differentiate the use of different CALDB and eSASS versions.

Some eSASS tasks were utilized within the eROSITA pipeline that was developed during the early phase of this thesis. The tasks can be called on the command line with some parameters. The tasks used in the projects in this thesis are described in the following list:

- `evtool`: to manipulate event files, such as merging several event files, creating photon images in a particular energy band, as well as filtering events on a subset of the columns,
- `flaregti`: to create a combined light curve of the telescope modules in a given energy band with a chosen time bin width that can be used to filter out the SPFs. Good-time intervals (GTIs) are selected based on a chosen rate threshold. A typical value is the 3σ threshold of the rate distribution. The GTIs surviving the filtering can be stored directly inside the event file, as an additional extension (FLAREGTI), or saved in an external file,
- `radec2xy`: to re-project the input event file at a given Right Ascension (RA) and Declination (Dec.),

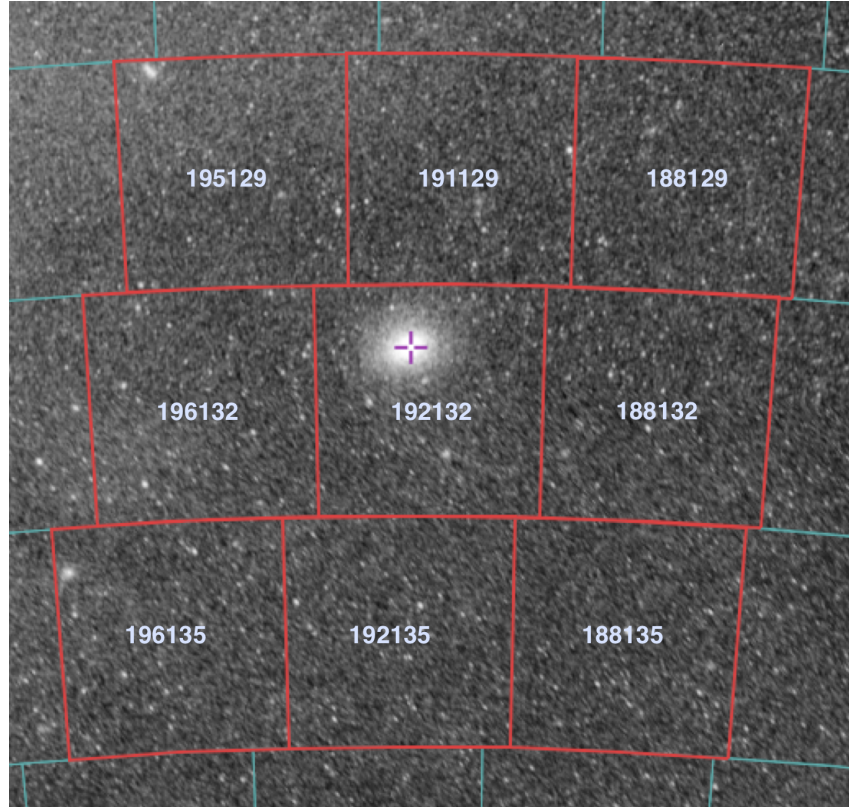


Figure 3.3: The 0.2 – 2.3 keV eRASS:1 count rate image (in counts pre second) taken from the [eRODat: eROSITA-DE Data Release 1 archive \(Sky View\)](#). Sky tiles utilized in the Centaurus cluster project are marked with red lines. The labels were added as guidance. The purple cross marked the position of the Centaurus cluster.

- `expmap`: to generate exposure maps in one or several energy bands simultaneously. Depending on the supplied parameters, the output exposure maps can be a 'merged' exposure map from several TMs and/or 'single' maps, energy-dependent vignetting corrected or not,
- `srctool`: to extract products required for spectral analysis steps, in particular, the spectrum for each TM and its corresponding response files, including an ancillary response file (ARF) and a response matrix file (RMF). The ARF contains the effective area (in cm^2) of the instrument as a function of energy averaged over the source region and instrumental effects, while the RMF characterizes the probability of an incoming photon of a given energy being redistributed across different channels in the spectrum due to detector's resolution ([Arnaud et al., 2011](#)).

3.2 Data Reduction

The received event files were already calibrated by the eSASS team. However, further checks and cleaning are still required before using them for science analysis to remove as many impurities and contaminations as possible. The data reduction and image generation steps relied on some of the tasks of the eSASS software. I developed scripts to automate the data reduction process (including optimization of the task parameters for our purpose, external calculation of count-rate threshold, and visualization of the lightcurve) and image generation step.

3.2.1 Event File Cleaning

The first step of the data reduction is to remove any unwanted pixels or portions of the event by using the eSASS `evtool` task. The task allows us to perform event file manipulations, including merging event files (e.g., combining several TMs or different sky tiles into one event file), filtering out events, and creating images. To remove unwanted and corrupted pixels and strongly vignettted pixels at the corner of the FoV, `flag=0xe00fff30` was specified³. Furthermore, we wanted to include all events confined in all pixel pattern fractions (single, double, triple, and quadruple), hence, we also supplied the `pattern=15` parameter⁴. Furthermore, we filtered the events with the existing good-time intervals (GTIs) stored in the original event files (`gti='GTI'`). In this first cleaning step, we ran the task for each event file where all TM (TM0) were combined in the broad energy range of 0.2 – 10.0 keV.

3.2.2 Soft Proton Flare Filtering

A hard band light curve can serve as a diagnostic for the contamination by soft proton flares (SPF; see Section 1.6.1). The light curve shows incoming rates per area as a function of observing time. The light curve of each observation was generated by using the `flaregti` task in the hard energy band. The hard band was chosen to limit the fraction of focussed X-ray emission (for instance, originating from the source of interest) since the effective area at high energy is small (Reiprich et al., 2021). We then fitted a Gaussian model, firstly, to the whole distribution of the rates per area to obtain the initial mean and the 3σ value, then to the new distribution where the outliers (above and below 3σ) were not considered. From the second Gaussian fitting, we acquired the new upper 3σ threshold ($3\sigma_{\text{clipped}}$), which was then supplied to the second run of the `flaregti` task (`threshold=3\sigma_{\text{clipped}}`). The task was run on the same event file in the same hard energy band and the additional `threshold` parameter now ensures that the events above the value were not considered for the GTI creation. As a result, a FLAREGTI extension was generated and passed to the `evtool` task to filter out the events in the bad time intervals. By the end of this step, a fully cleaned TM0 event file in the 0.2 – 10.0 keV band of each observation or sky tile was obtained.

We display a lightcurve generated in the 5.0 – 10.0 keV energy band from an eRASS:5 sky tile (195129) in the Centaurus field in the top panel of Figure 3.4. The distribution of the rates per area before (red) and after (blue) the first Gaussian fits are shown in the bottom panel. Similarly, the red and blue shaded areas in the top and bottom panels are the 3σ areas of the distributions before and after the first Gaussian fit.

3.2.3 Image Generations

Since we utilized several PV observations for the first and second projects, and nine eRASS:5 sky tiles for the third project, the next step was to re-project the fully-cleaned TM0 event file of each observation/sky tile onto a common coordinate (e.g., cluster X-ray center) which was done with the aid of the `radec2xy` task. Afterward, these re-projected event files were merged into one using the `evtool` task. As each TM

³The parameter `flag` is supplied to filter event file based on the input string given in hexadecimal. The list of the flag bits can be found in [the eROSITA-DE: Data Release 1 site – eROSITA standard FITS file extensions page](#). The `flag=0xe00fff30` sums all bits including bad pixels and strongly vignettted edges of the FoV of the TM

⁴The parameter `pattern` has the purpose of filtering the events based on the pixel pattern(s) as the charge cloud released by the X-ray photon can be confined within up to four pixels [eROSITA-DE: Data Release 1 site – Pattern Fraction](#). Different pixel patterns, such as 1-pixel (single), 2-pixel (double), 3-pixel (triple), and 4-pixel (quadruple) patterns are represented by a 4-bit mask, 1-bit per pattern. The task accepts an integer between 1 and 15. Within the eROSITA pipeline, a default value to select all pixel patterns is chosen to ensure enough statistics for science analyses, namely, `pattern=15` (the decimal value of 1111 in binary)

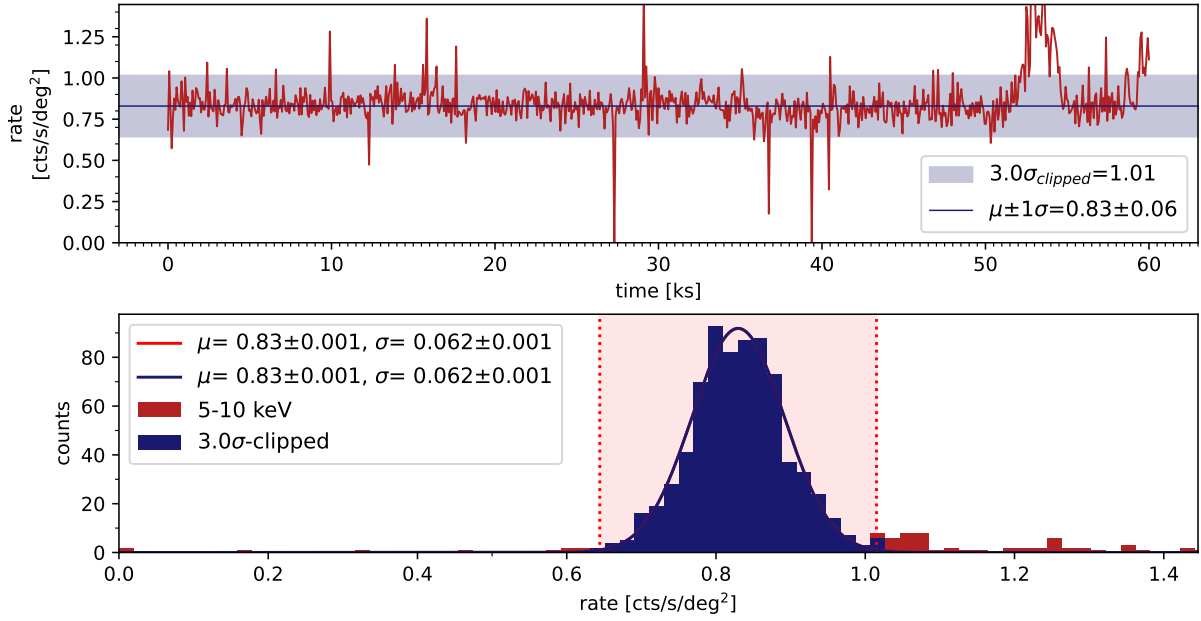


Figure 3.4: *Top*: An example lightcurve generated in the 5.0 – 10.0 keV band from an eRASS:5 sky tile (195129) in the Centaurus cluster field. *Bottom*: The rates per area distributions before (red) and after (blue) the first Gaussian fit, respectively. The red and blue shaded areas in the top and bottom panels are the 3σ areas of the distributions before and after the first Gaussian fit.

behaves differently, we needed to split the merged TM0 event files into individual TM event files before continuing. From these individual TM event files, further products (photon images and exposure maps in various energy bands, as well as spectra for spectral analysis) will be derived.

For image inspection and imaging analysis, individual TM photon images in a soft band were produced by the `evtool` task and their corresponding exposure maps by the `expmap` task. Due to the light-leak issue affecting TM9 (see Section 1.5.5), the lower energy limit of the soft energy band for TM9 was set higher (0.8 keV for Project 1, 0.5 keV for Project 2, and 0.8 keV for Project 3) than TM8 (0.5 keV for Project 1, 0.3 keV for Project 2, and 0.2 keV for Project 3). We were able to use a lower energy limit of TM9 in Project 2 because it was later found that the light leak contamination in the A3391/95 PV observations was milder compared to the other Cal/PV observations. Meanwhile, the lower energy limit of TM8 in the third project was due to the improvement in the suppression of low energy detector noise compared to the EDR calibration⁵. Individual TM photon images in the hard band were also generated for the later PIB map creation step. The pipeline generates two types of exposure maps: the vignetting-corrected exposure map used for the image correction steps and the non-vignetting-corrected exposure map used as the PIB map template. Each type of exposure map was produced by the `expmap` task with setting the parameter `withvignetting` to YES or NO, respectively.

All the images from each TM required for the image correction steps were generated automatically with one of the eROSITA pipeline scripts. The desired energy band is an input to the script such that different energy ranges could be considered, and also the possibility to exclude a sub-band. For instance, for Project 3, contribution between 1.35 keV and 1.60 keV was excluded because the Al-K α line at ~ 1.4 keV was found to be more prominent in FWC spectra than the observation. This was done to avoid overestimation of PIB estimation. For simplicity, the used energy range will be referred to as

⁵<https://erosita.mpe.mpg.de/dr1/eSASS4DR1/>

0.2(0.8) – 2.3 keV, where the lower bounds correspond respectively to the TM8(TM9) values. The energy band information of the different projects is listed in Table 3.2.

Project	Cluster	Processing	eSASS	Energy Range [‡]
1 ^a	A3391/95	c001 (EDR)	users_201009 (eSASS4EDR)	0.5(0.8) – 2.0 keV
2 ^b	A3391/95	c001 (EDR)	users_201009 (eSASS4EDR)	0.3(0.5) – 2.0 keV
3 ^c	Centaurus	c020	users_211214 (eSASS4DR1)	0.2(0.8) – 2.3 keV [†]

[‡]The lower bounds correspond respectively to the TM8(TM9) values,

[†]1.35 – 1.60 keV sub-band was excluded (see Section 3.2.3),

^aChapter 4 (Veronica et al., 2022), ^bChapter 5 (Veronica et al., 2024a), ^cChapter 6 (Veronica et al., 2024b).

Table 3.2: Information on the eROSITA data and software version used in each project, as well as the energy range for the imaging analysis.

3.3 Image Correction

Visual inspection and imaging analysis should be performed on images that are free of artifacts. This is especially important when assessing faint regions of the clusters and tracing filaments. In this section, we describe some procedures that correct for various effects that cause irregularities in the images. These procedures are implemented in the projects presented in this dissertation.

3.3.1 PIB Subtraction

The PIB (Section 1.6.1) that contaminates the entire FoV can be modeled and subtracted from a photon image. The PIB was modeled for each TM based on the analysis results of the available FWC observations. The PIB map creation technique for eROSITA images was developed in the Dark Energy group of the Argelander Institute for Astronomy and was first applied on the A3391/95 PV observations (Reiprich et al., 2021). In the early phase of the thesis, the procedure was wrapped in the eROSITA pipeline which allows full automatization and compatibility for any eROSITA datasets of different processing versions.

From the FWC analysis, it was discovered that the spatial variation of PIB across each detector is small ($\lesssim 10\%$), and hence the non-vignetted/flat exposure map can be used as a template for the distribution of the PIB component. Furthermore, the spectral shape of the PIB from different FWC observations shows little temporal variation, implying that the counts in the hard band (which is dominated by PIB events) can be converted into a contribution in other bands using the band ratios of the average PIB spectrum (which varies from TM to TM). Following these key elements, the procedure to create a PIB map of a given TM is as follows: first, the number of counts contributed by the PIB in a given soft band in the observation, $C_{\text{PIB,S}}$, was calculated by multiplying the hard band counts in the observation, $C_{\text{obs,H}}$, by the ratio of the number of counts in the soft band and the hard band found in the FWC data, $C_{\text{FWC,S}}/C_{\text{FWC,H}} = R$. Second, the PIB counts in the soft band, $C_{\text{PIB,S}}$, were spatially distributed across the FoV using the template map, that is the non-vignetted exposure map which was normalized to 1 by dividing each pixel by the sum of all pixel values, $\sum (\text{non - vig. exposuremap})$. The hard band used in the first and second projects was 6.0 – 9.0 keV, while for the third project, a higher lower bound of 6.7 keV was chosen to ensure no emission from the cluster was included in the calculation. The described procedure is summarized below:

$$\text{PIB map} = \underbrace{\frac{\text{non - vig. exposure map}}{\sum (\text{non - vig. exposuremap})}}_{\text{template map}} \times \underbrace{C_{\text{obs,H}} \times R}_{C_{\text{PIB,S}}}. \quad (3.1)$$

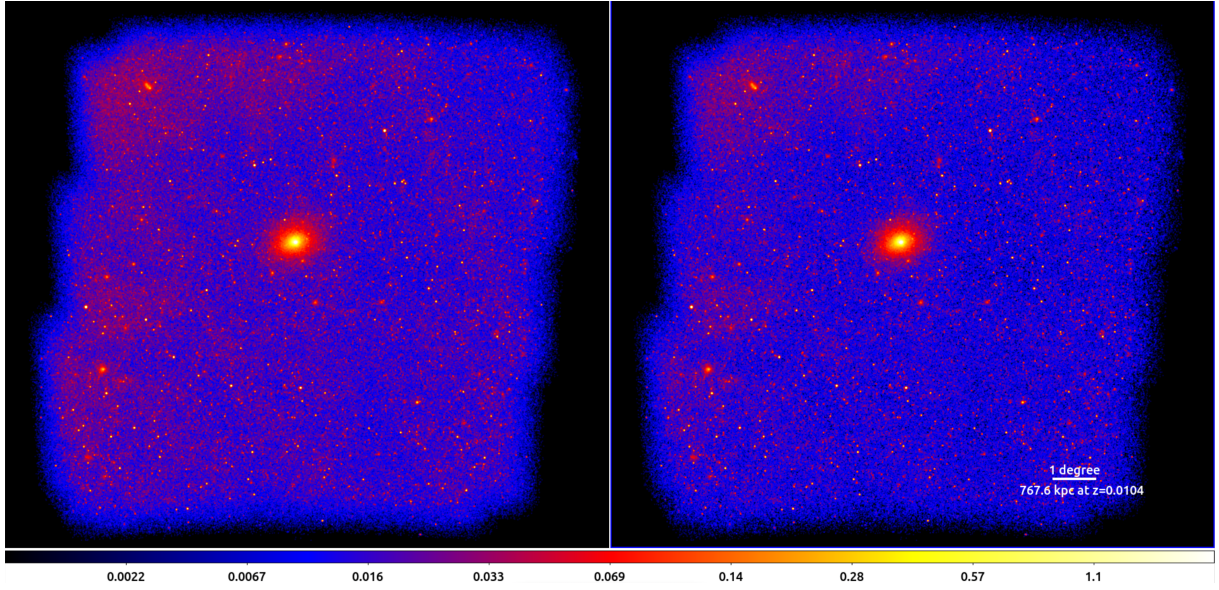


Figure 3.5: Fully-cleaned photon images of Centaurus field in the 0.2 – 2.3 keV for TM8 and 0.8 – 2.3 keV for TM9, before (*left*) and after (*right*) the PIB subtraction. Both images are shown in logarithmic scale and Gaussian-smoothed with a radius of 20 pixels. The colorbar is in the units of counts. The bright area at the left side of the images is caused by the Galactic foreground emission, the eROSITA Bubbles (Predehl et al., 2020, see Section 1.6.2)

PIB map for individual TM in the chosen soft band was generated and then co-added to yield a TM0 PIB map. In order to create a PIB-subtracted photon image in this soft band, the TM0 PIB map was subtracted from the fully-cleaned TM0 photon map in the corresponding energy band. Figure 3.5 shows a fully-cleaned TM0 photon map of the Centaurus field in the 0.2 – 2.3 keV band for TM8 and the 0.8 – 2.3 keV band for TM9 before (left) and after (right) PIB subtraction.

3.3.2 Relative Galactic Absorption Correction

When dealing with large areas, the Galactic foreground absorption (Section 1.4.1) can vary greatly across the FoV. Therefore, it is important to properly take the Galactic absorption into account, especially when studying the faintest area of a cluster. In order to do this, we constructed the relative Galactic absorption correction map for each type of eROSITA TM. For each cluster field, the process starts from a map of the total hydrogen column density along the LOS (N_{Htot}) which serves as a tracer for all absorbing material. For the A3391/95 field (the first project), the map was constructed from the IRAS 100 μm (Miville-Deschênes & Lagache, 2005) and the HI4PI data (HI4PI Collaboration et al., 2016) and provided by PD Dr. Jürgen Kerp. The details of the procedure for generating this map are described in Sect. 2.5 in Reiprich et al. (2021). The A3391/95 N_{Htot} map is shown in the left panel of Figure 3.6. The N_{Htot} values in this field vary between $3.240 \times 10^{20} \text{ atoms cm}^{-2}$ and $1.071 \times 10^{21} \text{ atoms cm}^{-2}$.

For the Centaurus field, the N_{Htot} map was obtained by adding the column density map of the atomic hydrogen N_{HI} and the column density map of the molecular hydrogen N_{H_2} . The first map was produced by cutting out and reprojecting the HI4PI all-sky Galactic neutral atomic hydrogen map (HI4PI Collaboration et al., 2016) to the observation field (left panel of Figure 3.7a). Meanwhile, the N_{H_2} map (right panel of Figure 3.7a) was generated by utilizing the Galactic column density of Hydrogen tool⁶ (UK Swift Science Data Centre, 2013) that employs the method described in Willingale et al. (2013).

⁶<https://www.swift.ac.uk/analysis/nhtot/>

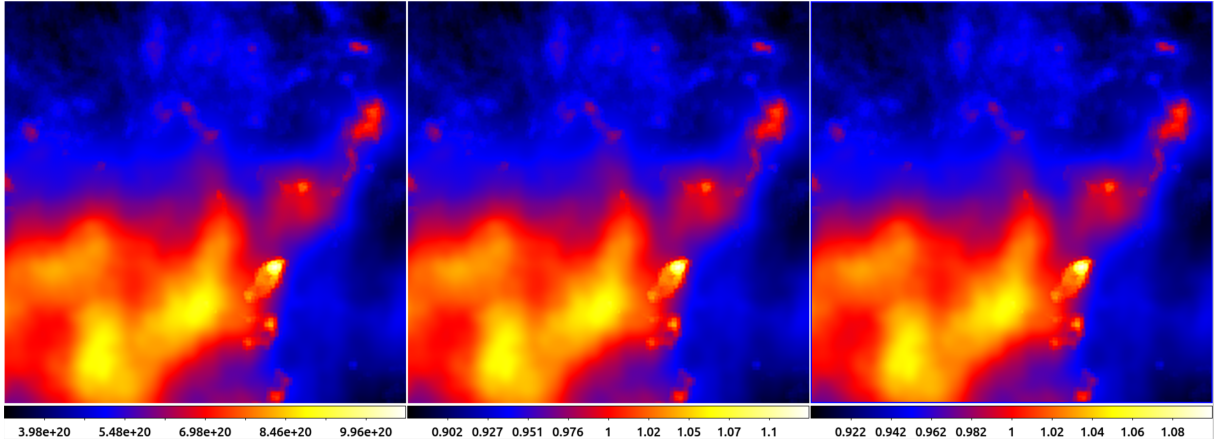


Figure 3.6: The N_{Htot} map used for the relative Galactic absorption correction of the A3391/95 field in the units of atoms cm^{-2} (left), and the corresponding absorption correction map for TM8 (middle) and TM9 (right).

The tool returns both mean and weighted Galactic hydrogen column density values within 1° of the input coordinates. It is, however, computationally demanding to query each pixel coordinates of the image (the size Centaurus image is $13000 \text{ pixels} \times 13000 \text{ pixels}$) and it is also not necessary since the spatial resolution of the underlying N_{H} survey in the tool ($\sim 0.75^\circ$) is larger than the adopted eROSITA image resolution (0.001°). Therefore, we reduced the number of coordinates by sampling the image into $20 \text{ pixels} \times 20 \text{ pixels}$ grids and querying the central coordinates of the grids instead. For each grid, the returned weighted N_{H_2} value at its central coordinates was interpolated into all pixels in this grid. The process was done automatically using one of the scripts that includes multiprocessing to speed up the processing time. Within the scrip the N_{HI} and N_{H_2} were combined to yield N_{Htot} map. The Centaurus N_{Htot} map is shown in the left panel of Figure 3.7b. The N_{H} values in this field vary between $4.160 \times 10^{20} \text{ atoms cm}^{-2}$ and $2.232 \times 10^{22} \text{ atoms cm}^{-2}$.

In order to generate the absorption correction map, we simulated a simple sky background model. The simulations were realized in the X-ray Spectral Fitting package (XSPEC; [Arnaud, 1996](#)) version 12.12.0 by using the `fakeit` command. The model consists of one unabsorbed and one absorbed diffuse thermal emission representing the Local Hot Bubble (LHB) and Milky Way Halo (MWH), and absorbed power-law component to account for the unresolved background sources. The simulations were done for the eROSITA with and without the on-chip filter separately, hence, the response files (RMF and ARF) for each TM type were supplied. We utilized the response files of TM1 and TM5 to represent the TMs with- and without on-chip filters, respectively. The energy ranges were set to be the same as the energy ranges used for creating the images (Table 3.2). For completeness, we simulated N_{H} values with an increment of $1 \times 10^{16} \text{ atoms cm}^{-2}$ between the minimum and maximum N_{H} values found in the N_{H} map. In total, 748 and 1817 values were simulated for the A3391/95 and Centaurus projects for each type of TM. From every simulation, a count rate value was obtained. In Figure 3.8, we showed the simulated eROSITA spectra using the response files of TM1 (left) and TM5 (right).

The absorption correction factor was calculated by taking the ratio of the estimated count rate of a given N_{H} value to the count rate of the median N_{H} value in the field. The absorption correction map was built by replacing the N_{H} value in a pixel with its corresponding absorption correction factor value. Each correction map was then multiplied by its corresponding exposure map to yield the absorption-corrected exposure map. The correction maps for both types of TMs in both projects are shown in the middle and right panels of Figure 3.6 and 3.7b. The information on the relative N_{H} correction procedure of the

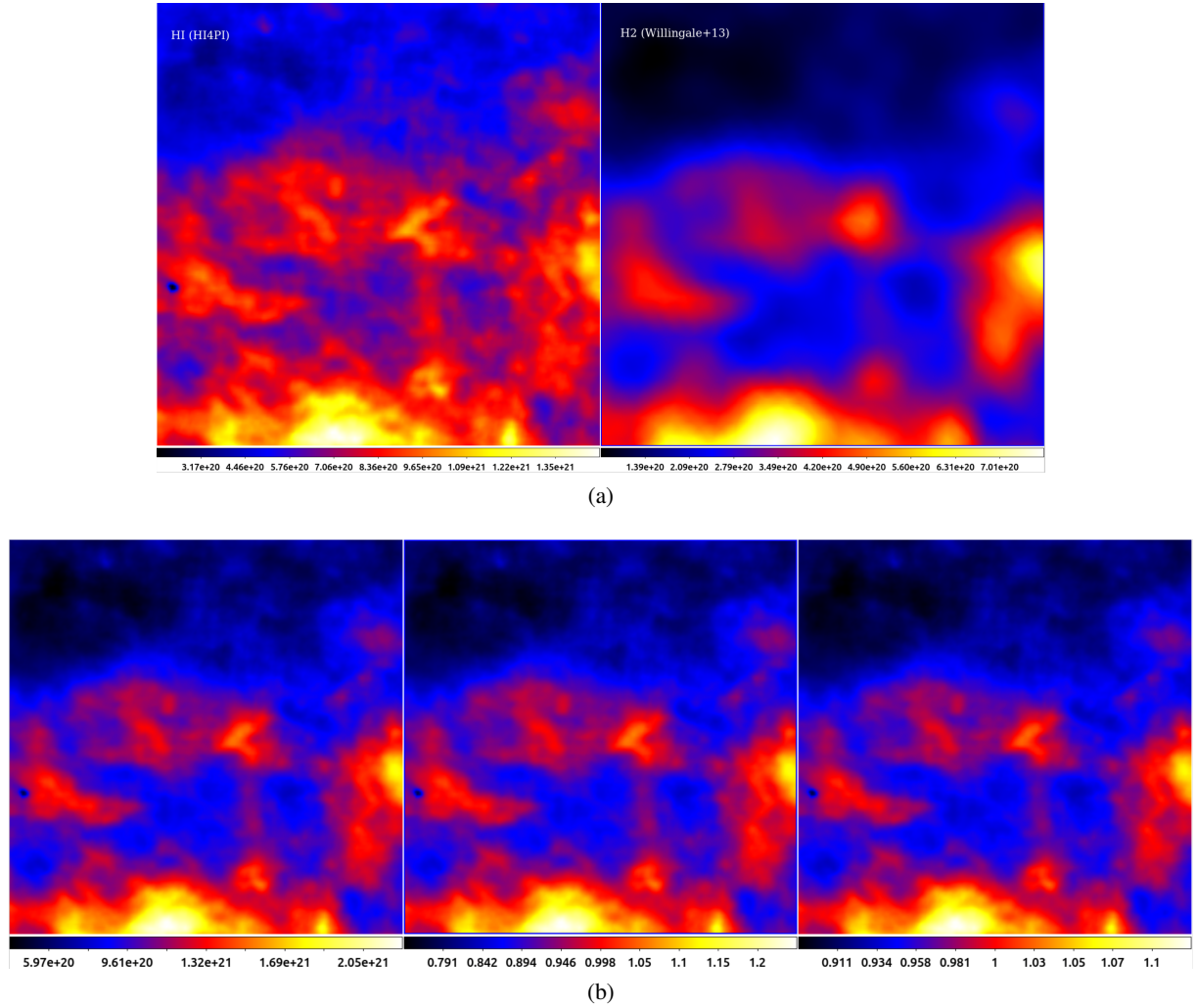


Figure 3.7: (a): N_{HI} (left) and N_{H_2} (right) maps in the units of atoms cm^{-2} . (b): The N_{Htot} map used for the relative Galactic absorption correction of the Centaurus cluster field in the units of atoms cm^{-2} (left), and the corresponding absorption correction map for TM8 (middle) and TM9 (right).

projects are summarized in Table 3.3.

To automate the entire procedure described above, I developed scripts that include: the generation of cut and reproject all-sky HI4PI map into the needed observation field, calculation of N_{H_2} map (subsequently, N_{Htot} map) utilizing the Galactic column density of Hydrogen tool⁷ (UK Swift Science Data Centre, 2013; Willingale et al., 2013), and the simulations of the N_{H} values to predict count rates of the two types of eROSITA TMs and create the respective relative absorption correction maps.

3.3.3 Exposure Correction

There are four observations and five eRASS data combined for the A3391/95 PV and Centaurus fields, respectively. Moreover, with different filter setups of TM8 and TM9, hence, different soft responses (Predehl et al., 2021; Reiprich et al., 2021), as well as the energy bands discrepancies between TM8 and TM9 caused by the light leak affecting the later (Table 3.2), further correction is necessary when

⁷<https://www.swift.ac.uk/analysis/nhtot/>

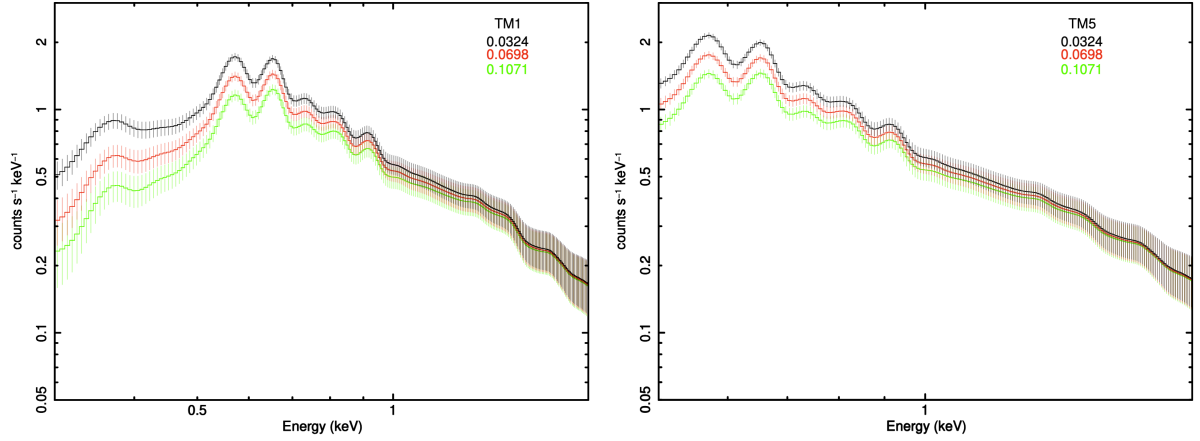


Figure 3.8: Simulated eROSITA spectra using the sky background model to obtain count rates of different N_{H} values. *Left*: Using TM1 response files (representing TMs with on-chip filter). *Right*: Using TM5 response files (representing TMs without on-chip filter). The simulated N_{H} values are labeled in each plot in units of 10^{22} atoms cm^{-2} .

Project	Cluster	N_{Htot} map	N_{H} range [10^{22} atoms cm^{-2}]	correction (TM8)	correction (TM9)
1	A3391/95	(HI4PI + IRAS) ^a	0.0324 – 0.1071	$\lesssim 12\%$	$\lesssim 3\%$
2	A3391/95	(HI4PI + IRAS) ^a	0.0324 – 0.1071	$< 14\%$	$< 11\%$
3	Centaurus	HI4PI ^b + Willingale ^c	0.0416 – 0.2232	$\lesssim 35\%$	$< 13\%$

^aProvided by PD Dr. J. Kerp (Reiprich et al., 2021), ^b HI4PI Collaboration et al. (2016), ^c Willingale et al. (2013)

Table 3.3: The summary of the relative Galactic absorption correction of both cluster fields studied in the projects. The energy ranges simulated for TM8 and TM9 for the different projects are as listed in Table 3.2.

combining all TMs. For instance, without an appropriate correction, the inhomogeneous coverage of the different A3391/95 observations (Table 3.1) results in underestimation of count rates in the upper part of the FoV that are only covered mostly by TM9 in the observation 300005 and 300006, and an overestimation of count rates in the left and bottom part of the FoV that are contributed mostly by TM8 of the observation 300016.

Since the source and X-ray background spectra vary across the FoV, the count rate bias is spatially variable. Also, the exposure maps of TM8 and TM9 are different, hence the fraction of missing photons in TM9 is also spatially variable. Taking into account all of these effects requires intricate methods. A first-order correction can be achieved by treating the combined TM8 and TM9 exposure maps separately and by using the full FoV PIB-subtracted count rate ratio of TM9 to TM8 for estimating the needed correction factor. The calculation is written as,

$$\text{corr} = \frac{CR_{\text{PIBsub, TM9}}}{CR_{\text{PIBsub, TM8}}}. \quad (3.2)$$

The correction factor, corr, was then multiplied by the combined exposure map of TM9 to yield TM9 exposure in the same band with the same soft response as TM8. The fully combined exposure map from all TMs and observations (exp. TM0) will be,

$$\text{exp.TM0} = \text{exp.TM8} + \text{corr} \times \text{exp.TM9}. \quad (3.3)$$

The PIB-subtracted, relative Galactic absorption-corrected, exposure-corrected image was acquired by dividing the TM0 PIB-subtracted photon image by the TM0 relative Galactic absorption-corrected and corrected exposure map (right panel in Figure 3.9). The resulting count rates from the fully-corrected image correspond to an effective area given by a single TM with an on-chip filter in the used energy band, i.e., 0.5 – 2.0 keV and 0.3 – 2.0 keV for each of the A3391/95 field, and 0.2 – 2.3 keV for the Centaurus field.

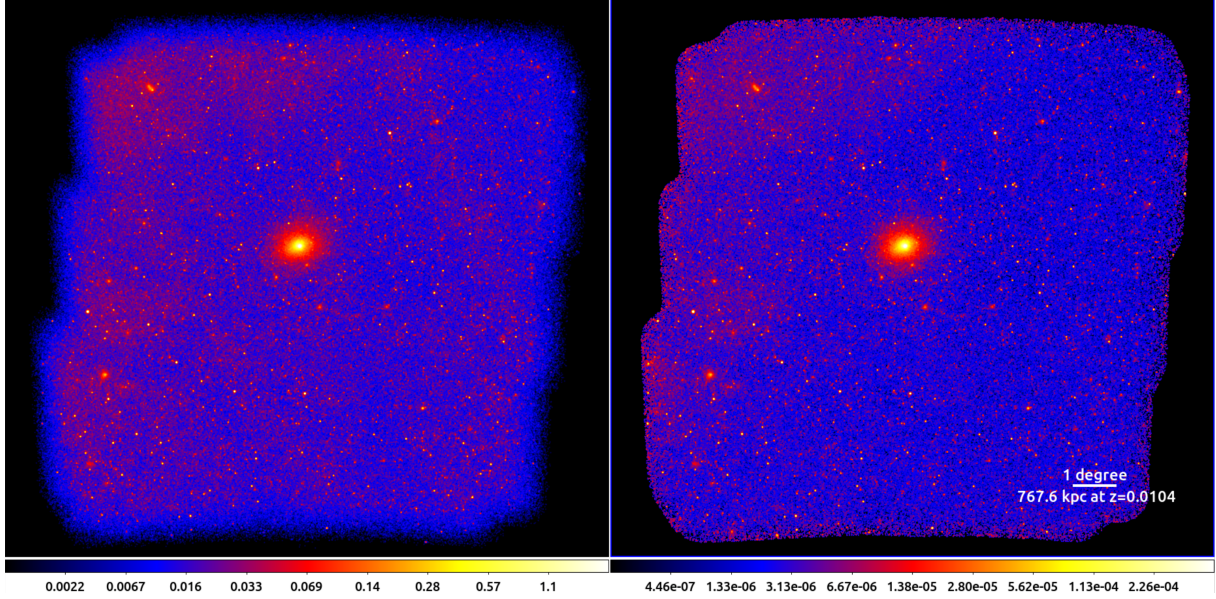


Figure 3.9: Fully-cleaned photon images of Centaurus field in the 0.2 – 2.3 keV for TM8 and 0.8 – 2.3 keV for TM9, before (*left*, in the units of counts) and the PIB-subtracted, relative Galactic absorption-corrected, exposure-corrected image (*right*, in the units of counts per second) in 0.2 – 2.3 keV band. The image on the right is the final, all-TM combined, fully-corrected image. Both images are shown in logarithmic scale and Gaussian-smoothed with a radius of 20 pixels. The bright area at the left side of the images is caused by the Galactic foreground emission, the eROSITA Bubbles (Predehl et al., 2020, see Section 1.6.2)

3.4 Imaging Analysis

3.4.1 Wavelet Filtering and Source Catalog Generation

When analyzing the cluster, we are only interested in the extended emission from the ICM. Therefore, any other sources that are irrelevant to the study, for instance, point sources (typically AGNs) and background/foreground extended sources, need to be excluded. In order to do this, we built a source catalog following the procedure described in Pacaud et al. (2006) and Ramos-Ceja et al. (2019). First, a wavelet-filtering algorithm was employed to suppress Poisson noise and enhance the signal from the sources. Afterward, the source detection was carried out by supplying the wavelet-filtered image to the Source Extraction software (SExtractor; Bertin & Arnouts, 1996). A visual inspection was also carried out to identify any sources that were missed by the algorithm. A source catalog was obtained and used to exclude the unwanted sources in the science analysis steps. Utilizing the position and size

information of the unwanted sources from the catalog, a cheese mask was also generated, which is an image consisting of 1- and 0-valued pixels. The cheese mask is used for removing pixels of the unwanted sources (0) and keeping the remaining pixels (1), resulting in an image with 'holes'. The fully-corrected TM0 wavelet-filtered image of the Centaurus cluster in the 0.2 – 2.3 keV band is displayed in the left panel of Figure 3.10. The cheese mask generated employing the acquired source catalog in the described procedure is shown in the right panel.

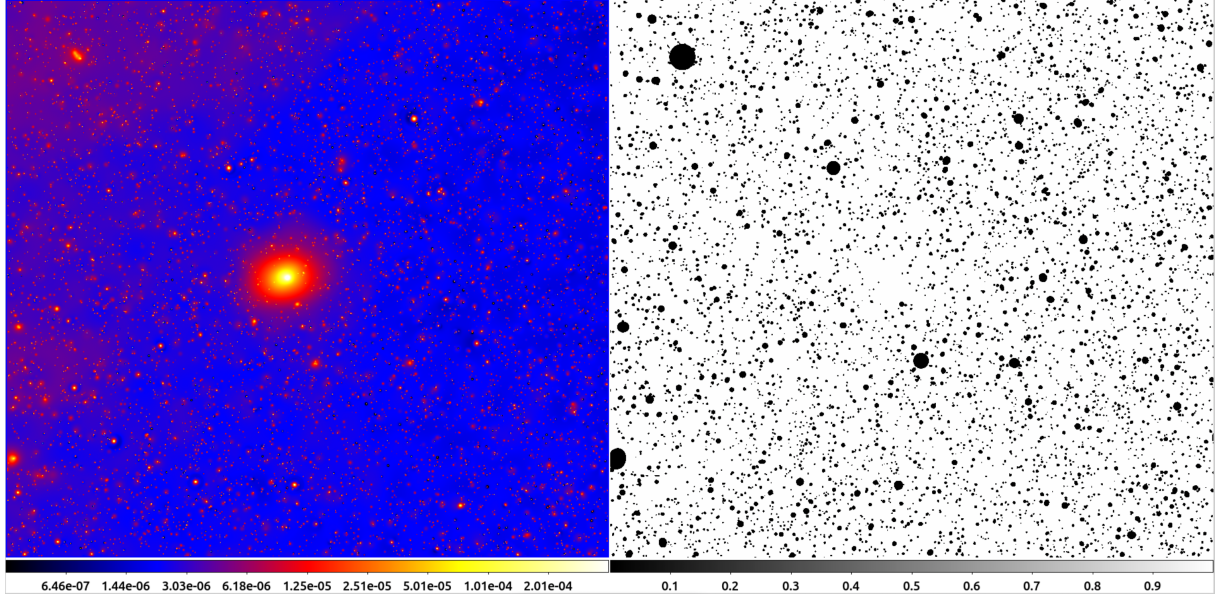


Figure 3.10: *Left*: The fully-corrected TM0 wavelet-filtered image of Centaurus cluster in the 0.2–2.3 keV band. *Right*: The cheese mask generated using the source catalog produced from the SExtractor run of the wavelet-filtered image.

3.4.2 Imaging Processing Techniques

Several image processing techniques were employed to enhance the features in ICM that will aid with visual inspection. We employed several methods that can be optimized for emphasizing ICM features in different scales.

Adaptive Smoothing

Adaptive smoothing produces an image where the signal-to-noise ratio (S/N) at each pixel is as close as possible to the desired S/N value, namely that the fainter areas (e.g., cluster outskirts and filaments) will be more thoroughly smoothed than the brighter areas. To adaptively-smoothed the images, we utilized the `asmooth` task of the *XMM-Newton* Science Analysis System (SAS; [ESA: XMM-Newton SOC, 2023a](#)) with the parameter `smoothstyle='adaptive'`. The contribution from point sources and other unwanted sources can be excluded by supplying cheese-masked input images (photon image, exposure map, PIB map). The task will refill the holes with the surrounding background pixel values. Any resulting adaptively-smoothed images are for visual inspection only. They are especially useful to trace large-scale structures and identify regions of interest for subsequent analysis.

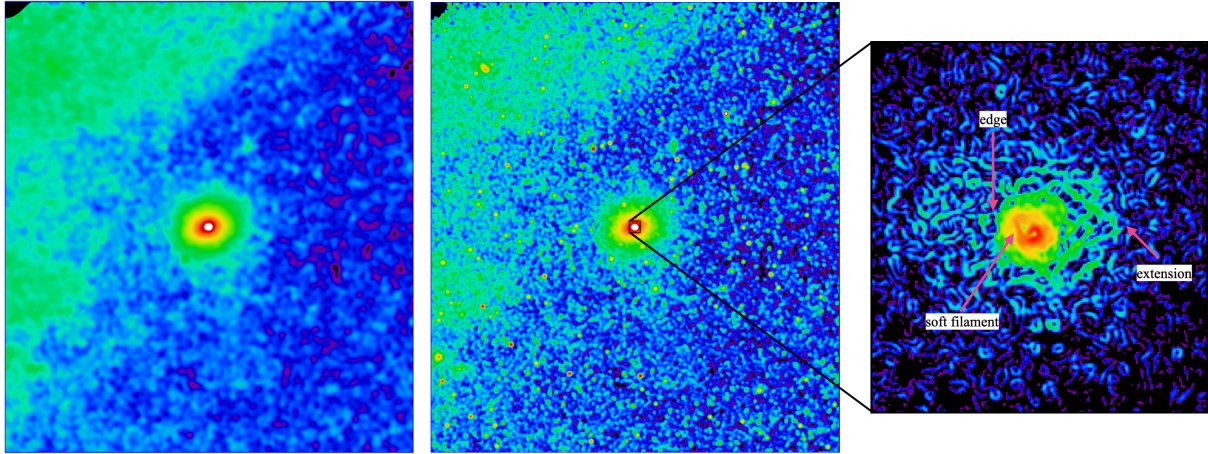


Figure 3.11: Image processing techniques applied to the Centaurus cluster field. *Left*: Adaptively-smoothed image with a S/N value of 45. Unwanted sources have been removed and the masked-out pixels have been refilled with surrounding background pixels. *Middle*: Fully-corrected image resulted from the image correction procedure described in Section 3.3. Gaussian smoothing with a kernel radius of 25 pixels has been applied. *Right*: GGM-filtered of the fully-corrected image zoom-in to the cluster core. Labeled are some features enhanced through the technique.

Gaussian Gradient Magnitude Filtering

The Gaussian Gradient Magnitude (GGM) filtering calculates the magnitude of the surface brightness gradient assuming Gaussian derivatives. The technique accentuates features, such as edges, as demonstrated in other galaxy cluster studies (e.g., Sanders et al., 2016a,b; Walker et al., 2016). The GGM filtering is adjusted with the Gaussian width σ , for instance, a smaller scale highlights features in bright regions (cluster center), while a larger scale is for regions with fewer counts (outskirts). The application of GGM filtering was done using the available implementation from SciPy⁸ (Virtanen et al., 2020).

RGB Image

The red-green-blue (RGB) image is an image visualization technique to represent images with different information as one. Usually, the RGB image can be a composition of three images of an object observed in different wavelengths (e.g., radio, optical, and X-ray) or a partition of three sub-energy bands.

We generated the latter RGB image, particularly, since we were interested in gaining a deeper understanding of the distribution of photons in the FoVs. Through the image, a prediction of the spectral shape of the sources (ICM and extended foreground emission) can be made, which gives a rough estimate of their temperature. We employed the image correction procedure (Section 3.3) to produce fully-corrected images in the 0.2 – 0.6 keV band (red channel), 0.6 – 1.0 keV band (green channel), and 1.0 – 2.3 keV band (blue channel) for the Centaurus field. The images in these color channels are displayed in Figure 3.12.

⁸<https://scipy.org>

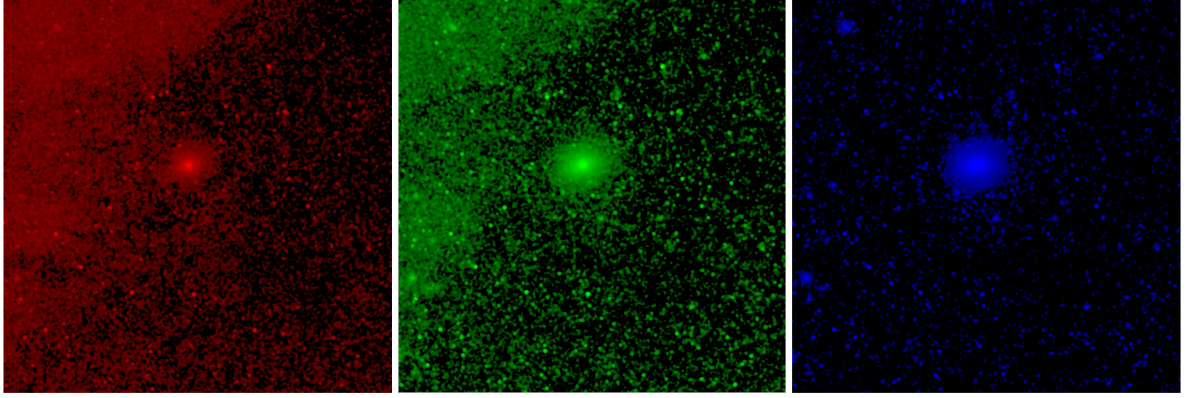


Figure 3.12: Fully-corrected image used for composing the RGB image. Gaussian smoothing of 25-pixel kernel radius has been applied to each image. *Left*: 0.2 – 0.6 keV band. *Middle*: 0.6 – 1.0 keV band. *Right*: 1.0 – 2.3 keV band.

3.4.3 Surface Brightness Profile

The morphology of the ICM emission of a cluster can be inspected by a surface brightness profile constructed around the cluster center. Various directions can also be probed to search for any features that deviate from a typical cluster surface brightness profile (β -mode; Section 1.4.2) or the average of all directions. It can also be used for quantifying any features that are visually present in the image, such as enhancements, jumps, or depression, and the significance level of emission in the outskirts of a cluster.

I wrote a series of scripts that enable surface brightness calculations and visualization. The first script employs the `functs` task of `Funtools` package⁹ to calculate the sum of all pixel values within a given source region, the Poissonian statistical uncertainties (\sqrt{n}), and the corresponding physical area in a unit of arcseconds. The excluded pixels belonging to the unwanted source were taken into account during these calculations. A photon image, an exposure map, a PIB map, and a region file consisting of the information of the source region and a list of unwanted sources were supplied to the script. Multiple source regions can also be given in one region file, then the calculation will be done per source region. For each run of the script, three files were generated and each file lists the sum of pixel values of the given regions following the order they were listed in the region file: photon counts ($\sum_{i=1}^N \text{cts}$) calculated

from the photon image, the sum of exposure ($\sum_{i=1}^N \text{exp}$) from the exposure map, and PIB counts ($\sum_{i=1}^N \text{cts}_{\text{PIB}}$) from the PIB map. Using these files, the second script calculates the surface brightness value of each source region. For the i -th source region, the calculation is formulated as follows

$$\text{SB}_i = \frac{(\sum \text{cts}_i - \sum \text{cts}_{\text{PIB}_i})/t_i}{A_i}, \quad (3.4)$$

where t_i is the average exposure per pixel which was calculated by dividing the sum of exposure $\sum \text{exp}_i$ by the number of pixels in the corresponding area, A_i . The statistical uncertainty of SB_i was obtained by propagating the Poissonian statistical uncertainties of $\sum \text{cts}_i$, $\sum \text{cts}_{\text{PIB}_i}$, and $\sum \text{exp}_i$ during the calculation.

An example of an SB profile constructed from the center of the Centaurus cluster out to 90 arcmin with a bin width of 0.25 arcmin is displayed in the right panel plot in Figure 3.13. The image on the left

⁹Funtools is a FITS library and utility package developed by Eric Mandel, CfA. <https://github.com/ericmandel/funtools>.

is the wavelet-filtered image multiplied by the cheese mask to indicate the removed sources. The green annuli depict the source region out of which the SB profile on the left plot was calculated. The number of the shown annuli was reduced for better visualization. The magenta boxes correspond to the regions used to estimate the local level of the CXB. The CXB level ($\overline{SB}_{\text{CXB}}$) shown in the SB plot (magenta dashed-line) is the mean SB of the six boxes. The 1σ error of the CXB level (magenta shaded area) was calculated by taking the standard deviation among the boxes to include the variation of the CXB,

$$\sigma_{\text{CXB}} = \sqrt{\frac{\sum_{i=1}^N (SB_{\text{CXB},i} - \overline{SB}_{\text{CXB}})^2}{N}} \quad (3.5)$$

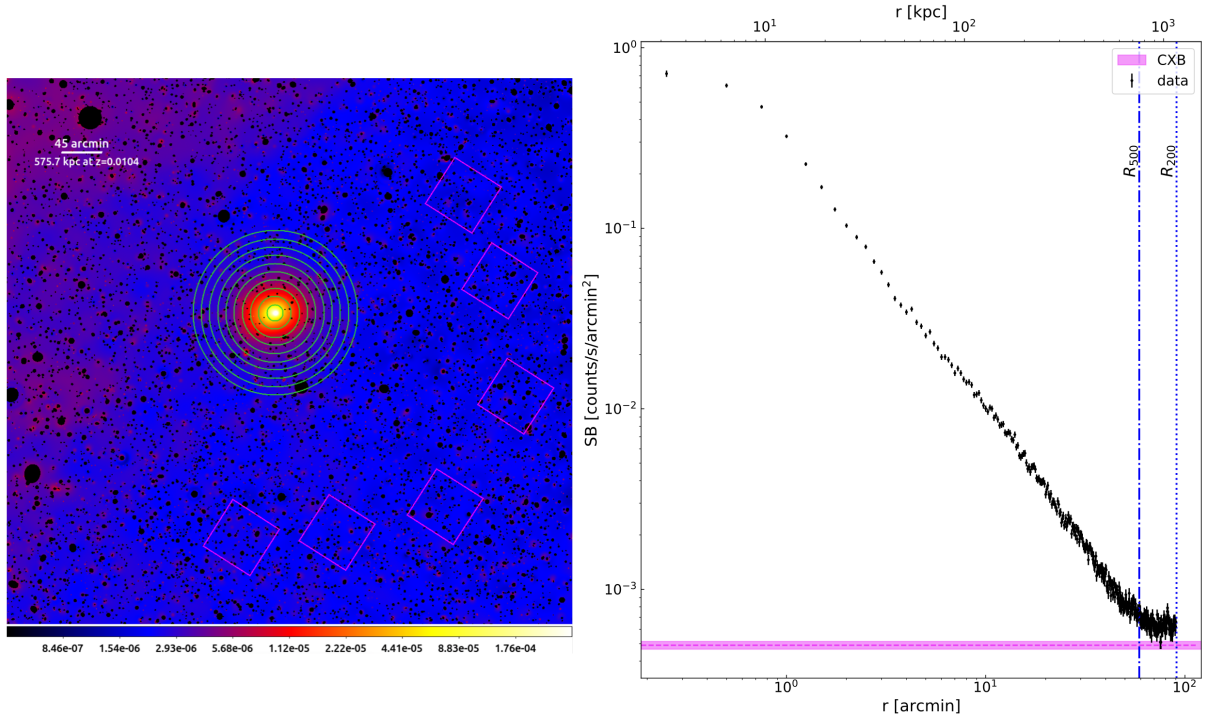


Figure 3.13: *Left*: Wavelet-filtered image of the Centaurus cluster multiplied by the cheese mask. The green annuli and pink boxes denote the source and CXB regions from which the cluster surface brightness profile and the CXB surface brightness level were calculated. The number of green annuli was reduced for better visualization. *Right*: The corresponding surface brightness plot (black data points). The CXB level and the 1σ error are shown as the magenta dashed line and shaded area.

Furthermore, when trying to compare surface brightness profiles extracted from different instruments, the instrumental effect, on top of the absorption, needs to be corrected first. The correction can be done by multiplying each surface brightness value with a conversion factor, that is, the ratio of the unabsorbed energy flux to the absorbed count rates. These quantities can be estimated by simulating the spectrum of the instrument by supplying the ICM properties and the response files of the instrument. In the case of the effective area on top of the vignetting has been accounted for in the exposure map, the conversion factor is simply the ratio of the unabsorbed energy flux to the absorbed photon flux.

3.5 Spectral Analysis

In this section, we will discuss the spectral fitting procedure that results in information on the X-ray properties of the ICM or filament, such as temperature ($k_B T$), metallicity (Z), redshift (z), and normalization ($norm$). The eROSITA cluster fitting strategy described in the eROSITA Final Equatorial-Depth Survey (eFEDS) works (Ghirardini et al., 2021; Liu et al., 2022) was adopted. All eROSITA spectra and response files were extracted using the eSASS `srctool` task and the spectral fitting was realized in XSPEC (Arnaud, 1996). We note that since clusters and their environments are never identical, minor differences in the spectral fitting procedure might occur in the different projects. If it is present, those differences will be stated in the respective chapters.

3.5.1 Components

The full model describing the observed eROSITA cluster spectrum is a summation of three main terms: the sky or CXB (see Section 1.6.2) term, the source term, and the instrumental background (PIB; see Section 1.6.1) term. Some XSPEC models were used to construct the components in each term. Those are:

- **apec**: a component to model an emission of optically thin, collisionally-ionized diffuse plasma (Smith et al., 2001). The parameters in this component are the plasma temperature ($k_B T$ in the unit of keV), the metal abundances/metallicity (Z in Z_\odot), redshift (z), and normalization ($norm$),
- **TBabs**: calculates the cross-section of the X-ray absorption by the interstellar medium (ISM) in the Galaxy (Wilms et al., 2000). The model is parametrized by the Galactic hydrogen column density along the line of sight (N_H in 10^{22} atoms cm^{-2} unit),
- **gauss**: to model Gaussian lines. The parameters include line energy (E in keV), line width (σ in keV), and the amplitude of the line (K in photons/ cm^2/s),
- **powerlaw**: to describe a simple photon power law spectrum controlled by a photon index (Γ) and the normalization in photons/keV/ cm^2/s at 1 keV.

In general, the total model used to fit the eROSITA cluster or filament spectrum is

$$\text{Model} = \underbrace{\text{apec}_{\text{LHB}} + \text{TBabs} \times (\text{apec}_{\text{MWH}} + \text{powerlaw})}_{\text{CXB component}} + \underbrace{\text{TBabs} \times \text{apec}_{\text{clus}}}_{\text{cluster/filament emission}} + \text{PIB}, \quad (3.6)$$

where apec_{LHB} and apec_{MWH} represent the foreground emission originated from the unabsorbed and absorbed Local Hot Bubble (LHB) and Milky Way Halo (MWH). During the fit, the temperatures of the LHB and MWH were fixed to 0.1 keV (Liu et al., 2017b) and 0.25 keV (Kuntz & Snowden, 2000), respectively, unless, there were enough statistics to constrain the values from the local background spectra. Their metallicities were set to $1Z_\odot$ and since these components are of Galactic origin, the redshifts were set to 0. The **powerlaw** component is to model the emission of the unresolved background sources. We froze the photon index of the power law at $\Gamma = 1.46$ (Luo et al., 2017). The absorbed thermal emission from the cluster or filament is described by the $\text{TBabs} \times \text{apec}_{\text{clus}}$ term. In the case of multi-phase gas, another **apec** component can be added to this term. The Galactic column density supplied to the **TBabs** component was taken to be the median of N_H values from the spectrum region taken from the N_H map (see Section 3.3.2).

The last term, PIB, accounts for the emission of the PIB. The modeling of the PIB employed the results of the analysis of the FWC data in the respective processing version, c001¹⁰ and c020¹¹ (Yeung et al., 2023; Freyberg et al., 2020). The PIB component comprises two power laws to account for the increase of detector noise at low energies, a combination of a power law and an exponential cut-off to model the signal above ~ 1 keV, and up to 21 Gaussian lines to model the fluorescence lines generated from the interaction of high-energy particles with detector material. The most prominent fluorescence lines are the Al-K α line at 1.486 keV and the Fe-K α line at 6.391 keV, while some of the weaker lines are Ti-K α at 4.504 keV, Co-K α at 6.915 keV, Ni-K α at 7.461 keV, Cu-K α at 8.027 keV, and Zn-K α at 8.615 keV.

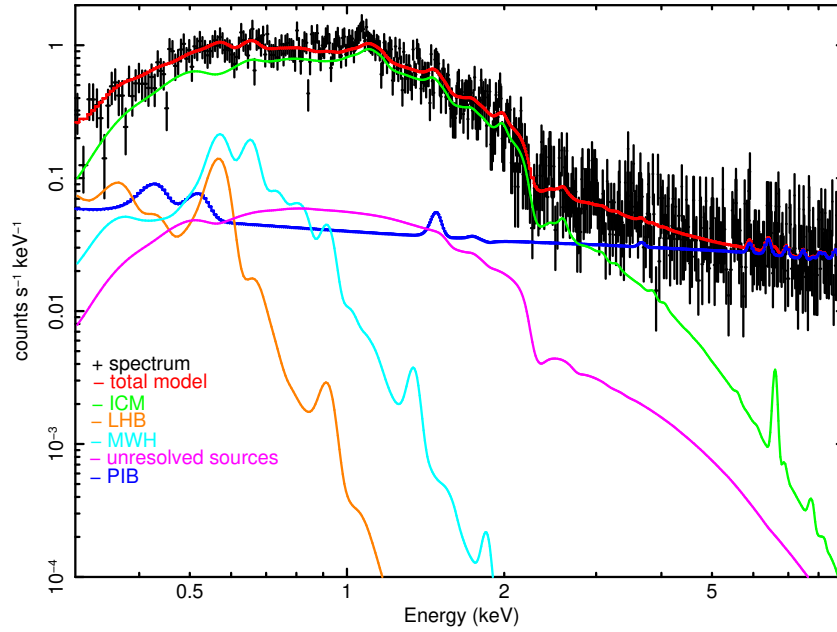


Figure 3.14: Centaurus cluster's TM1 spectrum (black data points) extracted from an annulus ($0.2 - 0.5R_{500}$) centered at the cluster center with its fitted total model (red line). The various components are denoted in different colors as indicated in the legend.

3.5.2 Strategy

The source (cluster or filament) and CXB spectra and their corresponding response files (RMFs and ARFs) were extracted by the eSASS srctool task individually. One of the parameters given to the task was a region file that includes the information of the source region(s) and a list of sources to be excluded from the spectral extraction (see Section 3.4.1). If multiple source regions were given in the region file, the task would generate spectra from all regions combined. The CXB region should be at some distance away from the cluster to avoid cluster emission, but not too far away that it might no longer be representative of the local CXB emission. Therefore, our CXB regions were typically at $\sim 2 \times R_{200}$ away from the cluster.

The fitting strategy is the following: The first step was to fit the CXB spectra of all TMs simultaneously to estimate the best-fit normalizations of the CXB components. Second, the source spectra were loaded and fitted simultaneously with the CXB spectra. The parameters of the CXB

¹⁰<https://erosita.mpe.mpg.de/edr/eROSITAObservations/EDRFWC/>

¹¹https://erosita.mpe.mpg.de/dr1/AllSkySurveyData_dr1/FWC_dr1/

components were linked across the spectra and the normalizations were set to the best-fit values from the first fit. However, the source and CXB N_{H} values were not linked and the values were fixed at the median N_{H} as described in the previous subsection. The cluster parameters were linked across the TMs and left to vary one after the other before fitting them all together, except for the redshift, which was fixed at a literature value or the optical redshift of the BCG. In the case of degeneracy, for example, due to low photon counts in low emissivity regions, the metallicity was fixed to a reasonable value, such as $0.2 - 0.3Z_{\odot}$ for cluster outskirts and $0.1 - 0.2Z_{\odot}$ for filament regions. These values are based on other galaxy cluster and filament metallicity measurements at the same regime (e.g., [Reiprich et al., 2009](#); [Werner et al., 2013](#); [Urban et al., 2017](#)) and cosmological hydrodynamical simulations (e.g., [Biffi et al., 2018b, 2022](#)). Lastly, the normalizations of the CXB components were left to vary, as well. The parameter estimation was done using C-statistics ([Cash, 1979](#)) within XSPEC which is more suitable for Poissonian data. The spectral fitting was performed in the $0.3 - 9.0$ keV band for TM8 and $0.5 - 9.0$ keV for TM9 and the solar abundance table from [Asplund et al. \(2009\)](#) was assumed. Unless stated otherwise, the reported uncertainties are at a 68.3% confidence interval.

The entire spectral fitting procedure is wrapped in a script for automatization. Information regarding the source and CXB regions (file names, N_{H} values, redshift of the source), PIB model files, and specific treatment to some parameters (e.g., freezing/thawing CXB normalizations in the second fit and freezing source metallicity at a certain value) were supplied. An XSPEC executable file tailored for a given source and CXB spectra were produced and subsequently, run in XSPEC. An example of an eROSITA cluster spectrum with its fitted model is shown in Figure 3.14.

3.5.3 Gas Properties and the Derivative Quantities

Through spectral fitting, the properties ($k_{\text{B}}T$, Z , and $norm$) of the cluster/filament emission were determined. Spectral profiles can be built by analyzing the spectra of concentric annuli or sectors around the cluster center. Similar to the surface brightness profile, these profiles are useful for identifying features caused by astrophysical processes. The temperature and normalization can also be used to derive other properties.

Determination of Characteristic Properties

The key ingredient of using galaxy clusters as a tool to probe the cosmological parameters is their total masses (including dark matter). They can be measured using direct methods such as gravitational lensing ([Hoekstra et al., 2013](#), see also Section 1.3.1), but it is expensive to be done on a large sample. Therefore, it is important to establish robust scaling relations, a more efficient mean to estimate the cluster total mass using some of the observable quantities, such as temperature, luminosity, and flux. Under the assumption of the self-similar evolution ([Kaiser, 1986](#)), correlations between the cluster observables and the total masses are expected in the form of simple power laws. Scaling relations provide important hints to understand the physics of galaxy cluster formation and evolution (see [Giodini et al., 2013](#), for a review on scaling relations).

When determining the total mass of a galaxy cluster or group, the mass–temperature ($M_{500} - T$) scaling relation by [Lovisari et al. \(2015\)](#) was used because the studied objects in the present thesis were closer to the considered sample in their work (low-mass systems at low- z). The scaling relation takes the following form

$$\log(M_{500}/C1) = a \cdot \log(k_{\text{B}}T/C2) + b, \quad (3.7)$$

where $C1 = 5 \times 10^{13} h_{70}^{-1} M_{\odot}$ and $C2 = 2$ keV. Meanwhile, the parameters a and b differ depending on the input temperature: if $k_{\text{B}}T > 3$ keV (a cluster), then $a = 1.62 \pm 0.08$, and $b = 0.24 \pm 0.04$, and

below the temperature cut (a group) the parameters are given as $a = 1.65 \pm 0.07$, and $b = 0.19 \pm 0.02$. By assuming spherical symmetry, subsequently, the R_{500} ¹² can be calculated

$$R_{500} = \left[\frac{3}{4\pi} \frac{M_{500}}{\rho_{500}(z)} \right]^{\frac{1}{3}}, \quad (3.8)$$

where $\rho_{500}(z)$ is the 500 times the critical density of the universe at a given redshift z .

Determining a more precise M_{500} (thus, R_{500}) were done through an iterative procedure. We initialized by extracting and fitting spectra of an annulus centered at the cluster center. The resulting temperature was then given to the scaling relation to obtain the characteristic radii. These steps were repeated until the inner and outer radii of the annulus correspond to the 0.2 and 0.5 of the calculated R_{500} . The temperature yield from the last step will be the average cluster temperature ($k_B T_{500}$). The cluster core was excluded during the calculation to not bias the estimation since some clusters have steep temperature drops toward their cores (Hudson et al., 2010), as well as to avoid contamination from the BCG. At $0.2 - 0.5 R_{500}$, typically no strong temperature gradient was observed. Furthermore, the area size was also chosen since studying the low- z clusters, the whole extent of these objects (at least to R_{500}) can not be covered by a single observation by previous X-ray instruments.

Gas density

The *apex* normalization parameter (*norm*) is related to the emission measure (EM, Equation 1.9) of the plasma, and hence, can be used to infer the ICM electron density. The *norm* is given by

$$norm = \frac{10^{-14}}{4\pi[D_A(1+z)]^2} \int n_e n_H dV, \quad (3.9)$$

where D_A is the angular diameter distance (Equation 1.26) to the source given in cm, n_e and n_H are the electron and hydrogen densities in cm^{-3} , and dV is the volume element in cm^3 . Equation 3.9 can be rearranged to

$$n_e n_H = \frac{4\pi[D_A(1+z)]^2}{V \cdot 10^{-14}}. \quad (3.10)$$

In the case of filament studies, typically, a simple geometrical shape is assumed, that is a cylinder of a given radius r and h with its axis lying in the plane of the sky. For an ionized plasma, $n_H \approx n_e/1.17$. For simplicity, a distance conversion of $1 \text{ Mpc} = 3.086 \times 10^{24} \text{ cm}$ can be used. Substituting these gives,

$$n_e = \left[1.52 \times 10^{-10} \text{ cm}^{-1} \times norm \times (1+z)^2 \times \left(\frac{D_A}{\text{Mpc}} \right)^2 \times \left(\frac{r}{\text{Mpc}} \right)^{-2} \times \left(\frac{h}{\text{Mpc}} \right)^{-1} \right]^{\frac{1}{2}}. \quad (3.11)$$

Using n_e , the gas density can be calculated with the following equation

$$\rho_{\text{gas}} = \mu_e \times n_e \times m_p, \quad (3.12)$$

where $\mu_e \approx 1.14$ is the mean molecular weight of the electron and $m_p = 1.6726 \times 10^{-24} \text{ g}$ is the proton mass.

¹²The R_X is the radius within which the density is X times the critical density of the Universe at the given redshift. We can convert the characteristic radii using the relations described in Reiprich et al. (2013), e.g., $R_{500} \approx 0.65 R_{200}$, $R_{100} \approx 1.36 R_{200}$, and $R_{2500} \approx 0.28 R_{200}$.

Chapter 4

The eROSITA view of the Abell 3391/95 field: The Northern Clump

The largest infalling structure in the longest known gas filament observed with eROSITA, XMM-Newton, and Chandra

The eROSITA view of the Abell 3391/95 field: The Northern Clump
The largest infalling structure in the longest known gas filament observed with eROSITA, XMM-Newton, and Chandra

A. Veronica, Y. Su, V. Biffi, T. H. Reiprich, F. Pacaud, P. E. J. Nulsen,
R. P. Kraft, J. S. Sanders, A. Bogdan, M. Kara, K. Dolag, J. Kerp,
B. S. Koribalski, T. Erben, E. Bulbul, E. Gatzuz, V. Ghirardini,
A. M. Hopkins, A. Liu, K. Migkas, T. Vernstrom
2022, A&A, 661, A46

<https://doi.org/10.1051/0004-6361/202141415>

Overview

About 30 – 40% of the total baryons in the local Universe are still unobserved. The cosmological hydrodynamic simulations predict that they reside in the warm-hot intergalactic medium (WHIM) in the cosmic filaments (Cen & Ostriker, 1999; Davé et al., 2001). Due to its elusive nature ($n_e \approx 10^{-6} - 10^{-4} \text{ cm}^{-3}$ and temperature in the range of $T = 10^5 - 10^7 \text{ K}$ ($k_B T \approx 0.009 - 0.862 \text{ keV}$), Nicastro et al., 2017), the detection of filaments has been challenging (e.g., Werner et al., 2008b; Nicastro et al., 2018). Attempts should be directed towards the densest part of the filaments, such as the outskirts of galaxy clusters (e.g., Reiprich et al., 2013) and between a nearby galaxy cluster pair (e.g., Kull & Böhringer, 1999; Werner et al., 2008b; Vazza et al., 2019).

The Abell 3391 and Abell 3395 cluster system (A3391/95) is a close-by galaxy cluster pair, located at $z \approx 0.05$. It has been observed extensively to detect filament emission between the two clusters. Earlier studies using X-ray instruments *ROSAT* and *ASCA* revealed the detection of diffused gas between the northern cluster, A3391, and the southern double-peaked cluster, A3395 (Tittley & Henriksen, 2001). More recent studies with *XMM-Newton*, *Chandra*, and *Suzaku* investigated the nature of the emission

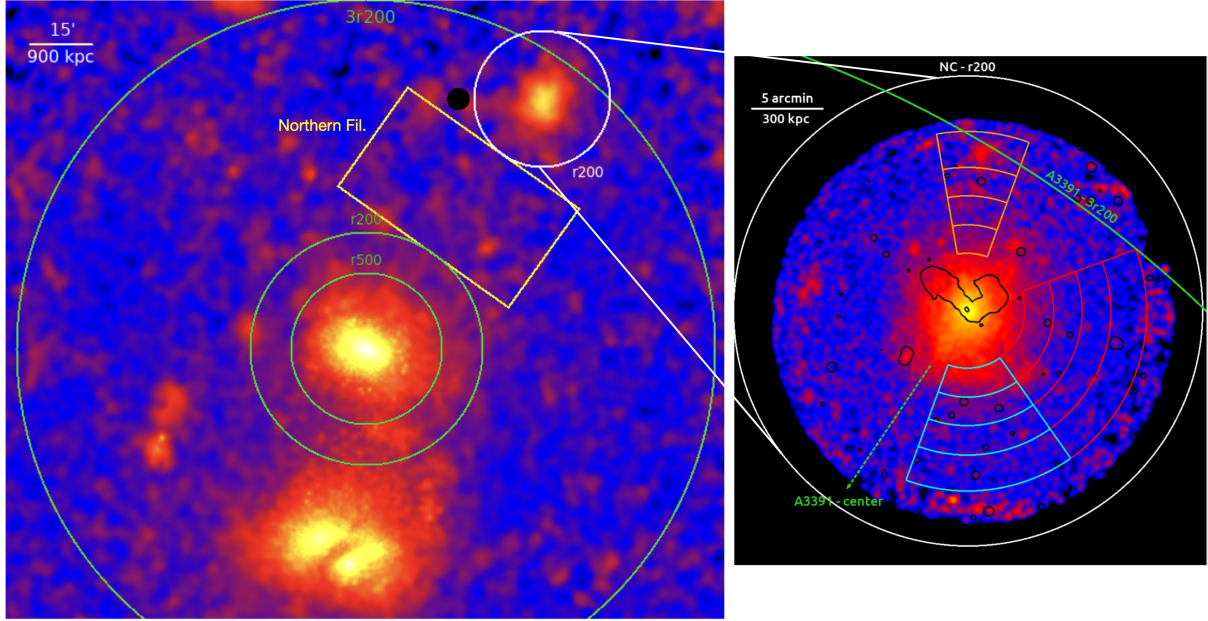


Figure 4.1: *Left*: eROSITA PIB-subtracted, relative-Galactic-absorption- and exposure-corrected image in the $0.5 - 2.0$ keV band centered at the A3391 cluster (see Section 3.3). The image has been adaptively smoothed with a S/N value of 15 (Section 3.4.2). The point sources were removed and replaced with surrounding background pixel values. The green circles indicate characteristic radii of A3391, while the white circle shows the R_{200} of the Northern Clump. The yellow box is the region used for the spectral analysis of the Northern Filament. *Right*: *XMM-Newton* PIB-subtracted, exposure-corrected, point-sources-removed and refilled image of the Northern Clump in the $0.5 - 2.0$ keV band. The radio emission contours from the ASKAP/EMU radio survey are plotted in black.

bridging the two clusters and reported that the gas properties are more consistent with a tidally-stripped ICM gas from the clusters, suggesting that they are in an early merging phase (Sugawara et al., 2017; Alvarez et al., 2018). The A3391/95 system was observed by eROSITA during the Cal-PV phase (see Section 3.1.1) in October 2019 (Reiprich et al., 2021). With three scans and one pointed observation, eROSITA covered about 15 degree^2 area, providing the deepest-large-scale X-ray view of the system. The eROSITA A3391/95 PV observations show not only a strong detection of the gas between the A3391 cluster and the A3395 cluster but also detections of three filaments outward these main clusters, as well as some clumps/substructures seemingly infalling towards the main clusters together with the filaments. Two of the filaments (Northern and Southern Filaments) are detected with good significance, while the detection of the other (Eastern Filament) is tentative (Reiprich et al., 2021). This work aims to assess the morphological, thermal, and chemical properties of the largest infalling substructure, and the filament that connects it with the parent cluster, to gain insight into the large-scale structure (LSS) formation.

This work was published in the *Astronomy & Astrophysics* journal (Veronica et al., 2022) and the original published form can be found in Appendix A. I conducted the *XMM-Newton* and eROSITA data reduction, image correction, and scientific analyses, as well as wrote the corresponding parts in the manuscript. I contributed most of the interpretation of the results. Parts of this work were contained in my Master’s thesis, where rigorous analysis in the inner regions of the Northern Clump was performed using *XMM-Newton* and then compared with the results from *Chandra*. Hence, these points will not

be discussed here. Further analyses were performed in the early phase of the Ph.D.¹ and the results are reported in the paper, as well. The analyses focus on the outskirts and filament aspects of the Northern Clump and, hence, serves as groundwork for the second paper. These new analyses and results will be discussed here and they correspond to Section 3.2.3, 3.3.3., and 3.3.6 in [Veronica et al. \(2022\)](#).

4.1 The Northern Clump

The MCXC J0621.7-5242 cluster ([Piffaretti et al., 2011](#)), or MS 0620.6-5239 cluster ([De Grandi et al., 1999](#)) is situated in the north of the A3391 cluster. In this and the subsequent eROSITA view of the Abell 3391/95 field works, this cluster is dubbed as the Northern Clump. The redshift of the cluster, $z = 0.0511$ ([Tritton, 1972](#); [Piffaretti et al., 2011](#)), indicates that it is a member of the A3391/95 cluster system. The brightest cluster galaxy (BCG) is 2MASX J06214330-5241333 ([Brüggen et al., 2021](#)) and it coincides with the X-ray center. The galaxy hosts a bright wide-angle tail radio source, named PKS 0620-52 ([Morganti et al., 1993](#); [Trussoni et al., 1999](#); [Venturi et al., 2000](#); [Brüggen et al., 2021](#)).

The Northern Clump is seen to have entered the atmosphere ($3 \times R_{200}$) of the A3391 cluster (see left panel of Figure 4.1), which might cause its pronounced boxy shape. The cluster was also found to be connected to the A3391 cluster by the Northern Filament. Upon discovery, simultaneous follow-up observations were performed by *XMM-Newton* (right panel of Figure 4.1) and *Chandra*. Together with the ASKAP/EMU radio data, the DECam optical image, and the Planck y -map, in-depth studies of the cluster central region were accomplished. Imaging and spectral analysis out to larger radii were also carried out utilizing the eROSITA and *XMM-Newton* data, which will be presented in the following sections. All uncertainties are at the 68.3% confidence interval unless stated otherwise.

4.2 Instrument Independent Surface Brightness Profiles

The X-ray surface brightness profiles of *XMM-Newton*, *Chandra*², and eROSITA in the 0.5 – 2.0 keV were constructed following the method described in Section 3.4.3. A comparison between these surface brightness profiles can only be done after applying some corrections: to account for the instrumental effect (effective area) from the different instruments and the Galactic absorption (see Section 3.4.3). The resulting instrument-independent, CXB-subtracted, surface brightness profiles of the three instruments are displayed in Figure 4.2 (*XMM-Newton* in blue, *Chandra* in green, and eROSITA in red) and it shows that the three X-ray instruments are complementary to each other. *Chandra* with the best on-axis spatial resolution can cover as far as 3 arcsec from the center, *XMM-Newton* can cover up to the intermediate radial range with good statistics, and eROSITA with wide FoV and scan mode observations complete the large-scale view.

The discrepancies observed in the central region can be explained by the PSF effect. Higher central surface brightness in the *XMM-Newton* and eROSITA profiles is likely contributed by emission from the bright central point source. In the intermediate range ($r < R_{500}$), the *XMM-Newton* data points are systematically lower than those of eROSITA. This is due to the CXB choice of *XMM-Newton*. Due to limited FoV, the CXB level of *XMM-Newton* was calculated from an annulus with a size of 12.0 – 13.25 arcmin ($0.7 - 0.8R_{200}$), which is indicated as the blue horizontal dashed-line in the plot (Figure 4.2). Ideally, to avoid including emission from the cluster, the CXB region should be at least $r \gtrsim 2R_{200}$, as was done with eROSITA CXB estimation (a larger annulus of 25 – 35 arcmin or $1.6 - 2.1R_{200}$ was used and represented by the horizontal-dashed line). We corrected the *XMM-Newton* CXB level

¹I started my Ph.D. on the 1st of December 2020. The manuscript was submitted to the journal on the 28th of May 2021 and was accepted on the 23rd of August 2021.

²*Chandra* images were provided by Y. Su, one of the collaborators.

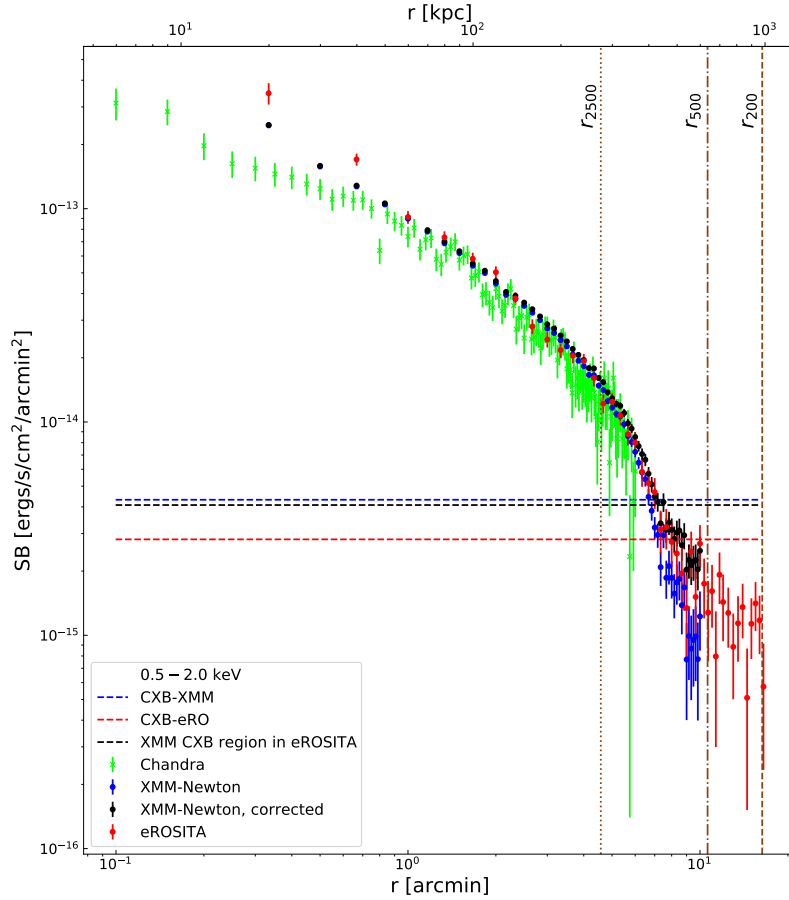


Figure 4.2: Instrument independent, CXB-subtracted, surface brightness profiles of the Northern Clump in the 0.5–2.0 keV band. Green, blue, and red data points represent the profiles of *Chandra*, *XMM-Newton*, and eROSITA, respectively. The CXB levels of *XMM-Newton* and eROSITA are plotted as the blue and red horizontal-dashed lines. The CXB-overestimated-corrected *XMM-Newton* surface brightness profile is indicated by the black data points.

overestimation by calculating the surface brightness of the *XMM-Newton* CXB region using eROSITA data (black horizontal dashed line). The excess was obtained by taking the difference between the value obtained for the *XMM-Newton* region using eROSITA and the eROSITA CXB value. The *XMM-Newton* surface brightness values were rectified after adding the excess emission of the CXB level (black data points), which yields better agreement with eROSITA data points. At larger radii ($R_{500} < r < R_{200}$), the surface brightness profile is only covered by eROSITA. The CXB-subtracted profile in this regime appears flat, which indicates the presence of additional emission, that could originate from either the cluster, filament, or both.

4.3 *XMM-Newton* Outer Spectral Profiles

The Northern Clump has entered the sphere of the influence of the A3391 cluster. Its ICM morphology shows some unique features, such as an overall boxy shape, sharp southern edge, and diffuse northern emission (tail). In order to assess the nature of these features, spectral analysis in an intermediate radial

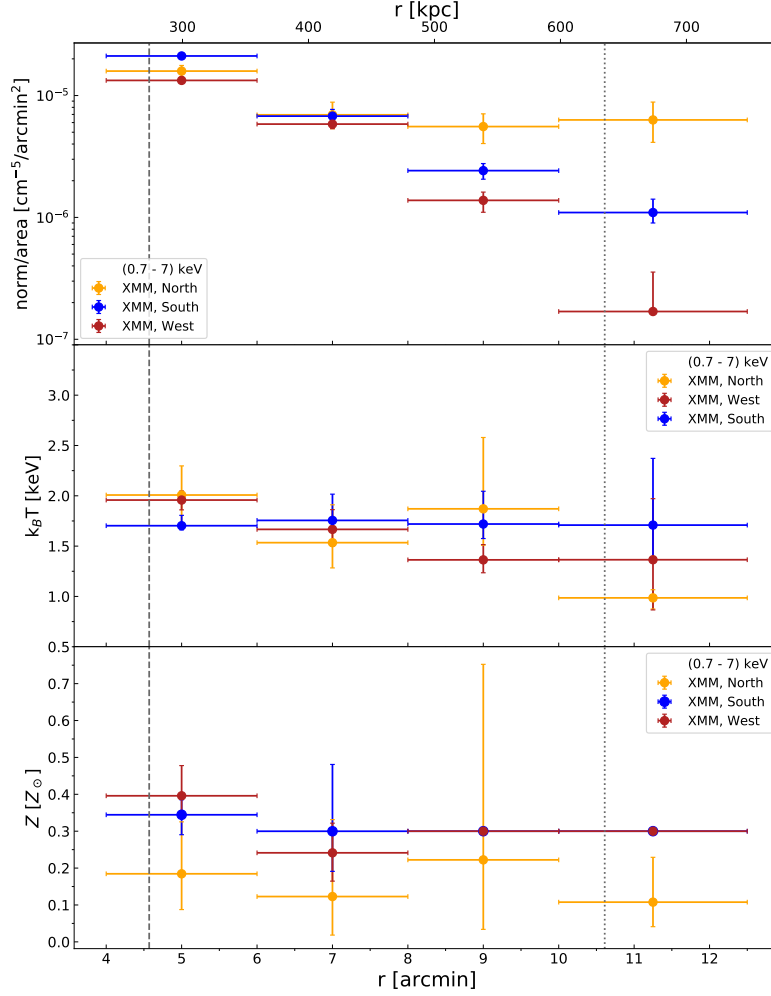


Figure 4.3: Profiles of gas properties of the Northern Clump in the intermediate regime of 4 – 12.5 arcmin: normalization per area (*top*), temperature (*middle*), and metallicity (*bottom*). The different colors indicate different sectors as demonstrated in Figure 4.1. The dashed and dotted vertical lines mark the R_{2500} and R_{500} of the cluster.

range of 4 – 12.5 arcmin ($0.4 - 1.2R_{500}$) in three sectors was carried out. The configuration of the sectors is overlaid on the *XMM-Newton* image in Figure 4.1, namely, the southern (blue) and northern (orange) directions that are in the on-filament axis, and the western direction (red) that is in the off-filament axis. The obtained gas properties (norm/A , $k_B T$, and Z) are presented in Figure 4.3. Our findings and their implications are presented below.

In the last two bins of the northern sector, significant enhancements of the normalization per area (see Section 3.5.3) are found. For the third bin, the normalization per area in the north is 56% (75%) higher than the corresponding bin in the south (west), with a significance value of 2.1σ (2.8σ). Similarly, for the fourth bin, we find an 83% (97%) excess compared to the south (west) with a significance of 2.3σ (2.8σ). These enhancements at the larger radii are consistent with the tail location observed in the image. Such X-ray trails of emission are frequently observed in merging systems and are associated with the ram-pressure-stripped gas from the smaller substructure as it merges with the parent cluster. Some examples are the tail observed in M86 and M49 galaxy groups that are infalling toward the Virgo cluster

(Randall et al., 2008; Su et al., 2019), the trail of emission and galaxies found in the northeast of A2142 cluster (Eckert et al., 2014; Liu et al., 2018), and the completely-stripped gas of one member galaxy of Z8338 cluster (Schellenberger & Reiprich, 2015).

In the south, higher best-fit temperature was acquired at the outermost bin ($k_B T_{\text{South}} = 1.71^{+0.66}_{-0.37}$ keV) in comparison to the corresponding bin in the opposite direction ($k_B T_{\text{North}} = 0.99^{+0.08}_{-0.11}$ keV). The temperature elevation is consistent with the shock or compression heating caused by movement towards the south (A3391). The normalizations per area at larger radii (third and fourth bins) are higher than those in the west, which supports the notion of the presence of an additional component in the on-filament axis.

4.4 Preliminary Assessment of the Northern Filament with eROSITA

We performed eROSITA spectral analyses of the Northern Filament to acquire the gas properties and compare them with the predicted WHIM properties. The source region of the filament is indicated by the yellow box in Figure 4.1, positioned at $r > R_{200}$ of the A3391 and the Northern Clump. The spectral fitting procedure performed in this work is the early version of that is described in Section 3.5.2 and the total model includes the foreground CXB emission from the Local Group at 0.5 keV (Ghirardini et al., 2021; Liu et al., 2022). Other necessary changes were also made to the CXB parameters for consistency with the spectral fitting of *XMM-Newton* and *Chandra*. Moreover, the CXB normalizations were frozen to the best-fit values found in the CXB spectral fitting. To account for multi-phase gas in the filament, a two-component fit (2T) was performed, as well. The metallicity of both components was linked together and frozen at $0.1 Z_{\odot}$ to reduce one degree of freedom. The calculation of the electron density from the *apec norm* parameter was done using Equation 3.11. We present the spectral analysis results of the Northern Filament in Table 4.1.

Fitting	$norm$ [10^{-3} cm^{-5}]	$k_B T$ [keV]	Z [Z_{\odot}]	n_e [10^{-5} cm^{-3}]
1T	$1.34^{+0.64}_{-0.30}$	$1.52^{+0.57}_{-0.54}$	$0.06^{+0.19}_{-0.06}$	$2.43^{+0.52}_{-0.29}$
2T	$1.06^{+0.25}_{-0.29}$	$1.72^{+1.02}_{-0.29}$	0.1	$2.16^{+0.24}_{-0.33}$
	$0.22^{+0.24}_{-0.19}$	$0.68^{+0.38}_{-0.64}$		$0.99^{+0.44}_{-0.62}$

Table 4.1: First results of eROSITA spectral analysis of the Northern Filament.

We compared our results with the predicted WHIM properties from the cosmological hydrodynamic simulations (e.g., Davé et al., 2001; Martizzi et al., 2019. See also, e.g., Shull et al., 2012; Nicastro et al., 2018; Kovács et al., 2019, for observational constraints), that is $n_e \approx 10^{-6} - 10^{-4} \text{ cm}^{-3}$ and $T = 10^5 - 10^7 \text{ K}$ ($k_B T \approx 0.009 - 0.862 \text{ keV}$). We report that the acquired temperature from a single-component fit (1T) is higher than the predicted WHIM temperature. Meanwhile, the n_e is within the expected range. From the 2T fit, a cooler component is detected. The gas temperature and electron density of the cooler component agree with the WHIM properties from the simulations. The temperature of the hotter component, on the other hand, is comparable to the last bin (10 – 12.5 arcmin) of the southern sector and might imply the emission is of cluster origin, either from the A3391 cluster, or the Northern Clump, or both.

4.5 Conclusions and Outlooks

The Northern Clump cluster (MCXC J0621.7-5242; [Piffaretti et al., 2011](#)) is the largest infalling substructure found in the A3391/95 cluster system. In this work ([Veronica et al., 2022](#)), morphological, thermodynamical, and chemical properties of the cluster were probed using three X-ray instruments, i.e., *Chandra*, *XMM-Newton*, and eROSITA. Within the scope of this dissertation, we report and discuss the results of the analyses toward larger radii which were carried out using *XMM-Newton* follow-up observation and eROSITA PV data.

Firstly, the eROSITA CXB-subtracted surface brightness profile flattens out toward larger radii $r > R_{500}$ (Figure 4.2), instead of gradually falling. This signifies the presence of emission at this regime that may be of cluster and/or filament origin and it is consistent with visual inspection of the image.

Afterward, spectral analysis of the outer regime was carried out with the *XMM-Newton* data. The temperature in the south (infalling head and on-filament axis) at $\sim R_{500}$ is hotter than in the opposite direction at the same radial range from the center. Considering that the Northern Clump is traveling southward and has entered the atmosphere of the A3391 cluster, this temperature elevation might be due to the shock or compression heating. In the north, a trail of X-ray emission pointing northward is observed and it has an approximated projected length of 5.3 arcmin ≈ 318 kpc. This tail-like feature is often observed in merging systems as the result of ram pressure stripping of the gas from the absorbed substructure. On the other hand, it is also plausible that this trail of gas is some material from the Northern Filament that is currently being accreted to the Northern Clump. While further investigation is required (e.g., deeper data or identification of member galaxies), the ram-pressure-stripped gas scenario is supported with findings from the analog A3391/95 system in the Magneticum Simulations ([Biffi et al., 2022](#)). When entering the periphery ($3 \times R_{200}$) of the analog A3391 cluster, the gas of the accreted substructure starts to lag with its infall velocity is reduced compared to the dark matter.

With eROSITA data, we constrained a preliminary gas temperature and electron density of the Northern Filament (defined as emission at $r > R_{200}$ of both the A3391 and the Northern Clump cluster). Through a two-component fitting, a cooler component is identified with $k_B T = 0.68^{+0.38}_{-0.64}$ keV and $n_e = 0.99^{+0.44}_{-0.62} \times 10^{-5} \text{ cm}^{-3}$, which are consistent with the predicted WHIM properties. The temperature of the hotter component is found to be comparable with the value at R_{500} in the southern sector, suggesting the presence of hot gas.

In order to draw more conclusions, detailed examinations are necessary. For instance, surface brightness and gas property profiles along cluster outskirts ($R_{500} - R_{200}$) and the filament will be helpful to discern any features related to accretion. Statistical tests should also be conducted to compare the goodness-of-fit between 1T and 2T spectral models. These examinations, among all else, will be carried out in the second paper (see Chapter 5) that presents extensive imaging and spectral analyses of the A3391/95 cluster outskirts and filaments.

Chapter 5

The eROSITA view of the Abell 3391/95 field: Cluster outskirts and filaments

The eROSITA view of the Abell 3391/95 field: Cluster outskirts and filaments

A. Veronica, T. H. Reiprich, F. Pacaud, N. Ota, J. Aschersleben,
V. Biffi, E. Bulbul, N. Clerc, K. Dolag, T. Erben, E. Gatzert,
V. Ghirardini, J. Kerp, M. Klein, A. Liu, T. Liu, K. Migkas,
M. E. Ramos-Ceja, J. Sanders, C. Spinelli
2024, A&A, 681, A108

<https://doi.org/10.1051/0004-6361/202347037>

Overview

The eROSITA PV observations of the A3391/95 galaxy cluster system show a snapshot of the LSS formation. Warm-hot continuous emission was seen spreading across the FoV with an approximate projected length of 15 Mpc (Reiprich et al., 2021). The emission connects at least five galaxy clusters and groups in the field, including the Northern Clump (see Section 4), the A3391 cluster, the ESO 161-IG 006 group, the A3395S/N cluster, and potentially the MCXC J0631.3-5610 cluster just south to the FoV. A small clump residing in the filament south of the A3395S/N cluster was also discovered, spatially resolved for the first time. With an intent to shed more light on the ongoing process of the structure assembly observed in this complex and dense neighborhood, we employed the eROSITA A3391/95 PV data. Detailed surface brightness emission out to $\sim 2 \times R_{200}$ of the A3391 and the A3395 clusters were constructed to assess the morphology of the ICM and trace the filament emission. We investigate the filament-facing cluster outskirts of the Northern Clump, the A3391, and the A3395 clusters and compare them with other cluster measurements to check for deviations. Spectral analysis was performed to characterize the gas properties of the detected filaments, as well. We compared the results with the prediction from simulations and other cluster outskirts and filament measurements. We took particular care of the sky/cosmic X-ray background (CXB), which is a dominant contributor in these faint regions. Our constraints on the gas properties in the cluster outskirts and individual spatially resolved filaments help increase the number of measurements in these challenging, yet important regimes. The presented methodology and tests may benefit future studies.

The work reported in this chapter was published in the Astronomy & Astrophysics journal (Veronica et al., 2024a) and attached in its original published form in Appendix B. In this publication, I performed the data reduction, image correction, and scientific analyses of the eROSITA data. I contributed most of the discussion of the results and wrote most of the manuscript.

5.1 Configurations

In this work, we conducted thorough imaging and spectral analyses using different configurations. Our focus was on the cluster outskirts, which we defined as the area between $R_{500} < r < R_{200}$, and the filaments, which we defined as the inter-cluster emission at $r > R_{200}$. We will present the various configurations we used and a description of the reasoning behind the choice.

5.1.1 Surface Brightness Analyses

We constructed two sets of surface brightness profiles, one that is centered at the A3391 cluster and the other at the A3395S cluster center. The configurations are overplotted on the images in Figure 5.1. For each cluster, the profiles are divided into different sectors, a couple of which are to show the emission in the filament direction.

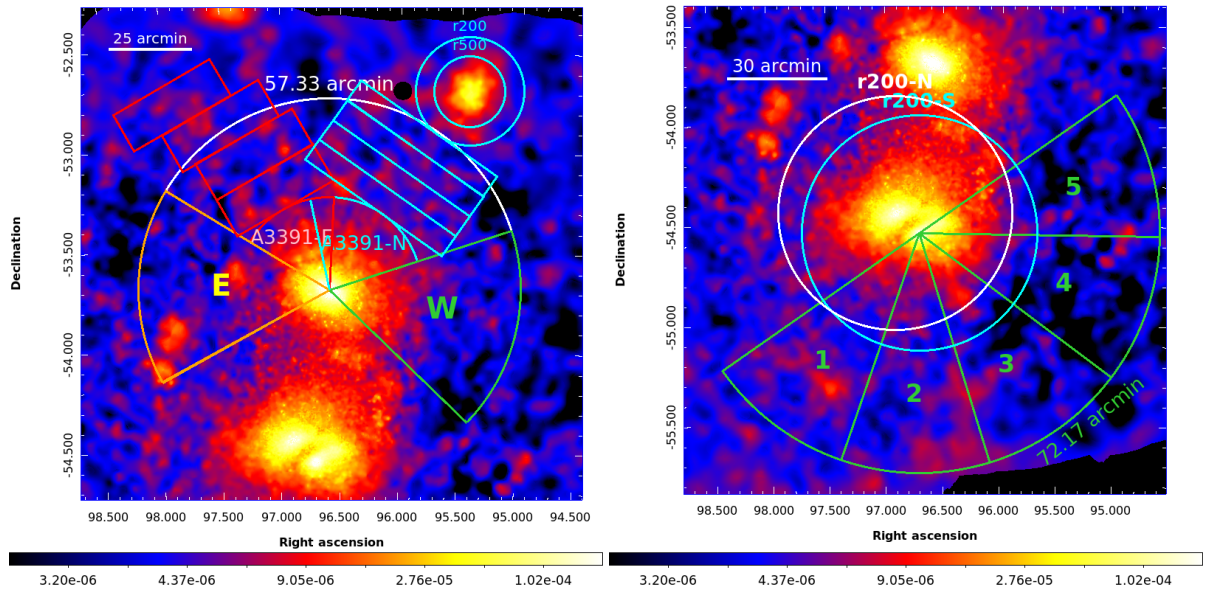


Figure 5.1: eROSITA PIB-subtracted, exposure- and Galactic-absorption- corrected image in the 0.3 – 2.0 keV band. The image has been adaptively smoothed with S/N set to 12. The point sources have been removed and refilled with their surrounding background values. Overplotted on the images are the configurations of surface brightness profiles for the A3391 cluster, NC, Northern and Eastern Filament (*left*), and the A3395S cluster and Southern Filament (*right*.)

- A3391: the configuration for the surface brightness profiles for the sectors centered at the A3391 center is displayed in the left panel of Figure 5.1. In total, five surface brightness were constructed: in the Northern Filament direction (blue sector labeled as A3391-N, the four blue boxes for the Northern Filament, and the full azimuth Northern Clump cluster), in the potentially Eastern Filament direction (red sector labeled as A3391-E and the four red boxes for the Eastern Filament), toward the east (E; orange) and west (W; green) of A3391 out to 57.33 arcmin ($\sim 2R_{200}$), and the average of all directions calculated out to R_{200} (excluding the southern direction due to emission from the A3395S/N cluster),
- A3395S: since the A3395 cluster is composed of two components, A3395N and A3395S, the configuration was set by treating each of the subcomponents as individual entities. As shown in the

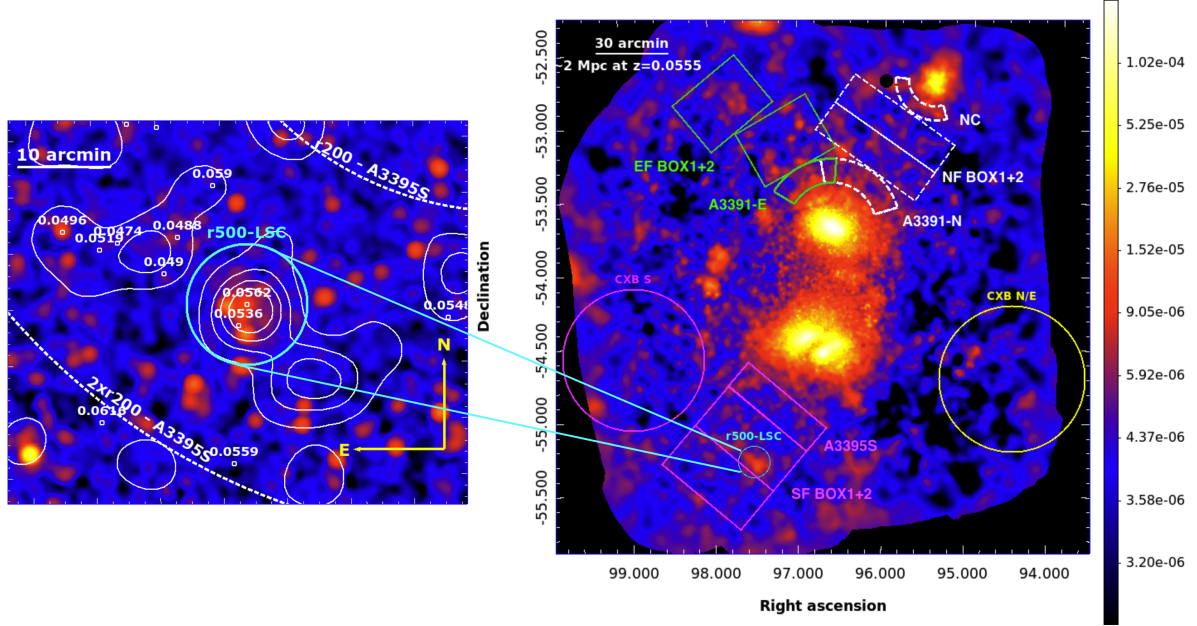


Figure 5.2: *Right*: Same as Figure 5.1 with spectral analysis configurations overplotted and labelled. The different sources and CXB regions are labeled (see Section 5.1). *Left*: Fully-corrected image in the same energy band, Gaussian-smoothed with a kernel radius of 10 pixels, and zoomed-in to the LSC area. The white contours are the optical DECam/DES galaxy number density map. White circles are known galaxies within the redshift range of $0.0424 \leq z \leq 0.0636$, compiled from the NED. Their redshifts are labeled on top.

right panel of Figure 5.1, we chose to construct surface brightness profiles from the lower half of the A3395S. This choice enables us to reduce the influence of the A3395N component, including the Southern Filament, and also not impacted by background sources (e.g., sources to the northeast of the A3395N). We sectioned the regions into five sectors of the same size with an opening angle of 36° each. An average surface brightness profile of all these sectors was also calculated. All of the A3395S surface brightness profiles were calculated out to 72.17 arcmin ($\sim 2R_{200}$),

- CXB: the CXB was determined from ten boxes spread out across the FoV (the same configuration as shown in Figure F.1. in Reiprich et al., 2021). They are positioned at $r > R_{200}$ of the clusters to avoid overestimation by the inclusion of emission from the sources. The CXB level was the mean surface brightness of the ten boxes, while its error was taken to be the standard deviation among these boxes (Equation 3.5) to also include the systematic uncertainty from the CXB variation.

5.1.2 Spectral Analyses

We display the configuration used for the spectral fitting in Figure 5.2. The regions are listed below:

- filament-facing outskirts ($R_{500} < r < R_{200}$): includes the A3391 cluster outskirts facing the Northern Filament (A3391-N; white-dashed sector) and the Eastern Filament (A3391-E; green sector), the Northern Clump outskirts facing the Northern Filament (NC; white-dashed sector), and the A3395 cluster outskirts facing the Southern Filament (A3395S; magenta box),
- filaments ($r > R_{200}$): the Northern Filament (NF BOX1 + 2), the Eastern Filament (EF BOX1 + 2),

the Southern Filament (SF BOX1 + 2). For the Southern Filament, a spectral analysis excluding the Little Southern Clump (LSC; its R_{500} region is indicated by the cyan circle) was also carried out. The LSC will be discussed in Section 5.3.2,

- CXB: we utilized two CXB regions for analysis of different source regions. This decision was made to take into account the variability of N_H in the different regions (see the left panel in Figure 3.6). The CXB S (magenta circle) was used to estimate the CXB normalizations of the spectral fittings in the south, while CXB N/E (yellow circle) was employed during the spectral fitting in the north and east.

5.2 Surface Brightness Profiles

The surface brightness profiles are presented at the top plots of Figure 5.3a for those that are centered at the A3391 cluster, and Figure 5.3b for those that are centered at the A3395S cluster. The different sectors are color-coded and labeled. The bottom plots of these panels show the significance of the surface brightness values for the bins at $r > R_{200}$ with respect to the CXB level ($S/N_{w.r.t.CXB}$). The values listed in the legend are the overall signal-to-noise of the whole regime in the different sectors and were calculated using the following equation

$$S/N_{all} = \frac{SB_{r>R_{200}} - SB_{CXB}}{\sqrt{\sigma_{r>R_{200}}^2 + \sigma_{CXB}^2}}, \quad (5.1)$$

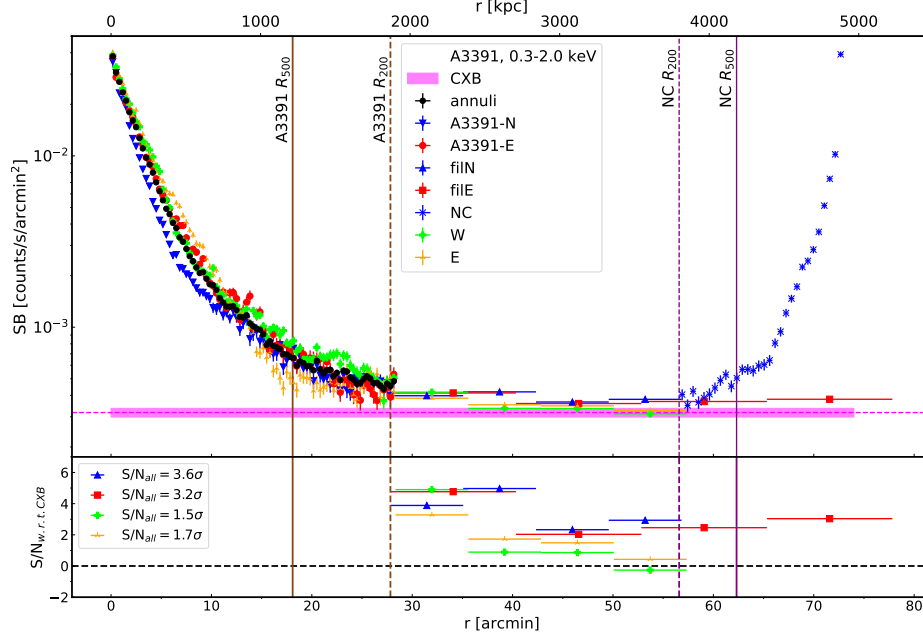
where $SB_{r>R_{200}}$ and $\sigma_{r>R_{200}}$ are the surface brightness value of the entire $r > R_{200}$ regime and its statistical uncertainty, while SB_{CXB} and σ_{CXB} are the CXB level and the standard deviation of the CXB.

We report that in the $r > R_{200}$ regime, the surface brightness values of the Northern Filament (filN; blue upward triangles in Figure 5.3a) and the Eastern Filament (filE; red squares) are higher than the values in the western (W; green) and eastern (E; orange) sectors. The overall significance values, S/N_{all} , are 3.6σ for filN, 3.2σ for filE, 1.5σ for W, and 1.7σ for E. We notice that the first bin after R_{200} in the different sectors is greater than 3.2σ , which could be from the ICM itself (e.g., apparent cluster elongation in the west) or background source (clumps in the east). Hence, to remove the bias, we recalculated the S/N_{all} values without these first $r > R_{200}$ bins, which yield: 3.5σ for filN, 2.5σ for filE, 0.5σ for W, and 1.2σ for E. The excess emission of all sectors decreases, but it still shows that the Northern and Eastern Filaments are brighter than the other sectors.

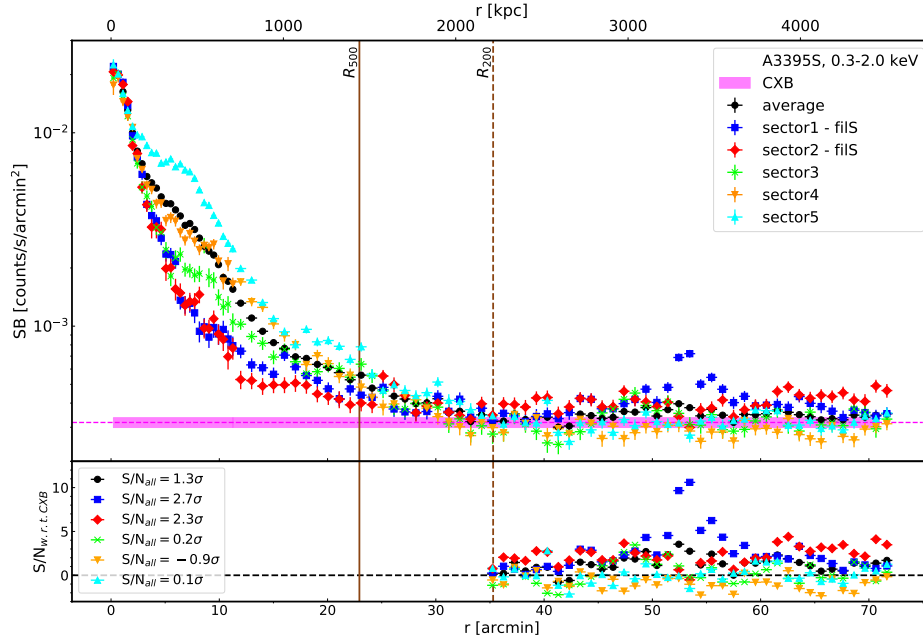
A striking feature seen in the A3395S surface brightness plot (Figure 5.3b) in the $r > R_{200}$ regime is the peak at around 54 arcmin ($\sim 1.5R_{200}$) of Sector1. The peak is ascribed to the emission from the LSC. The S/N_{all} values in the Sector1 and Sector2, where the Southern Filament (filS) are contained in, are 2.7σ and 2.3σ , respectively. Meanwhile, the S/N_{all} values of the other Sectors are consistent with the CXB level.

5.3 Spectral Analysis Results

In this section, we discuss the spectral analysis results in the outskirts and the detected filaments. The spectral analysis was carried out using the procedure described in Section 3.5.



(a) Northern and Eastern Filament



(b) Southern Filament

Figure 5.3: The surface brightness profiles in the 0.3 – 2.0 keV energy band and their significance to the CXB level (magenta-shaded horizontal-dashed lines), $S/N_{w.r.t.CXB}$, are shown in the top and bottom plot of each panel. The legends in the bottom plots list the overall signal-to-noise of the whole $r > R_{200}$ regime of the different sectors, S/N_{all} (Equation 5.1). (a): The surface brightness profiles are centered at the A3391 cluster. The surface brightness profiles of A3391-N, Northern Filament (filN), and NC are plotted in blue; the A3391-E and Eastern Filament (filE) in red; the west and east of A3391 in green and orange, respectively. (b): The surface brightness profiles are centered at the A3395S cluster. Sector1 (blue) and Sector2 (red) contain the Southern Filament (filS). The characteristic radii of each cluster are plotted as brown lines (R_{500}) and brown dashed lines (R_{200}). The configurations of these profiles can be found in Figure 5.1.

5.3.1 Cluster Outskirts

In Figure 5.4, we present temperature profiles of the outskirts and filament regions along the Northern (top left), Eastern (top right), and Southern Filaments (bottom). The magenta-shaded areas on the plots are the temperature profile yielded from fitting 162 *Suzaku* cluster outskirt measurements described in Reiprich et al. (2013). This temperature profile describes cluster temperatures within the range of $0.3R_{200} < r < 1.15R_{200}$ as follows,

$$k_B T(r) = \left(1.19 - 0.84 \frac{r}{R_{200}} \right) \cdot \langle k_B T \rangle. \quad (5.2)$$

In this work, the $\langle k_B T \rangle$ parameter was determined from eROSITA spectra within the $0.2-0.5R_{500,\text{lit}}$, where $R_{500,\text{lit}}$ is the literature R_{500} . From the $\langle k_B T \rangle$, we then calculated the R_{500} for the temperature profile of Reiprich et al. (2013) (see Section 3.5.3). The R_{200} were calculated using the characteristic radius relations in Reiprich et al. (2013), namely, $R_{500} \approx 0.65R_{200}$. The input parameters for the different clusters are listed in the third and fourth rows of Table 5.1.

Parameters	A3391	A3395S	NC
$k_B T_{lit}$ [keV]	5.40 ± 0.6^a	5.0 ± 0.3^a	1.99 ± 0.04^b
$R_{500,\text{lit}}$ [']	18.09^a	22.94^a	10.62^b
$k_B T_{0.2-0.5R_{500}}$ [keV]	3.86 ± 0.19	$5.05^{+0.52}_{-0.48}$	$1.50^{+0.18}_{-0.17}$
$R_{500,(0.2-0.5R_{500})}$ [']	14.68	17.30	9.00

^a ASCA temperatures (Reiprich & Böhringer, 2002),
^b XMM-Newton temperature (Veronica et al., 2022)

Table 5.1: Information on cluster parameters supplied to the temperature profile of Reiprich et al. (2013). The first row ($k_B T_{lit}$) shows the literature temperature values. The second row ($k_B T_{0.2-0.5R_{500}}$) lists the eROSITA temperatures over the $0.2-0.5R_{500}$, where the used R_{500} are also taken from the literature. The third row ($R_{500,(0.2-0.5R_{500})}$) is the corresponding characteristic radius derived using the $M - T$ scaling relation.

The eROSITA measurements in the filament-facing outskirts of the A3391 cluster and the Northern Clump are higher than their corresponding expected temperature profiles. The significance temperature enhancements are 2.4σ for A3391-N, 2.8σ for A3391-E, and 1.6σ NC. Temperature excesses in a specific cluster region have been reported in previous studies. For example, Kawaharada et al. (2010) report an excess temperature in the northeastern direction of the A1689 cluster with a factor of three compared to the other directions. These authors state that this is caused by shock heating from the infall of matter from the filament.

From the spectral analysis, gas metallicities (Z) were acquired, as well, except for the A3391-E, where the metallicity was frozen to $0.3Z_\odot$ due to lack of photon statistics. The Z values obtained for the A3391-N and NC are in the range of $0.1 < Z/Z_\odot < 0.3$, which is in good agreement with other cluster outskirts metallicity measurements, for example, *Suzaku* measurements of the Perseus cluster (Simionescu et al., 2011), the A3112 cluster (Ezer et al., 2017), and from a sample of ten nearby galaxy clusters (Urban et al., 2017). These values are also consistent with the results from the cosmological hydrodynamical simulations (e.g., Biffi et al., 2018b). On the other hand, we found higher Z in the A3395 outskirts, $0.72^{+0.60}_{-0.33}Z_\odot$, but it is still within the scatters of the literature values. The metal concentrations in the cluster outskirts gas are speculated to be the mixture of the already enriched-accreted-gas and more

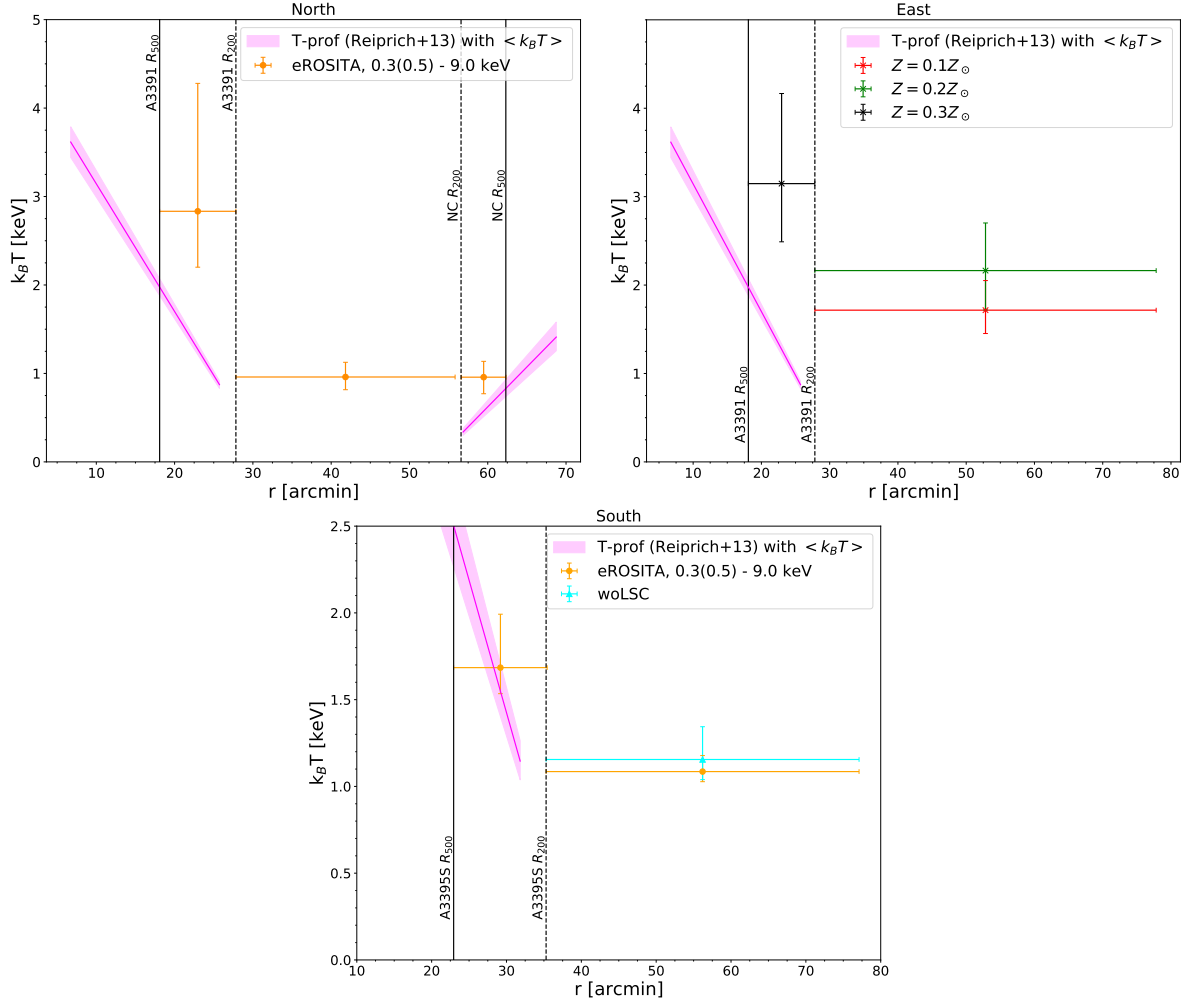


Figure 5.4: Temperature measurements of the outskirts and filaments for the northern (top), eastern (middle), and southern (bottom) regions. The pink-shaded areas are the 1σ temperature profiles from Reiprich et al. (2013) using $k_B T_{0.2-0.5 R_{500}}$ as mean temperature of each cluster (see Table 5.1). The black vertical solid (dotted) lines mark the R_{500} (R_{200}) of the parent clusters.

pristine gas from the cluster formation (Ezer et al., 2017; Biffi et al., 2018b). These metals are produced at high redshifts ($z \approx 2$) in stars and spread out by supernova events and asymptotic giant branch (see Werner et al., 2008a; Nomoto et al., 2013, for reviews). The mixing and distribution of this material throughout the ICM are done by some processes, such as the AGN feedback, ram-pressure stripping, and galactic winds (Vazza et al., 2010; Ettori et al., 2013).

5.3.2 Filaments

The results of the spectral analysis for the filament regions are tabulated in Table 5.2, including the derivative quantities, such as the electron density, n_e (Equation 3.11), and the gas overdensity, δ_b ¹. The information on specific spectral analysis treatments is indicated in the 'Fitting' column. For instance, for the Eastern Filament, the fit was done by fixing the metallicity to 0.1 and 0.2 Z_\odot , hence 'fix Z'. For the Southern Filament, we additionally performed an analysis where the contribution from the LSC was excluded (SFwoLSC). In order to do this, we first needed to characterize the properties of the LSC. A

small discussion of this object is presented below.

The Little Southern Clump

The LSC is a spatially resolved, extended object that is located at around $1.5R_{200}$ of the A3395 cluster and appears to be fully embedded in the Southern Filament. At the location of the X-ray emission of this clump, galaxy overdensity is evident (shown as the white contours in the inset panel of Figure 5.2), which implies the object might as well be a small galaxy group. This conjecture is further supported by the characterization results via spectral analysis. The information on the LSC is summarized below:

- center: WISEA J063004.80-551751.5 galaxy ($z = 0.0562$) at $(\alpha, \delta) = (6 : 30 : 04.8, -55 : 17 : 51.504)$,
- $k_B T_{500} = 0.94^{+0.06}_{-0.07}$ keV, which was done following the procedure in Section 3.5.3, and consequently,
- $M_{500} = (2.33^{+0.31}_{-0.34}) \times 10^{13} M_\odot$,
- $R_{500} = (6.44^{+0.29}_{-0.32})$ arcmin, which was the region definition utilized when removing the contribution of LSC in SFwoLSC analysis.

Furthermore, we also notice galaxy overdensities that do not coincide with extended X-ray emission, one of which extends further toward the southwest of the R_{500} and the other in the northeast. The latter coincides with six known galaxies of similar redshifts (indicated by small white circles), which was filtered from the galaxy catalog compiled from the NED². As seen in simulations, galaxy groups that are within the periphery of a cluster can grow by accreting field galaxies (Vijayaraghavan & Ricker, 2013; Kuchner et al., 2022), which seems to fit the LSC case. However, these galaxies and LSC might as well be currently infalling toward A3395S with the filament. A more conclusive answer can be achieved with deeper data.

Northern, Southern, and Eastern Filaments

Similarly to the first paper (Veronica et al., 2022, Chapter 4), here, the measured filament properties are also compared with the predicted properties. The WHIM properties from Shull et al. (2012) are adopted, such that, temperature range of $T = 10^5 - 10^7$ K ($k_B T = 0.009 - 0.862$ keV) and the gas overdensity range of $\delta_b = 0.001 - 316.22$.

The obtained δ_b of the A3391/95 filaments, $98 \leq \delta_b \leq 238$, are within the predicted WHIM δ_b range. The acquired temperatures for the Northern and Southern Filaments, $k_B T \approx 1$ keV, indicate that the gas is heated, however, the values are close to the upper limit of the WHIM defined in Shull et al. (2012). We note also that the filaments in the A3391/95 are short. The Northern Filament is only about 1.8 Mpc and the Southern Filament is about 2.7 Mpc. As shown by simulations, the properties of the filaments may vary according to their lengths. For instance, Galárraga-Espinosa et al. (2021) classify the filaments in the IllustrisTNG simulations into three populations: short ($L_f < 9$ Mpc), medium ($9 \leq L_f < 20$ Mpc), and long ($L_f \geq 20$ Mpc). Furthermore, since shorter filaments are typically found in denser large-scale environments, they are often identified as over-dense structures than the cosmic web

¹The gas overdensity is defined as $\delta_b = \rho_{\text{gas}}/\bar{\rho}_b(z)$, where $\bar{\rho}_b(z) = \Omega_b(z)\rho_{\text{cr}}(z)$ is the mean baryon density at redshift z . Assuming the cosmology of Planck Collaboration et al. (2020a), at the redshift assumed for the Northern and Eastern (Southern) Filament, $z = 0.0533(0.0525)$, the baryon density is $\Omega_b = 0.0561(0.0560)$, hence, the critical density of the Universe of $\rho_{\text{cr}} = 8.9861(8.9790) \times 10^{-30}$ g cm⁻³. These yield $\bar{\rho}_b(0.0533) = 5.0455 \times 10^{-31}$ g cm⁻³ and $\bar{\rho}_b(0.0525) = 5.0320 \times 10^{-31}$ g cm⁻³.

²The NASA/IPAC Extragalactic Database (NED) is funded by the National Aeronautics and Space Administration and operated by the California Institute of Technology.

skeletons (Galárraga-Espinosa et al., 2020, 2021, 2022; Vurm et al., 2023). That also means that they are in a deeper potential well and, hence, undergo stronger gravitational heating.

When excluding LSC from the spectral analysis, no significant changes are observed in the gas temperature and metallicity of the Southern Filament. Yet, the gas overdensity decreases by 30%. This demonstrates the importance of accounting for such dense clump to avoid overestimating the filament density (e.g., Nagai & Lau, 2011; Eckert et al., 2015b; Mirakhor & Walker, 2021).

Regarding the metallicity, Z , our findings suggest that the filaments are poorly enriched, in particular, the Northern Filament where only an upper limit of $0.01Z_{\odot}$ was constrained. Given that they are away from any metal production sites, e.g., star-forming regions, this is not unexpected. These values are still within the range predicted by simulations (see Figure 9b of Biffi et al., 2022), as well.

The gas temperature of the Eastern Filament ranges between 1.5 and 2.7 keV. However, from the surface brightness significance in Section 5.2 and as previously stated in Reiprich et al. (2021), the detection of this filament is tentative. Unlike the Northern and Southern Filaments, the Eastern Filament is not apparent in the *Planck*-SZ map and no trail of galaxy overdensity is observed, as well Reiprich et al. (2021).

Regions	Fitting	$norm$ [$10^{-6} \text{ cm}^{-5}/\text{arcmin}^2$]	$k_B T$ [keV]	Z [Z_{\odot}]	n_e [10^{-5} cm^{-3}]	δ_b	stat/dof
NF		$1.65^{+0.19}_{-0.18}$	$0.96^{+0.17}_{-0.14}$	< 0.01	$5.93^{+0.34}_{-0.34}$	225^{+13}_{-13}	10855.0/10743
EF	fix Z	$0.82^{+0.09}_{-0.09}$	$1.72^{+0.33}_{-0.26}$	0.1	$5.04^{+0.28}_{-0.30}$	191^{+11}_{-11}	11318.2/11078
	fix Z	$0.73^{+0.08}_{-0.08}$	$2.16^{+0.54}_{-0.45}$	0.2	$4.76^{+0.26}_{-0.29}$	180^{+10}_{-11}	11344.9/11078
SF		$0.74^{+0.13}_{-0.12}$	$1.09^{+0.09}_{-0.06}$	$0.10^{+0.05}_{-0.04}$	$4.37^{+0.36}_{-0.36}$	166^{+14}_{-14}	12756.4/11368
	woLSC	$0.39^{+0.13}_{-0.12}$	$1.16^{+0.19}_{-0.12}$	$0.11^{+0.13}_{-0.07}$	$3.08^{+0.46}_{-0.51}$	117^{+17}_{-19}	12620.0/11363

Table 5.2: eROSITA spectral analysis results and derived quantities of the Northern Filament (NF), Eastern Filament (EF), and Southern Filament (SF).

Additional Spectral Fittings

We performed a spectral fitting assuming the Northern Filament is composed of multi-temperature gas. The fit returns a cool and a warm component of 0.1 keV and 1.3 keV, respectively, which is consistent with the 2T-fit results in the preliminary eROSITA measurements (Chapter 4). To compare the 2T-model with the main model (Table 5.2), we utilized the Bayesian Information Criterion (BIC, Schwarz, 1978) and the Akaike Information Criterion (AIC, Akaike, 1974). The tests show that adding a second thermal emission component does not significantly improve the fit, therefore, we retain the results from the main 1T model.

Other spectral fitting exercises were also done, which included treating the filaments as sky backgrounds and leaving the redshift as a free parameter. In summary, the results of these tests confirm that the filaments are not of Galactic origin and they also further affirm the robustness of our main findings.

5.4 Summary and Conclusions

In this project, we conducted thorough surface brightness and spectral analyses of the A3391/95 cluster outskirts using the eROSITA PV data. Surface brightness profiles in various directions were calculated out to $\sim 2R_{200}$ of each cluster and compared with each other to identify any features. The gas properties in these regions were derived through spectral fitting. We compared the obtained properties of the filaments with the predicted WHIM properties from simulations, as well as other measurements. Our findings are outlined as follows:

- **Outskirts:** The filament-facing outskirts are brighter than the off-filament directions (except the cluster elongation directions). We also report temperature excesses in the A3391-N, A3391-E, and NC when comparing with the temperature profile from [Reiprich et al. \(2013\)](#), which might be caused by thermalization induced by accretion through the filaments. The metallicities are in good agreement with other cluster outskirts measurements of about $0.3Z_{\odot}$.
- **Filament properties:** A ~ 1 keV temperature was estimated for the Northern and Southern Filaments. Their gas overdensities are $212 < \delta_b < 237$ and $152 < \delta_b < 180$, respectively. While the gas overdensities are within the expected WHIM range, the temperatures are slightly higher than the upper limit of WHIM temperatures (~ 0.9 keV in [Shull et al., 2012](#)). Since these filaments are short and located in a dense large-scale environment, gravitational heating might have elevated their temperatures. Moreover, the filaments are poorly enriched by metals which can be explained by the lack of metal production sites. Nevertheless, the measurements are within the expected range of the simulations.
- **LSC contribution:** The LSC is a spatially resolved clump within the vicinity ($\sim 1.5R_{200}$) of the A3395 cluster, residing in the Southern Filament. From the X-ray spectral analysis, it is confirmed that the LSC is a small galaxy group. The DECam/DES galaxy number density map shows overdensities within and around the group. These galaxies may be being accreted to or traveling toward the A3395 cluster together with the LSC through the filament. The influence of the clump on the Southern Filament was investigated. A significant impact on the filament's temperature and metallicity is not observed, but the density decreases by 30%. Low-mass clumps such as the LSC are not always resolved, but in this work, we have demonstrated how much the filament gas density is biased when neglecting its influence.

As the cosmic gates that connect galaxy clusters and their large-scale environments, galaxy cluster outskirts are paramount in understanding large-scale structure formation. They provide not only a playground to study the physics of accretion processes but also the points to locate the cosmic filaments. Despite the importance, studying the cluster outskirts, even more so the filaments, has been challenging due to the low surface brightness and its location. Instruments of superior soft energy response and wide FoV, such as eROSITA, are required. Indeed, the A3391/95 PV observations have validated eROSITA's capability and confirmed the presence of large-scale structures in the Universe. Through this work, we have taken a significant step forward by conducting a comprehensive assessment of both the cluster outskirts and filaments in one large-scale environment. More such cluster system complexes will be cataloged in the eROSITA All-Sky Surveys, thus, the number of observational studies of inter-cluster filaments will increase. Future studies will benefit from the results, as well as, the methods presented in this work.

Chapter 6

The SRG/eROSITA All-Sky Survey: Large-scale view of the Centaurus cluster

The SRG/eROSITA All-Sky Survey: Large-scale view of the Centaurus cluster

A. Veronica, T. H. Reiprich, F. Pacaud, J. Sanders, E. Gatuzz, M. C. H. Yeung,
E. Bulbul, V. Ghirardini, A. Liu, C. Mannes, A. Morelli, N. Ota

Submitted to A&A,

<https://ui.adsabs.harvard.edu/abs/2024arXiv240404909V/abstract>

Overview

The Centaurus cluster (Abell 3526) is located at $z = 0.0104$ and it has a $0.1 - 2.4$ keV luminosity within its R_{500} of 6.9×10^{43} erg s $^{-1}$. As one among the closest and brightest galaxy clusters, the cluster is an ideal target to conduct astrophysical studies, and hence it has been extensively observed by most X-ray instruments (e.g., ASCA, Churazov et al., 1999; Dupke & Bregman, 2001; Furusho et al., 2001; ROSAT, Allen & Fabian, 1994; Churazov et al., 1999; Ikebe et al., 1999; Suzaku, Ota et al., 2007; Walker et al., 2013b; Ota & Yoshida, 2016; XMM-Newton, Walker et al., 2013a; Fukushima et al., 2022; Gatuzz et al., 2022, 2023; Chandra, Sanders & Fabian, 2002; Sanders et al., 2016b; Lakhchaura et al., 2019). From the X-ray images, the overall ICM morphology is elliptical with an apparent smoothness with a central peak at its brightest cluster galaxy (BCG), NGC 4696. However, based on early studies of the redshift of the cluster member galaxies, it was found that the cluster is composed of two substructures, called Cen 30 and the Cen 45 (Lucey et al., 1986a,b). Cen 30 is located in the center of the cluster and centered at the NGC 4696 galaxy. This central galaxy hosts a low-power radio source, PKS 1246 – 410 (Taylor et al., 2002, 2006). Meanwhile, Cen 45 is centered at the NGC 4709 galaxy and it is located about 15 arcmin eastward to the cluster center. Cen 45 is currently being accreted toward the main substructure.

The Centaurus cluster has a large apparent size ($R_{500} \approx 59.0$ arcmin) due to its proximity to us. Due to the FoV limitation of previous instruments, covering the whole extent of the cluster requires multiple observations. Hence, previous studies have mostly focused on the brightest central part ($r \lesssim 30$ arcmin) of the cluster. An investigation of the outskirts was carried out in Walker et al. (2013b), where these authors used six Suzaku observations along the northwestern direction out to $0.95 R_{200}$.

In the presented work, we utilized the eROSITA All-Sky Survey data (eRASS; Predehl et al., 2021; Merloni et al., 2024) to perform a large-scale analysis of the Centaurus cluster. ICM profiles (surface brightness, temperature, metallicity, and normalization) in full azimuth and four different directions out to R_{200} 90.7 arcmin are sampled. This study increases the probed volume of the Centaurus cluster by a factor of about 30. The work discussed in this chapter has been through reviews by the co-authors and the

eROSITA-DE consortium. The manuscript was submitted to the Astronomy & Astrophysics journal and the preprint version is accessible at <https://ui.adsabs.harvard.edu/abs/2024arXiv240404909V/abstract>. The submitted article is attached in Appendix C. In this publication, I performed the data reduction, image correction, and scientific analyses of the eROSITA data. I contributed most of the discussion of the results and wrote most of the manuscript.

6.1 Configurations

In order to gain as much statistics as possible, we employed all five available eRASS data (eRASS:5). Nine eRASS sky tiles were combined to cover out to $3 \times R_{200}$ of the cluster (Section 3.1.2). The data were processed and corrected following the steps described in Chapter 3. To visually inspect any small and large-scale features within and around the cluster, some image enhancement techniques (Section 3.4.2) were performed.

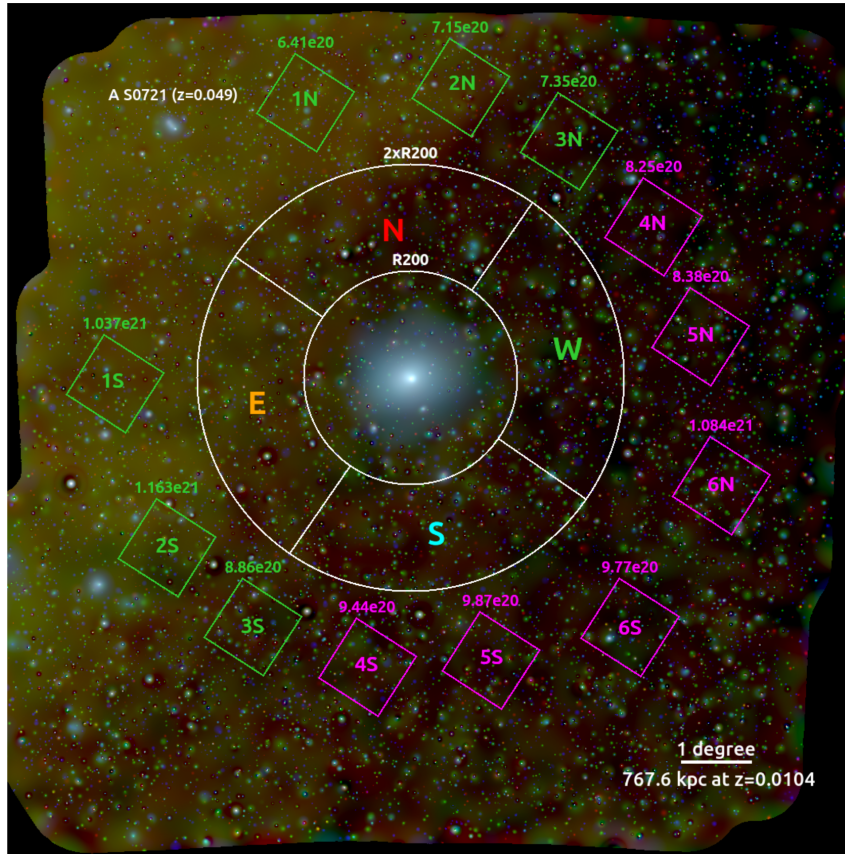


Figure 6.1: Composite image of the large-scale view of the Centaurus cluster using eRASS:5 data. Red, green, and blue channels are in the 0.2–0.6 keV, 0.6–1.0 keV, and 1.0–2.3 keV energy bands, respectively. The image in each channel is PIB-subtracted, exposure-corrected, Galactic-absorption-corrected, and wavelet-filtered.

6.1.1 The Cosmic X-ray Background

In Figure 6.1, the composite image of the Centaurus cluster field is shown. The image is composed of fully-corrected images in three different energy bands: the 0.2–0.6 keV, 0.6–1.0 keV, and 1.0–2.3 keV

images are shown in red, green, and blue channels, respectively. To reduce the Poissonian noise and enhance the signal from the sources, each image was wavelet-filtered (Section 3.4.1). From the image, we observe bright yellowish (red+green) emission in the left part of the FoV. This emission is a fraction of the outer part of the large-scale Galactic structure called the eROSITA Bubbles (Predehl et al., 2020, see also Section 1.6.2). This foreground contamination can be seen spreading into the $2R_{200}$ of the Centaurus cluster, especially inside the northern (N) and eastern (E) sectors.

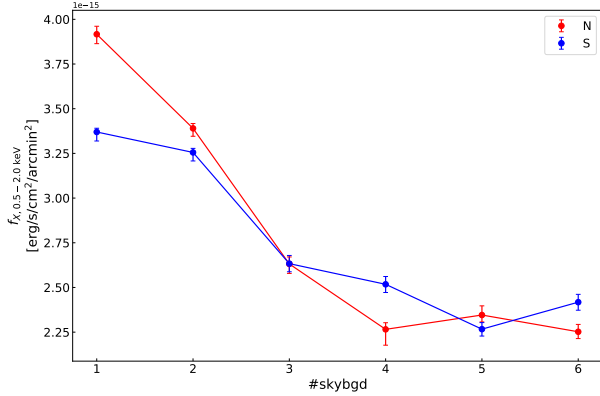


Figure 6.2: Soft band flux ($f_{X,0.5-2 \text{ keV}}$) of the CXB boxes acquired from fitting a typical CXB model.

For the science analyses, assigning the appropriate CXB region is important. The CXB level should be approximated, such that it is representative of that in the source regions. Therefore, an exhaustive investigation of various regions was carried out before deciding on a specific CXB region to be used in the science analyses. Six pairs of $1^\circ \times 1^\circ$ boxes were analyzed. They were placed outside the $2R_{200}$ to minimize the emission from the cluster and spread out from north to west (1–6N in Figure 6.1) and from east to south (1–6S). The boxes were first fitted with a typical CXB model (LHB, MWH, and unresolved sources; see Section 3.5). From this analysis, we notice that the soft band flux ($f_{X,0.5-2 \text{ keV}}$) decreases by a factor of 1.3 – 1.7

outwards (Figure 6.2) and flattens out at box 4N, 5N, 6N, 4S, 5S, and 6S (box 456; magenta boxes in Figure 6.1). We then utilized box 456 to redefine the temperatures and normalizations of the LHB and MWH, as well as the normalization of the unresolved sources. Afterward, we analyzed boxes 1N and 1S (box 1) to obtain the temperature of the eROSITA Bubbles. During this analysis, the parameters of the other CXB components were fixed at the values found in box 456 analysis. As a result, any spectral fitting performed on the cluster regions in this work was done using the following total model,

$$\text{Model} = \underbrace{\text{apec}_{\text{LHB}} + \text{TBabs} \times (\text{apec}_{\text{MWH}} + \text{apec}_{\text{eROBub}} + \text{powerlaw})}_{\text{CXB component}} + \underbrace{\text{TBabs} \times \text{apec}_{\text{clus}}}_{\text{cluster emission}} + \text{PIB}, \quad (6.1)$$

which is similar to Equation 3.6, except for the additional CXB component, $\text{apec}_{\text{eROBub}}$, to account for the eROSITA Bubble emission. The fitting strategy remains the same as outlined in Section 3.5.2. Based on the CXB analysis above, we used box 456 as the default CXB region for the science analyses: in the imaging analysis, the CXB level was calculated to be the average of surface brightness values amongst box 456 (SB_{CXB}) and the error is taken to be the root-mean-square deviation of these values (σ_{CXB}) to take into account the spatial variation of the CXB in the field; for the spectral analysis, we froze the temperatures of the CXB components from the CXB analysis (LHB and MWH from box 456, and the eROSITA Bubbles from box 1).

6.1.2 Surface Brightness and Spectral Analyses

As observed in Figure 6.1, the emission from the eROSITA Bubbles is dominant in the red (0.2 – 0.6 keV) and green (0.6 – 1.0 keV) channels. In addition to the surface brightness profiles calculated in the 0.2 – 2.3 keV energy band, profiles calculated in the 1.0 – 2.3 keV energy band were also calculated to exclude the contribution from this foreground structure. Furthermore, to assess the morphology of the

ICM, surface brightness profiles from four directions were constructed, namely north, west, south, and east. The opening angle of each sector was set according to the position angle of the elliptical detection of SExtractor (Bertin & Arnouts, 1996, see Section 3.4.1), such that the center of the opening angle of a sector is either the minor or major axis of the ellipse. The configuration of the sectors is plotted and labeled in Figure 6.1. Each profile was calculated out to the $2R_{200}$. Similarly, the spectral analysis was conducted for the full azimuth and four different sectors out to R_{200} .

6.2 Redshift Analysis

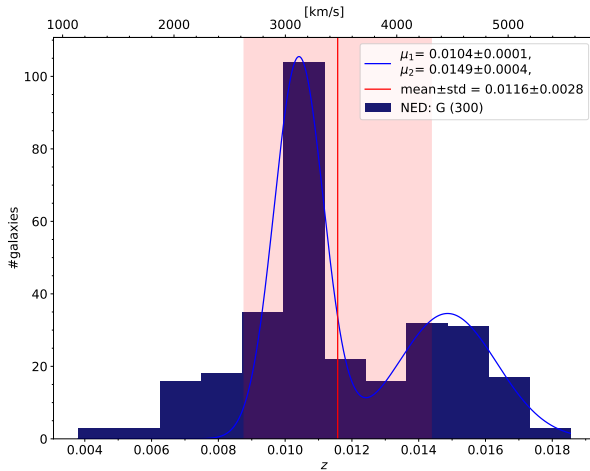


Figure 6.3: The galaxy redshift distribution within the R_{200} of the Centaurus cluster. The blue line is the double-Gaussian fit, the red vertical line and the red shaded area are the mean and the 1σ standard deviation of the whole sample.

of $(3117.8 \pm 30.0) \text{ km s}^{-1}$ and $(4466.9 \pm 119.9) \text{ km s}^{-1}$, respectively. These peaks are consistent with the previously determined redshifts of Cen 30 and Cen 45 (Lucey et al., 1986a).

To show the spatial distributions of the galaxies associated with the Cen 30 and Cen 45 substructures, we generated the galaxy number density maps by smoothing the spatial bins of the distributions (see Figure 6.4). The redshift ranges were set to be $0.009 \leq z \leq 0.0118$ for Cen 30 and $0.0119 \leq z \leq 0.0179$ for Cen 45 and constrained to a smaller FoV of R_{500} to better visualize the substructures. Contours from the fully-corrected eRASS:5 image are overplotted in white. From the plot (Figure 6.4a), we see that the galaxy distribution of the Cen 30 substructure is concentrated around the cluster center. The galaxy overdensity peaks around the position of the NGC 4696 (blue diamond), which also coincides with the cluster center (white cross). For the Cen 45 (Figure 6.4b), the concentration of the galaxies is positioned about 15 arcmin to the east and a peak around the second brightest galaxy in the cluster, NGC 4709 (magenta diamond). Additionally, another concentration of galaxies is also noticeable to the east.

Although there is a line-of-sight velocity separation of about 1500 km s^{-1} , Lucey et al. (1986a) reported that these substructures lie to the same cluster. The conclusion was made after several tests to

¹The NASA/IPAC Extragalactic Database (NED) is funded by the National Aeronautics and Space Administration and operated by the California Institute of Technology.

² $v_{\text{los}} = c \cdot z$, where c is the speed of light in vacuum.

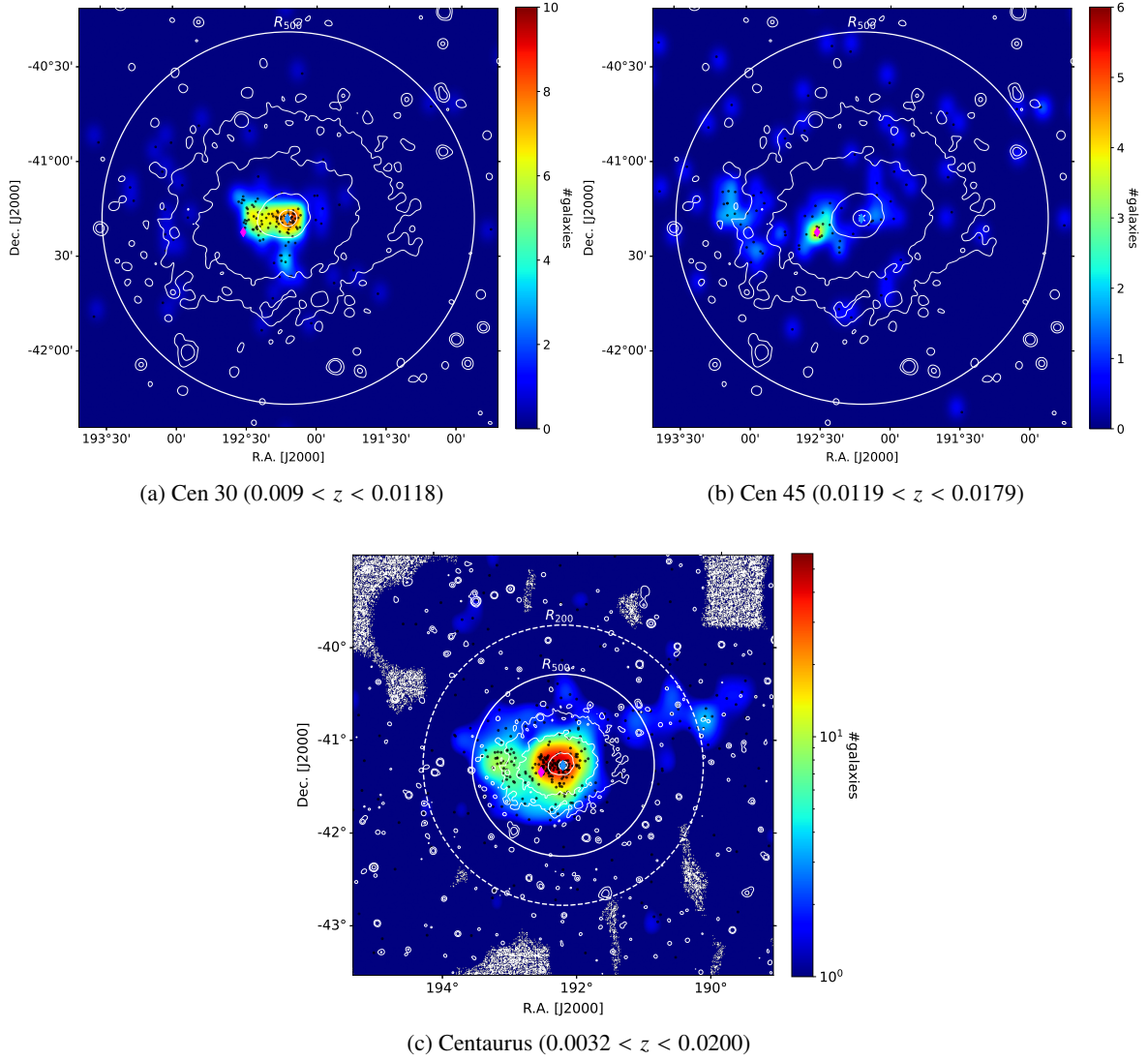


Figure 6.4: Galaxy number density maps in different redshift ranges. Blue and magenta diamonds denote the positions of the central galaxies of Cen 30 (NGC 4696) and Cen 45 (NGC 4709). The white contours are the eROSITA X-ray contours. The white circles and dashed-line circles in the different panels are the R_{500} and R_{200} of the cluster.

estimate their relative distance, including, comparisons of the color-magnitude relations of their member galaxies, luminosity functions, and galactic radius distributions of both substructures. On the other hand, the redshift inferred from the ICM velocity using *Suzaku* and *XMM-Newton* observations in previous studies reveals that the Cen 30 and Cen 45 are located at the same distance of $z \approx 0.0104$ (Ota & Yoshida, 2016; Gatuza et al., 2022). An offset between ICM mass centroids and the distribution of the galaxies is observed during cluster mergers (e.g., the Bullet cluster, Markevitch et al., 2004; Clowe et al., 2006; and A2744, Merten et al., 2011). During the merger, the different cluster components behave differently. The stars in galaxies and the collisionless dark matter just pass through without interacting, while the ICM is lagging due to the drag force. Hence, the observed galaxy and ICM separation of the Cen 45 substructure is an indication of previous merger activity (Ota & Yoshida, 2016).

Large-scale filaments can also be traced by trails of gas clumps and galaxies (Tuominen et al., 2021; Angelinelli et al., 2021). Therefore, we expanded the number galaxy density map view out to $1.5R_{200}$ (Figure 6.4c), which also includes all galaxies that potentially belong to the Centaurus cluster, that is $z = 0.0116 \pm 3 \cdot 0.0028$. A low significant stripe of overdensity is visible and stretches westward of the cluster. This structure is known as the “Western Branch” (Lucey et al., 1986a,b). The Western Branch is made up of galaxies with their redshift values within the ranges of the redshifts of both substructures. Although the direction of this structure is aligned with the elongation of the cluster, however, there is no X-ray emission correlated with it. Moreover, given the large separation between the peak concentration of Cen 45 and the Western Branch location, it is unlikely that the galaxies with similar redshifts are associated with the substructure. This decreases further the significance of the Western Branch.

6.3 Imaging Analysis

6.3.1 GGM Images

Besides the wavelet-filtered and RGB images, more images were produced with other image enhancement techniques, e.g., the Gaussian Gradient Magnitude (GGM) Filtering (see Section 3.4.2). The GGM filtering is adjusted with the Gaussian width σ , where a smaller scale highlights features in bright regions (cluster center), while a larger scale is for regions with fewer counts (outskirts). We display the GGM-filtered images of the brighter region ($r < R_{500}$) of the Centaurus cluster in Figure 6.5. From left to right, the images were filtered with $\sigma = 2, 4, 8, 32$ and progressively showed wider FoV from the very core of the cluster. Some features in the central region of the Centaurus cluster are visible: the soft filament/plume that extends toward the northeast (2-pixel), the eastern and western edges that are about ~ 2.1 arcmin and 3.6 arcmin from the cluster center, respectively (4-pixel), east-west ICM emission with longer extension toward the east (8- and 32-pixel). This eastern extension coincides with galaxy overdensity (Section 6.2).

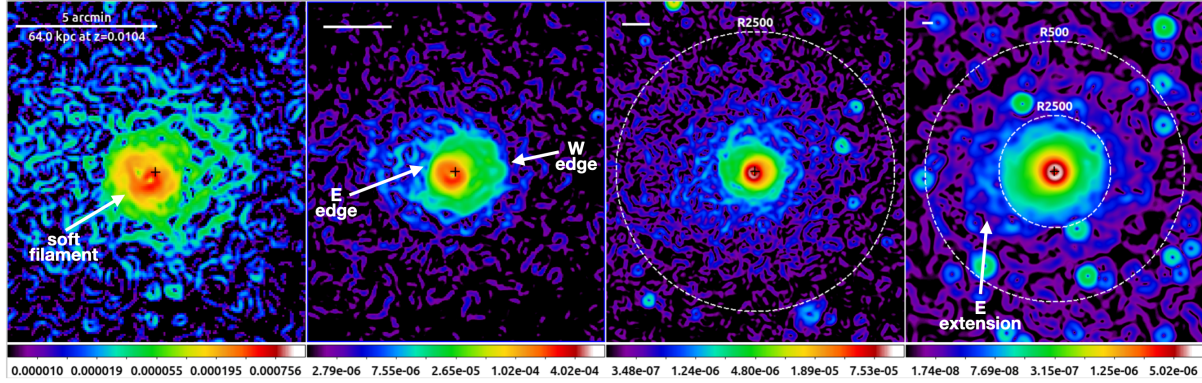


Figure 6.5: GGM-filtered images of the fully-corrected images in the 0.2 – 2.3 keV using $\sigma = 2, 4, 8, 32$ (left to right). The white line at the top left of each panel indicates a 5 arcmin (64kpc).

The core of the Centaurus cluster is known to host numerous astrophysical features. The area has been studied in great detail using multi-wavelength data, including *Chandra* X-ray data (e.g., Sanders & Fabian, 2002; Fabian et al., 2005; Sanders et al., 2016b), VLA and VLBA radio data (Taylor et al., 2002, 2006), and optical data (Fabian et al., 1982; Sparks et al., 1989; Hamer et al., 2019). One of the structures is the soft plume-like filament spreading out from the core toward the northeast. It was discovered that the plume is most prominent below ~ 1 keV and it consists of three soft filaments. The nucleus, where

the plume seems to originate, coincides with optical filaments and dust lane from the NGC 4696 galaxy (Fabian et al., 1982; Sparks et al., 1989; Hamer et al., 2019). On the sides of the nucleus are cavities that anti-correlate with radio lobes. These authors concluded that the plume and other features in the core of the Centaurus cluster (cavities, edges, shocks, bay, etc.), are the result of AGN feedback from NGC 4696, as well as sloshing motion.

6.3.2 Surface Brightness Analysis

Figure 6.6a and Figure 6.6b show the surface brightness profiles out to R_{500} in the 0.2 – 2.3 keV and 1.0 – 2.3 keV bands (top plot). The different sectors are color-coded to the labels in Figure 6.1: west in green, south in blue, east in orange, and north in red. The grey-shaded area indicates the 1σ surface brightness profile of the full azimuth (average of all directions). The significance deviation profile of each sector with respect to the full azimuthal surface brightness profile ($\sigma_{\text{w.r.t.annuli}}$) is shown in the bottom panel of each plot. The characteristic radii are shown as the brown dotted and dashed-dotted vertical lines, while the position of the center of the Cen 45 substructure is marked with a purple vertical line (only relevant for the eastern sector). In the $r < R_{500}$ regime, the profiles in various directions appear almost identical in both energy bands, but with a lower amplitude in the 1.0 – 2.3 keV band (including the CXB level). This suggests that there is little to no impact from the eROSITA Bubbles in this brighter cluster region. Moreover, we employed the full azimuthal surface brightness profile in the 0.2 – 2.3 keV band to generate a spherical surface brightness image out to $2R_{200}$. By subtracting the fully-corrected image in the corresponding band with this spherical surface brightness image, a residual image was acquired. The residual image helps spatially inspect the surface brightness features seen in the profiles. The Gaussian-smoothed ($\sigma = 25$ pixels) residual image is displayed in Figure 6.7.

The eastern and western edges that are detected in the 4-pixel GGM-filtered image, are also evident from the surface brightness profiles (Fig. 6.6a for 0.2 – 2.3 keV or 6.6b for 1.0 – 2.3 keV). For instance, in the east at 1.5 arcmin (before the edge) we notice a 5.7σ significance excess to the full azimuth value, and in the following bin, it drops to -2.1σ . For the western edge, a 3.8σ significance excess at 2 – 3 arcmin is detected and followed by a drop to 1.3σ .

The most striking feature is the bump of the excess along the eastern surface brightness profile (orange data points) between 4 arcmin and 25 arcmin with $3 - 5\sigma$. This enhancement coincides with the interaction location between Cen 30 and Cen 45, which is shown as the galaxy overdensity in Figure 6.4. In the residual image (Figure 6.7), it can also be seen as the bow-shaped excess in the east of NGC 4696. Spatially tracing surface brightness features in the Centaurus cluster, similar to the residual image in this work, has previously been done using the *ROSAT* PSPC data (Churazov et al., 1999) and the *XMM-Newton* image (Walker et al., 2013a). The eastern excess was detected in these residual images, but the eRASS:5 residual image shows the full extent of this feature. Up to R_{2500} , we acquired an average surface brightness excess with 4.1σ significance to the average surface brightness values. Between R_{2500} and $0.6R_{500}$, the average eastern significance drops to 2.5σ .

In the top panels of Figure 6.6c and Figure 6.6d, the surface brightness profiles between R_{500} and $2R_{200}$ in the 0.2 – 2.3 keV and 1.0 – 2.3 keV bands are displayed. In the bottom panel of each plot, the significance level of the source surface brightness to the CXB level ($S/N_{\text{w.r.t.CXB}}$) are shown and calculated as follows,

$$S/N_{\text{w.r.t.CXB}} = \frac{SB_{r>R_{500}} - SB_{\text{CXB}}}{\sqrt{\sigma_{r>R_{500}}^2 + \sigma_{\text{CXB}}^2}}, \quad (6.2)$$

where SB_r is the surface brightness value of the bin at $r > R_{500}$ regime, σ_r is its statistical uncertainties, while SB_{CXB} and σ_{CXB} are the sky background surface brightness and its standard deviation

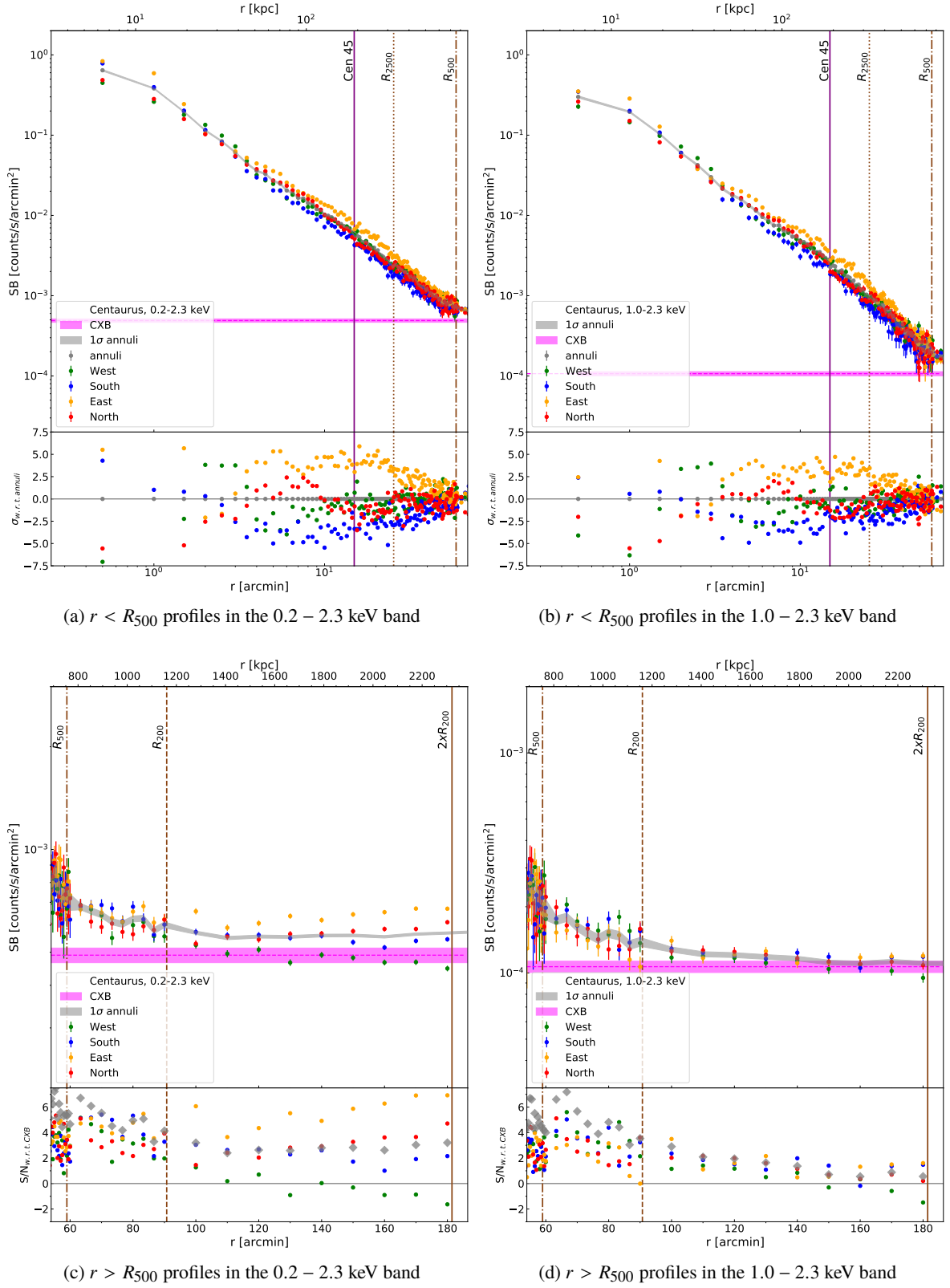


Figure 6.6: Surface brightness profiles of the Centaurus cluster are shown in the top panel in each plot. The bottom panels show the significance with respect to the full azimuthal surface brightness profile ($\sigma_{w.r.t.annuli}$) and the CXB level ($S/N_{w.r.t.CXB}$).

as described in Section 6.1.1. In the outskirts ($R_{500} < r < R_{200}$), the full azimuthal surface brightness values in both energy bands are detected with above 3σ significances. At larger radii of $r > R_{200}$, the trends seen in both profiles differ. For the profiles in the $0.2 - 2.3$ keV band, the different levels of eROSITA Bubbles contamination in the different sectors are noticeable: the strongest in the east and north, mild in the south, and none in the west. This also agrees with the visual inspection, for instance, in the residual image (Figure 6.7) we observe that the left part of the outer ring is brighter than the right. In the $1.0 - 2.3$ keV profiles, the contamination seems to diminish. The surface brightness values of the different sectors decrease outward toward the CXB level. We report emission with a 3.5σ significance at the 90.0 arcmin (R_{200}) mark and a 2.9σ significance at 100 arcmin ($\sim 1.1R_{200}$). The surface brightness hits the 1σ level detection around 140 arcmin ($\sim 1.5R_{200}$).

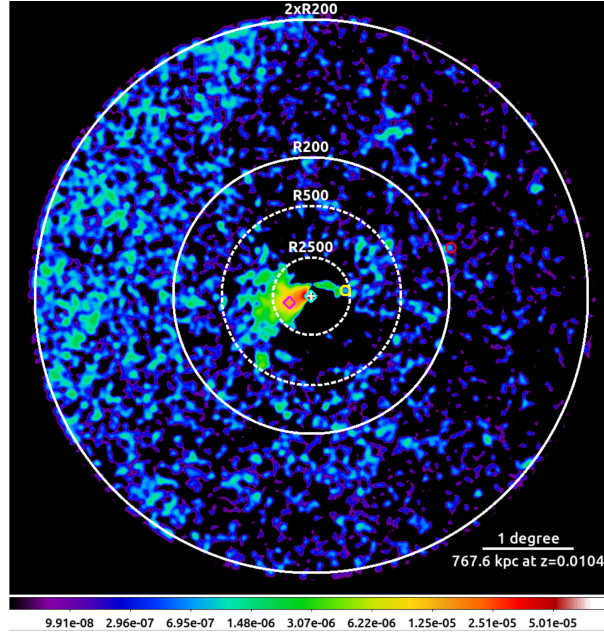


Figure 6.7: The residual image within $2R_{200}$ in the $0.2 - 2.3$ keV energy band. The white cross marks the cluster center, and the cyan and red diamonds mark the center of Cen 30 and Cen 45.

6.4 Spectral Analysis

The profiles of the ICM properties estimated through the spectral analysis are presented in Figure 6.8. These are the first detailed profiles of the Centaurus cluster for the radial range $r > 30$ arcmin. We display the profiles of the eastern (orange data points) and western (green) sectors in the left panel, and the profiles of the northern (red) and southern (blue) sectors in the right panel. In each panel, we show the normalization per unit area (top), gas temperature (middle), and metallicity (bottom). In each plot, the full azimuthal profile of each parameter is shown as the grey-shaded area. The purple vertical line is the position of the center of Cen 45 from the X-ray center (only relevant for the eastern sector). The characteristic radii are denoted with the black vertical-dotted (R_{2500}), dashed-dotted (R_{500}), and dashed (R_{200}) lines.

Overall, the temperature profiles from all directions follow a similar shape, that is, except for the first bins, the temperatures of the four sectors are within 1.6σ of the full azimuthal values. We note that the large error bars in the temperature profile of the southern sector can be attributed to the fewer

statistics that are evident in the imaging analysis (for example, the residual image in Fig. 6.7 and surface brightness profiles in these directions in Fig. 6.6). Furthermore, to compare the outskirts temperatures, temperature fit from a sample of *Suzaku* cluster outskirts measurements described in Reiprich et al. (2013) (Equation 5.2) and the temperature profile from simulations from Burns et al. (2010) are overplotted as purple-shaded and pink-shaded areas. The profile from Burns et al. (2010) is the average temperature of the two-dimensional profile of the simulated clusters using the *Enzo* *N*-body plus hydrodynamics cosmology code Bryan et al. (2014), which is formulated as follows,

$$k_B T(r) = A \cdot \langle k_B T \rangle \left[1 + B \left(\frac{r}{R_{200}} \right) \right]^\alpha, \quad (6.3)$$

where $A = 1.74 \pm 0.03$, $B = 0.64 \pm 0.10$, and $\alpha = -3.2 \pm 0.4$. In the profiles from Reiprich et al. (2013) and Burns et al. (2010), $\langle k_B T \rangle$ is given as the eRASS:5 temperature of Centaurus cluster obtained from an annulus of $0.2 - 0.5 R_{500}$, that is $2.64^{+0.08}_{-0.07}$ keV. Additionally, for the inner region of $r \lesssim 13$ arcmin, we compare the eRASS:5 profiles with *Chandra* results (colored-shaded areas), which is the adaptation of Figure 3 or Figure 6 of Sanders et al. (2016b)³.

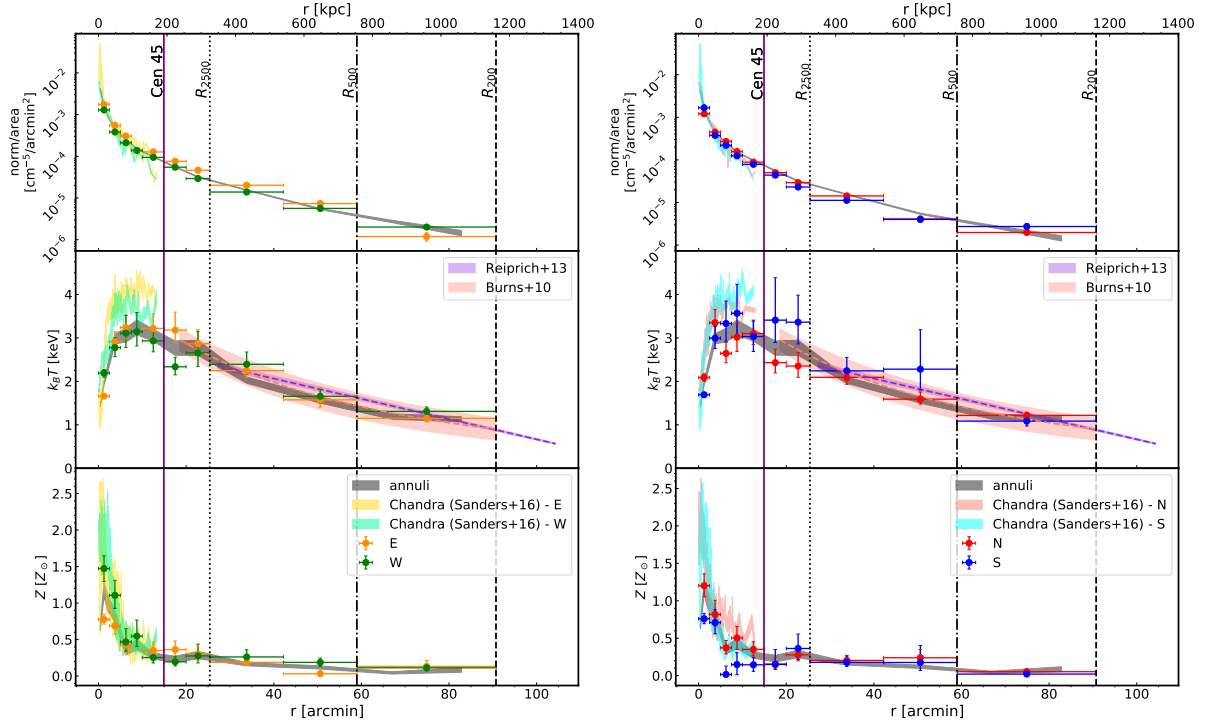


Figure 6.8: The ICM property profiles of the Centaurus cluster constrained with eRASS:5 data. *Left*: Eastern (orange data points) and western (green) profiles. *Right*: Northern (red) and southern (blue) profiles. In each panel, we show the normalization per unit area (top), gas temperature (middle), and metallicity (bottom) plots. The full azimuthal profile of each parameter is shown as the grey-shaded area. In the temperature panels (middle), *Suzaku* cluster temperature fit (purple-shaded area; Reiprich et al., 2013) and the average two-dimensional cluster profile from simulations (pink-shaded area; Burns et al., 2010) are plotted.

³The *Chandra* ICM profiles were provided by J. Sanders, one of the collaborators.

6.4.1 Core

In the core region of the Centaurus cluster, low-temperature ($1.43^{+0.03}_{-0.01}$ keV), metal-rich ($0.67 \pm 0.05 Z_{\odot}$) gas is observed. This feature is also seen in other X-ray data (e.g., [Allen & Fabian, 1994](#); [Sanders et al., 2016b](#); [Gatuzz et al., 2022](#)). Looking at the full azimuthal profile, the temperature increases gradually to ~ 3.0 keV at 6.3 arcmin, then it drops from 22.7 arcmin ($0.9R_{2500}$) outward. From the peak to the outermost bin, the temperature decreases by a factor of 2.8. For the metallicity profile, we identified a peak at 1.3 arcmin of $1.18^{+0.10}_{-0.09} Z_{\odot}$. From 3.8 arcmin to 6.3 arcmin, the metallicity drops by a factor of 2 to a sub-solar value of $0.34^{+0.06}_{-0.05} Z_{\odot}$. The metallicity stays around this value in the larger radii.

Two-temperature profile

Two-temperature (2T) fitting was also performed to the full azimuthal bins up to 2.5 arcmin from the center. The metallicity parameters of the two components were linked to each other to reduce the degree of freedom. The resulting temperatures of the hotter component align with the values from the single component fit, while the temperatures of the cooler component across the bins are relatively flat, ranging between 0.8 and 1.7 keV. We note that based on the AIC ([Akaike, 1974](#)) and the BIC ([Schwarz, 1978](#)) statistical tests, there is no significant improvement in the fit when adding a second component, except for the first bin (0 – 0.8 arcmin) where the 2T fit is a more suitable model to describe the spectra. Including only the 2T fit results of the first bin, the lowest best-fit temperature value decreases from 1.4 keV (1T) to 1.0 keV (2T). [Sanders et al. \(2016b\)](#) argue that the multi-phase structure of the ICM in the core ($r < 10$ kpc) is contributed by the plume structure and not due to the projection effects from the temperature gradient. A similar conclusion was drawn in [Ikebe et al. \(1999\)](#) using *ROSAT* PSPC and *ASCA* data.

The metallicity value obtained from the 2T fit in the first bin is $1.59^{+0.22}_{-0.18} Z_{\odot}$, which is about 2.4 times higher than the 1T value ($0.67^{+0.05}_{-0.05} Z_{\odot}$) with a significance of 4.9σ . This so-called ‘iron bias’ was investigated in [Buote \(2000\)](#) with *ASCA* data. Iron lines, in particular, the Fe L line at ~ 1.4 keV and the Fe K at ~ 6.5 keV are used to determine the ICM metallicity. In the presence of multi-temperature components with the average temperature of ~ 1.0 keV and contributions of both components are equal, the 1T model accommodates the flat spectral shape near 1.0 keV by decreasing the iron abundance at the expense of increasing the contribution of the flatter bremsstrahlung continuum. At higher temperatures, the iron bias decreases because the Fe K complex becomes more dominant and therefore, more pertinent for determining the metallicity. [Buote \(2000\)](#) analyzed a sample of 12 bright galaxy groups and found that the subsolar metallicity previously found in their cores is a fitting artifact caused by assuming an isothermal model. After fitting the data with a more appropriate model, namely, the 2T model, the issue was rectified, increasing the metallicity by a factor 2.6 than the value obtained by using the 1T model.

Asymmetry

At the central bin (0 – 2.5 arcmin), the western sector shows a higher temperature ($2.19^{+0.08}_{-0.10}$ keV) in comparison to the eastern sector (1.66 ± 0.03 keV) with a significance of 5.2σ . In comparison to the first bin of the eastern best-fit metallicity ($0.78 Z_{\odot}$), the value in the west is higher by a factor of two ($1.47 Z_{\odot}$). Similarly, the temperature and metallicity asymmetry are also observed for the first bins of the northern and southern sectors. Higher temperature ($2.09^{+0.09}_{-0.09}$ keV) is observed in the north in comparison to the south ($1.69^{+0.04}_{-0.03}$ keV) with a significance of 4.2σ . The metallicity in the north is $1.2^{+0.16}_{-0.15} Z_{\odot}$ and $0.76^{+0.07}_{-0.07} Z_{\odot}$ in the south.

The eastern and western edges at ~ 2.1 arcmin and 3.6 arcmin from the cluster center (see Figure 6.5) are also accompanied by temperature jumps (first to second bin). The temperature jumps and surface

density drops in front of the edges are hints of cold fronts (Markevitch & Vikhlinin, 2007). The cold fronts, the core east-west and north-south temperature and metal asymmetries, and the east-west ICM asymmetry are common signatures of sloshing motions that could be triggered by the interaction between Cen 30 and Cen 45 (Sanders & Fabian, 2002; Fabian et al., 2005; Sanders et al., 2016b). Sloshing motions in the cluster cores are the results of disturbance of the ICM due to an infalling subcluster (e.g., Ascasibar & Markevitch, 2006; ZuHone et al., 2010, 2019). The perturbation causes the displacement of the cool core ICM from the center of the gravitational potential well. The gas is uplifted, decoupled from the dark matter through ram pressure, falls back, and starts to oscillate ("sloshing"). It leaves distinctive imprints on the ICM, such as cold fronts and spiral patterns.

6.4.2 Eastern Excess

In agreement with the findings from the surface brightness analysis, excess emission in the east is also observed from the spectral analysis. The normalizations per area in the east are higher than the full annuli and other sectors, except for the outermost bin ($R_{500} - R_{200}$). Compared to the full azimuthal values, a 31% and 36% enhancement of 5.4σ are found at the bin before ($10.0 - 15.0$ arcmin) and after the center of Cen 45 ($15 - 20.0$ arcmin), respectively. The peak excess is found at the $20.0 - 25.4$ arcmin bin with 45% and 7.7σ , then it continues until the $0.7 - 1.0R_{500}$ bin with a relative difference of 36% and 2.6σ significance. This supports the findings from surface brightness profiles and residual image, that the Cen 45 substructure extends even further out than previously measured (Churazov et al., 1999; Walker et al., 2013a). A higher ICM redshift with respect to the Cen 30 optical redshift at a $r > 15$ arcmin bin, east of Cen 45, is reported in Gatuzz et al. (2022). This signifies that the eastern extension may be a stripped gas from Cen 45 emerging from the merger activity.

At the $15 - 20.0$ arcmin bin, temperature enhancements are observed in the east ($3.18^{+0.41}_{-0.29}$ keV) and south ($3.41^{+0.98}_{-0.51}$ keV) in compared to their opposite western and northern bins. The temperatures in the east and south in the mentioned bin are 0.8 keV and 1.0 keV higher than their counterpart directions. Temperature enhancements in the same directions are also discovered by other instruments. Using ASCA observations, Churazov et al. (1999) and Furusho et al. (2001) found a temperature value of 4.4 ± 0.2 keV and 4.3 ± 0.2 keV, respectively. Meanwhile, using *XMM-Newton* observations Walker et al. (2013a) reported hotter gas of 5.0 ± 0.4 keV (this value is in good agreement with the eROSITA value after accounting for the cross-calibration between the two instruments Migkas et al., 2024). This temperature enhancement might be due to shock heating and further supports the notion of the ongoing interaction between Cen 30 and Cen 45.

6.4.3 $r > 0.5R_{500}$

The average metallicity value across the sectors in the intermediate radial range of $R_{2500} - R_{500}$ ($25.4 - 59.0$ arcmin) is $\sim 0.2Z_{\odot}$. Walker et al. (2013b) analyzed *Suzaku* observations of Centaurus cluster along the north-western strip out to $0.95R_{200}$. At $45 - 50$ arcmin, they measured a metallicity of $0.1Z_{\odot}$, which is broadly in agreement with the value reported in this work. Other galaxy cluster studies (e.g., Urban et al., 2017; Ghizzardi et al., 2021) report a metallicity value of $\sim 0.3Z_{\odot}$ at a similar distance range. Our metallicity is within the scatters of the literature values

The outskirts ($R_{500} < r < R_{200}$) metallicity values in the northern and southern sectors appear to be slightly lower than in the eastern and western sectors. They range between 0.003 and $0.08Z_{\odot}$ for the former and between 0.07 and $0.21Z_{\odot}$ for the latter, which may be related to the merger along the east-west direction. Nevertheless, our metallicity values in this regime, $0.003/Z_{\odot} < Z < 0.21/Z_{\odot}$, are consistent within the measurement ranges of other galaxy clusters; for example *Suzaku* outskirts metallicity of A2204 (Reiprich et al., 2009), Perseus cluster (Simionescu et al., 2011; Werner et al., 2013), and ten

nearby clusters (Urban et al., 2017), as well as the *XMM-Newton* measurement of the northern outskirts of the Virgo cluster (Urban et al., 2011).

The temperature values in the different sectors at $R_{500} - R_{200}$ are consistent with each other, with an average of 1.2 keV. The outskirts temperatures closely adhere to the predicted temperature profiles derived from simulations and fit from *Suzaku* outskirts measurements. The absence of temperature deviations, such as excess, in the outskirts of the Centaurus cluster corresponds to the lack of large-scale filaments connected to the cluster. As reported in other works (e.g., Kawaharada et al., 2010; Veronica et al., 2024a), connectivity with large-scale structures may induce faster thermalization along the connected direction of the cluster outskirts.

6.5 Summary and Conclusions

In this work, we employed the eRASS:5 data to perform comprehensive imaging analysis out to $2R_{200}$ (~ 181 arcmin) and spectral analyses out to R_{200} (~ 91 arcmin). We present the first detailed large-scale view of the Centaurus cluster, namely, sampling the whole azimuth beyond 30 arcmin. Thus, we increase the probed volume of the cluster by a factor of almost 30. Due to partial foreground contamination by the eROSITA Bubbles, we took particular care of the CXB, such as probing different energy bands and performing extensive CXB spectral analysis in the FoV. We compared the constructed temperature profiles with other cluster measurements and simulations. Additionally, we compiled a galaxy redshift catalog from a public database. Galaxy member analysis was done to distinguish any substructures. We outline our results below:

- Optical redshift analysis: The bimodality in the distribution of the galaxy member redshifts is observed. The peaks correspond to Cen 30 at $z = 0.0104$ and Cen 45 at $z = 0.0149$. The peak of galaxy member number density of each substructure is centered at their respective brightest galaxy; NGC 4696 for Cen 30 (coincides with the cluster X-ray center) and NGC 4709 for Cen 45 (15 arcmin east of the cluster center). A large-scale trail of galaxies spreading westward reaching the $1.5R_{200}$ (Western Branch) is observed. However, the detection is not significant and it does not correlate with X-ray emission.
- Core: The known structures in the cores of the Centaurus cluster are emphasized using the GGM filtering, e.g., the soft filament emission originated from the nucleus (plume), temperatures and metallicities asymmetry in the core, as well as the eastern and western cold fronts. These features are induced by AGN feedback from NGC 4696 galaxy and the sloshing motion triggered by substructure merger.
- Eastern excess: The X-ray eastern excess emission, along the Cen 45 direction, is traceable up to R_{500} . Based on previous ICM velocity (redshift) measurements, the excess behind Cen 45 might be ram-pressure-stripped gas from this substructure. Moreover, we confirm the previously detected temperature enhancements in the east and south, which are consistent with shock-heated gas resulting from the interaction between Cen 30 and Cen 45.
- Outskirts: Significant X-ray emission is measured at R_{200} with a 3.5σ above the CXB level and at $\sim 1.1R_{200}$ with 2.9σ . Aligning with the results from visual inspections and optical redshift analysis, no apparent large-scale structures seem to be connected with the cluster. The measured temperature profiles at larger radii ($r > 0.3R_{200}$) closely follow the predicted temperature profiles derived from simulations and fit from *Suzaku* outskirts measurements. We attribute the absence of temperature deviations, such as excess, in the outskirts of the Centaurus cluster to the lack of large-scale filaments connected to the cluster. There is a little asymmetry in the outskirts metallicity, with the

eastern and western metallicities range between 0.07 and $0.21Z_{\odot}$, while the northern and southern metallicities range between 0.003 and $0.08Z_{\odot}$. Higher metallicity in the east-west direction might be related to the merger direction. However, we note that the metallicity estimates of these sectors are in good agreement with the other cluster outskirts measurements.

Bibliography

- Abell, G. O. 1958, [ApJS](#), **3**, 211
- Abell, G. O., Corwin, Harold G., J., & Olowin, R. P. 1989, [ApJS](#), **70**, 1
- Akaike, H. 1974, [IEEE Transactions on Automatic Control](#), **19**, 716
- Akamatsu, H., Fujita, Y., Akahori, T., et al. 2017, [A&A](#), **606**, A1
- Allen, S. W., Evrard, A. E., & Mantz, A. B. 2011, [ARA&A](#), **49**, 409
- Allen, S. W. & Fabian, A. C. 1994, [MNRAS](#), **269**, 409
- Alvarez, G. E., Randall, S. W., Bourdin, H., Jones, C., & Holley-Bockelmann, K. 2018, [ApJ](#), **858**, 44
- Alvarez, G. E., Randall, S. W., Su, Y., et al. 2022, [ApJ](#), **938**, 51
- Angelinelli, M., Etti, S., Vazza, F., & Jones, T. W. 2021, [A&A](#), **653**, A171
- Arnaud, K., Smith, R., & Siemiginowska, A. 2011, Handbook of X-ray Astronomy, Cambridge Observing Handbooks for Research Astronomers (Cambridge University Press)
- Arnaud, K. A. 1996, in Astronomical Society of the Pacific Conference Series, Vol. 101, Astronomical Data Analysis Software and Systems V, ed. G. H. Jacoby & J. Barnes, **17**
- Arnaud, M. 2005, in Background Microwave Radiation and Intracluster Cosmology, ed. F. Melchiorri & Y. Rephaeli, **77**
- Ascasibar, Y. & Markevitch, M. 2006, [ApJ](#), **650**, 102
- Asplund, M., Grevesse, N., Sauval, A. J., & Scott, P. 2009, [ARA&A](#), **47**, 481
- Bartelmann, M. 2010, [Classical and Quantum Gravity](#), **27**, 233001
- Bennett, C. L., Banday, A. J., Gorski, K. M., et al. 1996, [ApJ](#), **464**, L1
- Bennett, C. L., Halpern, M., Hinshaw, G., et al. 2003, [ApJS](#), **148**, 1
- Bennett, J. O., Donahue, M. O., Schneider, N., & Voit, M. 2013, The Cosmic Perspective, 7th edn. (Pearson Education Limited)
- Bertin, E. & Arnouts, S. 1996, [A&AS](#), **117**, 393
- Biffi, V., Dolag, K., Reiprich, T. H., et al. 2022, [A&A](#), **661**, A17

- Biffi, V., Mernier, F., & Medvedev, P. 2018a, [Space Sci. Rev.](#), **214**, 123
- Biffi, V., Planelles, S., Borgani, S., et al. 2018b, [MNRAS](#), **476**, 2689
- Bleem, L. E., Stalder, B., de Haan, T., et al. 2015, [ApJS](#), **216**, 27
- Böhringer, H., Schuecker, P., Guzzo, L., et al. 2001, [A&A](#), **369**, 826
- Böhringer, H., Voges, W., Huchra, J. P., et al. 2000, [ApJS](#), **129**, 435
- Boller, T., Freyberg, M. J., Trümper, J., et al. 2016, [A&A](#), **588**, A103
- Bonamente, M., Lieu, R., & Bulbul, E. 2009, [ApJ](#), **696**, 1886
- Bonamente, M., Mirakhor, M., Lieu, R., & Walker, S. 2022, [MNRAS](#), **514**, 416
- Bond, J. R., Kofman, L., & Pogosyan, D. 1996, [Nature](#), **380**, 603
- Bonjean, V., Aghanim, N., Salomé, P., Douspis, M., & Beelen, A. 2018, [A&A](#), **609**, A49
- Briel, U. G., Aschenbach, B., Hasinger, G., et al. 1996, The ROSAT Users' Handbook
- Brüggen, M., Reiprich, T. H., Bulbul, E., et al. 2021, [A&A](#), **647**, A3
- Brunner, H., Liu, T., Lamer, G., et al. 2022, [A&A](#), **661**, A1
- Bryan, G. L., Norman, M. L., O'Shea, B. W., et al. 2014, [ApJS](#), **211**, 19
- Bulbul, E., Liu, A., Kluge, M., et al. 2024, [arXiv e-prints](#), [arXiv:2402.08452](#)
- Bulbul, E., Randall, S. W., Bayliss, M., et al. 2016, [ApJ](#), **818**, 131
- Buote, D. A. 2000, [MNRAS](#), **311**, 176
- Buote, D. A. 2002, in *Astrophysics and Space Science Library*, Vol. 272, *Merging Processes in Galaxy Clusters*, ed. L. Feretti, I. M. Gioia, & G. Giovannini, 79–107
- Buote, D. A., Zappacosta, L., Fang, T., et al. 2009, [ApJ](#), **695**, 1351
- Burns, J. O., Skillman, S. W., & O'Shea, B. W. 2010, [ApJ](#), **721**, 1105
- Carlstrom, J. E., Holder, G. P., & Reese, E. D. 2002, [ARA&A](#), **40**, 643
- Cash, W. 1979, [ApJ](#), **228**, 939
- Cavaliere, A. & Fusco-Femiano, R. 1976, [A&A](#), **500**, 95
- Cen, R. & Ostriker, J. P. 1999, [ApJ](#), **514**, 1
- Churazov, E., Gilfanov, M., Forman, W., & Jones, C. 1999, [ApJ](#), **520**, 105
- Clowe, D., Bradač, M., Gonzalez, A. H., et al. 2006, [ApJ](#), **648**, L109
- Davé, R., Cen, R., Ostriker, J. P., et al. 2001, [ApJ](#), **552**, 473
- De Grandi, S., Böhringer, H., Guzzo, L., et al. 1999, [ApJ](#), **514**, 148

- Dietl, J., Pacaud, F., Reiprich, T. H., et al. 2024, [arXiv e-prints](#), [arXiv:2401.17281](#)
- Dupke, R. A. & Bregman, J. N. 2001, [ApJ](#), **562**, 266
- Eckert, D., Jauzac, M., Shan, H., et al. 2015a, [Nature](#), **528**, 105
- Eckert, D., Molendi, S., Owers, M., et al. 2014, [A&A](#), **570**, A119
- Eckert, D., Roncarelli, M., Ettori, S., et al. 2015b, [MNRAS](#), **447**, 2198
- Egger, R. J. & Aschenbach, B. 1995, [A&A](#), **294**, L25
- Elvis, M. 1976, [MNRAS](#), **177**, 7P
- ESA: XMM-Newton SOC. 2023a, *Users Guide to the XMM-Newton Science Analysis System*, https://xmm-tools.cosmos.esa.int/external/xmm_user_support/documentation/sas_usg/USG/ [Accessed: March 2024]
- ESA: XMM-Newton SOC. 2023b, XMM-Newton Users Handbook, Issue 2.21
- Ettori, S. 2000, [MNRAS](#), **318**, 1041
- Ettori, S., Gastaldello, F., Gitti, M., et al. 2013, [A&A](#), **555**, A93
- Ezer, C., Bulbul, E., Nihal Ercan, E., et al. 2017, [ApJ](#), **836**, 110
- Fabian, A. C., Atherton, P. D., Taylor, K., & Nulsen, P. E. J. 1982, [MNRAS](#), **201**, 17P
- Fabian, A. C., Sanders, J. S., Taylor, G. B., & Allen, S. W. 2005, [MNRAS](#), **360**, L20
- Feretti, L. & Giovannini, G. 2008, in *A Pan-Chromatic View of Clusters of Galaxies and the Large-Scale Structure*, ed. M. Plionis, O. López-Cruz, & D. Hughes, Vol. 740, 24
- Fixsen, D. J. 2009, [ApJ](#), **707**, 916
- Freyberg, M., Perinati, E., Pacaud, F., et al. 2020, in *Society of Photo-Optical Instrumentation Engineers (SPIE) Conference Series*, Vol. 11444, *Space Telescopes and Instrumentation 2020: Ultraviolet to Gamma Ray*, ed. J.-W. A. den Herder, S. Nikzad, & K. Nakazawa, [114441O](#)
- Fujita, Y., Tawa, N., Hayashida, K., et al. 2008, [PASJ](#), **60**, S343
- Fukushima, K., Kobayashi, S. B., & Matsushita, K. 2022, [MNRAS](#), **514**, 4222
- Furusho, T., Yamasaki, N. Y., Ohashi, T., et al. 2001, [PASJ](#), **53**, 421
- Galárraga-Espinosa, D., Aghanim, N., Langer, M., Gouin, C., & Malavasi, N. 2020, [A&A](#), **641**, A173
- Galárraga-Espinosa, D., Aghanim, N., Langer, M., & Tanimura, H. 2021, [A&A](#), **649**, A117
- Galárraga-Espinosa, D., Langer, M., & Aghanim, N. 2022, [A&A](#), **661**, A115
- Gatuzz, E., Sanders, J. S., Canning, R., et al. 2022, [MNRAS](#), **513**, 1932
- Gatuzz, E., Sanders, J. S., Dennerl, K., et al. 2023, [MNRAS](#), **525**, 6394
- Geller, M. J. & Huchra, J. P. 1989, [Science](#), **246**, 897

- Ghirardini, V., Bulbul, E., Hoang, D. N., et al. 2021, [A&A](#), **647**, A4
- Ghizzardi, S., Molendi, S., van der Burg, R., et al. 2021, [A&A](#), **652**, C3
- Giodini, S., Lovisari, L., Pointecouteau, E., et al. 2013, [Space Sci. Rev.](#), **177**, 247
- Gott, J. Richard, I., Jurić, M., Schlegel, D., et al. 2005, [ApJ](#), **624**, 463
- Gursky, H., Kellogg, E., Murray, S., et al. 1971, [ApJ](#), **167**, L81
- Hamer, S. L., Fabian, A. C., Russell, H. R., et al. 2019, [MNRAS](#), **483**, 4984
- Hattori, S., Ota, N., Zhang, Y.-Y., Akamatsu, H., & Finoguenov, A. 2017, [PASJ](#), **69**, 39
- HI4PI Collaboration, Ben Bekhti, N., Flöer, L., et al. 2016, [A&A](#), **594**, A116
- Hlavacek-Larrondo, J., Li, Y., & Churazov, E. 2022, in Handbook of X-ray and Gamma-ray Astrophysics, **5**
- Hoekstra, H., Bartelmann, M., Dahle, H., et al. 2013, [Space Sci. Rev.](#), **177**, 75
- Huang, N., Bleem, L. E., Stalder, B., et al. 2020, [AJ](#), **159**, 110
- Hudson, D. S., Mittal, R., Reiprich, T. H., et al. 2010, [A&A](#), **513**, A37
- Ikebe, Y., Makishima, K., Fukazawa, Y., et al. 1999, [ApJ](#), **525**, 58
- Jansen, F., Lumb, D., Altieri, B., et al. 2001, [A&A](#), **365**, L1
- Kaiser, N. 1986, [MNRAS](#), **222**, 323
- Kalberla, P. M. W., Burton, W. B., Hartmann, D., et al. 2005, [A&A](#), **440**, 775
- Kawaharada, M., Okabe, N., Umetsu, K., et al. 2010, [ApJ](#), **714**, 423
- Kellogg, E., Gursky, H., Leong, C., et al. 1971, [ApJ](#), **165**, L49
- King, I. 1962, [AJ](#), **67**, 471
- Koribalski, B. S., Veronica, A., Brüggen, M., et al. 2023, [arXiv e-prints](#), [arXiv:2304.11784](#)
- Kovács, O. E., Bogdán, Á., Smith, R. K., Kraft, R. P., & Forman, W. R. 2019, [ApJ](#), **872**, 83
- Kravtsov, A. V. & Borgani, S. 2012, [ARA&A](#), **50**, 353
- Kuchner, U., Haggard, R., Aragón-Salamanca, A., et al. 2022, [MNRAS](#), **510**, 581
- Kull, A. & Böhringer, H. 1999, [A&A](#), **341**, 23
- Kuntz, K. D., Collado-Vega, Y. M., Collier, M. R., et al. 2015, [ApJ](#), **808**, 143
- Kuntz, K. D. & Snowden, S. L. 2000, [ApJ](#), **543**, 195
- Kuntz, K. D. & Snowden, S. L. 2008, [A&A](#), **478**, 575
- Lakhchaura, K., Mernier, F., & Werner, N. 2019, [A&A](#), **623**, A17

- Lin, Y.-T., Mohr, J. J., & Stanford, S. A. 2003, [ApJ](#), 591, 749
- Liu, A., Bulbul, E., Ghirardini, V., et al. 2022, [A&A](#), 661, A2
- Liu, A., Yu, H., Diaferio, A., et al. 2018, [ApJ](#), 863, 102
- Liu, W., Chiao, M., Collier, M. R., et al. 2017a, [ApJ](#), 834, 33
- Liu, W., Chiao, M., Collier, M. R., et al. 2017b, [ApJ](#), 834, 33
- Lovisari, L., Reiprich, T. H., & Schellenberger, G. 2015, [A&A](#), 573, A118
- Lucey, J. R., Currie, M. J., & Dickens, R. J. 1986a, [MNRAS](#), 221, 453
- Lucey, J. R., Currie, M. J., & Dickens, R. J. 1986b, [MNRAS](#), 222, 427
- Lumb, D. H., Warwick, R. S., Page, M., & De Luca, A. 2002, [A&A](#), 389, 93
- Luo, B., Brandt, W. N., Xue, Y. Q., et al. 2017, [ApJS](#), 228, 2
- Malavasi, N., Aghanim, N., Douspis, M., Tanimura, H., & Bonjean, V. 2020, [A&A](#), 642, A19
- Markevitch, M., Gonzalez, A. H., Clowe, D., et al. 2004, [ApJ](#), 606, 819
- Markevitch, M. & Vikhlinin, A. 2007, [Phys. Rep.](#), 443, 1
- Martizzi, D., Vogelsberger, M., Artale, M. C., et al. 2019, [MNRAS](#), 486, 3766
- Mathiesen, B., Evrard, A. E., & Mohr, J. J. 1999, [ApJ](#), 520, L21
- McCall, H., Reiprich, T. H., Veronica, A., et al. 2024, [arXiv e-prints](#), arXiv:2401.17296
- McNamara, B. R. & Nulsen, P. E. J. 2007, [ARA&A](#), 45, 117
- Merloni, A., Lamer, G., Liu, T., et al. 2024, [A&A](#), 682, A34
- Merloni, A., Predehl, P., Becker, W., et al. 2012, [arXiv e-prints](#), arXiv:1209.3114
- Mernier, F., Biffi, V., Yamaguchi, H., et al. 2018, [Space Sci. Rev.](#), 214, 129
- Merten, J., Coe, D., Dupke, R., et al. 2011, [MNRAS](#), 417, 333
- Migkas, K., Kox, D., Schellenberger, G., et al. 2024, [arXiv e-prints](#), arXiv:2401.17297
- Mills, B. Y. 1960, [Australian Journal of Physics](#), 13, 550
- Mirakhor, M. S. & Walker, S. A. 2021, [MNRAS](#), 506, 139
- Mitsuda, K., Bautz, M., Inoue, H., et al. 2007, [PASJ](#), 59, S1
- Miville-Deschênes, M.-A. & Lagache, G. 2005, [ApJS](#), 157, 302
- Morganti, R., Killeen, N. E. B., & Tadhunter, C. N. 1993, [MNRAS](#), 263, 1023
- Morrison, R. & McCammon, D. 1983, [ApJ](#), 270, 119
- Nagai, D. & Lau, E. T. 2011, [ApJ](#), 731, L10

- NASA's HEASARC. 2006, *Suzaku Mission Overview*, <https://heasarc.gsfc.nasa.gov/docs/suzaku/about/overview.html> [Accessed: April 2024]
- Nicastro, F., Kaastra, J., Krongold, Y., et al. 2018, *Nature*, **558**, 406
- Nicastro, F., Krongold, Y., Mathur, S., & Elvis, M. 2017, *Astronomische Nachrichten*, **338**, 281
- Nicastro, F., Mathur, S., Elvis, M., et al. 2005, *Nature*, **433**, 495
- Nomoto, K., Kobayashi, C., & Tominaga, N. 2013, *ARA&A*, **51**, 457
- Norris, R. P., Marvil, J., Collier, J. D., et al. 2021, *PASA*, **38**, e046
- O'Dea, C. P. & Baum, S. A. 2023, *Galaxies*, **11**, 67
- Ota, N. 2012, *Research in Astronomy and Astrophysics*, **12**, 973
- Ota, N., Fukazawa, Y., Fabian, A. C., et al. 2007, *PASJ*, **59**, 351
- Ota, N. & Yoshida, H. 2016, *PASJ*, **68**, S19
- Pacaud, F., Pierre, M., Refregier, A., et al. 2006, *MNRAS*, **372**, 578
- Piffaretti, R., Arnaud, M., Pratt, G. W., Pointecouteau, E., & Melin, J. B. 2011, *A&A*, **534**, A109
- Planck Collaboration, Adam, R., Ade, P. A. R., et al. 2016, *A&A*, **594**, A1
- Planck Collaboration, Ade, P. A. R., Aghanim, N., et al. 2013, *A&A*, **550**, A134
- Planck Collaboration, Aghanim, N., Akrami, Y., et al. 2020a, *A&A*, **641**, A6
- Planck Collaboration, Akrami, Y., Ashdown, M., et al. 2020b, *A&A*, **641**, A4
- Pottschmidt, K. 2015, *The Suzaku Technical Description*, https://heasarc.gsfc.nasa.gov/docs/suzaku/prop_tools/suzaku_td/ [Accessed: April 2024]
- Pratt, G. W., Arnaud, M., Biviano, A., et al. 2019, *Space Sci. Rev.*, **215**, 25
- Predehl, P., Andritschke, R., Arefiev, V., et al. 2021, *A&A*, **647**, A1
- Predehl, P., Sunyaev, R. A., Becker, W., et al. 2020, *Nature*, **588**, 227
- Ramos-Ceja, M. E., Pacaud, F., Reiprich, T. H., et al. 2019, *A&A*, **626**, A48
- Randall, S., Nulsen, P., Forman, W. R., et al. 2008, *ApJ*, **688**, 208
- Reiprich, T. H., Basu, K., Ettori, S., et al. 2013, *Space Sci. Rev.*, **177**, 195
- Reiprich, T. H. & Böhringer, H. 2002, *ApJ*, **567**, 716
- Reiprich, T. H., Hudson, D. S., Zhang, Y. Y., et al. 2009, *A&A*, **501**, 899
- Reiprich, T. H., Veronica, A., Pacaud, F., et al. 2021, *A&A*, **647**, A2
- Roncarelli, M., Ettori, S., Borgani, S., et al. 2013, *MNRAS*, **432**, 3030
- Sanders, J. S. & Fabian, A. C. 2002, *MNRAS*, **331**, 273

- Sanders, J. S., Fabian, A. C., Russell, H. R., Walker, S. A., & Blundell, K. M. 2016a, *MNRAS*, **460**, 1898
- Sanders, J. S., Fabian, A. C., Taylor, G. B., et al. 2016b, *MNRAS*, **457**, 82
- Sarazin, C. L. 1988, X-ray Emission from Clusters of Galaxies
- Sarazin, C. L. 2002, in *Astrophysics and Space Science Library*, Vol. 272, Merging Processes in Galaxy Clusters, ed. L. Feretti, I. M. Gioia, & G. Giovannini, 1–38
- Sarkar, A., Randall, S., Su, Y., et al. 2022, *ApJ*, **935**, L23
- Schellenberger, G. & Reiprich, T. H. 2015, *A&A*, **583**, L2
- Schneider, P. 2015, *Extragalactic Astronomy and Cosmology* (Springer, Berlin, Heidelberg)
- Schneider, P., Ehlers, J., & Falco, E. E. 1992, *Gravitational Lenses*
- Schwarz, G. 1978, *The Annals of Statistics*, **6**, 461
- Shull, J. M., Smith, B. D., & Danforth, C. W. 2012, *ApJ*, **759**, 23
- Simionescu, A., Allen, S. W., Mantz, A., et al. 2011, *Science*, **331**, 1576
- Simionescu, A., Werner, N., Urban, O., et al. 2013, *ApJ*, **775**, 4
- Smith, R. K., Brickhouse, N. S., Liedahl, D. A., & Raymond, J. C. 2001, *ApJ*, **556**, L91
- Smith, S. 1936, *ApJ*, **83**, 23
- Smoot, G. F., Bennett, C. L., Kogut, A., et al. 1992, *ApJ*, **396**, L1
- Snowden, S. L., Egger, R., Freyberg, M. J., et al. 1997, *ApJ*, **485**, 125
- Snowden, S. L., Mushotzky, R. F., Kuntz, K. D., & Davis, D. S. 2008, *A&A*, **478**, 615
- Sparks, W. B., Macchetto, F., & Golombek, D. 1989, *ApJ*, **345**, 153
- Springel, V., Frenk, C. S., & White, S. D. M. 2006, *Nature*, **440**, 1137
- Su, M., Slatyer, T. R., & Finkbeiner, D. P. 2010, *ApJ*, **724**, 1044
- Su, Y., Kraft, R. P., Nulsen, P. E. J., et al. 2019, *AJ*, **158**, 6
- Sugawara, Y., Takizawa, M., Itahana, M., et al. 2017, *PASJ*, **69**, 93
- Sunyaev, R. A. & Zeldovich, Y. B. 1972, *Comments on Astrophysics and Space Physics*, **4**, 173
- Taylor, G. B., Fabian, A. C., & Allen, S. W. 2002, *MNRAS*, **334**, 769
- Taylor, G. B., Sanders, J. S., Fabian, A. C., & Allen, S. W. 2006, *MNRAS*, **365**, 705
- Tittley, E. R. & Henriksen, M. 2001, *ApJ*, **563**, 673
- Tripp, T. M., Bowen, D. V., Sembach, K. R., et al. 2006, in *Astronomical Society of the Pacific Conference Series*, Vol. 348, *Astrophysics in the Far Ultraviolet: Five Years of Discovery with FUSE*, ed. G. Sonneborn, H. W. Moos, & B. G. Andersson, 341

- Tritton, K. P. 1972, *MNRAS*, **158**, 277
- Trussoni, E., Vagnetti, F., Massaglia, S., et al. 1999, *A&A*, **348**, 437
- Tuominen, T., Nevalainen, J., Tempel, E., et al. 2021, *A&A*, **646**, A156
- UK Swift Science Data Centre. 2013, *About the NHtot tool*, <https://www.swift.ac.uk/analysis/nhtot/docs.php> [Accessed: March 2024]
- Unsöld, A. & Baschek, B. 2001, *The New Cosmos*, 5th edn., An Introduction to Astronomy and Astrophysics (Springer-Verlag Berlin Heidelberg)
- Urban, O., Werner, N., Allen, S. W., Simionescu, A., & Mantz, A. 2017, *MNRAS*, **470**, 4583
- Urban, O., Werner, N., Simionescu, A., Allen, S. W., & Böhringer, H. 2011, *MNRAS*, **414**, 2101
- van Weeren, R. J., de Gasperin, F., Akamatsu, H., et al. 2019, *Space Sci. Rev.*, **215**, 16
- Vazza, F., Ettori, S., Roncarelli, M., et al. 2019, *A&A*, **627**, A5
- Vazza, F., Gheller, C., & Brunetti, G. 2010, *A&A*, **513**, A32
- Venturi, T., Morganti, R., Tzioumis, T., & Reynolds, J. 2000, *A&A*, **363**, 84
- Veronica, A., Reiprich, T. H., Pacaud, F., et al. 2024a, *A&A*, **681**, A108
- Veronica, A., Reiprich, T. H., Pacaud, F., et al. 2024b, *arXiv e-prints*, arXiv:2404.04909
- Veronica, A., Su, Y., Biffi, V., et al. 2022, *A&A*, **661**, A46
- Vijayaraghavan, R. & Ricker, P. M. 2013, *MNRAS*, **435**, 2713
- Vikhlinin, A., Forman, W., & Jones, C. 1999, *ApJ*, **525**, 47
- Virtanen, P., Gommers, R., Oliphant, T. E., et al. 2020, *Nature Methods*, **17**, 261
- Voges, W. 1993, *Advances in Space Research*, **13**, 391
- Voit, G. M. 2005, *Reviews of Modern Physics*, **77**, 207
- Vurm, I., Nevalainen, J., Hong, S. E., et al. 2023, *A&A*, **673**, A62
- Walker, S., Simionescu, A., Nagai, D., et al. 2019, *Space Sci. Rev.*, **215**, 7
- Walker, S. A., Fabian, A. C., & Sanders, J. S. 2013a, *MNRAS*, **435**, 3221
- Walker, S. A., Fabian, A. C., Sanders, J. S., Simionescu, A., & Tawara, Y. 2013b, *MNRAS*, **432**, 554
- Walker, S. A., Sanders, J. S., & Fabian, A. C. 2016, *MNRAS*, **461**, 684
- Weisskopf, M. C., Tananbaum, H. D., Van Speybroeck, L. P., & O'Dell, S. L. 2000, in *Society of Photo-Optical Instrumentation Engineers (SPIE) Conference Series*, Vol. 4012, X-Ray Optics, Instruments, and Missions III, ed. J. E. Truemper & B. Aschenbach, 2–16
- Werner, N., Durret, F., Ohashi, T., Schindler, S., & Wiersma, R. P. C. 2008a, *Space Sci. Rev.*, **134**, 337
- Werner, N., Finoguenov, A., Kaastra, J. S., et al. 2008b, *A&A*, **482**, L29

- Werner, N., Urban, O., Simionescu, A., & Allen, S. W. 2013, [Nature](#), 502, 656
- Willingale, R., Starling, R. L. C., Beardmore, A. P., Tanvir, N. R., & O’Brien, P. T. 2013, [MNRAS](#), 431, 394
- Willson, M. A. G. 1970, [MNRAS](#), 151, 1
- Wilms, J., Allen, A., & McCray, R. 2000, [ApJ](#), 542, 914
- Yeung, M. C. H., Freyberg, M. J., Ponti, G., et al. 2023, [A&A](#), 676, A3
- ZuHone, J. & Su, Y. 2022, in Handbook of X-ray and Gamma-ray Astrophysics, 93
- ZuHone, J. A., Markevitch, M., & Johnson, R. E. 2010, [ApJ](#), 717, 908
- ZuHone, J. A., Zavala, J., & Vogelsberger, M. 2019, [ApJ](#), 882, 119
- Zwicky, F. 1933, Helvetica Physica Acta, 6, 110
- Zwicky, F. 1937, [ApJ](#), 86, 217
- Zwicky, F., Herzog, E., Wild, P., Karpowicz, M., & Kowal, C. T. 1961, Catalogue of galaxies and of clusters of galaxies, Vol. I

Appendix A


The eROSITA view of the Abell 3391/95 field: The Northern Clump

The largest infalling structure in the longest known gas filament observed with eROSITA, XMM-Newton, and Chandra

The publication *Veronica et al. A&A (2022), 661, A46* is reproduced below in its original form with permission ©ESO.

The eROSITA view of the Abell 3391/95 field: The Northern Clump

The largest infalling structure in the longest known gas filament observed with eROSITA, XMM-Newton, and Chandra

Angie Veronica¹ , Yuanyuan Su², Veronica Biffi^{5,6,7}, Thomas H. Reiprich¹, Florian Pacaud¹, Paul E. J. Nulsen^{3,13}, Ralph P. Kraft³, Jeremy S. Sanders⁴, Akos Bogdan³, Melih Kara¹², Klaus Dolag⁵, Jürgen Kerp¹, Bärbel S. Koribalski^{9,10}, Thomas Erben¹, Esra Bulbul⁴, Efrain Gatzuz⁴, Vittorio Ghirardini⁴, Andrew M. Hopkins⁸, Ang Liu⁴, Konstantinos Migkas¹, and Tessa Vernstrom¹¹

¹ Argelander-Institut für Astronomie (AIfA), Universität Bonn, Auf dem Hügel 71, 53121 Bonn, Germany
e-mail: averonica@astro.uni-bonn.de

² Physics and Astronomy, University of Kentucky, 505 Rose street, Lexington, KY 40506, USA

³ Center for Astrophysics, Harvard and Smithsonian, 60 Garden Street, Cambridge, MA 02138, USA

⁴ Max-Planck-Institut für extraterrestrische Physik, Gießenbachstraße 1, 85748 Garching, Germany

⁵ Universitaets-Sternwarte Muenchen, Ludwig-Maximilians-Universität München, Scheinerstraße, München, Germany

⁶ INAF – Osservatorio Astronomico di Trieste, via Tiepolo 11, 34143 Trieste, Italy

⁷ IFPU – Institute for Fundamental Physics of the Universe, Via Beirut 2, 34014 Trieste, Italy

⁸ Australian Astronomical Optics, Macquarie University, 105 Delhi Rd, North Ryde, NSW 2113, Australia

⁹ CSIRO Astronomy and Space Science, PO Box 76, Epping, NSW 1710, Australia

¹⁰ Western Sydney University, Locked Bag 1797, Penrith, NSW 2751, Australia

¹¹ CSIRO Astronomy and Space Science, PO Box 1130, Bentley, WA 6102, Australia

¹² Institute for Astroparticle Physics, Karlsruhe Institute of Technology, 76021 Karlsruhe, Germany

¹³ ICRAR, University of Western Australia, 35 Stirling Hwy, Crawley, WA 6009, Australia

Received 28 May 2021 / Accepted 23 August 2021

ABSTRACT

Context. Galaxy clusters grow through mergers and the accretion of substructures along large-scale filaments. Many of the missing baryons in the local Universe may reside in such filaments as the warm-hot intergalactic medium (WHIM).

Aims. SRG/eROSITA performance verification observations revealed that the binary cluster Abell 3391/3395 and the Northern Clump (the MCXC J0621.7-5242 galaxy cluster) are aligning along a cosmic filament in soft X-rays, similarly to what has been seen in simulations before. We aim to understand the dynamical state of the Northern Clump as it enters the atmosphere ($3 \times R_{200}$) of Abell 3391.

Methods. We analyzed joint eROSITA, XMM-Newton, and Chandra observations to probe the morphological, thermal, and chemical properties of the Northern Clump from its center out to a radius of 988 kpc (R_{200}). We utilized the ASKAP/EMU radio data, the DECam optical image, and the Planck y-map to study the influence of the wide-angle tail (WAT) radio source on the Northern Clump's central intracluster medium. Using eROSITA data, we also analyzed the gas properties of the Northern Filament, the region between the virial radii of the Northern Clump and the A3391 cluster. From the Magneticum simulation, we identified an analog of the A3391/95 system along with an infalling group resembling the Northern Clump.

Results. The Northern Clump is a weak cool-core cluster centered on a WAT radio galaxy. The gas temperature over $0.2\text{--}0.5R_{500}$ is $k_B T_{500} = 1.99 \pm 0.04$ keV. We employed the mass-temperature ($M - T$) scaling relation and obtained a mass estimate of $M_{500} = (7.68 \pm 0.43) \times 10^{13} M_\odot$ and $R_{500} = (636 \pm 12)$ kpc. Its X-ray atmosphere has a boxy shape and deviates from spherical symmetry. We identify a southern surface brightness edge, likely caused by subsonic motion relative to the filament gas in the southern direction. At $\sim R_{500}$, the southern atmosphere (infalling head) appears to be 42% hotter than its northern atmosphere. We detect a downstream tail pointing toward the north with a projected length of ~ 318 kpc, plausibly the result of ram pressure stripping. Through a two-temperature fit, we identify a cooler component in the Northern Filament with $k_B T = 0.68^{+0.38}_{-0.64}$ keV and $n_e = 1.99^{+0.88}_{-1.24} \times 10^{-5} \text{ cm}^{-3}$, which are consistent within the expected ranges of WHIM properties. The analog group in the Magneticum simulation is experiencing changes in its gas properties and a shift between the position of the halo center and that of the bound gas, while approaching the main cluster pair.

Conclusions. The Northern Clump is a dynamically active system and far from being relaxed. Its atmosphere is affected by an interaction with the WAT and by gas sloshing or its infall toward Abell 3391 along the filament, consistent with the analog group-size halo in the Magneticum simulation.

Key words. galaxies: clusters: individual: Northern Clump – galaxies: clusters: individual: MCXCJ0621.7-5242 – galaxies: clusters: individual: A3391 – galaxies: clusters: intracluster medium – X-rays: galaxies: clusters

1. Introduction

Clusters of galaxies are formed by the gravitational infall and mergers of smaller structures (Sarazin 2002; Springel et al. 2006; Markevitch & Vikhlinin 2007). They are the high density nodes of the so-called Cosmic Web, connected by cosmic filaments (Bond et al. 1996). These cosmic filaments are of importance, such that they are the passages for matter being accreted onto galaxy clusters (West et al. 1995; Bond et al. 2010), as well as where the warm-hot intergalactic medium (WHIM) can be found (Rost et al. 2021). The large-scale cosmological simulations of a Λ -dominated cold dark matter (Λ CDM) model (Cen & Ostriker 1999; Davé et al. 2001) predict that about 30–40% of the total baryons in the Universe reside in the WHIM, and thus it is believed that the WHIM might be a solution to the missing baryon problem. However, with electron densities falling between $n_e \approx 10^{-6}$ – 10^{-4} cm $^{-3}$ and temperatures in the range of $T = 10^5$ – 10^7 K (Nicastrò et al. 2017), detecting the WHIM is rather difficult (Werner et al. 2008). Bond et al. (1996) predicted that the presence of the filaments are expected to be the strongest between highly clustered and aligned clusters of galaxies. Based on this prediction, it is sensible to conduct the search for the WHIM between a pair of galaxy clusters (e.g., Kull & Böhringer 1999; Werner et al. 2008; Fujita et al. 2008), and also in the outskirts of galaxy clusters (e.g., Reiprich et al. 2013; Bulbul et al. 2016; Nicastrò et al. 2018). The binary galaxy cluster system Abell 3391 and Abell 3395 (A3391/95) is amongst the best candidates to conduct this search.

The A3391/95 system has been observed by numerous instruments of different wavelengths. Earlier studies of the system using ROSAT and ASCA show that the gas from the region between the northern cluster (A3391) and the double-peaked southern cluster (A3395S/N) is consistent with a filament (Tittley & Henriksen 2001). Meanwhile, more recent studies using *XMM-Newton*, *Chandra*, and *Suzaku* show that the properties of the gas are more in agreement with tidally stripped intracluster medium (ICM) gas that originated from A3391 and A3395, indicating an early phase of the cluster merger (Sugawara et al. 2017; Alvarez et al. 2018).

The A3391/95 system is also one of the performance verification (PV) targets of the newly launched German X-ray telescope on board the Spectrum-Roentgen-Gamma (SRG) mission, the extended ROentgen Survey with an Imaging Telescope Array (eROSITA). With large field-of-view (FoV) of ~ 1 degree in diameter, the scan-mode observation, and superior soft X-ray effective area (the effective area of the combined seven eROSITA telescope modules (TMs) is slightly higher than the one of *XMM-Newton* (MOS1+MOS2+pn) in the 0.5–2.0 keV energy band) (Merloni et al. 2012; Predehl et al. 2021), eROSITA allows us to capture the A3391/95 system beyond R_{100} with a good spectral resolution.

In total, four eROSITA PV observations were performed on the A3391/95 system, including three raster scans and one pointed observation. By combining all the available observations, an area of ~ 15 deg 2 is covered. This reveals a breathtaking view of the A3391/95 system that has only been seen in simulations before, such as the discovery of a long continuous filament (~ 15 Mpc) from the projected north toward the south of the A3391/95 system. This indicates that the system is part of a large structure. eROSITA also found that the bridge gas consists of not only the hot gas, which further confirms the tidally stripped originated gas scenario, but also of warm gas from a filament (Reiprich et al. 2021). A detailed eROSITA study focusing on the bridge will be discussed in Ota et al. (in prep.)

Additionally, some clumps that seem to fall into the system have also been discovered, two of which reside in the Northern and the Southern Filaments, namely the Northern Clump¹ (MCXC J0621.7-5242 cluster, Piffaretti et al. 2011 and also referred to as MS 0620.6-5239 cluster, De Grandi et al. 1999; Tittley & Henriksen 2001) and the Little Southern Clump, respectively (Reiprich et al. 2021).

After eROSITA's discovery, follow-up observations were performed by *XMM-Newton* and *Chandra* on the Northern Clump. This biggest infalling clump in the A3391/95 field is a galaxy cluster, located at redshift $z = 0.0511$ (Tritton 1972; Piffaretti et al. 2011). It hosts a Fanaroff-Riley type I (FRI) radio source, PKS 0620-52 (Trussoni et al. 1999; Venturi et al. 2000). This source is associated with the cluster's brightest cluster galaxy (BCG), 2MASX J06214330-5241333 (Brüggen et al. 2021). This source is featured with a pair of asymmetric wide-angle tail (WAT) radio lobes (Morganti et al. 1993; Trussoni et al. 1999; Venturi et al. 2000), with the northeast lobe extending up to $4'$ (240 kpc), while the northwestern lobe up to $2.5'$ (150 kpc) (Brüggen et al. 2021).

In this work, we investigate the morphology, thermal, and chemical properties of the Northern Clump utilizing all available eROSITA, *XMM-Newton*, and *Chandra* observations of the cluster. The cluster core is probed further with the help of the ASKAP/EMU radio data (Norris et al. 2011), the *Planck*-y map, and the DECam optical data. Furthermore, we identify an infalling galaxy group, resembling the observed Northern Clump, in the analog A3391/95 system from the Magneticum Simulation (Biffi et al. 2022) and discuss its properties in comparison to observations to support their interpretation.

This paper is organized as follows: in Sect. 2, we describe the observations, the data reduction steps, and the analysis strategy. In Sect. 3, we present and discuss the analysis results. In Sect. 4, we provide some insights about the analog A3391/95 system and the infalling group from the Magneticum Simulation. In Sect. 5, we summarize our findings and conclude the results.

Unless stated otherwise, all uncertainties are at the 68.3% confidence interval. The assumed cosmology in this work is a flat Λ CDM cosmology, where $\Omega_m = 0.3$, $\Omega_\Lambda = 0.7$, and $H_0 = 70$ km s $^{-1}$ Mpc $^{-1}$. At the Northern Clump redshift $z = 0.0511$, $1''$ corresponds to 0.998 kpc.

2. Data reduction and analysis

We list all eROSITA, *XMM-Newton*, and *Chandra* observations used for imaging and spectral analysis in Table 1.

2.1. eROSITA

The A3391/95 PV observations are listed in Table 1. In this work we used eROSITA data processing of configuration c001. The data reduction of all 16 eROSITA data sets were realized using the extended Science Analysis Software (eSASS, Brunner et al. 2022) version eSASSUsers_201009. The eROSITA data reduction and image correction steps are described in great detail in Sect. 2.1 of Reiprich et al. (2021). The image correction includes particle-induced background (PIB) subtraction, exposure correction, and Galactic absorption correction across the FoV.

¹ As the extended objects detected in the A3391/95 field are called “clumps”, we refer this specific galaxy cluster found in the north of the main system as the Northern Clump.

Table 1. All observations of the Northern Clump used in this work.

Observing date	ObsID	Exposure ^(*) [ks]	RA (J2000)	Dec (J2000)
eROSITA				
October 2019	300005 (scan)	55	06h 26m 49.44s	−54d 04′ 19.20″
October 2019	300006 (scan)	54	06h 26m 49.44s	−54d 04′ 19.20″
October 2019	300016 (scan)	58	06h 26m 49.44s	−54d 04′ 19.20″
October 2019	300014 (pointed)	35	06h 26m 49.44s	−54d 04′ 19.20″
XMM-Newton				
March 2020	0852980601	73, 77, 65	06h 21m 42.55s	−52d 41′ 47.4″
Chandra				
October 2010	11499	20	06h 21m 43.30s	−52d 41′ 33.3″
April 2020	22723	30	06h 21m 25.05s	−52d 43′ 09.9″
May 2020	22724	30	06h 21m 42.53s	−52d 45′ 24.7″
April 2020	22725	30	06h 21m 22.30s	−52d 42′ 10.7″

Notes. ^(*)The exposure times listed for eROSITA are the average filtered exposure time across the available TMs of each observation. The listed *XMM-Newton* exposure times are the values after the SPF filtering for MOS1, MOS2, and pn cameras, respectively. The exposure times listed for *Chandra* are also the filtered exposure time.

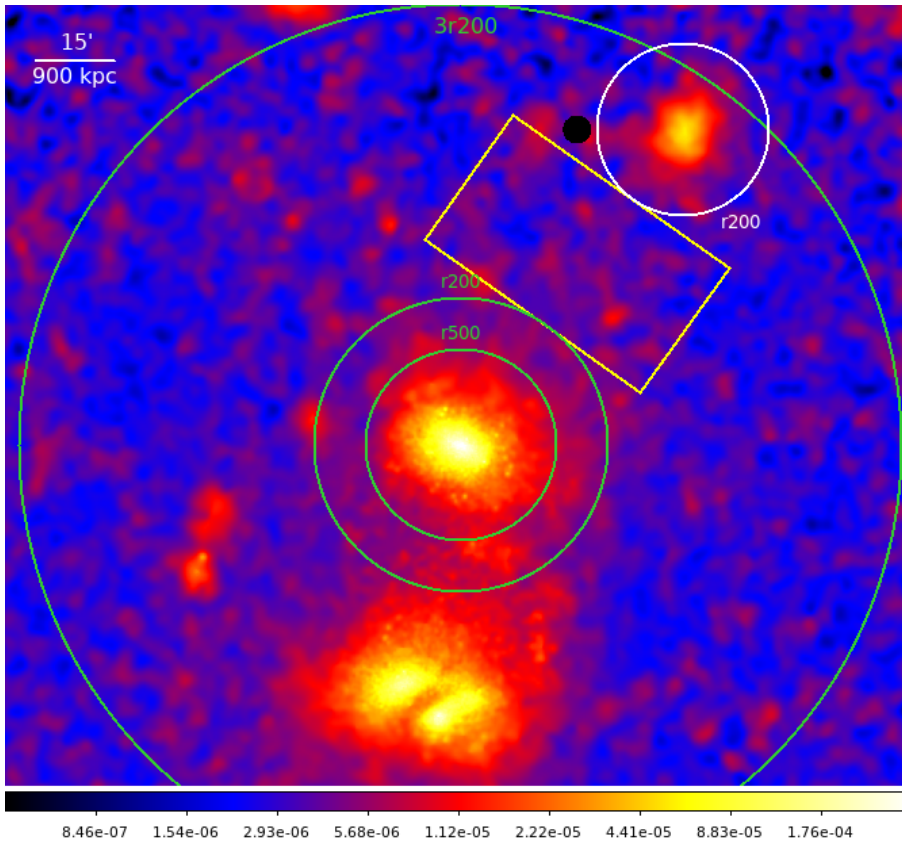


Fig. 1. eROSITA particle-induced background subtracted, exposure corrected, absorption corrected image in the energy band 0.5–2.0 keV, zoomed-in to A3391 and the Northern Clump region. The image has been adaptively-smoothed with S/N set to 15. The point sources have been removed and refilled with their surrounding background values. The green circles depict some characteristic radii of A3391, while the white circle depicts the R_{200} of the Northern Clump. The yellow box marks the region used for the spectral analysis of the Northern Filament.

2.1.1. Imaging analysis

The energy band for the imaging analysis was restricted to 0.5–2 keV, with the lower energy limit used for the telescope modules (TMs) with on-chip filter (TM1, 2, 3, 4, 6; the combination of these TMs is referred to as TM8) set to 0.5 keV, while for the TMs without on-chip filter (TM5 and 7; the combination of these TMs is referred to as TM9) it was set to 0.8 keV due to the optical light leak contamination (Predehl et al. 2021). The count rates of the final combined image correspond to an

effective area given by one TM with on-chip filter in the energy band 0.5–2 keV. The final PIB subtracted, exposure corrected, and Galactic absorption corrected image is shown in Fig. 1. The image has been adaptively-smoothed to enhance low surface brightness emission and large scale features, with signal-to-noise ratio (S/N) was set to 15. We note that the Northern Clump appears boxy, which could be the result of ram-pressure stripping as it interacts with the atmosphere of the A3391 cluster or the filament, or both. In this work, we focus on studying the properties of the Northern Clump out to its R_{200} , while a more

detailed study about the filaments observed by eROSITA around the A3391/95 system will be carried out by Veronica et al. (in prep.).

Thanks to the large eROSITA FoV and the SRG scan mode, in which most of the observations were taken, the cosmic X-ray background (CXB) could be modeled from an annulus with an inner and outer radius of 25' and 35', respectively. The annulus is centered at the X-ray emission peak of the cluster determined by *Chandra* at $(\alpha, \delta) = (6 : 21 : 43.344, -52 : 41 : 33.0)$. Since the CXB region is at 1.5–2.1 R_{200} ², it ensures minimum cluster emission in the CXB region. This region also stays beyond R_{100} of A3391. Within the 13.5' radius, we utilized the *XMM-Newton* point source catalog and beyond this radius we used eROSITA detected point source catalog, which was generated following the same procedure as *XMM-Newton* (see Sect. 2.2). The point sources are excluded both in imaging and spectral analyses.

2.1.2. Spectral analysis

All eROSITA spectra, the Ancillary Response Files (ARFs), and the Response Matrix Files (RMFs) for the source and background region were extracted using the eSASS task `srctool`. Unless stated otherwise, the spectral fitting for all eROSITA spectra was performed with XSPEC (Arnaud 1996) version: 12.10.1.

We use the third eROSITA scan observation (ObsID: 300016), where all seven eROSITA TMs are available, for the spectral analysis of the Northern Clump. Due to the contamination by the nearby bright star, Canopus, some portions of the data were rejected from the analysis (see Reiprich et al. 2021), which further reduces the number of photons for the Northern Clump. To ensure enough photon counts, the only eROSITA spectral analysis done for the Northern Clump in this work is to constrain the $k_B T_{500}$ from an annulus with inner and outer radii of 2.4' and 6' (corresponding to 0.2–0.5 R_{500} , see Sect. 2.2.2). The same definition of CXB region as in the imaging analysis was used.

Spectral analysis was also performed for the filament region between the R_{200} of the Northern Clump and the A3391 cluster, the Northern Filament. The filament region was chosen as a box centered at $(\alpha, \delta) = (6 : 23 : 54.654, -53 : 05 : 16.637)$ with height and width of 29' and 50', respectively. The configuration of the Northern Filament box is shown in Fig. 1 (yellow box). The CXB region for this analysis is a circular region with a radius of 30' centered at $(\alpha, \delta) = (6 : 18 : 18.275, -54 : 33 : 37.880)$. The average hydrogen column density at the box and its corresponding CXB region is $N_H = 0.048 \times 10^{22}$ atoms cm^{-2} .

We followed the X-ray spectral fitting procedure described in Ghirardini et al. (2021) and Liu et al. (2022) with some modifications for consistency with the *XMM-Newton* and *Chandra* spectral fitting. The total eROSITA model includes the absorbed thermal emission for the cluster, which is modeled using `phabs` × `apec`, two absorbed thermal models for the Milky Way Halo (MWH) and the Local Group (LG), an unabsorbed thermal model for the Local Hot Bubble (LHB), and an absorbed power-law for the unresolved AGN. The parameters of the eROSITA CXB components are listed in Table 2. The instrumental background was modeled based on the results of the eROSITA Filter Wheel Closed (FWC) data analysis. The normalizations of the instrumental background components

Table 2. Information of the parameters and their starting fitting values of the eROSITA CXB components for the Northern Clump R_{500} analysis.

Component	Parameter	Value	Comment
<i>phabs</i>	$N_H^{(\dagger)}$	0.04	Fix
<i>apec</i> (LHB)	$k_B T$ [keV]	0.099	Fix
	$Z [Z_\odot]$	1	Fix
	z	0	Fix
	$\text{norm}^{(*)}$	1.0×10^{-8}	Vary
<i>apec</i> (MWH)	$k_B T$ [keV]	0.225	fix
	$Z [Z_\odot]$	1	Fix
	z	0	Fix
	$\text{norm}^{(*)}$	1.0×10^{-8}	Vary
<i>apec</i> (LG)	$k_B T$ [keV]	0.5	vary
	$Z [Z_\odot]$	1	Fix
	z	0	Fix
	$\text{norm}^{(*)}$	1.0×10^{-8}	Vary
<i>pow</i> (unresolved AGN)	Γ	1.4	Fix
	$\text{norm}^{(**)}$	3.4×10^{-7}	Vary

Notes. ^(†) $[10^{22}$ atoms $\text{cm}^{-2}]$, ^(*) $[\text{cm}^{-5} \text{ arcmin}^{-2}]$, ^(**) $[\text{photons keV}^{-1} \text{ cm}^2 \text{ s}^{-1} \text{ arcmin}^{-2} \text{ at 1 keV}]$.

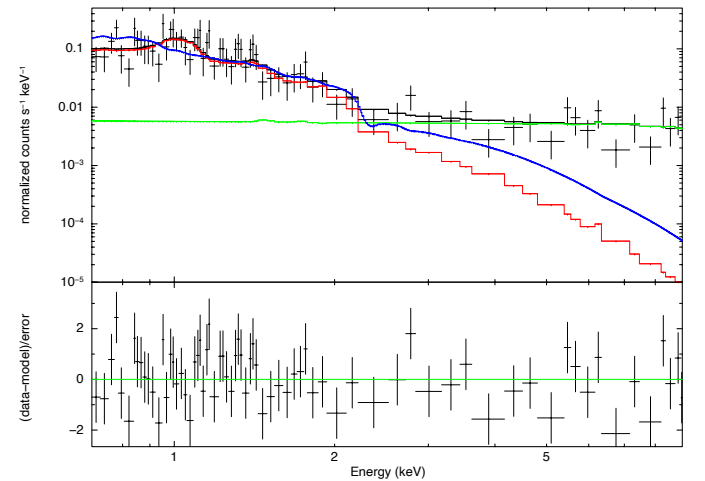


Fig. 2. eROSITA spectrum of the Northern Clump from an annulus of 2.4–6', fitted in the energy range 0.7–9.0 keV. The spectra and the corresponding response files of TM3 and TM4 are merged for a better visualization. The black points are the Northern Clump spectral data, while the black, red, green, and blue lines represent the total model, the cluster model, the instrumental background model, and the CXB model, respectively.

were thawed during the fit. The fitting was restricted to the 0.7–9.0 keV band, with the lower energy limit set to 0.8 keV for TM5 and TM7 and to 0.7 keV for the other TMs. Source and CXB spectra for the individual TMs were fitted simultaneously. An example of eROSITA spectrum and its fitted model is shown in Fig. 2.

The solar abundance table from Asplund et al. (2009) was adopted and the C-statistic (Cash 1979) was implemented.

2.2. XMM-Newton

The data reduction steps of the *XMM-Newton* data sets of the Northern Clump observation were realized using HEASoft

² All the cluster radii in this work are calculated using the relations stated in Reiprich et al. (2013), e.g., $r_{500} \approx 0.65r_{200}$, $r_{100} \approx 1.36r_{200}$, and $r_{2500} \approx 0.28r_{200}$.

version 6.25 and the Science Analysis Software (SAS) version 18.0.0 (`xmmsas_20190531_1155`). For all *XMM-Newton* instruments, we filtered out the time intervals contaminated by soft proton flares (SPF) (e.g., [De Luca & Molendi 2004](#); [Kuntz & Snowden 2008](#); [Snowden et al. 2008](#)). The procedure started by constructing the light curve in the energy band 0.3–10.0 keV from the entire FoV. The mean value of the counts was estimated by fitting a Poisson law to the counts histogram. Then a $\pm 3\sigma$ clipping was applied, such that any time intervals above and below the 3σ threshold were considered contaminated by the SPF and rejected from further steps. Light curves from each of *XMM-Newton*'s detectors are shown in Appendix A. To check whether there was still any persisting soft proton background in our data, we calculated the ratio of count rates within the FoV (IN) to those of the unexposed region of the MOS detectors (OUT) ([De Luca & Molendi 2004](#)). The obtained IN/OUT ratios for each detector are around unity, which implies that the retained data are not contaminated by soft protons. After this SPF filtering, we are left with ~ 73 , ~ 77 , and ~ 65 ks for MOS1, MOS2, and pn, respectively.

We checked for “anomalous state” in the detectors’ chips. This is usually indicated by a low hardness ratio and high total background rate ([Kuntz & Snowden 2008](#)). Since, in such cases, there is not a robust method yet to model the spectral distribution of the low energy background, any CCD affected by this anomalous state was rejected in further analysis. This resulted in the conservative exclusion of MOS1-CCD4 and MOS2-CCD5. In addition, MOS1-CCD6 and MOS1-CCD3 were not operational during this observation, due to the previous micro-meteorite impacts ([ESA: XMM-Newton SOC 2020](#)).

Utilizing the FWC data, the quiescent particle background (QPB) ([Kuntz & Snowden 2008](#)) was modeled and then subtracted from the observation. We followed the procedure described in [Ramos-Ceja et al. \(2019\)](#). First, the cleaned observation data were matched with the suitable FWC data and then this FWC template was re-projected to the sky position. Afterwards, rescaling factors were calculated to renormalize the QPB template to a level comparable with that of the observation. This renormalization was calculated separately for each MOS CCD and pn quadrant based on their individual count rates in unexposed regions. The renormalization of the central MOS CCD chips that do not have any unexposed regions relies on the unexposed regions of the best correlated surrounding CCD chips as determined by [Kuntz & Snowden \(2008\)](#). For spectroscopic analysis, global renormalization factors were calculated in the energy bands 2.5–5.0 keV and 8.0–9.0 keV for MOS cameras, and 2.5–5.0 keV for pn camera. This energy selection aims to include the bands where the instrumental background would have the most impact on the spectral analysis, while avoiding the fluorescence X-ray (FX) emission lines present for the EPIC cameras. For imaging analysis, on the other hand, the template renormalization process relies on the exact same band that was used for the science analysis.

Another contamination when studying the ICM gas might come from the point sources that are distributed across the FoV. Therefore, it is required to detect and excise the point sources, for example, in the calculation of surface brightness profiles and spectral analysis. To detect the point sources in the observation, we implemented the procedure described in [Pacaud et al. \(2006\)](#) and [Ramos-Ceja et al. \(2019\)](#). Firstly, wavelet filtering was applied on the combined detector image in the soft energy band (0.5–2.0 keV). Afterwards, an automatic detection of point sources and catalog generation were performed on the wavelet-filtered image by the Source Extractor software (SExtractor,

[Bertin & Arnouts 1996](#)). Lastly, we carried out a manual inspection on the soft and hard energy band images (2.0–10.0 keV) to list any point sources that were missed by the automatic detection. To generate a surface brightness image, the areas where the point sources were removed were refilled with random background photons, that is the ghosting procedure. The ghosted surface brightness images were used only for visual inspection.

2.2.1. Imaging analysis

We constructed *XMM-Newton*'s X-ray surface brightness (S_X) profiles using the combined photon image and exposure map from the *XMM-Newton* detectors (MOS1, MOS2, and pn) in the energy band 0.5–2.0 keV. Since the ghosting procedure used for generating surface brightness images does not represent the exact true counts from the ICM gas, we preferred to mask these point source regions in the calculation of the S_X profile. The first S_X profile was calculated from 60 concentric annuli placed around the *Chandra* X-ray emission peak at $(\alpha, \delta) = (6 : 21 : 43.344, -52 : 41 : 33.0)$. With $10''$ increments between each annulus, the whole arrangement covers radial distance of $10'$ from the center. While the QPB was subtracted from the data, the CXB was estimated from an annulus with an inner radius of $12'$ and an outer radius of $13.25'$, respectively. Then, the estimated S_X from this background region was subtracted from the source regions.

A second S_X profile was also constructed. The setup consists of 45 concentric box-shaped “annuli” centered at the same peak coordinates. Between each annulus there is a $20''$ width increment. This implies that the width of each box-shaped annulus corresponds to the diameter of each circular annulus. The half-width of the outermost box annulus is $7.5'$. The setup was angled at 173° , which was chosen visually to follow the shape of the Northern Clump. The same X-ray background region as in the circular annuli setup was used. To investigate, whether the box-iness could be an artifact originating from the MOS detectors’ central chips, a S_X profile from pn-only data and using the box annuli setup was calculated as well.

We fit each of the setups with a single β -model ([Cavaliere & Fusco-Femiano 1976](#)), which is written as

$$S_X(R) = S_X(0) \left(1 + \frac{R^2}{r_c^2} \right)^{-3\beta + \frac{1}{2}}, \quad (1)$$

where R is the projected distance from the center, $S_X(0)$ is the normalization factor, r_c is the estimated core radius, and β is the surface brightness slope.

To better address the features in any particular direction, the S_X profiles in the projected south, west, northwest, north, northeast, and east directions were constructed, as well. For these sectorized S_X profiles, all *XMM-Newton* detectors were employed in both circular and box annuli setups. The configuration of the sectors is displayed in Fig. 3.

2.2.2. Spectral analysis

Unless stated otherwise, the spectral fitting for all *XMM-Newton* spectra was performed with XSPEC ([Arnaud 1996](#)) version: 12.10.1 using the following model,

$$\begin{aligned} \text{Model}_{\text{XMM}} = & \text{constant} \times (\text{apec}_1 + \text{phabs} \times (\text{apec}_2 \\ & + \text{powerlaw}) + \text{gauss}_1 + \text{gauss}_2 + \text{gauss}_3 \\ & + \text{gauss}_4 + \text{gauss}_5) + \text{phabs} \times \text{apec}_3, \end{aligned} \quad (2)$$

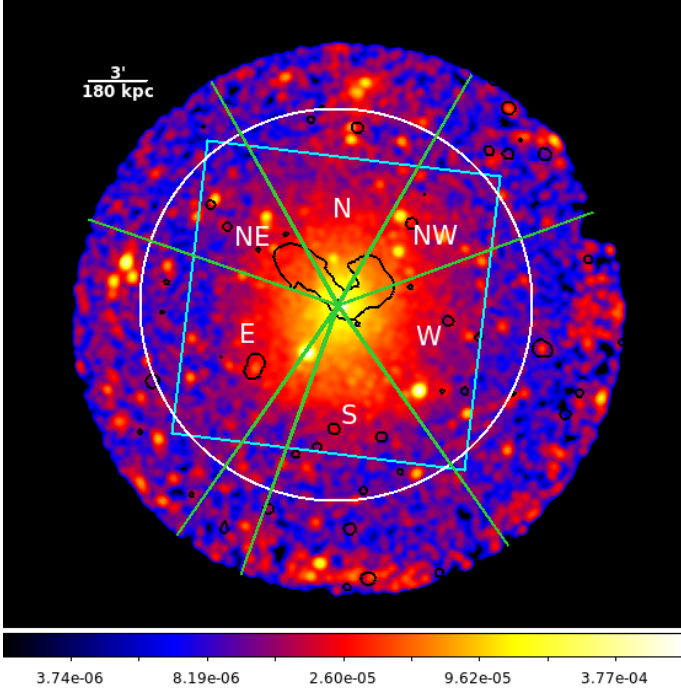


Fig. 3. *XMM-Newton* count rate image of the Northern Clump in the energy band 0.5–2.0 keV, overlaid with the ASKAP/EMU radio contour (black). The anomalous CCD chips are removed and the QPB is subtracted from the image. The sectors are south (S), west (W), northwest (NW), north (N), northeast (NE), and east (E). The white circle and cyan square depict the outermost annuli of corresponding setups. The radius of the circle is 10' and the half-width of the square is 7.5'. Gaussian smoothing with kernel radius of 7 pixels is applied to the image.

where the first term consists of the CXB and *XMM-Newton*'s known instrumental lines, scaled to the areas of the source regions (constant, specified in units of arcmin²). The absorption parametrized by the hydrogen column density, N_{H} , along the line of sight is represented by *phabs*. The N_{H} values used in this work are taken from the A3391/95 total N_{H} map described in Sect. 2.5 of Reiprich et al. (2021). The X-ray emission components to account for the LHB and the MWH are represented by *apec*₁ and *apec*₂, respectively. The power-law component, *powerlaw*, is to account for the unresolved AGN. The information regarding the CXB components and their starting fitting parameter values are listed in Table 3. Since the FX emission lines of the *XMM-Newton* cameras are not convoluted in the ARF, we modeled the lines with the other background components as the *gauss*_i's. The modeled FX lines include the Al-K_α at 1.48 keV (for MOS and pn cameras), Si-K_α at 1.74 keV (MOS cameras), Ni-K_α at 7.47 keV (pn camera), Cu-K_α at 8.04 keV (pn camera), and Zn-K_α at 8.63 keV (pn camera), respectively. The second term, *phabs* × *apec*₃, represents the absorbed cluster emission from the source region. The temperature $k_{\text{B}}T$, metallicity Z , and normalization norm of this cluster emission component were left to vary and linked across the detectors.

The *apec*'s parameter norm is defined as

$$\text{norm} = \frac{10^{-14}}{4\pi[D_{\text{A}}(1+z)]^2} \int n_e N_{\text{H}} dV, \quad (3)$$

where D_{A} is the angular diameter distance to the source in the unit of cm, while n_e and N_{H} are the electron and hydrogen densities in the unit of cm⁻³, respectively.

Table 3. Information of the parameters and their starting fitting values of the *XMM-Newton* CXB components.

Component	Parameter	Value	Comment
<i>phabs</i>	$N_{\text{H}}^{(\dagger)}$	0.046	Fix
<i>apec</i> ₁ (LHB)	$k_{\text{B}}T$ [keV]	0.099	Fix
	Z [Z_{\odot}]	1	Fix
	z	0	Fix
	norm ^(*)	1.7×10^{-6}	Vary
<i>apec</i> ₂ (MWH)	$k_{\text{B}}T$ [keV]	0.225	Fix
	Z [Z_{\odot}]	1	Fix
	z	0	Fix
	norm ^(*)	7.3×10^{-7}	Vary
<i>pow</i>	Γ	1.4	Fix
(unresolved AGN)	norm ^(**)	5×10^{-7}	Vary

Notes. ^(†)[10²² atoms cm⁻²], ^(*)[cm⁻⁵ arcmin⁻²], ^(**)[photons keV⁻¹ cm⁻² s⁻¹ arcmin⁻² at 1 keV].

To ensure a cluster-emission-free background region, the ROSAT All-Sky Survey (RASS) data were utilized to constrain all of the sky background components, in particular the MWH as well as CXB normalization. The RASS data were extracted using the X-ray background tool³. The specified background region is an annulus centered at the *Chandra* center, with an inner radius of 0.58° and an outer radius of 0.9°. To avoid having cluster emission from A3391, we manually removed some of the RASS background region that is within R_{100} of the A3391 cluster. This reduces the number of detected pixels from 38 to 34.

The variety of overlap area between each annulus and each individual camera and CCD combination can result in some very low S/N spectra being extracted, for which a background model can not always be robustly constrained. For this reason, we opted to combine the spectra of all CCDs for a given annulus, and statistically subtract the rescaled FWC spectrum rather than modeling their spectra. The co-addition of rescaled spectra for the different CCDs implies that our background spectra no longer follow Poisson statistics and therefore we used the χ^2 -statistic for parameter estimation, after ensuring that each bin contains enough photons (>25). Additionally, since we use the RASS background, which is Gaussian data, to estimate the CXB normalizations, the choice is believed to be sensible. However, we also performed several tests using pgstat statistic from XSPEC, where the source data were treated as Poisson data (C-statistic) and the background as Gaussian. The resulting cluster parameters of these tests are always consistent within the 1 σ error bars of the χ^2 -statistic fitting results. Hence, the choice of the used statistics for *XMM-Newton* spectral fitting would not change any main conclusions. We present the results of the pgstat tests in Fig. D.1. To minimize the effect of the detector noise in the lower energy, photons with $E < 0.7$ keV were ignored. The solar abundance table from Asplund et al. (2009) was adopted.

We determined the $k_{\text{B}}T_{500}$ in order to calculate the M_{500} , consequently the R_{500} . We note that $k_{\text{B}}T_{500}$ was calculated through an iterative procedure, such that we extracted and fit spectra from an annulus centered at the *Chandra* center, varying the inner and outer radii until they correspond roughly to the 0.2–0.5 R_{500} cluster region. Based on this, we obtained $k_{\text{B}}T_{500} = 1.99 \pm 0.04$ keV from an annulus with inner and outer

³ HEASARC: X-Ray Background Tool

radii of $2.4'$ and $6.0'$, respectively. We input this value into the mass-temperature ($M - T$) scaling relation by [Lovisari et al. \(2015\)](#),

$$\log(M/C_1) = a \cdot \log(T/C_2) + b, \quad (4)$$

where $a = 1.65 \pm 0.07$, $b = 0.19 \pm 0.02$, $C_1 = 5 \times 10^{13} h_{70}^{-1} M_{\odot}$, and $C_2 = 2.0$ keV. Assuming spherical symmetry and taking 500 times the critical density of the Universe at the Northern Clump redshift as $\rho_{500}(z = 0.0511) = 4.82 \times 10^{-27} \text{ g cm}^{-3}$, we obtain $M_{500} = (7.68 \pm 0.43) \times 10^{13} M_{\odot}$ and $R_{500} = (10.62 \pm 0.20)' \approx (636.03 \pm 12.03) \text{ kpc}$. These values are 19 and 7% lower than the reported values in [Piffaretti et al. \(2011\)](#) ($M_{500} = 9.47 \times 10^{13} M_{\odot}$ and $R_{500} = 682 \text{ kpc}$), which are determined using the $L - M$ relation, instead.

We also analyzed the spectra in three different directions of the cluster, such as the south, west, and north with position angle (PA) from 250° to 305° , 20° to 305° , and 70° to 100° , respectively. At larger radii, i.e., $4\text{--}12.5'$, due to the removed MOS1-CCD chips we used pn-only spectra in the north, and MOS2+pn spectra in the south and west.

We always keep the first bin as a full annulus, instead of a sector in any specific directions. We conducted a more detailed analysis to take into account the emission originated from the AGN of the BCG, such that we implemented three different fitting methods for this particular bin. The first method is to mask the AGN with a circle of $15''$ radius. This is the method that is implemented to the central bin during the simultaneous fitting described above. The second method involves constraining the AGN photon index and normalization from *Chandra* observation. Here, the masking was lifted out. Since *XMM-Newton* and *Chandra* observations of the Northern Clump were performed almost simultaneously, little to no temporal variation from the AGN can be expected (e.g., [Maughan & Reiprich 2019](#)). The method and the resulting AGN parameter values from the spectral fitting are discussed in Sect. 2.3.3. We froze *Chandra*'s parameter values during the *XMM-Newton* spectral fitting of the first bin. Lastly, to account for the expected multi-temperature structure in this region, we performed a two-temperature structure fit in addition to the AGN component. Due to the statistics, the normalization and the metallicity of the multi-temperature components were linked, while the second temperature were set to be half of the first.

2.3. Chandra

We analyzed a total of 110 ks *Chandra* observations on the Northern Clump as listed in Table 1, including three ACIS-I observations taken in 2020 and one ACIS-S observation in 2010. CIAO 4.12 and CALDB 4.9.3 were used for the *Chandra* data reduction. All the observations were reprocessed from level 1 events using the CIAO tool `chandra_repro` to guarantee the latest and consistent calibrations. Readout artifacts from the central bright AGN were removed from the reprocessed events using `acisreadcorr`. We filtered background flares beyond 3σ using the light curve filtering script `lc_clean`; clean exposure times are listed in Table 1. We combined all the observations to resolve faint point sources. The *Chandra* PSF varies significantly across the FoV. For each observation, we produced a PSF map for an energy of 2.3 keV and an enclosed count fraction of 0.393. We obtain an exposure-time weighted average PSF map from these four observations. Point sources were detected in a $0.3\text{--}7.0$ keV mosaic image with `wavdetect`, supplied with this exposure-time weighted PSF map. The detection

threshold was set to 10^{-6} . The scales ranged from 1 to 8 pixels, increasing in steps of a factor of 2. We adopted the blank sky background for the imaging and spectral analyses. A compatible blank sky background file was customized to each of the event file using the `blanksky` script. As shown in Sect. 3.2, the surface brightness of our blank sky background is consistent with the sum of the stowed background and the astrophysical background.

2.3.1. Imaging analysis

We only include the three ACIS-I observations taken in 2020 for the imaging analysis due to the different backgrounds, responses, FoVs, and calibrations between these observations and the ACIS-S observation taken in 2010. All the observations were reprojected to a common tangent point using `reproject_obs`. Images in the $0.5\text{--}2.0$ keV energy band and their exposure maps were produced using `flux_obs`. Point sources identified by `wavdetect` were replaced with the surface brightness from the immediate surrounding regions using `dmfilth`. Scaled `blanksky` images were produced using `blanksky_image`. A final background subtracted and exposure corrected mosaic image of the Northern Clump is shown in Fig. 4.

2.3.2. Spectral analysis

We include all four existing *Chandra* observations for the spectral analysis. Spectra were extracted using `specextract` from point-source excised event files for regions of consecutive sectional annuli in the south and west directions, ranging from $\delta r = 0.5'$ at the cluster center to $\delta r = 1.67'$ at $r = 6.68'$. The corresponding response files and matrices were produced for each spectrum using `specextract`. `Blanksky` background normalized to the count rate in the $9.5\text{--}12.0$ keV energy band of each observation was applied. All the spectra were grouped to have at least one count per energy bin and restricted to the $0.7\text{--}7.0$ keV range. The spectral fitting was performed with `PyXspec 2.0.3`. Our spectral model takes the form of `phabs × apec`, representing a foreground-absorbed thermal component. The total N_{H} value of $4 \times 10^{20} \text{ cm}^{-2}$ is taken from the A3391/95 total N_{H} map described in [Reiprich et al. \(2021\)](#). C-statistics ([Cash 1979](#)) was used for parameter estimation. The solar abundance table of [Asplund et al. \(2009\)](#) was adopted. Due to low photon counts, we found it necessary to fix the metallicity at $0.3 Z_{\odot}$.

2.3.3. Central AGN

We characterize the property of the central AGN detected at equatorial coordinates of $(\alpha, \delta) = (6 : 21 : 43.304, -52 : 41 : 33.153)$. Spectra of the central $r = 2''$ were extracted from clean events files with point sources included. Spectra from the surrounding $r = 2\text{--}5''$ were used as the local background. We fit the spectrum to a simple absorbed power-law model and fixed the column density $N_{\text{H}} = 4 \times 10^{20} \text{ cm}^{-2}$. We obtain a steep photon index of 2.5 ± 0.07 and a best-fit luminosity of $5.7 \pm 0.3 \times 10^{41} \text{ erg s}^{-1}$ in the $2.0\text{--}10.0$ keV when using the observation taken in 2020, which is used for the AGN modelling in the *XMM-Newton* analysis.

2.4. ASKAP/EMU, DECAM, and Planck data

We use the ASKAP/EMU radio image and DECAM images, as well as the *Planck* γ -map for overlays generated as described in detail in [Reiprich et al. \(2021\)](#).

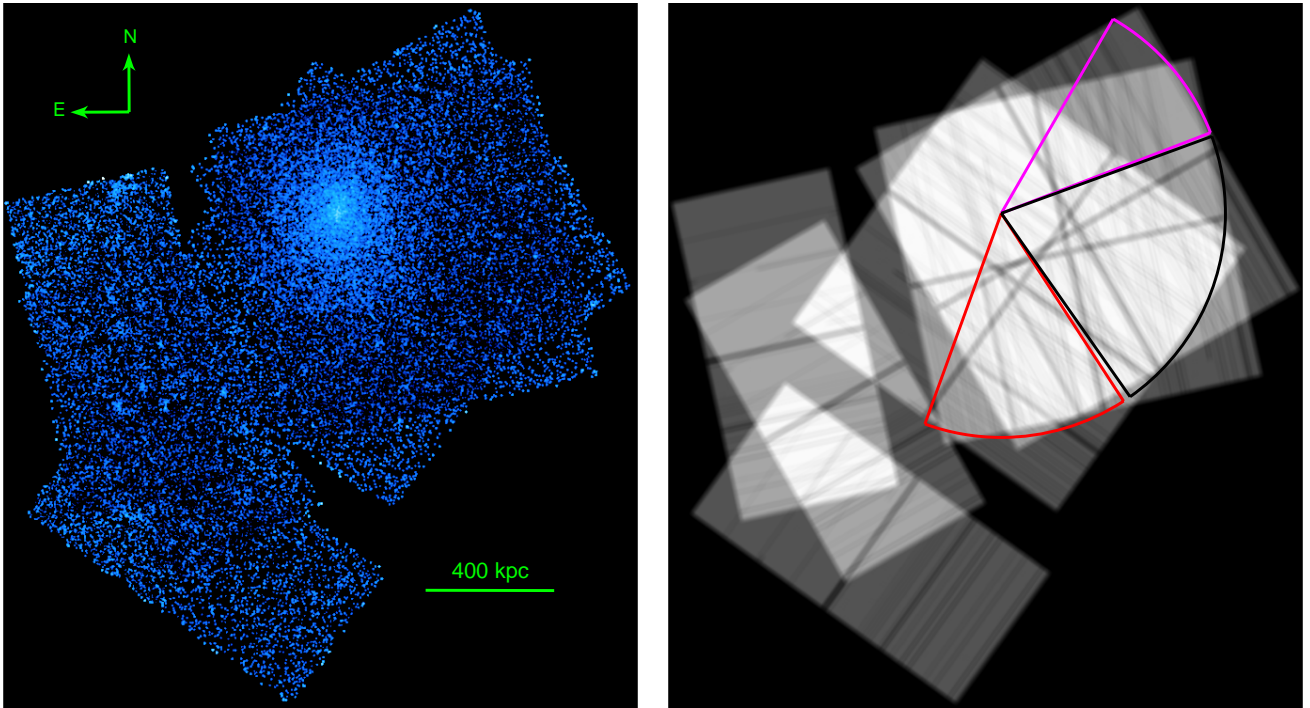


Fig. 4. *Left:* mosaic *Chandra* ACIS-I image of the northern clump. The image is blanksky background subtracted, exposure corrected, and point-source refilled. *Right:* mosaic exposure map corresponding to the left image. Red, black, and magenta pie regions represent the regions used to derive the surface brightness profiles of the south, west, and northwest directions as shown in Fig. 9.

3. Results

3.1. Boxiness, tail, and X-ray cavity in images

As observed in the clean images shown in Fig. B.1, the main body of the Northern Clump is well-embedded in the central chips of MOS1 (top left) and MOS2 (top right) cameras. A question arises, whether the boxyness of the system is intrinsic to the cluster itself, or rather an artifact caused by the central MOS chips. The boxy shape of the cluster can still be recognized in the pn image (bottom left), although not as prominent. To further investigate this question, we generated exposure corrected images, as well as adaptively-smoothed images using MOS1+2+pn data and pn-only data, where the latter should not be affected by the CCD chips placement. The adaptive smoothing procedure was realized using the SAS task, `asmooth`, `smoothstyle='adaptive'`. We set the S/N of the adaptive smoothing to 15. Through adaptive smoothing we also aim to enhance any soft emission, especially in the cluster outskirts. The resulting images are displayed in Fig. 5. We observe similarity in the morphology of the cluster in the two types of images, such that the boxy shape and indication of tail-like emission projected northward.

We present a composite X-ray+radio+optical image in Fig. 6 (right), focusing on the central region of the Northern Clump. We utilized the *XMM-Newton* count rate image in soft band (blue color and white contour), the ASKAP/EMU radio image (red color and yellow contour), and DECam Sloan g-band image (green). The denser X-ray emission of the Northern Clump shows an asymmetrical morphology and has a sharp edge pointing at the projected southwest direction – towards the A3391 center. We notice that the opening angle of the WAT radio source indicates movement towards the south. While looking at the bent direction of both radio lobes towards the northeast, the

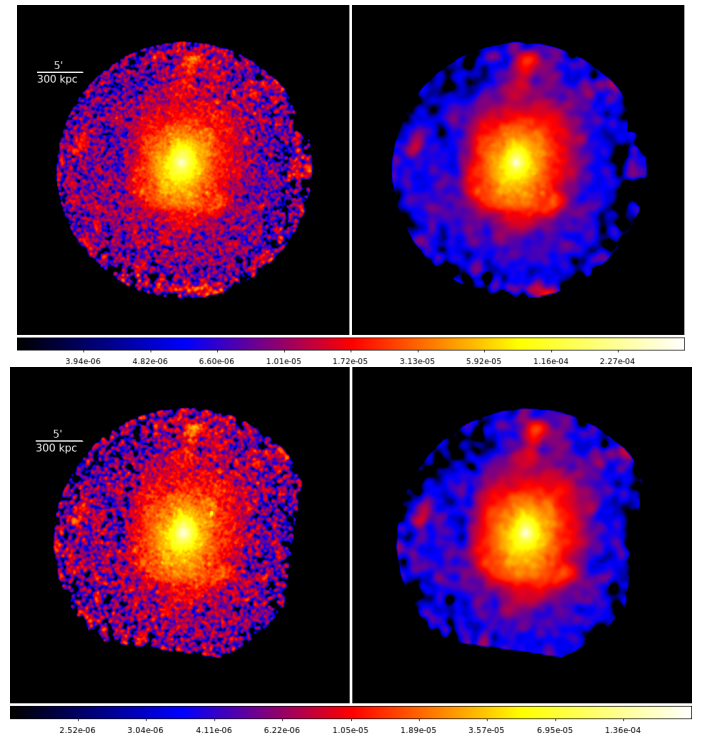


Fig. 5. *XMM-Newton* surface brightness images (*left*) and adaptively-smoothed images (*right*) in the energy band 0.5–2 keV. The S/N of the adaptively-smoothed images is set to 15. *Top:* MOS1+2+pn combined. *Bottom:* pn-only.

central radio source seems to move towards the southwest. We speculate that the radio lobes might have “escaped” from hot gas confinement and the change in direction is due to motion

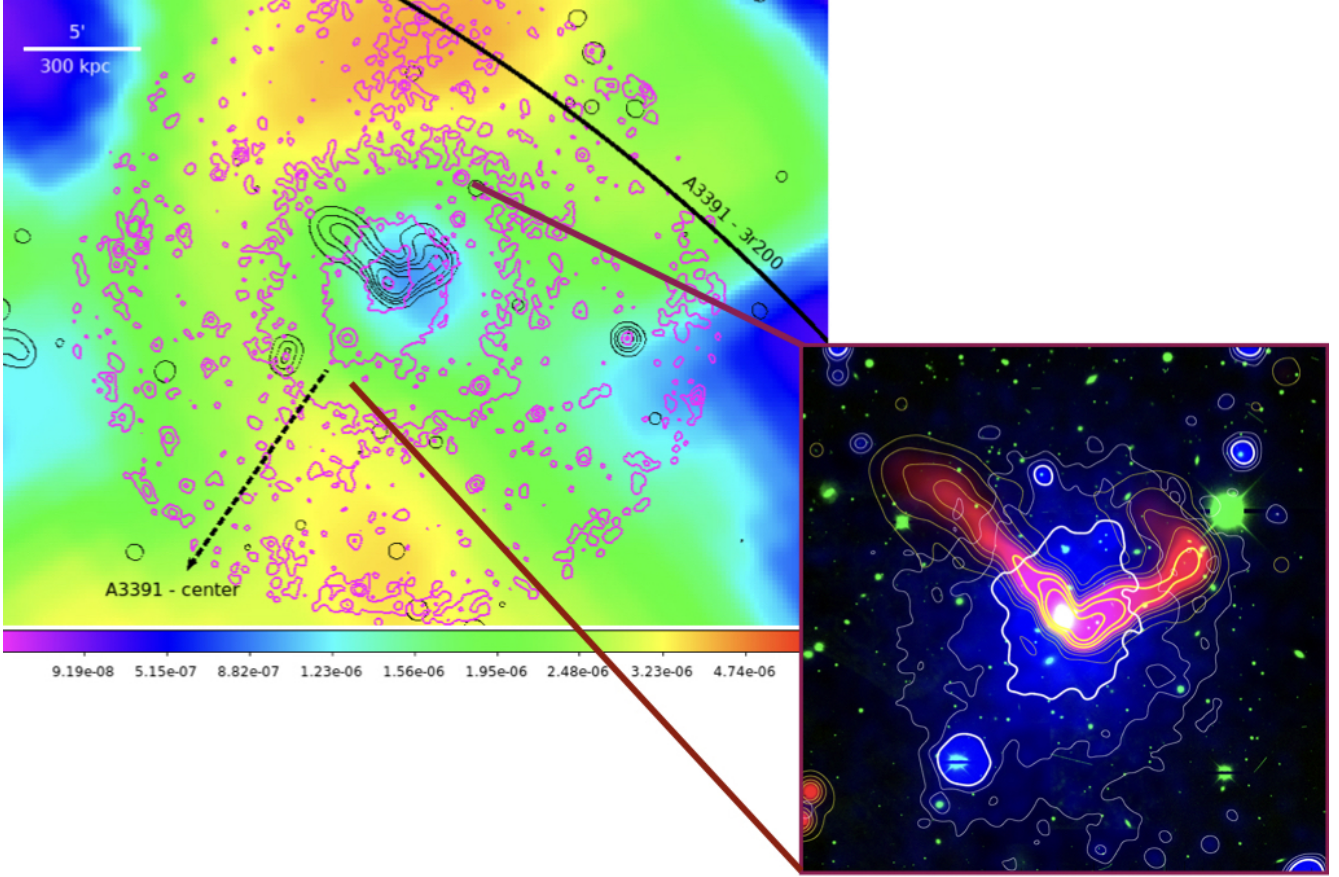


Fig. 6. *Left:* Planck y-map overlaid with X-ray (from *XMM-Newton*, in magenta) and radio (ASKAP/EMU, in black) contours. Black line depicts the $3 \times R_{200}$ of A3391 and black dashed-line points toward the center of A3391. *Right:* radio+X-ray+optical composite image of the central region of the Northern Clump. The image is generated utilizing ASKAP/EMU image (red color and yellow contour), *XMM-Newton* image (blue color and white contour), and DECAM Sloan *g*-band image (green color).

through a lower density medium, as indicated by the contours. The central radio source may be moving locally within the Northern Clump towards the southwest as a result of, for example, sloshing, while globally, the Northern Clump moves towards the southeast.

We used unsharp masks in the *Chandra* image to highlight substructures in the ICM. The original image was smoothed using two different scales and one smoothed image was subtracted from the other to make the edges more visually appealing. This technique can be mathematically expressed as

$$\hat{U} = I * g - I * h \quad (5)$$

where I stands for the original image and g and h are the two smoothing scales, for which we chose $g=30$ and $h=100$ pixels. As shown in Fig. 7 (left), the unsharp masked image reveals regions with a possible deficient surface brightness $r \approx 2.09'$ (125 kpc) to the east and west of the cluster center. We further overlaid the ASKAP/EMU radio continuum emission of the cluster center. A seeming picture of X-ray cavities filled with radio lobes starts to emerge, as observed for other clusters (e.g., Bîrzan et al. 2004; McNamara & Nulsen 2007).

From the presented *XMM-Newton* and *Chandra* images, and with the help from ASKAP/EMU radio image, as well as the DECAM optical image, we identify clear indications of Northern Clump's boxyness, tail-like emission in the north, and hint of X-ray cavities that coincide with the radio lobes.

3.2. X-ray surface brightness (S_X) profiles

3.2.1. *XMM-Newton*

The full azimuthal S_X profiles of the three different setups can be found in Appendix C. In all three profiles we observe a steep drop at around $5' < r < 6'$ ($299.4 \text{ kpc} < r < 359.28 \text{ kpc}$). Moreover, the overall shapes and residuals seen in the S_X profiles of the box annuli setups using all *XMM-Newton* detectors and pn-only data support the case that the boxy appearance of the cluster is not an artifact caused by the placement of the central MOS chip.

We present the sectorized S_X profiles (using the box annuli setup) in Fig. 8 (right, top plot). The bottom plot of the figure shows the relative differences with respect to the corresponding S_X of the full azimuthal setups, which is to examine any excess or deficit of the surface brightness. The 1σ confidence region of the full azimuthal S_X is plotted in gray. Hereafter, the full azimuthal S_X profile will be referred to as the average S_X profile. The sectorized S_X profiles using the circular annuli setup can be found in Appendix C.

Some noticeable features among the different directions are present, such as the S_X depression in the northeast, excess of the S_X in the south, and the enhancement towards the north. These features are seen in both setups, but they are more pronounced in the box annuli setup.

The depression in the northeast is at $1' < r < 3'$ ($59.88 \text{ kpc} < r < 179.64 \text{ kpc}$). The S_X gets closer to the average at around $4'$ (239.52 kpc) and drops rapidly beyond this point. The largest

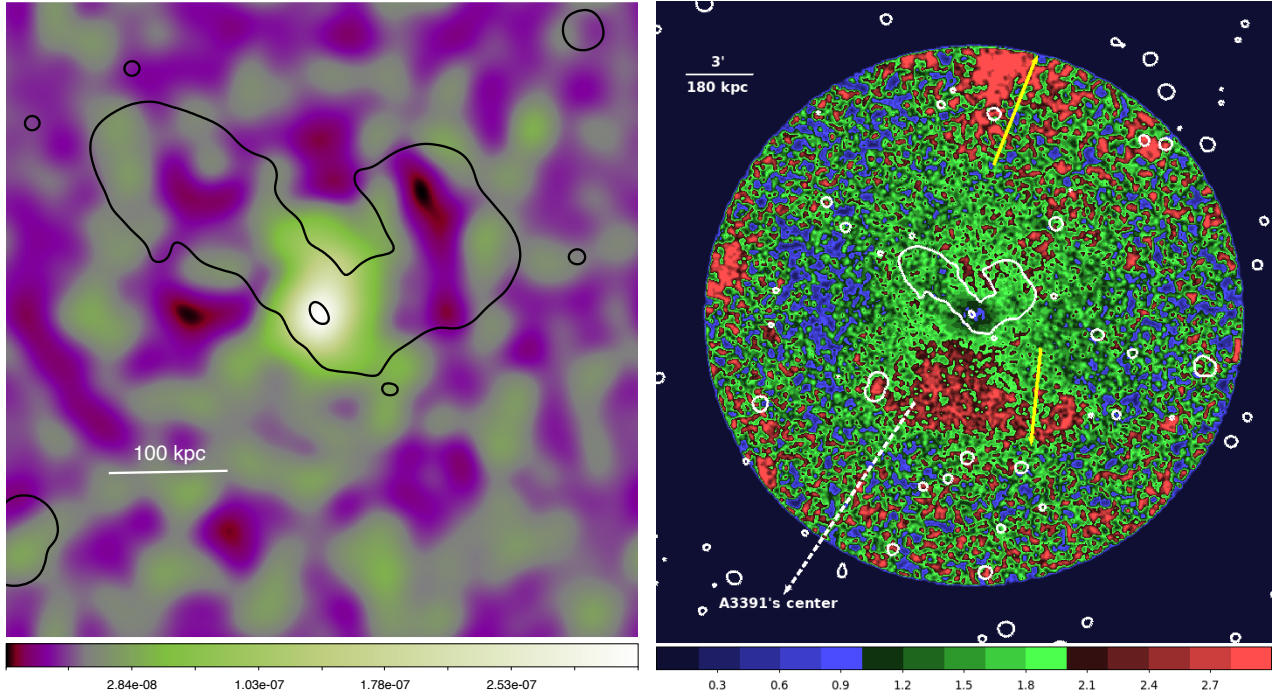


Fig. 7. *Left:* *Chandra* unsharp masked image of the central region of the Northern Clump. *Right:* *XMM-Newton* residual image. The northern yellow arrow shows the 5.3' projected length of the tail emission. The enhancement in the south is indicated by the southern yellow arrow and the center of A3391 cluster is pointed by the dashed-line white arrow. Gaussian smoothing with kernel radius of 3 pixels is applied to the image. Black and white contours in both images represent the ASKAP/EMU radio continuum emission.

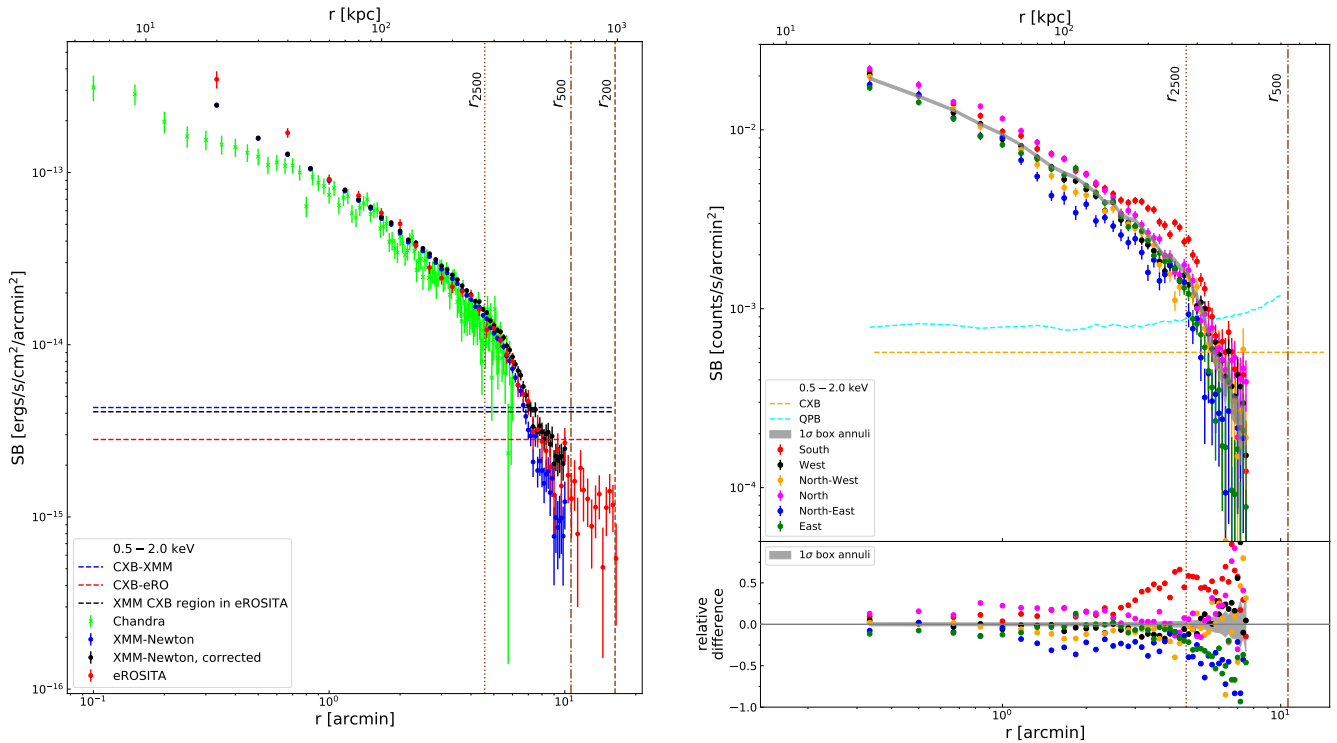


Fig. 8. *Left:* instrument independent, absorption corrected, and background subtracted S_X profiles of *Chandra* (green), *XMM-Newton* (blue), and *eROSITA* (red) in the energy band 0.5–2.0 keV. The blue, red, and black horizontal dashed lines are the CXB levels of *XMM-Newton*, *eROSITA*, and *eROSITA* with *XMM-Newton* defined CXB region, respectively. Black points are the CXB corrected *XMM-Newton* S_X . The various radii are plotted in brown. *Right:* *XMM-Newton* S_X profiles in different directions of the Northern Clump using the box annuli setup (*top*) and the relative differences with respect to the average surface brightness (*bottom*). The grey shaded areas in both plots are the 1σ confidence region of the average S_X . The various radii are plotted in brown. The CXB and QPB level are plotted in orange and cyan dashed lines.

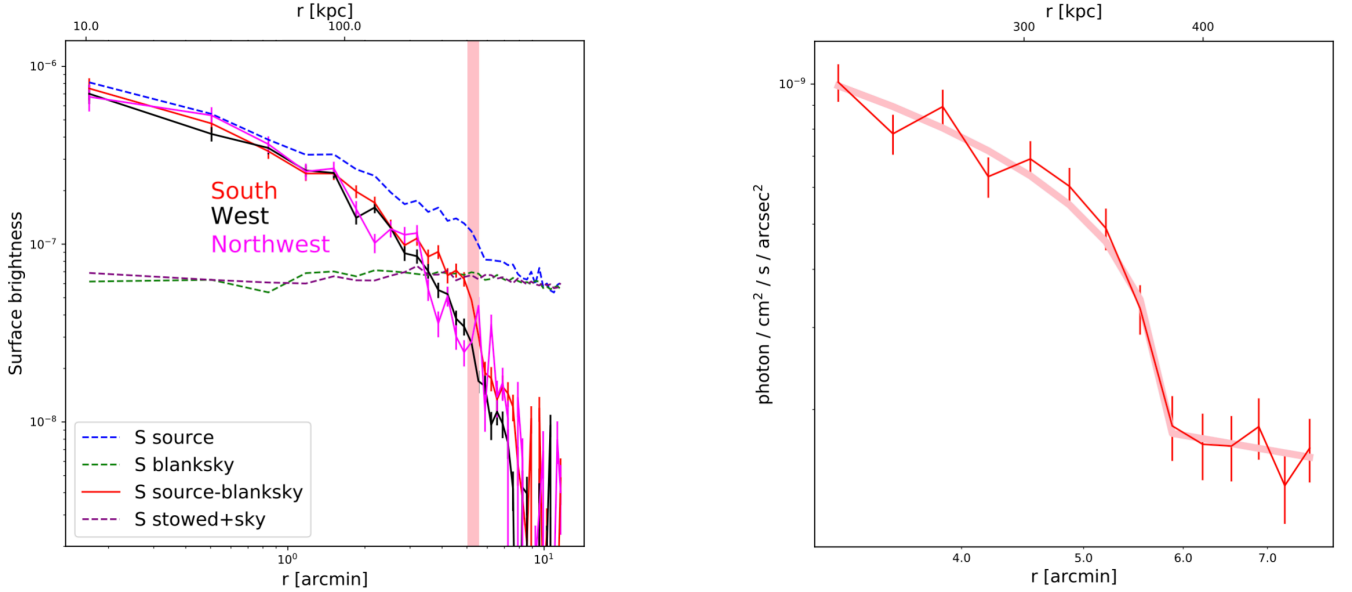


Fig. 9. *Left:* Blanksky background subtracted surface brightness profiles of the south (red), west (west), and northwest (magenta) directions in units of counts $\text{s}^{-1} \text{arcsec}^{-2}$ as measured with *Chandra*. The level of the tailored blanksky background (green dashed) and that of the stowed background plus the astrophysical background (purple dashed) for the south direction are consistent. The blue dashed line represents the total emission from both the source and background of the south direction. The vertical pink line marks the position of a possible density jump in the south direction. *Right:* surface brightness profile zoomed in around the surface brightness edge in the south direction in units of photon $\text{s}^{-1} \text{cm}^{-2} \text{arcsec}^{-2}$. We fit the data with a broken powerlaw density model (pink) and obtain a best-fit density jump of 1.45.

fractional decrement in this direction, of 36%, occurs at $1.67'$ (100 kpc).

In the southern sector, S_X enhancement is observed at around $2' < r < 6'$ ($119.76 \text{ kpc} < r < 359.28 \text{ kpc}$). The peak is at $4.33'$ (259.20 kpc) with a 66% enhancement. We suggest that the origin of the surface brightness excess in this specific direction is either from compressed gas caused by ram pressure or an accreted clump of cold gas from the Northern Filament, where the cluster resides. In both scenarios, the Northern Clump should be falling towards the A3391 cluster along with the filament and within the region where its mean density dominates, collapses from the filament will continue onto the system.

We observe significant enhancement at larger radii in the north direction consistent with the observed tail feature in the image. A relative difference of 170% occurs at $7.5'$ (449.1 kpc).

The features seen in the sectorized S_X profiles are present in the residual image (Fig. 7, right). The residual image is the result of dividing the surface brightness image by the spherically symmetric model. We overlaid the residual image with the ASKAP/EMU radio contour (white contour). Surface brightness depression at around $r \approx 2.05'$ (122.75 kpc) to the northeast and northwest of the center are observed. They coincide with the lobes of the WAT radio source and also in agreement with what is found in *Chandra* unsharp masked image (Fig. 7, left). In the south, a density enhancement relative to other directions is revealed at predominantly around $2' < r < 5'$ ($119.76 \text{ kpc} < r < 229.40 \text{ kpc}$). Furthermore, we detect a clear tail of emission north of the Northern Clump, $\sim 7'$ (419.16 kpc) away from the center. This tail has a projected length of $\sim 5.3'$ (317.4 kpc), as indicated by the northern yellow arrow in Fig. 7 (right).

3.2.2. *Chandra*

We derived the X-ray surface brightness profiles in south, west, and northwest directions, ranging from the cluster center to radii

of $11.70'$ (700 kpc) as shown in Fig. 9. We note a region of enhanced brightness at around $r = 5.84'$ (350 kpc) in the south direction relative to other directions. We fit the profile to a broken power law profile with a density jump projected along the line of sight

$$S(r) = \text{norm} \int F(\omega)^2 d\omega, \quad \text{where } \omega^2 = r^2 + l^2. \quad (6)$$

$F(\omega)$ is the deprojected density profile:

$$F(\omega) = \begin{cases} \omega^{-\alpha_1} & \text{if } \omega < r_{\text{break}} \\ \frac{1}{\text{jump}} \omega^{-\alpha_2} & \text{otherwise,} \end{cases} \quad (7)$$

where α_1 , α_2 , jump, and r_{break} are free parameters. We obtain a best-fit density jump of 1.45 ± 0.32 at $r = 5.74 \pm 0.17'$ ($344 \pm 10 \text{ kpc}$). As the ICM temperature appears to be uniform across the edge (Fig. 10), we assume that the pressure discontinuity equals the density jump and calculate the associated Mach number (Landau & Lifshitz 1959):

$$\frac{p_0}{p_1} = \left(1 + \frac{\gamma - 1}{2} \mathcal{M}\right)^{\gamma/(\gamma-1)} \quad (8)$$

for which we obtain $\mathcal{M} = 0.48^{+0.30}_{-0.34}$. Given a sound speed of 802 km s^{-1} for a 2.5 keV ICM, the central region of the Northern Clump is moving towards south at a speed of $386^{+239}_{-274} \text{ km s}^{-1}$ relative to the motion of the gas in the southern direction.

3.2.3. eROSITA, *XMM-Newton*, and *Chandra*

We present S_X profiles of all the used X-ray instruments in the energy band 0.5–2.0 keV in Fig. 8 (left). To correct for the effective area of different instruments and absorption, each of the three profiles had been multiplied by a conversion factor. For eROSITA and *XMM-Newton*, this conversion factor was

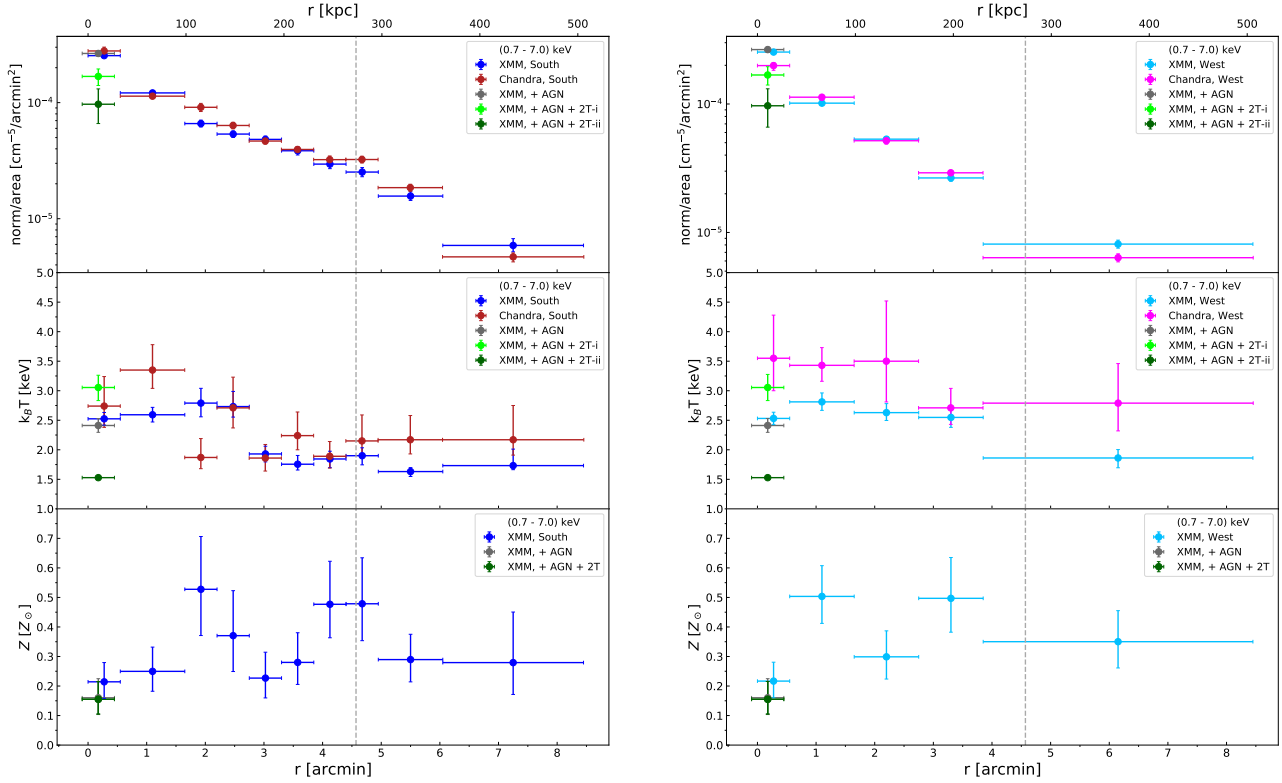


Fig. 10. Normalization (*top*), temperature (*middle*), and metallicity (*bottom*) profiles of the Northern Clump derived in the energy band 0.7–7.0 keV. *Left*: southern region profiles. The blue and red data points represent *XMM-Newton* and *Chandra*, respectively. *Right*: western region profiles. The cyan and magenta data points represent *XMM-Newton* and *Chandra*, respectively. Due to modest photon counts, *Chandra* metallicity could not be constrained in any sectors. The central data points fitted with AGN component are shown in grey, light green and dark green. These data points are shifted for visualization purposes. The grey dashed lines indicate the R_{2500} of the cluster. The x -axis error bars are not the 1σ error range, but the full width of the bins.

calculated by taking the ratio of the unabsorbed energy flux to the absorbed count rates in the 0.5–2 keV band. We supplied the best-fit cluster parameters in the 2.4–6', the ($k_B T_{500}$) region and the on-axis response files of an on-chip TM and MOS camera. To account for possible temperature changes across the radial ranges, we computed the conversion factor for 3 keV and 1.5 keV cluster emission, as well. The variation is found to be less than 3%. For *Chandra*, whose exposure maps already include a correction for the telescope effective area in addition to vignetting, the conversion factor is simply the ratio of the unabsorbed energy flux to the absorbed photon flux. The factor is 9.87×10^{-12} ergs cm $^{-2}$ counts $^{-1}$ for eROSITA, 7.55×10^{-12} ergs cm $^{-2}$ counts $^{-1}$ for *XMM-Newton*, and 1.72×10^{-9} ergs photons $^{-1}$ for *Chandra*.

The annulus used to estimate the *XMM-Newton* CXB level (12.0–13.25' (1.13–1.24 R_{500}), shown as the horizontal blue line) may still contain some cluster emission. In order to correct for this, we calculated the surface brightness of this same background region using eROSITA data (horizontal black dashed lines) and estimated the excess cluster surface brightness as the difference between the two background estimate (horizontal red dashed line). We added back this excess surface brightness to obtain the corrected *XMM-Newton* data points (plotted in black). The CXB correction results in better agreement between *XMM-Newton* and eROSITA, especially in the 7.0–10.0' radial range. The CXB subtracted surface brightness profile is nearly flat beyond the R_{500} and out to the R_{200} . This may imply that at this regime, there is still some emission either from the cluster or the filament in which the Northern Clump resides, or both.

Through this exercise, we show the complementary nature of the three instruments. For instance, *Chandra* (green points) with the best on-axis spatial resolution can cover as far as 3'' from the center, *XMM-Newton* (blue and black points) covers the intermediate radial range with good statistics, and eROSITA (red points) with its wide FoV and scan mode delivers the cluster surface brightness out to R_{200} . The discrepancies in the center can be well-explained by the PSF effect. Moreover, although masked, the bright point source in the cluster center is likely to contribute some of its emission to the central bins of eROSITA and *XMM-Newton* profiles. Other causes, such as point source detection and different background treatment could also play a role in the observed differences among the profiles.

3.3. Spectral analysis

3.3.1. eROSITA cluster parameters

We list the eROSITA cluster parameters for the $k_B T_{500}$ region (an annulus of 2.4–6.0') in Table 4. The metallicity returned by eROSITA is consistent with the one returned by *XMM-Newton*, both in the wide and the small soft energy band, while the normalizations and temperatures are lower. Fitting in the soft band does improve the consistency between eROSITA and *XMM-Newton* temperatures while not fully solving the discrepancies. While this could be an effect of instrumental calibration uncertainties, it could also be caused by multi-temperature structure. As predicted by simulations, in the case of multi-temperature plasma eROSITA that has superior soft response was shown to

Table 4. eROSITA and *XMM-Newton* cluster parameters from the $k_B T_{500}$ region ($0.2-0.5R_{500}$).

Instrument	norm ^(†)	$k_B T$ [keV]	Z [Z_\odot]
Full energy band ^(*)			
eROSITA	$1.59^{+0.17}_{-0.19}$	$1.67^{+0.20}_{-0.11}$	$0.36^{+0.11}_{-0.12}$
<i>XMM-Newton</i>	$2.35^{+0.046}_{-0.045}$	1.99 ± 0.04	$0.31^{+0.025}_{-0.026}$
0.8–2.0 keV			
eROSITA	$1.62^{+0.26}_{-0.23}$	$1.70^{+0.22}_{-0.11}$	$0.36^{+0.19}_{-0.14}$
<i>XMM-Newton</i>	$2.45^{+0.053}_{-0.052}$	$1.99^{+0.050}_{-0.054}$	$0.27^{+0.027}_{-0.025}$

Notes. ^(†) $[10^{-5} \text{ cm}^{-5} \text{ arcmin}^{-2}]$, ^(*)0.7/0.8–9.0 keV for eROSITA TM8/TM9. 0.7–7.0 keV for *XMM-Newton*.

return lower temperatures in comparison to other instruments (Reiprich et al. 2013). Fitting in the soft band only should minimize such effects as the relative effective areas are similar in this range for eROSITA and *XMM-Newton*. This issue will be addressed further in the future, employing also eROSITA mock observations based on hydrodynamical simulations, and devising methodologies similar to the algorithm suggested by Vikhlinin (2006) to predict the temperature in the case of multi-temperature plasma.

3.3.2. Inner of south and west

We plot the results of the spectral analysis of *XMM-Newton* and *Chandra* in the south and west directions of the Northern Clump in Fig. 10 left and right panel, respectively. The top, middle, and bottom panels are the normalization per area, temperature, and metallicity profiles. Due to modest photon counts, the metallicities in *Chandra* could only be constrained using bins of full azimuthal direction. The profile can be found in Fig. D.2. The information regarding the source regions and their best-fit parameter values are listed in Table D.2.

In both directions, we observe a flattening towards the central region of the cluster. The temperature profile towards the south indicates an elevated temperature around $2' < r < 3'$ ($119.76 \text{ kpc} < r < 179.64 \text{ kpc}$). The metallicity also appears enhanced in this region. Beyond the fourth bin, the temperature profile flattens at an average temperature of 1.94 keV.

3.3.3. Outskirts of north, south, and west

We compare spectral properties of the north, south, and west directions over R_{2500} to R_{500} ($r = 4 - 12.5' = 239.52 - 733.53 \text{ kpc}$) as shown in Fig. 11. We compare only *XMM-Newton* values since, unfortunately, the outer north of the Northern Clump is not covered by the *Chandra* observations. We found it necessary to fix the metallicity in the last two bins of the south and west to $0.3 Z_\odot$. The best-fit temperatures and normalizations vary within 1σ when we fixed the metallicity of south and west to the best-fit value of the north or fixed the metallicity of the north to $0.3 Z_\odot$. In general, our treatment of metallicity does not change the following results.

We note a higher normalization per area in the last two bins of the northern region. In comparison to the south (west) third

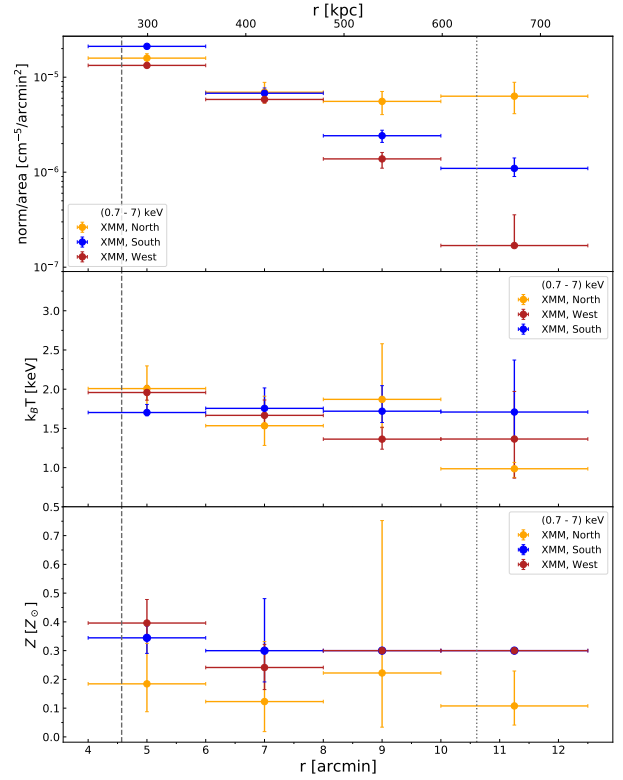


Fig. 11. *XMM-Newton* normalization (top), temperature (middle), and metallicity (bottom) profiles of the outer regions of the Northern Clump in the different directions in the energy band 0.7–7.0 keV. The northern, southern, and western regions are represented by orange, blue, and red data points, respectively. The grey dashed (dotted) lines indicate the R_{2500} (R_{500}) of the cluster. The x-axis error bars are not the 1σ error range, but the full width of the bins. The metallicity in the last two bins of the south and west has been frozen to $0.3 Z_\odot$.

and fourth data points, the normalization per area in the north are 56 (75)% and 83 (97)% higher, respectively. From *XMM-Newton* residual image (Fig. 7, right), we estimated that the excess emission in the north associated with the tail feature is located at $\sim 7'$ (419.16 kpc) from the center and stretched out to $12.5'$ (733.53 kpc). Therefore, we see an agreement between the imaging and spectral analyses results. This tail feature is often observed in other merging systems as a result of ram pressure stripping. For example, the tail from M 86 and M 49 as they fall into the Virgo Cluster (Randall et al. 2008; Su et al. 2019). Also see Su et al. 2014, 2017a,b, the northeast tail feature observed in A2142 cluster (Eckert et al. 2014. Further confirmed through dynamical study of the member galaxies in Liu et al. 2018), and a more extreme case of complete stripping is observed in the galaxy cluster Zwicky 8338 (Schellenberger & Reiprich 2015).

In the south, higher temperature in comparison to the other two directions is apparent. At $11.25'$ (673.65 kpc), the temperature in the south is higher by 42 (20)% than in the north (west). This elevated temperature may be associated with shock or compression heated gas as the Northern Clump falls towards the south, into the A3391 cluster. At $5.0'$ (299.4 kpc), the normalization per area is higher than the other two directions, which is in agreement with the residual image (Fig. 7, right) and the southern S_X profile (Fig. 8, right).

The properties of the outskirts of the Northern Clump are similar to those systems listed above, particularly the case of the M 49 group residing beyond the virial radius of the Virgo Cluster (Su et al. 2019). In addition to the stripped tail, a temperature

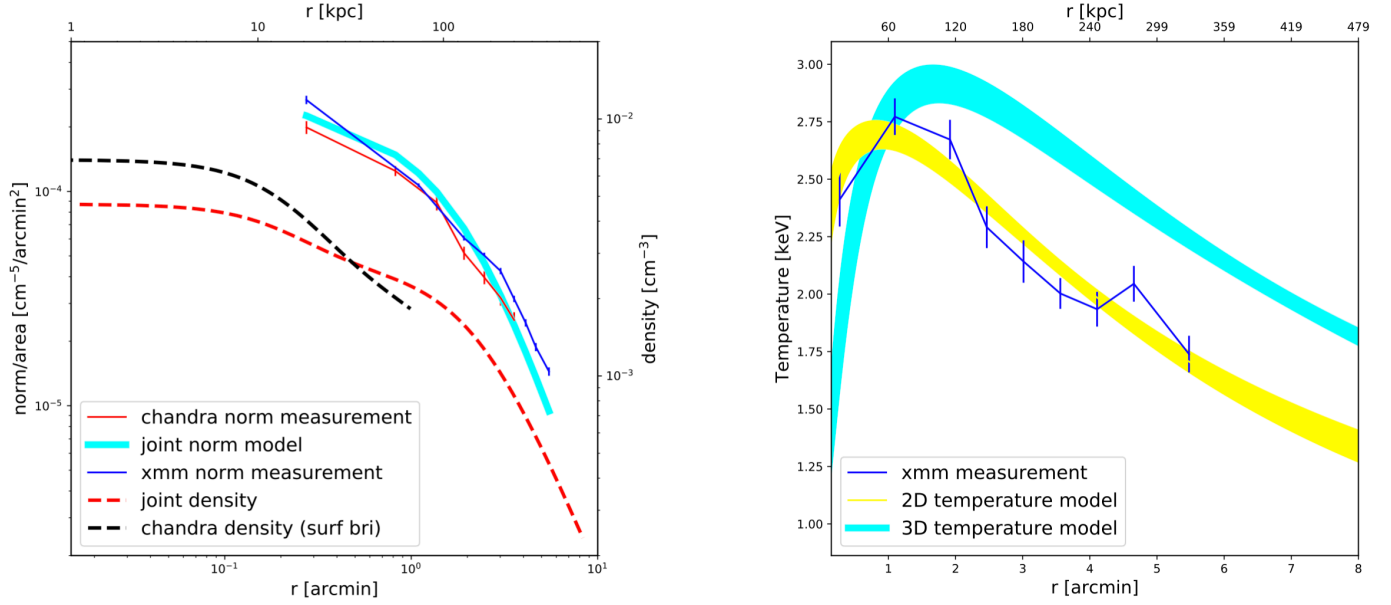


Fig. 12. *Left:* profiles of apec normalization per area measured with *XMM-Newton* (blue solid) and *Chandra* (red solid). Red dashed lines indicate the best-fit 3D density profiles for an empirical density profile of Eq. (9) through a joint-fit of *XMM-Newton* and *Chandra* normalization profile. The corresponding normalization per area profiles derived with the best-fit 3D density profiles are shown in the cyan line, displaying good agreement with the measurements. Black dashed line is the deprojected density profile derived from *Chandra* surface brightness profile and the *Chandra* spectral analysis of the innermost bin. *Right:* projected temperature profile measured with *XMM-Newton* (blue solid line). The best-fit deprojected temperature profile is shown in cyan. The corresponding projected temperature profile derived from Eq. (16) is shown in yellow, in good consistent with the measurement.

enhancement is noted in front of the cold front in M 49, resembling the temperature elevation and surface brightness edge (see Sect. 3.2.2) observed at $\sim 11.25'$ (673.65 kpc) and $5'$ (299.4 kpc), respectively in the south of the Northern Clump. Our findings indicate that the Northern Clump may be undergoing the same infalling process with M 49.

3.3.4. Central AGN

We notice a metallicity drop in the core of the Northern Clump. While it is commonly believed that this phenomena, which is often observed in galaxy groups and clusters with X-ray cavities, is the result of the AGN mechanical feedback and/or depletion of Fe into cold dust grains (Panagoulia et al. 2015; Lakhchaura et al. 2019; Liu et al. 2019), it could also be an artifact that surfaces as the central AGN is not accounted properly in the spectral fitting (Mernier et al. 2017). To investigate this, we therefore implemented the second and third fitting methods (Sect. 2.2.2). We present the best-fit parameter values of the three methods in Table D.1 and the spectra with their best-fit model are displayed in Fig. D.3.

Since the on-axis encircled energy fraction (EEF) for MOS1 camera is 68% at a $15''$ radius⁴, this indicates that there might be some AGN emission left in the source region while performing the fit using the first method. While 92% of the total energy are encircled within a $60''$ radius, having a mask of this size in the core region is undesirable. The second and third methods are a better solution to this problem. However, as noticed from the metallicity profiles, the low metallicity persists even when the AGN component is added.

The apparent low core metallicity is better explained by the above-mentioned mechanical processes, for instance by the AGN

feedback, through which a fraction of the core metal-rich ICM gas is distributed outwards (Sanders et al. 2016; Mernier et al. 2017) and/or depletion of core Fe into dust grains (Panagoulia et al. 2015; Lakhchaura et al. 2019; Liu et al. 2019).

Additionally, we also observe lower Sunyaev-Zel'dovich (SZ) signal at the center of the cluster, as shown in Fig. 6. The decrease of the SZ signal at this region is likely due to the core of the radio AGN, and similarly seen at the center of the Perseus Cluster (Fig. 5 in Erler et al. 2019). For more detailed review on AGN contamination of SZ clusters see Lin et al. 2009; Gupta et al. 2017). Unless special effort is done, such clusters may be missed in SZ surveys.

3.3.5. Deprojection analysis and central entropy

We obtain the best-fit apec normalization profiles for *Chandra* spectra extracted from concentric annuli ranging from $r = 20$ kpc to $r = 200$ kpc and for *XMM-Newton* ranging from $r = 20$ kpc to $r = 400$ kpc as shown in Fig. 12 (left). We assume the deprojected density profile takes the form of

$$n(r) = \sqrt{n_{01}^2 \left(1 + \frac{r^2}{r_{c1}^2}\right)^{-3\beta_1} + n_{02}^2 \left(1 + \frac{r^2}{r_{c2}^2}\right)^{-3\beta_2}}. \quad (9)$$

A normalization profile can be derived by substituting the 3D density profile (Eq. (9)) into Eq. (3). We can obtain the best-fit parameters for the deprojected density profiles by fitting the normalization profiles measured with *Chandra* and *XMM-Newton* to Eq. (3), as shown in Fig. 12 (left). We use the R^2 -score to evaluate the goodness of the fit, defined as

$$R^2(y, \hat{y}) = 1 - \frac{\sum_{i=1}^n (y_i - \hat{y}_i)^2}{\sum_{i=1}^n (y_i - \bar{y})^2} \quad (10)$$

⁴ *XMM-Newton* Science Analysis System: Encircled energy function

where \hat{y}_i is the best-fit value of the i -th data point and y_i is the measured value for total n data points, and $\bar{y} = \frac{1}{n} \sum_{i=1}^n y_i$. We obtain a R^2 -score of 0.95 for the deprojected density analysis.

We also derived the deprojected density profiles using the *Chandra* surface brightness profile following [Hudson et al. \(2010\)](#). We fit the surface brightness profile of the west direction to a double- β model, which takes the form of

$$S(r) = S_{01} \left(1 + \frac{r^2}{r_{c1}^2}\right)^{(-3\beta_1+0.5)} + S_{02} \left(1 + \frac{r^2}{r_{c2}^2}\right)^{(-3\beta_2+0.5)}, \quad (11)$$

corresponding to a density profile of Eq. (9). The central density $n_0 = \sqrt{n_{01}^2 + n_{02}^2}$ can be estimated from

$$n_0 = \left[\frac{10^{14} 4\pi (\Sigma_{12} \text{LI}_2 + \text{LI}_1) D_A D_L \zeta N}{\Sigma_{12} \text{LI}_2 \text{EI}_1 + \text{LI}_1 \text{EI}_2} \right]^{\frac{1}{2}}, \quad (12)$$

where $\Sigma_{12} = S_{01}/S_{02}$ is the ratio of the central surface brightness as in Eq. (11) and N is the normalization of the *apec* model for the innermost bin of *Chandra* projected spectral analysis. Additionally, D_A and D_L are the angular diameter distance and the luminosity distance, respectively, and $\zeta = 1.2$ is the ratio of electrons to protons. EI_i is the emission integral divided by the central density for component i :

$$\text{EI}_i \equiv \int \left(\frac{n}{n_0}\right)^2 dV = 2\pi \int_{-\infty}^{\infty} \int_0^R x \left(1 + \frac{x^2 + l^2}{r_{ci}^2}\right)^{-3\beta_i} dx dl, \quad (13)$$

where R is the outer radius of the spectrum extraction region. The line emission measure for component i , LI_i , is defined as

$$\text{LI}_i \equiv \int_{-\infty}^{\infty} \left(1 + \frac{l^2}{r_{ci}^2}\right)^{-3\beta_i} dl, \quad (14)$$

and n_{01} and n_{02} can be further related by,

$$\frac{n_{01}^2}{n_{02}^2} = \frac{\Sigma_{12} \text{LI}_2}{\text{LI}_1}. \quad (15)$$

We can solve these equations using the surface brightness parameters to obtain a density profile of Eq. (9) as shown in Fig. 12 (left).

We adopted an empirical formula to model the deprojected temperature profile ([Andrade-Santos et al. 2017; Su et al. 2019](#))

$$T_{3D}(r) = \frac{T_0}{[1 + (r/r_t)^2]} \times \frac{[r/(0.075r_t)]^{1.9} + T_m/T_0}{[r/(0.075r_t)]^{1.9} + 1}. \quad (16)$$

The corresponding projected temperature can be obtained by projecting the gas density weighted T_{3D} along the line of sight. We fit the azimuthally averaged projected temperature profile measured with *XMM-Newton* to the 2D formula,

$$T_{2D} = \frac{\int \rho_g^2 T_{3D}^{1/4} dz}{\int \rho_g^2 T_{3D}^{-3/4} dz}, \quad (17)$$

for which the density profile derived with *XMM-Newton* is applied. The best-fit 2D and 3D temperature profiles are plotted in Fig. 12 (right). The 2D temperature model and the measured projected temperature profile give a R^2 -score of 0.88. The discrepancies between *XMM-Newton* and *Chandra* normalizations may be caused by, such as, different bin size, scattering, point source detection, as well as instrumental calibration uncertainties.

Table 5. eROSITA properties of Northern filament.

Fitting	norm [10^{-3} cm^{-5}]	$k_B T$ [keV]	Z [Z_\odot]	n_e [10^{-5} cm^{-3}]
1T	$1.34^{+0.64}_{-0.30}$	$1.52^{+0.57}_{-0.54}$	$0.06^{+0.19}_{-0.06}$	$4.85^{+1.05}_{-0.58}$
2T	$1.06^{+0.25}_{-0.29}$ $0.22^{+0.24}_{-0.19}$	$1.72^{+1.02}_{-0.29}$ $0.68^{+0.38}_{-0.64}$	0.1	$4.32^{+0.48}_{-0.65}$ $1.99^{+0.88}_{-1.24}$

The Northern Clump has an extrapolated central electron density of $\lesssim 7 \times 10^{-3} \text{ cm}^{-3}$, falling short of $\sim 1.5 \times 10^{-2} \text{ cm}^{-3}$, a conventional threshold for cool-core clusters ([Andrade-Santos et al. 2017; Su et al. 2020](#)). Based on the deprojected density and temperature profiles, we extrapolate an entropy ($K \equiv k_B T_{\text{gas}}/n_e^{2/3}$) of 30 keV cm^2 for the central $r < 0.004 R_{500}$. According to [Hudson et al. \(2010\)](#), the Northern Clump can be best described as a weak cool-core (WCC) cluster.

3.3.6. Northern filament

We consider the region between the virial radii of the Northern Clump and the A3391 cluster as an inter-cluster filament as shown in Fig. 1. We used the measured *apec* normalization to derive the electron density, n_e , of the filament. We assume a simple geometry, such that the filament is a cylinder with its axis in the plane of the sky and located at the mean redshift of both clusters, $z = 0.0533$, such that Eq. (3) can be rewritten as,

$$n_e = \left[1.52 \times 10^{-10} \text{ cm}^{-1} \times \text{norm} \times (1+z)^2 \times \left(\frac{D_A}{\text{Mpc}}\right)^2 \times \left(\frac{r}{\text{Mpc}}\right)^{-2} \times \left(\frac{h}{\text{Mpc}}\right)^{-1} \right]^{\frac{1}{2}}, \quad (18)$$

where $D_A(z=0.0533) = 214.09 \text{ Mpc}$, radius of the cylinder $r = 1.56 \text{ Mpc}$, and its height $h = 1.81 \text{ Mpc}$. The Hydrogen density is taken to be $n_H \approx n_e/1.17$.

We present the results of the eROSITA spectral analysis for the Northern Filament in Table 5. Comparing our results to the WHIM properties predicted by the cosmological hydrodynamic simulations (e.g., [Davé et al. 2001](#). For observational constraints of WHIM properties see, e.g., [Nicastró et al. 2018; Kovács et al. 2019](#)), we find that the best-fit projected temperature obtained from the one-temperature (1T) component fit is beyond the expected temperature range of $T = 10^5 - 10^7 \text{ K}$, while the electron density is within the expected range of $n_e \approx 10^{-6} - 10^{-4} \text{ cm}^{-3}$.

We further performed a two-temperature (2T) component fit, for which we fixed the abundances of the filament to 0.1 of [Asplund et al. \(2009\)](#) due to the statistics. We identify a cooler component whose temperature and electron density are consistent with the properties of WHIM. The hotter component is likely to be cluster emission from either or both the Northern Clump and the A3391 cluster. Further study, for instance, constraining the properties of the ICM in the outskirts of A3391, as well as calculating the surface brightness profile along the filament, is needed to draw more conclusions (Veronica et al., in prep.).

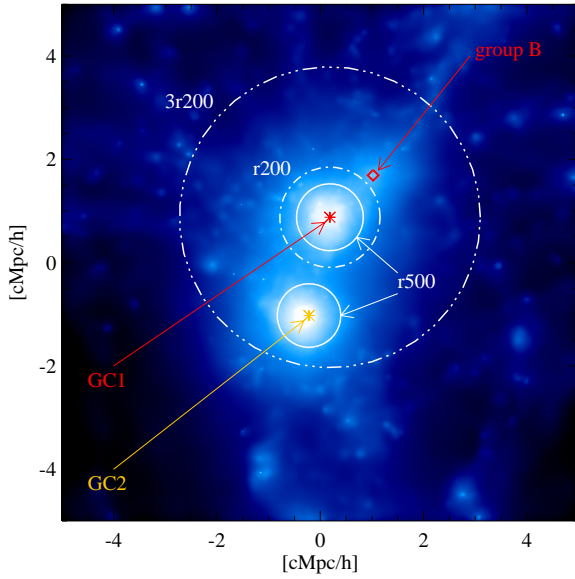


Fig. 13. Gas density map of the A3391/95 analog pair from the Magneticum Simulation, at $z=0.07$. The region shown comprises a cubic volume of 10 cMpc/h per side centered on the pair center of mass. The two main clusters GC1 and GC2 are marked, with their R_{200} and R_{500} (defined w.r.t. the critical density of the Universe), as well as the position of group B.

4. Insights from the Magneticum Simulation

In the 20 cMpc/h-scale region extracted from the Magneticum Simulation volume, that comprises an analog of the A3391/95 system (see Reiprich et al. 2021) at $z=0.07$, we also identify various structures with the size of galaxy groups (Biffi et al. 2022). Among these additional structures, we consider in particular a small halo (hereafter, “group B”), in order to better interpret the history of the observed Northern Clump. Group B is a group-size object that has entered the atmosphere of the upper pair member (marked as “GC1”; Biffi et al. 2022) at about $z=0.16$, and has reached its outskirts (at $d_{3D} \sim 1.5 \times R_{200}^{GC1}$) by $z=0.07$. The configuration at redshift $z=0.07$ of the simulated pair and the group B is shown in Fig. 13. The figure shows the gas density map projected along the z axis of the simulation box, and comprises a volume of 10 cMpc/h per side, centered on the pair center of mass. There we mark the positions of the two pair members, GC1 and GC2, and of group B. Furthermore, we mark cluster radii that are of interest for the present discussion.

Group B has a mass of $M_{500} \sim 3.6 \times 10^{13} M_{\odot}$ at redshift $z \sim 0.16$, just before the merging starts. At lower redshifts, ($0.07 < z \leq 0.16$) the group is identified as a gravitationally-bound substructure of the GC1 cluster. By tracking the history of its most-massive progenitor, we investigate its properties along the trajectory towards the node of the Cosmic Web where the cluster pair is finally settling by $z=0.07$.

In the simulation analog, we find that the group movement towards the GC1 cluster is well defined below $z \lesssim 1$, according to several indicators. In Fig. 14 (upper inset) we show the redshift evolution of the alignment between the subhalo velocity and the infall direction, quantified by the cosine of the angle defined by those two directions. Different colors refer to the direction towards the final positions at $z=0.07$ of the pair center of mass (c.m.; blue) and the center of GC1 (red), as in the legend. We note that values of the cosine below $z \sim 1$ are always comprised between -0.8 and -0.95 , indicating a preferential alignment

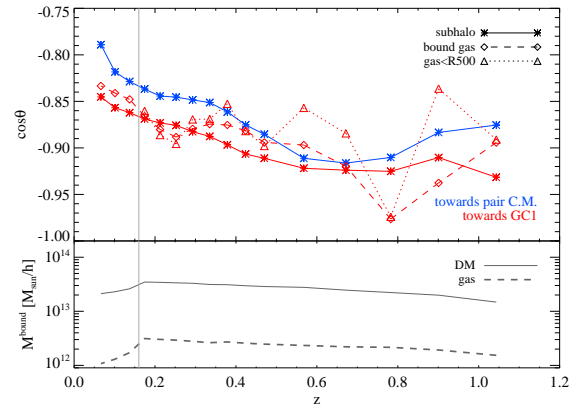


Fig. 14. Redshift evolution of the cosine of the angle between the radial direction towards the pair (center of mass, blue; GC1, red) and the velocity of the subhalo (bulk, solid; bound gas, dashed; all gas within R_{500} , dotted). The gas velocity alignment is reported only for the infall direction towards GC1. Data points for all the gas within R_{500} are only defined for the redshifts when the clump is an independent group from GC1 ($z \gtrsim 0.16$). We also report the redshift evolution of the subhalo DM (solid lines) and gas (dashed lines) bound mass in the lower inset of the figure.

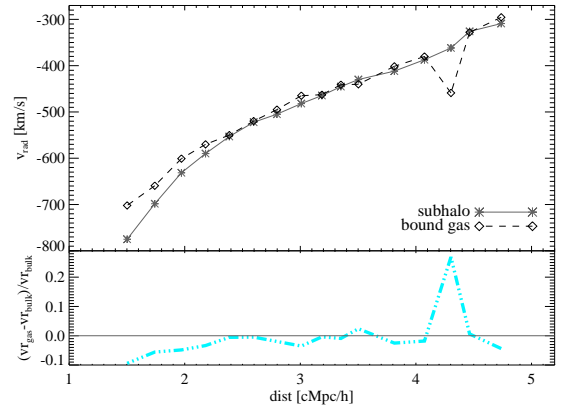


Fig. 15. *Top:* radial component of the bulk (solid lines) and bound-gas velocity (dashed lines) as a function of the radial distance from the final position of GC1. *Bottom:* relative difference between bound-gas and bulk radial velocity, as a function of the radial distance.

towards the GC1 final position: this confirms that group B is actually moving towards the GC1 cluster. This result holds for both the total bound dark matter (DM; solid line) and gas (dashed line) components and for all the gas (either bound or not) located within R_{500} (dotted lines). While the total bound gas follows more closely the DM trend, the gas within R_{500} is more subject to oscillations due to the fact that the selection is purely geometrical and can therefore comprise matter not yet gravitationally bound to the main halo potential. At redshift $z \lesssim 0.2$ the cosine absolute value decreases and marks a weaker alignment, and is also accompanied by a decrease of the total mass of the DM and gas that are gravitationally bound to group B (lower inset). This indicates a stripping process occurring while the group enters the cluster virial radius: the bound gas mass, in particular, decreases by a factor of ~ 3 between $z \sim 0.16$ and $z=0.07$.

The infall of group B towards GC1 is furthermore characterized by an increasing difference between the radial components of gas and subhalo bulk velocities below redshift $z \sim 0.25$. This is shown in Fig. 15, where we report the radial components of

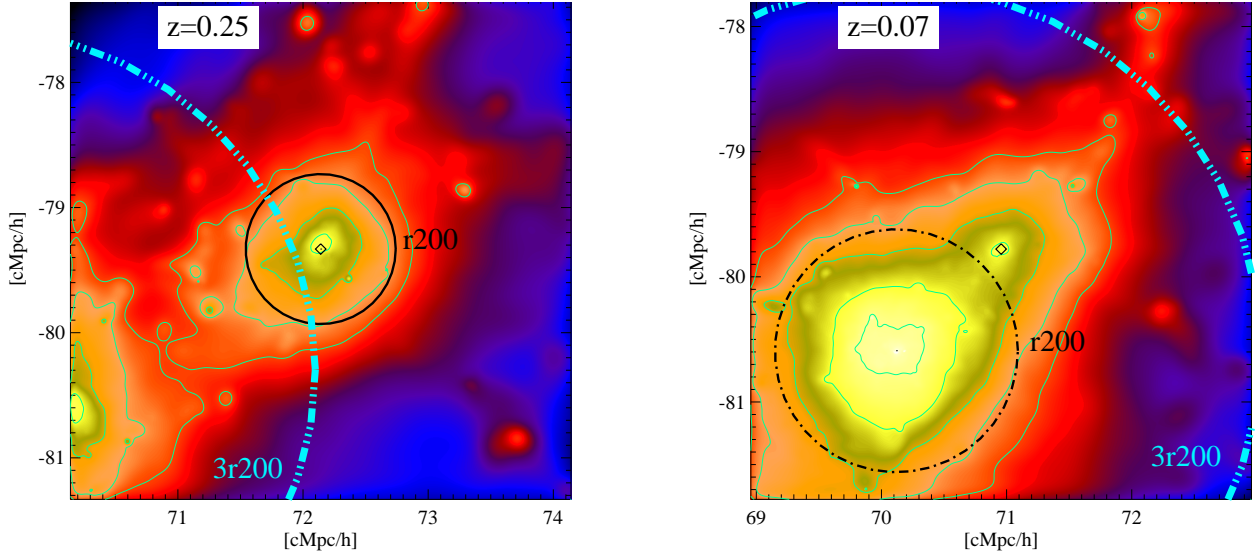


Fig. 16. Simulated projected maps of gas surface density, centered on the infalling group B (black diamond marking its center), at $z=0.25$ (left) and $z=0.07$ (right). The gas surface density map encloses a comoving volume of $(4 \text{ cMpc}/h)^3$. In both panels, we mark the circles corresponding to three times the GC1 cluster virial radius ($3 \times R_{200}^{\text{GC1}}$) and R_{200} of the group at $z=0.25$ (solid) and of the GC1 cluster at $z=0.07$ (dot-dashed; when group B is a substructure of GC1).

bulk (solid) and bound gas (dashed) velocity, as a function of the distance (comoving units) between the position of group B at each redshift and the final position of GC1 (upper inset) – here larger radial distances correspond to earlier times.

From the Figure, one can note the slowing down of the gas component with respect to the DM (traced by the halo bulk velocity) at the smaller distances, corresponding to the redshifts $0.07 < z < 0.25$. This is better quantified in the lower inset of Fig. 15, where we report the relative difference between gas and bulk radial velocities at each point. We note a monotonic increase of such difference, while group B is getting closer than $\sim 2.5 \text{ cMpc}/h$ from the final position of GC1, which corresponds to $z \lesssim 0.25$. At $z=0.25$, the actual distance between the center of group B and the GC1 progenitor corresponds to $d_{3D} \sim 3.5 \text{ cMpc}/h$, namely $d_{3D} \sim 1.7 \times (R_{100}^B + R_{100}^{\text{GC1}}) \sim 4 \times R_{200}^{\text{GC1}}$. In the reference projection (xy plane; see Reiprich et al. 2021 and Biffi et al. 2022, for more details), this corresponds to a distance of $\sim 3 \times R_{200}^{\text{GC1}}$ from GC1. The projected configuration and distance relative to the GC1 cluster found at $z=0.25$ are similar to the observed Northern Clump case, supporting the possibility for the bigger accreting cluster (A3391 in the observed system) and the infall movement to leave an observable signature on the Northern Clump properties (such as the emission tail – see Sect. 3.1). At such distances, we indeed expect to observe the effects of the closeness to the GC1 cluster. In fact, this is also the typical distance from clusters at which simulations predict to observe changes in the gas properties of main filaments connected to them (namely at three to four times the cluster virial radius; e.g., Dolag et al. 2006). A zoom-in onto the group is shown in Fig. 16 by the simulated map of the projected gas density within a $4 \text{ cMpc}/h$ -side FoV centered on group B at redshift $z=0.25$ (left) and $z=0.07$ (right). In the maps, the movement of the group occurs roughly in the top-right to bottom-left direction and the dot-dashed circle indicates the radius corresponding to $\sim 3 \times R_{200}^{\text{GC1}}$ from the GC1 progenitor at $z=0.25$. The black circles approximate the R_{200} radius of group B at $z=0.25$ (solid line), and the R_{200} radius of GC1 at $z=0.07$ (dot-dashed line), when group B is no more identified as a separate halo by our

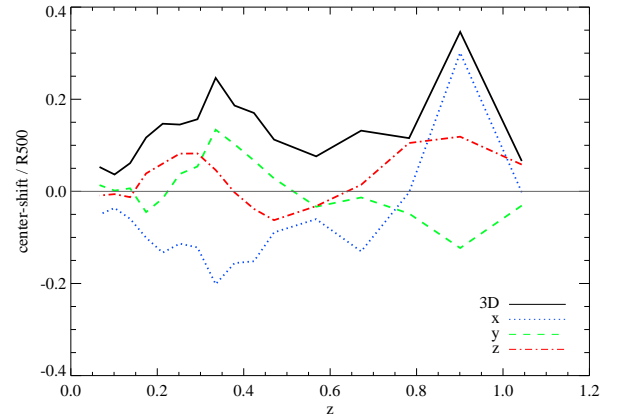


Fig. 17. Redshift evolution of the center shift between the position of the halo center (coinciding with the position of the minimum of the halo potential well) and the bound-gas center of mass, in units of R_{500} . The three-dimensional value of the shift and its three separate components along the major Cartesian axes of the simulations are reported, as in the legend.

substructure-finding algorithm (SUBFIND, Springel et al. 2001; Dolag et al. 2009).

We also find indications of halo sloshing throughout its evolution. This can be inferred from the oscillations described in the radial velocity cosine (upper inset in Fig. 14), when all the gas within R_{500} is considered (dotted curve) in comparison to the corresponding DM trend. This effect is further confirmed by Fig. 17, where we report the redshift evolution of the center shift for group B between $z \sim 1$ and $z=0.07$. The center shift is computed as the three-dimensional difference between the halo center⁵ and the bound gas center of mass, in units of the group R_{500} . In the figure, we also report the separate components along the major axes of the simulation volume, from which we note

⁵ The halo center is identified with the position corresponding to the minimum of the potential well.

an oscillating feature, especially between the x and y components – i.e. in the plane perpendicular to the chosen l.o.s. This effect is likely connected to the merging and accretion of smaller galaxy-size substructures (such as between $z \sim 1$ and $z \sim 0.8$), which perturb the gas component in the group and also produces elongated density contours.

5. Discussion and conclusions

We presented results of the X-ray imaging and spectral analyses of the MCXC J0621.7-5242 galaxy cluster, also known as the Northern Clump of the A3391/95 system, utilizing eROSITA, *XMM-Newton*, and *Chandra* observations. We used the ASKAP/EMU radio data, *Planck* y -map, and DECam data to study the influence of the wide-angle tail (WAT) radio source to the central intracluster medium (ICM) gas. We compared the observations with an analog of the A3391/95 system found in the Magneticum simulation. Our findings include:

- The Northern Clump is not a relaxed system and its morphology deviates from the common spherical or elliptical shapes. In fact, it has an interesting pronounced boxy shape.
- We identified a southern density enhancement, which indicates motion of the filament gas relative to the Northern Clump resulting in compression, e.g., by filament gas being accreted towards the Northern Clump while the whole system, filament and the Northern Clump is being accreted towards A3391. The temperature and density enhancement at around the same distance support this.
- We detected a tail of emission north of the Northern Clump that supports the relative motion as well. The tail starts at $\sim 7'$ (419.16 kpc) from the center with a projected length of $\sim 5.3'$ (317.4 kpc). We speculate that the gas is either stripped from the Northern Clump and lagging behind, or infalling gas from a possible continuation of the filament north of the Northern Clump. While a more detailed analysis is required, the first picture is nevertheless consistent with findings from the analog system identified in the Magneticum simulations, where the gas in the clump start to lag behind with its infall velocity reduced compared to dark matter, while getting closer than $3 \times R_{200}$ from the accreting cluster.
- A bright WAT radio galaxy occupies the center of the Northern Clump. A weak hint of X-ray surface brightness depressions coincident with the radio lobes is found, suggesting interaction of the radio plasma with the Northern Clump ICM.
- We note that the morphology of the denser X-ray gas is asymmetric with a sharp edge that points towards the A3391 center, in the southeast direction. The lower density gas at around $\sim 5'$ appears boxy, which may be the result of ram pressure stripping as it enters the atmosphere of A3391 and/or sloshing. However, the northeast bend of both lobes is not quite consistent with them being “swept back” by that global motion. We speculate that the lobes might have “escaped” some hot-gas confinement and the change of direction is due to motion through a lower-density ambient medium. The central radio source may be moving locally within the cluster toward the southwest as a result of sloshing, while the Northern Clump is moving toward the southeast.
- The electron density and entropy derived for the central region of the Northern Clump indicates that the Northern Clump is a weak cool-core (WCC) cluster. The temperature

flattening towards the center further supports this indication. The WCC nature could indicate some disturbance of the core either through effects caused by entering the sphere of influence of A3391, through infalling filament gas, or through the central radio AGN.

- The low core metallicity derived for the core using three different methods signifies AGN feedback blowing the metal-rich ICM gas outwards the central region. This is consistent with the strong radio emission of the central galaxy and with the fact that the cooling flow in this cluster is suppressed, which as a result only forming a weak cool-core.
- We performed spectral analyses in the region between the R_{200} of the Northern Clump and the A3391 cluster, the Northern Filament, where we assumed a simple cylindrical geometry on the plane of the sky. Through a 2T fit, we identified a cooler component whose temperature ($k_B T = 0.68^{+0.38}_{-0.64}$ keV) and electron density ($n_e = 1.99^{+0.88}_{-1.24} \times 10^{-5} \text{ cm}^{-3}$) are consistent with the expected ranges of WHIM properties.
- Analysis of a similar system found in the Magneticum simulation reveals that an infalling clump (equivalent to the observed Northern Clump) starts to “feel” the influence of the main accreting system (equivalent to the observed A3391) at around $3 \times R_{200}$, possibly related to accretion shocks expected to be present at such distance. For instance, the infall velocity of the gas component starts to decrease compared to the radial velocity of the dark matter. Once the group approaches the cluster virial radius, it undergoes further stripping processes with a decrease by a factor of ~ 3 in the gravitationally-bound gas mass between $z = 0.16$ and $z = 0.07$. Throughout its redshift evolution, we find evidences for halo sloshing marked by oscillations of the infall velocity and the center shift of the gas component compared to dark matter. In general, the findings in the Magneticum simulation are consistent with the properties of the observed system.

Thanks to the wide eROSITA FoV and its superior soft response, significant emission was observed in the A3391/95 system beyond the virial radii, R_{100} , with good resolution. This has allowed us to discover the soft X-ray emission from filaments connected to the system, as well as some infalling clumps residing in these filaments, one of which is the Northern Clump. This infalling galaxy cluster appears to have just entered the atmosphere, or sphere of influence, of the A3391 cluster.

In this work, we demonstrated how eROSITA is complementary not only to other X-ray instruments, e.g., *XMM-Newton* and *Chandra*, but also instruments from other wavelengths, e.g., the ASKAP radio telescope, the DECam optical survey, and the *Planck* microwave satellite. We also found that the eROSITA image of the A3391/95 system and the results of our Northern Clump analysis are consistent with each other, as well as with the analog simulated system from the Magneticum simulations.

Acknowledgements. We would like to thank the anonymous referee for their valuable feedback that helped improve the manuscript. We thank Kaustuv moni Basu for discussion about the *Planck* y -map. Funded by the Deutsche Forschungsgemeinschaft (DFG, German Research Foundation) – 450861021. This research was supported by the Excellence Cluster ORIGINS which is funded by the Deutsche Forschungsgemeinschaft (DFG, German Research Foundation) under Germany’s Excellence Strategy – EXC-2094 – 390783311. V.B. acknowledges funding by the Deutsche Forschungsgemeinschaft (DFG, German Research Foundation) – 415510302. Y.S. acknowledges support from *Chandra* grants AR8-19020A and GO1-22126X. A.V. is a member of the Max-Planck International School for Astronomy and Astrophysics (IMPRS) and of the Bonn-Cologne Graduate School for Physics and Astronomy (BCGS), and thanks for their support. This work is based on data from eROSITA, the soft X-ray instrument

aboard SRG, a joint Russian-German science mission supported by the Russian Space Agency (Roskosmos), in the interests of the Russian Academy of Sciences represented by its Space Research Institute (IKI), and the Deutsches Zentrum für Luft- und Raumfahrt (DLR). The SRG spacecraft was built by Lavochkin Association (NPOL) and its subcontractors, and is operated by NPOL with support from the Max Planck Institute for Extraterrestrial Physics (MPE). The development and construction of the eROSITA X-ray instrument was led by MPE, with contributions from the Dr. Karl Remeis Observatory Bamberg and ECAP (FAU Erlangen-Nuernberg), the University of Hamburg Observatory, the Leibniz Institute for Astrophysics Potsdam (AIP), and the Institute for Astronomy and Astrophysics of the University of Tübingen, with the support of DLR and the Max Planck Society. The Argelander Institute for Astronomy of the University of Bonn and the Ludwig Maximilians Universität Munich also participated in the science preparation for eROSITA. The eROSITA data shown here were processed using the eSASS/NRTA software system developed by the German eROSITA consortium. Partly based on observations obtained with *XMM-Newton*, an ESA science mission with instruments and contributions directly funded by ESA Member States and NASA. We acknowledge the Wajarri Yamatji people as the traditional owners of the Murchison Radio-astronomy Observatory, where ASKAP is located.

References

- Alvarez, G. E., Randall, S. W., Bourdin, H., Jones, C., & Holley-Bockelmann, K. 2018, *ApJ*, **858**, 44
- Andrade-Santos, F., Jones, C., Forman, W. R., et al. 2017, *ApJ*, **843**, 76
- Arnaud, K. A. 1996, *ASP Conf. Ser.*, **101**, 17
- Asplund, M., Grevesse, N., Sauval, A. J., & Scott, P. 2009, *ARA&A*, **47**, 481
- Bertin, E., & Arnouts, S. 1996, *A&AS*, **117**, 393
- Biffi, V., Dolag, K., Reiprich, T. H., et al. 2022, *A&A*, **661**, A17 (eROSITA EDR SI)
- Birzan, L., Rafferty, D. A., McNamara, B. R., Wise, M. W., & Nulsen, P. E. J. 2004, *ApJ*, **607**, 800
- Bond, J. R., Kofman, L., & Pogosyan, D. 1996, *Nature*, **380**, 603
- Bond, N. A., Strauss, M. A., & Cen, R. 2010, *MNRAS*, **409**, 156
- Brüggen, M., Reiprich, T. H., Bulbul, E., et al. 2021, *A&A*, **647**, A3
- Brunner, H., Liu, T., Lamer, G., et al. 2022, *A&A*, **661**, A1 (eROSITA EDR SI)
- Bulbul, E., Randall, S. W., Bayliss, M., et al. 2016, *ApJ*, **818**, 131
- Cash, W. 1979, *ApJ*, **228**, 939
- Cavaliere, A., & Fusco-Femiano, R. 1976, *A&A*, **500**, 95
- Cen, R., & Ostriker, J. P. 1999, *ApJ*, **514**, 1
- Davé, R., Cen, R., Ostriker, J. P., et al. 2001, *ApJ*, **552**, 473
- De Grandi, S., Böhringer, H., Guzzo, L., et al. 1999, *ApJ*, **514**, 148
- De Luca, A., & Molendi, S. 2004, *A&A*, **419**, 837
- Dolag, K., Meneghetti, M., Moscardini, L., Rasia, E., & Bonaldi, A. 2006, *MNRAS*, **370**, 656
- Dolag, K., Borgani, S., Murante, G., & Springel, V. 2009, *MNRAS*, **399**, 497
- Eckert, D., Molendi, S., Owers, M., et al. 2014, *A&A*, **570**, A119
- Erlar, J., Ramos-Ceja, M. E., Basu, K., & Bertoldi, F. 2019, *MNRAS*, **484**, 1988
- ESA: XMM-Newton SOC. 2020, *XMM-Newton Users Handbook*, Issue 2.18 (USA: NASA)
- Fujita, Y., Tawa, N., Hayashida, K., et al. 2008, *PASJ*, **60**, S343
- Ghirardini, V., Bulbul, E., Hoang, D. N., et al. 2021, *A&A*, **647**, A4
- Gupta, N., Saro, A., Mohr, J. J., et al. 2017, *MNRAS*, **467**, 3737
- Hudson, D. S., Mittal, R., Reiprich, T. H., et al. 2010, *A&A*, **513**, A37
- Kovács, O. E., Bogdán, Á., Smith, R. K., Kraft, R. P., & Forman, W. R. 2019, *ApJ*, **872**, 83
- Kull, A., & Böhringer, H. 1999, *A&A*, **341**, 23
- Kuntz, K. D., & Snowden, S. L. 2008, *A&A*, **478**, 575
- Lakhchaura, K., Mernier, F., & Werner, N. 2019, *A&A*, **623**, A17
- Lin, Y.-T., Partridge, B., Poher, J. C., et al. 2009, *ApJ*, **694**, 992
- Liu, A., Yu, H., Diaferio, A., et al. 2018, *ApJ*, **863**, 102
- Liu, A., Zhai, M., & Tozzi, P. 2019, *MNRAS*, **485**, 1651
- Liu, A., Bulbul, E., Ghirardini, V., et al. 2022, *A&A*, **661**, A2 (eROSITA EDR SI)
- Lovisari, L., Reiprich, T. H., & Schellenberger, G. 2015, *A&A*, **573**, A118
- Markevitch, M., & Vikhlinin, A. 2007, *Phys. Rep.*, **443**, 1
- Maughan, B. J., & Reiprich, T. H. 2019, *Open J. Astrophys.*, **2**, 9
- McNamara, B. R., & Nulsen, P. E. J. 2007, *ARA&A*, **45**, 117
- Merloni, A., Predehl, P., Becker, W., et al. 2012, *ArXiv e-prints* [arXiv:1209.3114]
- Mernier, F., de Plaa, J., Kaastra, J. S., et al. 2017, *A&A*, **603**, A80
- Morganti, R., Killeen, N. E. B., & Tadhunter, C. N. 1993, *MNRAS*, **263**, 1023
- Nicastro, F., Krongold, Y., Mathur, S., & Elvis, M. 2017, *Astron. Nachr.*, **338**, 281
- Nicastro, F., Kaastra, J., Krongold, Y., et al. 2018, *Nature*, **558**, 406
- Norris, R. P., Hopkins, A. M., Afonso, J., et al. 2011, *PASA*, **28**, 215
- Pacaud, F., Pierre, M., Refregier, A., et al. 2006, *MNRAS*, **372**, 578
- Panagoulia, E. K., Sanders, J. S., & Fabian, A. C. 2015, *MNRAS*, **447**, 417
- Piffaretti, R., Arnaud, M., Pratt, G. W., Pointecouteau, E., & Melin, J. B. 2011, *A&A*, **534**, A109
- Predehl, P., Andritschke, R., Arefiev, V., et al. 2021, *A&A*, **647**, A1
- Ramos-Ceja, M. E., Pacaud, F., Reiprich, T. H., et al. 2019, *A&A*, **626**, A48
- Randall, S., Nulsen, P., Forman, W. R., et al. 2008, *ApJ*, **688**, 208
- Reiprich, T. H., Basu, K., Ettori, S., et al. 2013, *Space Sci. Rev.*, **177**, 195
- Reiprich, T. H., Veronica, A., Pacaud, F., et al. 2021, *A&A*, **647**, A2
- Rost, A., Kuchner, U., Welker, C., et al. 2021, *MNRAS*, **502**, 714
- Sanders, J. S., Fabian, A. C., Taylor, G. B., et al. 2016, *MNRAS*, **457**, 82
- Sarazin, C. L. 2002, *The Physics of Cluster Mergers*, eds. L. Feretti, I. M. Gioia, & G. Giovannini (Berlin: Springer), 272, 1
- Schellenberger, G., & Reiprich, T. H. 2015, *A&A*, **583**, L2
- Snowden, S. L., Mushotzky, R. F., Kuntz, K. D., & Davis, D. S. 2008, *A&A*, **478**, 615
- Springel, V., White, S. D. M., Tormen, G., & Kauffmann, G. 2001, *MNRAS*, **328**, 726
- Springel, V., Frenk, C. S., & White, S. D. M. 2006, *Nature*, **440**, 1137
- Su, Y., Gu, L., White, Raymond E., I., & Irwin, J. 2014, *ApJ*, **786**, 152
- Su, Y., Kraft, R. P., Nulsen, P. E. J., et al. 2017a, *ApJ*, **835**, 19
- Su, Y., Kraft, R. P., Roediger, E., et al. 2017b, *ApJ*, **834**, 74
- Su, Y., Kraft, R. P., Nulsen, P. E. J., et al. 2019, *AJ*, **158**, 6
- Su, Y., Zhang, Y., Liang, G., et al. 2020, *MNRAS*, **498**, 5620
- Sugawara, Y., Takizawa, M., Itahana, M., et al. 2017, *PASJ*, **69**, 93
- Tittley, E. R., & Henriksen, M. 2001, *ApJ*, **563**, 673
- Tritton, K. P. 1972, *MNRAS*, **158**, 277
- Trussoni, E., Vagnetti, F., Massaglia, S., et al. 1999, *A&A*, **348**, 437
- Venturi, T., Morganti, R., Tzioumis, T., & Reynolds, J. 2000, *A&A*, **363**, 84
- Vikhlinin, A. 2006, *ApJ*, **640**, 710
- Werner, N., Finoguenov, A., Kaastra, J. S., et al. 2008, *A&A*, **482**, L29
- West, M. J., Jones, C., & Forman, W. 1995, *ApJ*, **451**, L5

Appendix A: *XMM-Newton* – Lightcurves

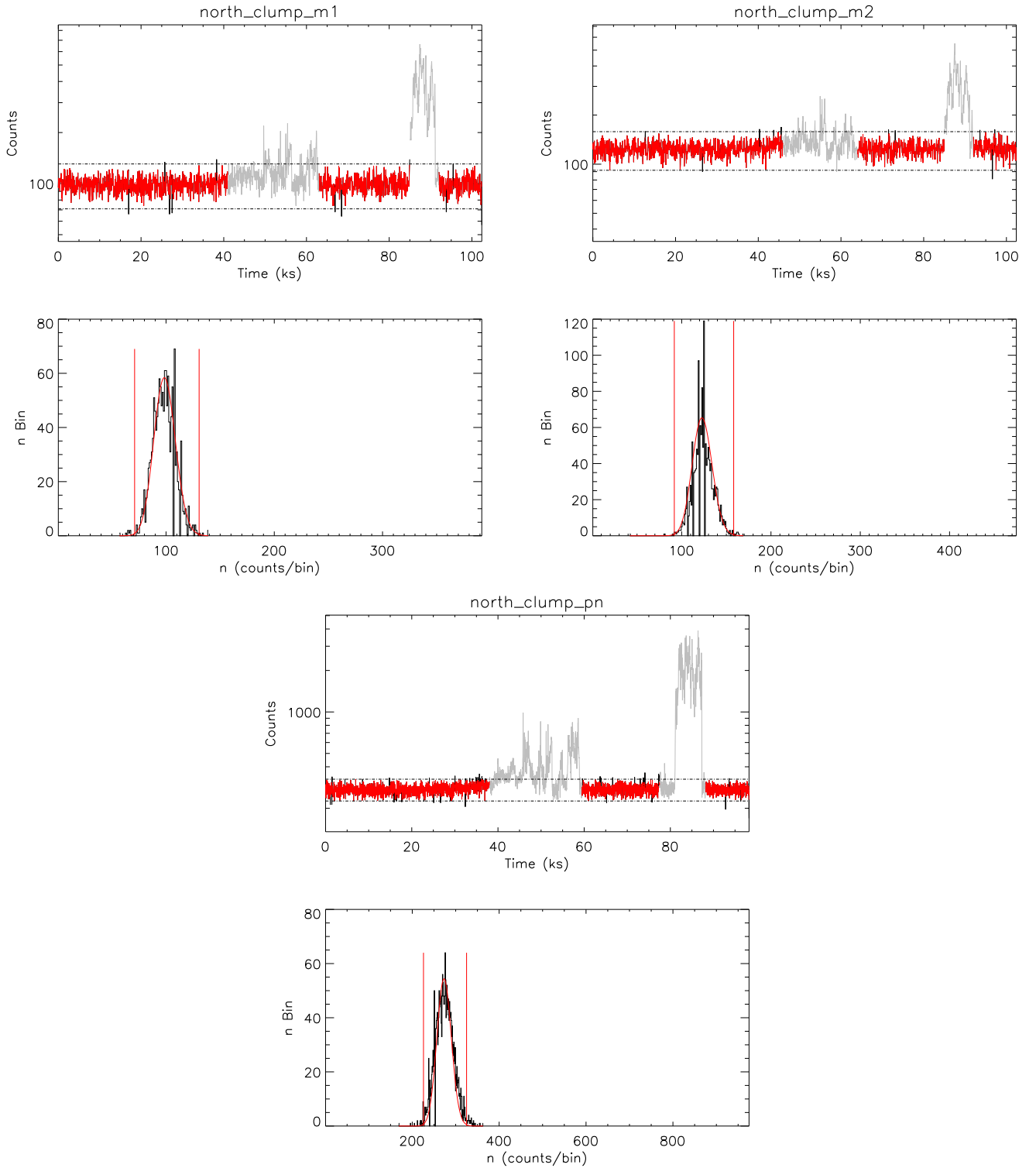


Fig. A.1: Top panels show the lightcurves of MOS1 (*top left*), MOS2 (*top right*), and pn (*bottom*) of the Northern Clump observation (ObsID: 0852980601). The red line depicts the accepted portion of the observation, while the grey is the rejected portion due to SPF. The dashed lines mark the 3σ . The bottom panels show the histograms of the associated lightcurves, fitted with Gaussian (red curve). The red vertical lines mark the 3σ .

Appendix B: *XMM-Newton* – Images

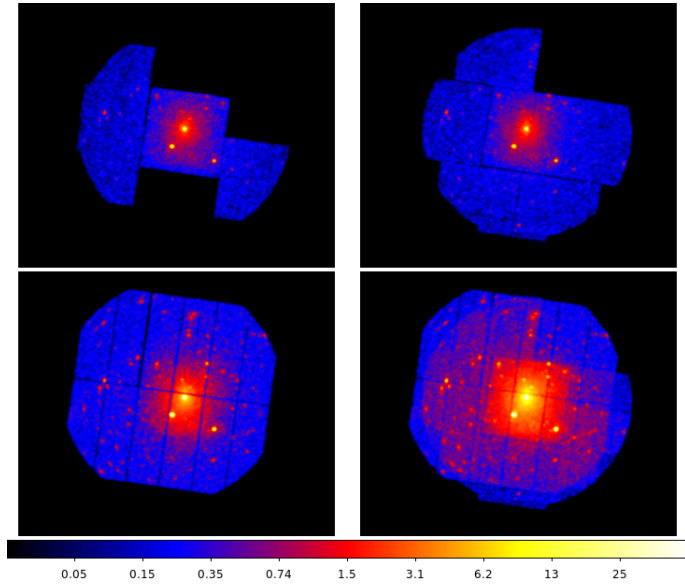


Fig. B.1: *XMM-Newton* cleaned photon images, i.e., SPF filtered, QPB subtracted, anomalous CCDs removed, in the energy band 0.5 – 2 keV. *Top left*: MOS1 image. *Top right*: MOS2 image. *Bottom left*: pn image. *Bottom right*: MOS1+2+pn image.

Appendix C: *XMM-Newton* – Surface brightness profile

The S_X profiles of the three setups are compared in Fig. C.1 (left). The blue, green, and red solid lines are the S_X profiles for circular annuli, box annuli, and pn-only box annuli setup. The dotted lines of the respective colors are their β -model fits. The β -model best-fit parameters can be found in Table C.1. In the bottom panel, their residuals are plotted in the unit of σ .

Table C.1: The β -model best-fit parameters.

Setups	$S_X(0)$ [cts/s/arcmin ²]	β	r_c [']
circular	0.05 ± 0.004	0.368 ± 0.007	0.310 ± 0.04
box	0.0218 ± 0.001	0.396 ± 0.010	0.660 ± 0.053
pn box	0.0715 ± 0.002	0.404 ± 0.011	0.718 ± 0.053

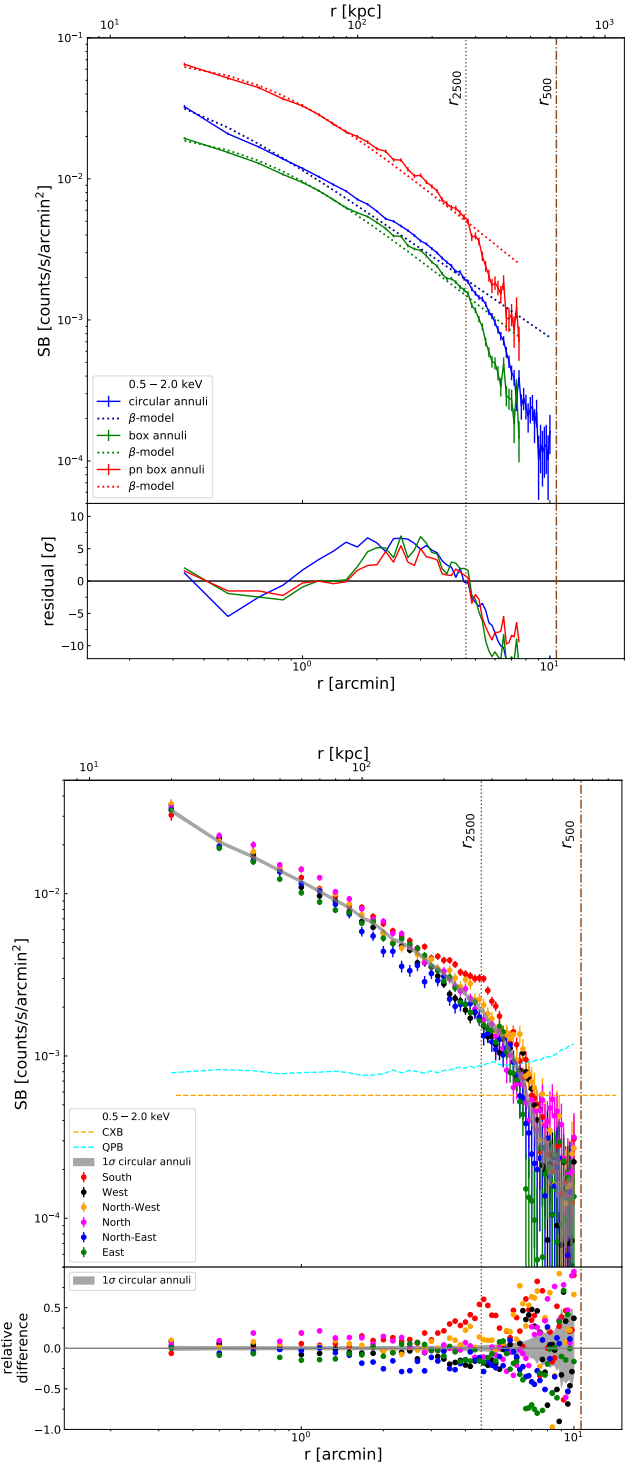


Fig. C.1: *XMM-Newton* S_X profiles calculated from *XMM-Newton* data in the energy band 0.5 – 2.0 keV. *Top*: The full azimuthal S_X profiles. The top panel shows the S_X profiles (solid lines) and the corresponding β -model fits (dotted lines) of all *XMM-Newton* detectors with circular annuli setup (blue) and box annuli setup (green), as well as the pn-only box annuli setup (red). The bottom panel shows the residuals in unit of σ . *Bottom*: *XMM-Newton* S_X profiles of different sectors *top* and their relative differences *bottom* from circular annuli setup. The grey shaded areas are the 1σ confidence regions of the full azimuthal S_X . The brown vertical lines indicate the various radii.

Appendix D: Spectral analysis

We performed several tests using `pgstat` statistic provided in `XSPEC`, where the *XMM-Newton* source data were treated as Poisson data (C-statistic) and the background as Gaussian. Initially, we fit spectra that are grouped to have a minimum of 5 counts (`grouping5`) and 25 counts (`grouping25`) per bin. Then, we grouped the source spectra based on the background spectra, as such we would have 25 counts per bin for the background spectra (`bgdGrouping25`). This ensures the background spectra to be Gaussian. These tests were carried out for all the Northern Clump spectral analysis regions. We show the results from the full azimuthal region in Fig. D.1 as a representative. In the plots we compare the fitting results using χ^2 -statistic (blue points, $\text{stat}/\text{dof}=0.97$), `pgstat` `grouping5` (red, $\text{stat}/\text{dof}=1.06$), `pgstat` `grouping25` (green, $\text{stat}/\text{dof}=1.09$), and `pgstat` `bgdGrouping25` (orange, $\text{stat}/\text{dof}=1.12$). The resulting cluster parameters of these tests in various regions are always consistent within the 1σ error bars of the χ^2 -statistic fitting results.

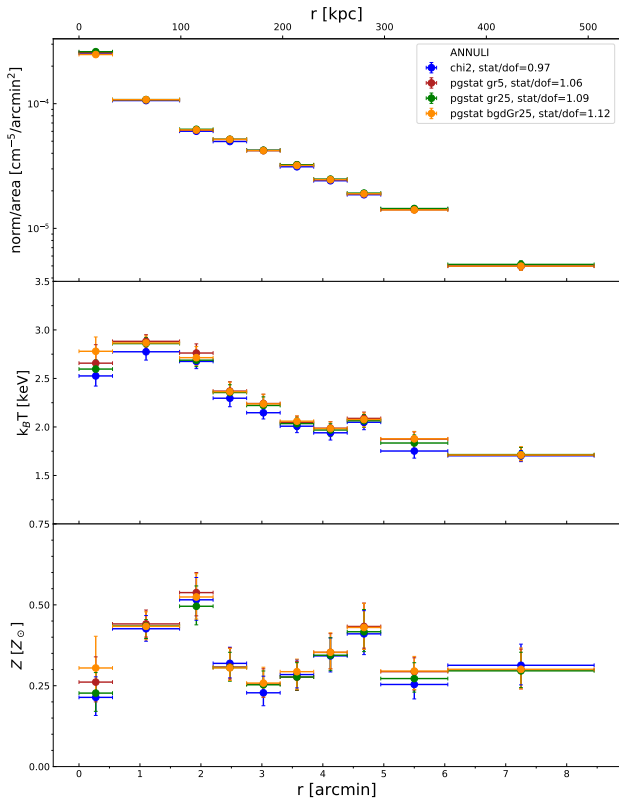


Fig. D.1: Normalization (top), temperature (middle), and metallicity (bottom) profiles of the Northern Clump derived in the energy band 0.7 – 7.0 keV. Blue points are estimated using χ^2 -statistics, while the red, green, and orange points are estimated using `pgstat` statistic with source spectrum grouping 5, 25, and background spectrum grouping 25.

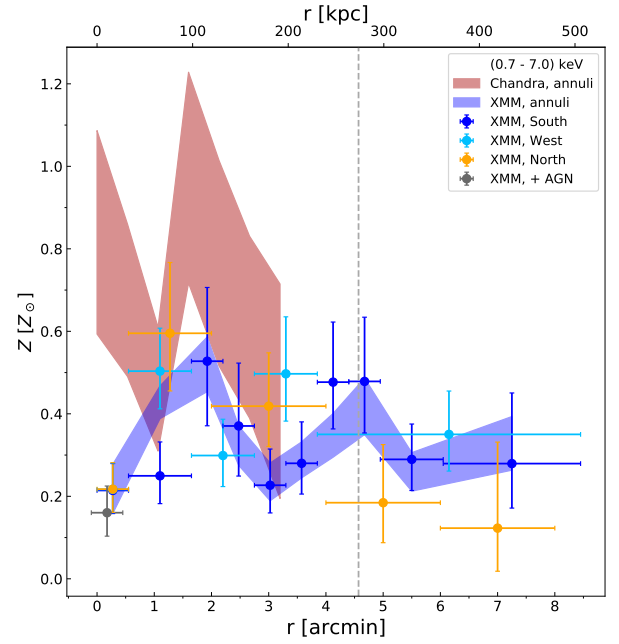


Fig. D.2: Metallicity profiles of various regions in the Northern Clump cluster in the energy band 0.7 – 7.0 keV. The blue and red shaded areas represent *XMM-Newton* and *Chandra* metallicity in full azimuthal direction. Due to modest photon counts, *Chandra* cannot constrain the metallicity. The dark blue, cyan, and magenta data points represent *XMM-Newton* metallicity profiles in the south, west, and north directions, respectively. The grey dashed lines indicate the R_{2500} of the Northern Clump. The x-axis error bars are not the 1σ error range, but the full width of the bins.

Table D.1: *XMM-Newton* best-fit values of central bin with different methods in energy 0.7 – 7.0 keV.

AGN method	$norm^{\dagger}$	$k_B T$ [keV]	Z [Z_{\odot}]
1	$2.535^{+0.096}_{-0.095}$	2.532 ± 0.105	$0.217^{+0.064}_{-0.056}$
2	$2.651^{+0.12}_{-0.118}$	$2.411^{+0.118}_{-0.116}$	$0.16^{+0.065}_{-0.057}$
3	$1.682^{+0.268}_{-0.277}$	$3.055^{+0.208}_{-0.221}$	$0.155^{+0.06}_{-0.05}$
	$0.969^{+0.344}_{-0.308}$	1.528	–

† the presented values have been normalized by their respective source areas [$10^{-4} \text{ cm}^{-5}/\text{arcmin}^2$]

Table D.2: *XMM-Newton* and *Chandra* best-fit spectral fitting values in the south, west, and north in the energy band 0.7 – 7.0 keV.

<i>XMM-Newton</i>				<i>Chandra</i>	
annulus [']	$norm^\dagger$ [$10^{-4} \text{ cm}^{-5}/\text{arcmin}^2$]	$k_B T$ [keV]	Z [Z_\odot]	$norm^\dagger$ [$10^{-4} \text{ cm}^{-5}/\text{arcmin}^2$]	$k_B T$ [keV]
South					
0.0 – 0.55	$2.539^{+0.096}_{-0.094}$	$2.524^{+0.107}_{-0.106}$	$0.214^{+0.065}_{-0.056}$	$2.787^{+0.22}_{-0.22}$	$2.74^{+0.5}_{-0.36}$
0.55 – 1.65	$1.212^{+0.051}_{-0.052}$	$2.593^{+0.125}_{-0.123}$	$0.25^{+0.082}_{-0.067}$	$1.137^{+0.046}_{-0.046}$	$3.35^{+0.43}_{-0.31}$
1.65 – 2.2	$0.66^{+0.046}_{-0.043}$	$2.791^{+0.25}_{-0.232}$	$0.528^{+0.179}_{-0.157}$	$0.911^{+0.073}_{-0.073}$	$1.87^{+0.32}_{-0.19}$
2.2 – 2.75	$0.536^{+0.034}_{-0.034}$	$2.732^{+0.256}_{-0.178}$	$0.371^{+0.152}_{-0.121}$	$0.636^{+0.041}_{-0.041}$	$2.71^{+0.52}_{-0.34}$
2.75 – 3.3	$0.482^{+0.033}_{-0.033}$	$1.93^{+0.131}_{-0.134}$	$0.227^{+0.088}_{-0.067}$	$0.467^{+0.033}_{-0.027}$	$1.86^{+0.23}_{-0.22}$
3.3 – 3.85	$0.385^{+0.029}_{-0.031}$	$1.756^{+0.148}_{-0.098}$	$0.28^{+0.1}_{-0.075}$	$0.395^{+0.023}_{-0.028}$	$2.24^{+0.4}_{-0.24}$
3.85 – 4.4	$0.295^{+0.026}_{-0.026}$	$1.845^{+0.131}_{-0.147}$	$0.477^{+0.146}_{-0.113}$	$0.323^{+0.024}_{-0.024}$	$1.89^{+0.25}_{-0.2}$
4.4 – 4.95	$0.252^{+0.024}_{-0.022}$	$1.9^{+0.134}_{-0.155}$	$0.479^{+0.156}_{-0.125}$	$0.324^{+0.022}_{-0.022}$	$2.15^{+0.44}_{-0.24}$
4.95 – 6.05	$0.157^{+0.014}_{-0.013}$	$1.631^{+0.067}_{-0.083}$	$0.29^{+0.086}_{-0.075}$	$0.185^{+0.013}_{-0.013}$	$2.17^{+0.41}_{-0.24}$
6.05 – 8.45	$0.059^{+0.008}_{-0.007}$	$1.732^{+0.279}_{-0.069}$	$0.279^{+0.171}_{-0.108}$	$0.047^{+0.004}_{-0.004}$	$2.17^{+0.58}_{-0.26}$
4.0 – 6.0	$0.211^{+0.011}_{-0.011}$	$1.703^{+0.103}_{-0.042}$	$0.344^{+0.041}_{-0.054}$	*	*
6.0 – 8.0	$0.068^{+0.009}_{-0.009}$	$1.756^{+0.261}_{-0.098}$	$0.3^{+0.181}_{-0.109}$	*	*
8.0 – 10.0	$0.024^{+0.003}_{-0.004}$	$1.72^{+0.326}_{-0.144}$	0.3	*	*
10.0 – 12.5	$0.011^{+0.003}_{-0.002}$	$1.709^{+0.663}_{-0.368}$	0.3	*	*
West					
0.0 – 0.55	$2.536^{+0.096}_{-0.095}$	$2.531^{+0.105}_{-0.105}$	$0.217^{+0.064}_{-0.056}$	$1.99^{+0.108}_{-0.161}$	$3.55^{+0.73}_{-0.55}$
0.55 – 1.65	$1.015^{+0.041}_{-0.041}$	$2.811^{+0.151}_{-0.144}$	$0.503^{+0.104}_{-0.091}$	$1.129^{+0.04}_{-0.034}$	$3.43^{+0.3}_{-0.27}$
1.65 – 2.75	$0.532^{+0.023}_{-0.023}$	$2.629^{+0.153}_{-0.133}$	$0.299^{+0.088}_{-0.075}$	$0.518^{+0.034}_{-0.03}$	$3.5^{+1.02}_{-0.69}$
2.75 – 3.85	$0.266^{+0.016}_{-0.015}$	$2.548^{+0.159}_{-0.168}$	$0.497^{+0.138}_{-0.115}$	$0.291^{+0.013}_{-0.013}$	$2.71^{+0.33}_{-0.28}$
3.85 – 8.45	$0.081^{+0.006}_{-0.006}$	$1.861^{+0.142}_{-0.166}$	$0.35^{+0.105}_{-0.089}$	$0.064^{+0.005}_{-0.005}$	$2.79^{+0.67}_{-0.47}$
4.0 – 6.0	$0.133^{+0.006}_{-0.006}$	$1.958^{+0.09}_{-0.098}$	$0.396^{+0.082}_{-0.053}$	*	*
6.0 – 8.0	$0.058^{+0.005}_{-0.005}$	$1.666^{+0.196}_{-0.166}$	$0.241^{+0.08}_{-0.077}$	*	*
8.0 – 10.0	$0.014^{+0.002}_{-0.003}$	$1.363^{+0.152}_{-0.128}$	0.3	*	*
10.0 – 12.5	$0.002^{+0.002}_{-}$	$1.365^{+0.607}_{-0.499}$	0.3	*	*
North					
0.0 – 0.55	$2.537^{+0.096}_{-0.095}$	$2.53^{+0.11}_{-0.1}$	$0.22^{+0.06}_{-0.06}$	*	*
0.55 – 2.0	$0.989^{+0.056}_{-0.056}$	$2.95^{+0.21}_{-0.21}$	$0.6^{+0.17}_{-0.14}$	*	*
2.0 – 4.0	$0.363^{+0.023}_{-0.024}$	$2.22^{+0.19}_{-0.12}$	$0.42^{+0.13}_{-0.1}$	*	*
4.0 – 6.0	$0.159^{+0.018}_{-0.016}$	$2.01^{+0.29}_{-0.28}$	$0.18^{+0.14}_{-0.1}$	*	*
6.0 – 8.0	$0.069^{+0.019}_{-0.016}$	$1.53^{+0.38}_{-0.25}$	$0.12^{+0.21}_{-0.1}$	*	*
8.0 – 10.0	$0.056^{+0.015}_{-0.015}$	$1.87^{+0.71}_{-0.36}$	$0.22^{+0.53}_{-0.19}$	*	*
10.0 – 12.5	$0.063^{+0.025}_{-0.022}$	$0.99^{+0.08}_{-0.11}$	$0.11^{+0.12}_{-0.07}$	*	*
[†] the presented values have been normalized by their respective source areas * <i>Chandra</i> observations do not cover these regions					

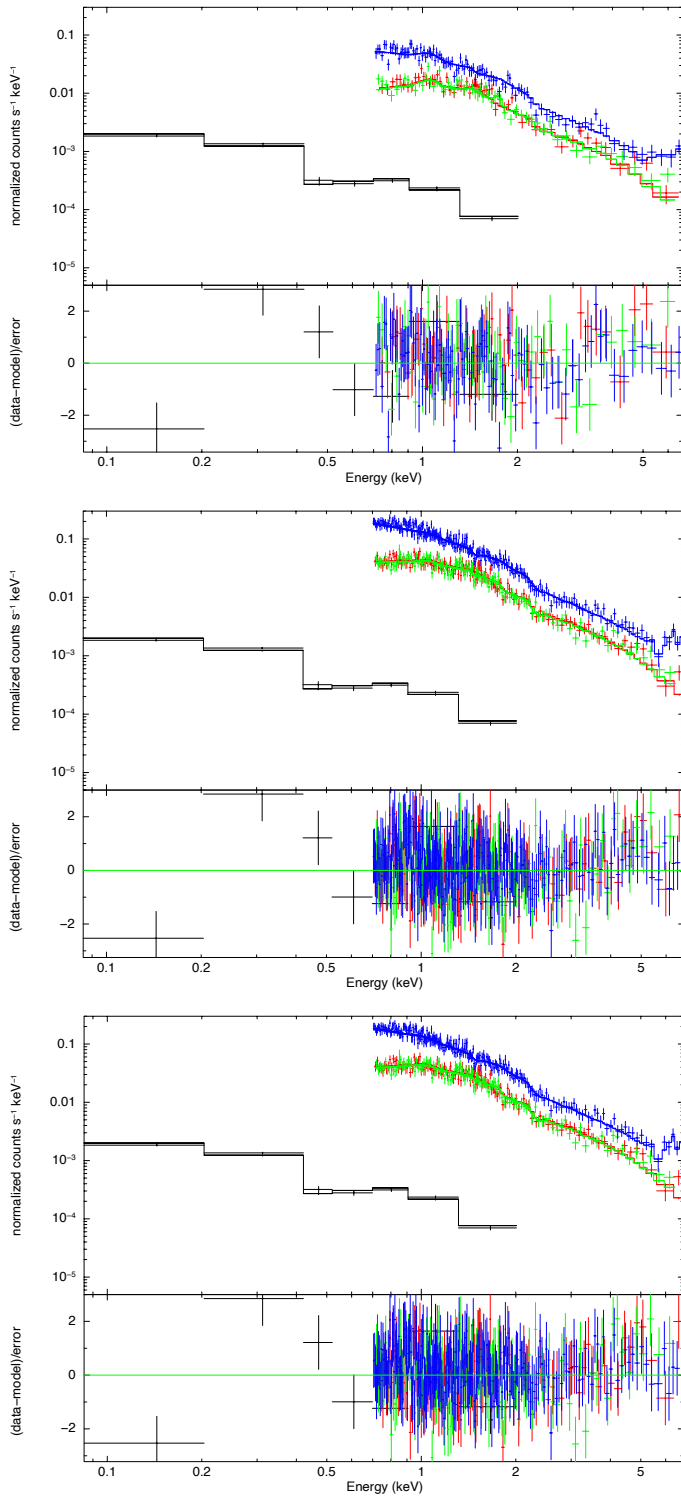


Fig. D.3: *XMM-Newton* and RASS background spectra (black) of the central bin fitted with the three different central AGN models in the energy range of 0.7 – 7.0 keV. *Top*: Method 1 – with 15'' mask to mask the central AGN. *Middle*: Method 2 – AGN component is modeled from *Chandra* best fit values. *Bottom*: Method 3 – AGN is modeled and additional thermal component is added.

Appendix B

The eROSITA view of the Abell 3391/95 field: Cluster outskirts and filaments

The publication *Veronica et al. A&A (2024), 681, A108* is reproduced below in its original form.

The eROSITA view of the Abell 3391/95 field

Cluster outskirts and filaments[★]

Angie Veronica¹, Thomas H. Reiprich¹, Florian Pacaud¹, Naomi Ota^{1,7}, Jann Aschersleben^{1,6},
Veronica Biffi^{4,5}, Esra Bulbul², Nicolas Clerc², Klaus Dolag³, Thomas Erben¹, Efrain Gatzuz², Vittorio Ghirardini²,
Jürgen Kerp¹, Matthias Klein², Ang Liu², Teng Liu², Konstantinos Migkas^{1,8}, Miriam E. Ramos-Ceja²,
Jeremy Sanders², and Claudia Spinelli¹

¹ Argelander-Institut für Astronomie (AIfA), Universität Bonn, Auf dem Hügel 71, 53121 Bonn, Germany
e-mail: averonica@astro.uni-bonn.de

² Max-Planck-Institut für extraterrestrische Physik, Gießenbachstraße 1, 85748 Garching, Germany
e-mail: egatzuz@mpe.mpg.de

³ Universitäts-Sternwarte, Fakultät für Physik, Ludwig-Maximilians-Universität München, Scheinerstr.1,
81679 München, Germany

⁴ INAF – Osservatorio Astronomico di Trieste, via Tiepolo 11, 34143 Trieste, Italy

⁵ IFPU – Institute for Fundamental Physics of the Universe, Via Beirut 2, 34014 Trieste, Italy

⁶ Kapteyn Astronomical Institute, University of Groningen, PO Box 800, 9700 AV Groningen, The Netherlands

⁷ Nara Women's University, Kitauoyanishi-machi, Nara 630-8506, Japan

⁸ Leiden Observatory, Leiden University, PO Box 9513, 2300 RA Leiden, The Netherlands

Received 29 May 2023 / Accepted 31 October 2023

ABSTRACT

Context. About 30% – 40% of the baryons in the local Universe remain unobserved. Many of these “missing” baryons are expected to reside in the warm-hot intergalactic medium (WHIM) of the cosmic web filaments that connect clusters of galaxies. SRG/eROSITA performance verification (PV) observations covered about 15 square degrees of the A3391/95 system and have revealed a ~15 Mpc continuous soft emission connecting several galaxy groups and clusters.

Aims. We aim to characterize the gas properties in the cluster outskirts ($R_{500} < r < R_{200}$) and in the detected inter-cluster filaments ($> R_{200}$) and to compare them to predictions.

Methods. We performed X-ray image and spectral analyses using the eROSITA PV data in order to assess the gas morphology and properties in the outskirts and the filaments in the directions of the previously detected Northern and Southern Filament of the A3391/95 system. We constructed surface brightness profiles using particle-induced background-subtracted, exposure- and Galactic absorption-corrected eROSITA products in the soft band (0.3–2.0 keV). We constrained the temperatures, metallicities, and electron densities through X-ray spectral fitting and compared them with the expected properties of the WHIM. We took particular care of the foreground.

Results. In the filament-facing outskirts of A3391 and the Northern Clump, we find higher temperatures than typical cluster outskirts profiles, with a significance of between 1.6 and 2.8 σ , suggesting heating due to their connections with the filaments. We confirm surface brightness excess in the profiles of the Northern, Eastern, and Southern Filaments. From spectral analysis, we detect hot gas of $0.96^{+0.17}_{-0.14}$ keV and $1.09^{+0.09}_{-0.06}$ keV for the Northern and Southern Filament, respectively, which are close to the upper WHIM temperature limit. The filament metallicities are below 10% solar metallicity and the electron densities are ranging between 2.6 and $6.3 \times 10^{-5} \text{ cm}^{-3}$. The characteristic properties of the Little Southern Clump (LSC), which is located at a distance of $\sim 1.5R_{200}$ from A3395S in the Southern Filament, suggest that it is a small galaxy group. Excluding the LSC from the analysis of the Southern Filament does not significantly change the temperature or metallicity of the gas, but it decreases the gas density by 30%. This shows the importance of taking into account any clumps in order to avoid overestimation of the gas measurement in the outskirts and filament regions.

Conclusions. We present measurements of morphology, temperature, metallicity, and density of individual warm-hot filaments. The electron densities of the filaments are consistent with the WHIM properties as predicted by cosmological simulations, but the temperatures are higher. As both filaments are short (1.8 and 2.7 Mpc) and located in a denser environment, stronger gravitational heating may be responsible for this temperature enhancement. The metallicities are low, but still within the expected range from the simulations.

Key words. galaxies: clusters: individual: Abell 3391 – galaxies: clusters: individual: Abell 3395 – galaxies: groups: general – large-scale structure of Universe – X-rays: galaxies – X-rays: galaxies: clusters

1. Introduction

The missing baryon problem states that about 30% – 40% of the total baryons in the Universe are still unaccounted for (e.g.,

Shull et al. 2012). According to the large-scale cosmological simulations (e.g., Cen & Ostriker 1999; Davé et al. 2001), they should be found in the warm-hot intergalactic medium (WHIM) located in the so-called cosmic web filaments (Bond et al. 1996). These filaments connect galaxy clusters and play an important role in transferring matter onto the clusters, thus supporting their growth (West et al. 1995; Tanaka et al. 2007; Bond et al. 2010).

[★] Image that is displayed in Fig. 1 is available at the CDS via anonymous ftp to cdsarc.cds.unistra.fr (130.79.128.5) or via <https://cdsarc.cds.unistra.fr/viz-bin/cat/J/A+A/681/A108>

Due to the faint nature of the WHIM emission (the electron densities and temperature ranging between $n_e \approx 10^{-6} - 10^{-4} \text{ cm}^{-3}$ and $T = 10^5 - 10^7 \text{ K}$ (Nicastro et al. 2017), respectively) detecting the WHIM is challenging. However, with the X-ray emissivity being proportional to the square of the density, it is reasonable to direct attempts at the densest part of this tenuous gas, for example between a pair of galaxy clusters (e.g., Kull & Böhringer 1999; Fujita et al. 2008; Vazza et al. 2019), as well as at the outskirts of a galaxy cluster (e.g., Reiprich et al. 2013; Nicastro et al. 2018). Studies of the WHIM at these locations include measurements of the filament between the Abell 222 and 223 cluster pair (Werner et al. 2008b), the Abell 399 and 401 system (e.g., Akamatsu et al. 2017; Bonjean et al. 2018), the Abell 98N/S system (Sarkar et al. 2022; Alvarez et al. 2022), the outskirts of the Coma cluster (Bonamente et al. 2009, 2022), the Abell 2744 cluster (Eckert et al. 2015a; Hattori et al. 2017), and the Abell 1750 cluster (Bulbul et al. 2016).

The binary galaxy cluster system Abell 3391 and Abell 3395 (A3391/95) is also one of the systems where a search for the WHIM has been carried out, and the system has therefore been observed extensively using various instruments of different wavelengths, including several X-ray telescopes; for example by ROSAT and ASCA and more recently by *XMM-Newton*, *Chandra*, and *Suzaku*. Earlier studies showed that the gas between the A3391 and the double-peaked A3395S/N (hereafter referred to as the bridge) is consistent with a filament (Tittley & Henriksen 2001). While latter studies concluded that the gas properties in these regions are more typical of tidally stripped intracluster medium (ICM) gas from A3391 and A3395, a sign of an early cluster merger phase (Sugawara et al. 2017; Alvarez et al. 2018). A study of the A3391/95 system was also carried out using *Planck* data, and a significant excess of signal near the A3395S/N system in the thermal Sunyaev-Zel'dovich (tSZ) residual map was reported (Planck Collaboration Int. VIII 2013). However, the individual components of this cluster cannot be resolved by the data due to the modest resolution of *Planck*.

The extended Roentgen Survey with an Imaging Telescope Array (eROSITA, Predehl et al. 2021) is the newly launched German X-ray telescope on board the Spectrum-Roentgen-Gamma (SRG) mission. It has a wide field-of-view (FoV) of 1.03 degrees in diameter. In the soft energy band of 0.5–2.0 keV, the effective area of the seven combined eROSITA telescope modules (TMs) is slightly higher than the combined *XMM-Newton* cameras (MOS1+MOS2+pn; Predehl et al. 2021). Additionally, eROSITA operates in the scan and survey modes, which allows us to easily reach the virial radii of clusters and to constrain foreground and background emission. The FoV-averaged PSF ($\sim 26''$) is significantly better than that of the *Suzaku* satellite, allowing us to remove unrelated background sources to much lower flux levels. The energy resolution at soft energies is better than for any other operating X-ray satellite CCD, allowing us to better characterize soft band emission lines. And the short focal length of 1.6 m minimizes the particle-induced background (PIB) levels. These properties make eROSITA an excellent instrument for studying the outskirts of galaxy clusters and finding large-scale structures.

In October 2019, the A3391/95 system was observed as one of the eROSITA performance verification (PV) targets. The field was observed four times during this phase, with three raster-scan observations and one pointing observation. The combination of all four observations covers an area of about 15 square degrees, which gives us the deepest large-scale X-ray view of the system to date. Using these observations, eROSITA revealed indications of the presence of warm gas in the bridge region, on top of the tidally stripped hot ICM gas (Reiprich et al. 2021). This

Table 1. eROSITA A3391/95 PV observations used in this work.

Observing date	ObsID (mode)	TM	Exposure ^(*) (ks)
October 2019	300005 (scan)	5–7	55
October 2019	300006 (scan)	5–7	54
October 2019	300016 (scan)	1–7	58
October 2019	300014 (pointed)	5–7	35

Notes. There are 16 datasets in total among the observations. ^(*)The exposure times listed are the average filtered on-axis exposure time across the available TMs of each observation.

finding is also seen in the analogous A3391/95 cluster system from Magneticum simulations (Biffi et al. 2022). Furthermore, a continuous soft emission extending from the north to the south was discovered. This $\sim 15 \text{ Mpc}$ filamentary structure seems to connect at least five galaxy groups and clusters. Those are A3391, A3395S, A3395N, the Northern Clump¹ (NC; MCXC J0621.7-5242 cluster or MS 0620.6-5239 cluster, Tittley & Henriksen 2001; Piffaretti et al. 2011; Veronica et al. 2022), the Little Southern Clump (LSC), and the MCXC J0631.3-5610 cluster. The LSC is embedded in the Southern Filament and has fully entered the $2R_{200}$ of A3395, while the center of the MCXC J0631.3-5610 cluster is just outside the FoV of these PV observations.

In this work, we utilize the eROSITA A3391/95 PV data to investigate the gas properties of the outskirts and the detected filaments. These filaments are the Northern and Eastern Filaments extending north and northeastward from the A3391 cluster, and the Southern Filament in the south of the A3395S/N cluster. The present paper is structured as follows: in Sect. 2, we describe our observations, the data reduction steps, and our analysis strategy. In Sect. 3, we present the results of our imaging analysis (Sect. 3.1) and those of our spectral analysis (Sect. 3.2). In Sect. 4, we discuss these results. Finally, in Sect. 5, we summarize our findings and conclude the results.

Unless stated otherwise, all uncertainties are at the 68.3% confidence interval. The assumed cosmology in this work is a flat Λ CDM cosmology adopted from Planck Collaboration VI (2020), such that the Hubble constant $H_0 = 67.4 \text{ km s}^{-1} \text{ Mpc}^{-1}$, $\Omega_m = 0.315$, $\Omega_\Lambda = 0.6847$, and $\Omega_b = 0.0493$. At the redshift of A3391 cluster, $z = 0.0555$, $1''$ corresponds to 1.119 kpc .

2. Data reduction and analysis

All eROSITA A3391/95 PV observations are listed in Table 1. We used eROSITA data processing in configuration c001. The data reduction steps of all 16 eROSITA data sets were performed using the extended Science Analysis Software (eSASS, Brunner et al. 2022) version eSASSUsers_201009. The data reduction steps and the image-correction steps were done following the procedure described in Sects. 2.1 and 3.3 of Reiprich et al. (2021), which include the particle-induced background (PIB) subtraction, exposure correction (including vignetting), and Galactic absorption correction across the FoV.

2.1. Imaging analysis

To focus on the soft emission in the outskirts and from the filaments, we used the energy band of 0.3–2.0 keV for the imaging

¹ The extended objects detected in the A3391/95 field are referred to as “clumps”, although, the Northern Clump, for example, is a galaxy cluster.

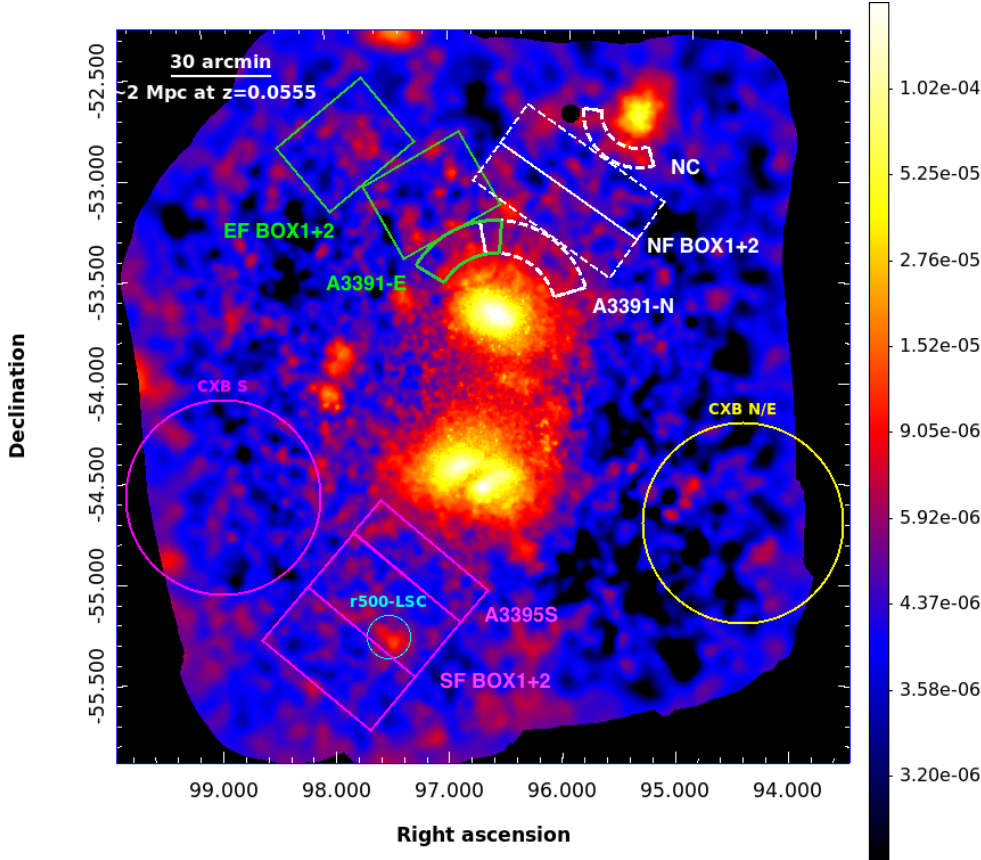


Fig. 1. eROSITA PIB-subtracted, exposure- and Galactic-absorption-corrected image in the 0.3–2.0 keV band. The image has been adaptively smoothed with S/N set to 12. The point sources have been removed and refilled with their surrounding background values. The defined regions are used for spectral analyses (see Sect. 2.2). The colorbar is in the units of counts per second (as well as the following X-ray images).

analysis. The lower energy limit used for the telescope modules (TMs) with an on-chip filter (TM1, 2, 3, 4, 6; the combination of these TMs is referred to as TM8) was set to 0.3 keV, while for the TMs without an on-chip filter (TM5 and 7; the combination of these TMs is referred to as TM9) due to the optical light leak contamination (Predehl et al. 2021), the lower energy limit was set to 0.5 keV. The count rates of the final image (all observations combined, and fully corrected) correspond to an effective area given by one TM with an on-chip filter in the energy band 0.3–2.0 keV.

The Galactic absorption across the FoV was corrected by calculating the ratio of the expected eROSITA count rates with the total hydrogen column density (N_H) at a given position to the count rate of the median N_H across the FoV. The count rates of different N_H values were estimated assuming a typical X-ray fore- and background model, that is one unabsorbed with one absorbed from diffuse thermal components and one power law component. These components represent the Local Hot Bubble (LHB), the Milky Way halo (MWH), and unresolved sources, respectively. The computed N_H values are from the A3391/95 total N_H map (for more details, see Sect. 2.5 of Reiprich et al. 2021) generated from the IRAS 100 μ m (Miville-Deschênes & Lagache 2005) and the HI4PI data (HI4PI Collaboration 2016). A ratio map relative to the median N_H was generated for each type of eROSITA TMs. We divided each exposure map by its corresponding ratio map for the Galactic absorption correction.

The point source catalog was generated using the method described in Pacaud et al. (2006) and Ramos-Ceja et al. (2019), that is, the point sources were detected on a wavelet-filtered image by the Source Extractor software (Bertin & Arnouts

1996). Using the obtained catalog, we excluded them from our analyses. The so-called ghosting procedure was also performed to generate the surface brightness image. Through this procedure, the areas from which the point sources were excised were refilled with surrounding background photons. Any ghosted images generated in this work were only used for visualization purposes. To avoid any biases introduced by using the artificially refilled pixels in the analysis, we excluded these pixels from any calculations and the missing area was properly taken into account. The final PIB-subtracted, point-sources-subtracted and refilled, exposure-corrected, and Galactic-absorption-corrected image is shown in Fig. 1. The image has been adaptively smoothed with a signal-to-noise ratio (S/N) set to 12 in order to enhance low-surface-brightness emission and large-scale features.

The X-ray surface brightness profiles were calculated using the final eROSITA products in the 0.3–2.0 keV energy band, including the photon image, the fully corrected exposure map, and the PIB map, as well as the point source catalog. The large eROSITA FoV and the SRG scan mode in which most of the observations were taken, allow us to model the cosmic X-ray background (CXB) from regions within the FoV. To account for the variation of the CXB, we placed ten boxes across the field. To ensure minimum emission from the clusters and the filaments, which could cause overestimation in the CXB level (and therefore underestimation of the surface brightness values), they were placed beyond the R_{200}^2 of each cluster and the defined area of the filaments. The configuration of these CXB boxes can

² All the cluster radii in this work are calculated using the relations stated in Reiprich et al. (2013), e.g., $r_{500} \approx 0.65r_{200}$, $r_{100} \approx 1.36r_{200}$, and $r_{2500} \approx 0.28r_{200}$.

Table 2. Information of the A3391/95 groups and clusters.

Object	RA (J2000)	Dec (J2000)	z	R_{500} ($'$) (Mpc)	R_{200} ($'$) (Mpc)
A3391 ^(a)	06h 26m 20.86s	−53d 41m 30.48s	0.0555	18.090 1.170	27.830 1.800
A3395N ^(a)	06h 27m 37.56s	−54d 26m 48.12s	0.0518	22.81 1.383	35.09 2.128
A3395S ^(a)	06h 26m 48.58s	−54d 32m 45.60s	0.0517	22.94 1.388	35.29 2.136
Northern ^(b) Clump	06h 21m 43.34s	−52d 41m 33.00s	0.0511	10.620 0.636	16.340 0.978
Little ^(c) Southern Clump	06h 30m 04.80s	−55d 17m 51.50s	0.0562	6.44 0.437	10.03 0.682

Notes. ^(a)Reiprich et al. (2021), ^(b)Veronica et al. (2022), ^(c)this work.

be found in Fig. F.1. of Reiprich et al. (2021). The average of the surface brightness values of these ten boxes was taken to be the CXB level in the field, SB_{CXB} , while the root-mean-square deviation of these values was taken as the standard deviation, σ_{CXB} , which is larger than the statistical uncertainty. We report that the CXB surface brightness value in the A3391/95 system is of the typical value. The CXB value we obtained is of the same order of magnitude as, for example, to the CXB surface brightness value calculated for the A3158 surface brightness profile using the eROSITA calibration data (Whelan et al. 2022), which is not affected by additional foreground components, such as the eROSITA Bubble or other extended Galactic sources.

In their review, Reiprich et al. (2013) define the outskirts of galaxy clusters as the regions found within the range of $R_{500} < r < 3R_{200}$. In the present work, we also define the lower boundary of the outskirts region to be R_{500} , but as the $3R_{200}$ of the A3391/95 clusters extends to the entire FoV of the eROSITA PV data, we chose an arbitrary upper boundary of R_{200} . The filament was defined as the inter-cluster emission beyond the R_{200} of a cluster. The used cluster radii, as well as their corresponding emission peak coordinates and their references, are listed in Table 2. The R_{500} of A3391 and A3395N/S were calculated from ROSAT and ASCA observations (Reiprich & Böhringer 2002); the R_{500} of the NC was estimated from a dedicated *XMM-Newton* observation (Veronica et al. 2022); and the R_{500} of the LSC is a product of the present study (eROSITA PV data; see Sect. 3.2.1).

2.2. Spectral analysis

We utilized the eSASS task `srcctool` to extract all eROSITA spectra, the Ancillary Response Files (ARFs), and the Response Matrix Files (RMFs) for the source and background regions. The spectral fitting was performed with XSPEC (Arnaud 1996) version: 12.10.1f.

For the spectral analysis, we used the third eROSITA scan observation (ObsID: 300016), where all seven eROSITA TMs are available. The configuration of the regions used in the spectral analysis is shown in Fig. 1. Any source regions related to the Northern (Eastern) Filament are indicated with dashed white (green) color. For instance, the A3391 outskirts region ($R_{500} - R_{200}$) in the direction of the Northern (Eastern) Filament is plotted as a white (green) sector, labeled A3391-N (A3391-E).

The Northern (Eastern) Filament source regions are represented by two white (green) boxes, labeled NF BOX1+2 (EF BOX1+2). In the south, the source regions are depicted with magenta boxes, labeled A3395S and SF BOX1+2 for the outskirts and filament regions, respectively. The cyan circle marks the R_{500} of the LSC. For each filament, we placed two identical boxes in line with one another outside the R_{200} of the corresponding parent clusters. For the analyses of the Northern and the Eastern Filament, we took the average redshift between the A3391 cluster and the NC, $z_{N/E} = 0.0533$. While for the Southern Filament, we used the average redshift between the A3395N, A3395S, and the MCXC J0631.3-5610 clusters, $z_S = 0.0525$. The height (h) and width ($2r$) of each box are $14'$ (0.90 Mpc) and $50'$ (3.23 Mpc) for the Northern Filament, $25'$ (1.62 Mpc) and $33'$ (2.13 Mpc) for the Eastern Filament, and $20.83'$ (1.33 Mpc) and $41.67'$ (2.66 Mpc) for the Southern Filament, respectively.

The X-ray spectral fitting model, including the CXB and the source emission, is described in the following equation:

$$\text{Model} = (\text{apec}_1 + \text{TBabs} \times (\text{apec}_2 + \text{powerlaw})) + \text{TBabs} \times \text{apec}_3 + \text{PIB}, \quad (1)$$

where the first term represents the CXB components. The absorption parametrized by the hydrogen column density along the line of sight, N_H , is represented by TBabs (Wilms et al. 2000). The N_H values used in this work are taken from the A3391/95 total N_H map (see Sect. 2.1). The X-ray foreground emission from the LHB and the MWH are described by apec_1 and apec_2 , respectively. Lastly, the cosmic X-ray background from the unresolved sources (e.g., Luo et al. 2017) is represented by the power law component, powerlaw .

The second term, $\text{TBabs} \times \text{apec}_3$, represents the absorbed cluster or filament emission. The apec parameters include temperature $k_B T$, metallicity Z , redshift z , and normalization norm . The parameter norm is defined as

$$\text{norm} = \frac{10^{-14}}{4\pi[D_A(1+z)]^2} \int n_e n_H dV, \quad (2)$$

where D_A is the angular diameter distance to the source in centimeters (cm), while n_e and n_H are the electron and hydrogen densities in cm^{-3} , respectively.

To take into account the N_{H} variations in the FoV, two different CXB regions were used. These were defined based on how closely the average N_{H} (see Sect. 2.1) values within them resemble the average N_{H} values of the sources. The first region (Fig. 1, yellow circle) was used for the Northern and Eastern Filament, and the second (magenta circle) was used for the Southern Filament. We fixed the N_{H} values of the source and CXB spectra to their respective average values in the X-ray spectral fitting. The placement of the source and CXB regions on the N_{H} map is shown in Fig. A.1. In this figure, we also labeled the used average N_{H} value of each region.

The third term of Eq. (1), PIB, represents the instrumental background model. We utilized the results of the eROSITA EDR Filter Wheel Closed (FWC)³ data analysis to model the instrumental background of TM8 and the modified version for TM9, where the parameters were constrained including the lower-energy FWC spectra. The components of the instrumental background consist of a combination of a power law and an exponential cut-off to model the signal above ~ 1 keV and two power laws to model the background increase due to the detector noise at low energy. Additionally, 14 Gaussian lines are included to model the fluorescence lines caused by the interaction between the cosmic particles with the detector components. Among these, the brightest lines are Al- K_{α} at 1.486 keV and Fe- K_{α} at 6.391 keV, and the weaker lines are Ti- K_{α} at 4.504 keV, Co- K_{α} at 6.915 keV, Ni- K_{α} at 7.461 keV, Cu- K_{α} at 8.027 keV, and Zn- K_{α} at 8.615 keV. Further details of the eROSITA in-flight background are discussed in Freyberg et al. (2022).

We performed the fitting in the energy band of 0.3–9.0 keV for the TMs with an on-chip filter. Below 0.3 keV, the detector noise becomes stronger, while no strong source signal is expected above 9.0 keV given eROSITA's effective area. We find that the light leak contamination in the A3391/95 eROSITA PV observations is lower than in the other Cal/PV observations. Based on the light-leak diagnostic of this field, we can use a low energy limit of 0.5 keV for TM5 and TM7.

The spectral fitting procedure started with fitting the CXB spectra of all TMs in order to obtain best-fit values and the errors on the normalizations of the CXB components. The information from this first fitting in the respective CXB regions, including the CXB components and the resulting best-fit values are listed in Table 3. Subsequently, the source and CXB spectra of all TMs were fitted simultaneously. In this second fitting, we freed the apec₃ parameters, $k_{\text{B}}T$, Z , and $norm$, of the source spectra whenever the statistics allowed. Otherwise, we fixed Z to 0.3 of Asplund et al. (2009) for the cluster outskirts (e.g., Reiprich et al. 2013; Urban et al. 2017), and 0.1 and 0.2 for the filaments (e.g., Tanimura et al. 2020; Biffi et al. 2022). The normalizations of the instrumental background components were also freed. The normalizations of the CXB components in this second fitting were also initially freed. However, we found one case where the fit was seen to be driven by one of the CXB components, that is the Eastern Filament fit with metallicity fixed to 0.1 solar. In this case, the obtained temperature for the Eastern Filament is 0.23 keV, which is close to the MWH temperature of 0.25 keV. This temperature drop is accompanied by an increase in source normalization, while the MWH normalization decreases. Translating the Eastern Filament normalization value in this case to the gas overdensity (δ_b), we find $\delta_b \approx 356$ (3.5 times higher than the value obtained when the CXB normalizations are restricted; see Table 4). This value is not physical

Table 3. Information on the parameters of the eROSITA CXB components and their best-fit normalization values from the first fitting step (see Sect. 2.2).

Component	Parameter	Value
TBabs	$N_{\text{H}}^{(\ddagger, N/E)}$	0.046
	$N_{\text{H}}^{(\ddagger, S)}$	0.077
apec ₁ (LHB)	$k_{\text{B}}T$ (keV)	0.1
	Z (Z_{\odot})	1
	z	0
	$norm^{(*, N/E)}$	$(1.48 \pm 0.12) \times 10^{-6}$
	$norm^{(*, S)}$	$(1.80^{+0.08}_{-0.10}) \times 10^{-6}$
apec ₂ (MWH)	$k_{\text{B}}T$ (keV)	0.25
	Z (Z_{\odot})	1
	z	0
	$norm^{(*, N/E)}$	$(3.63^{+0.25}_{-0.28}) \times 10^{-7}$
	$norm^{(*, S)}$	$(5.90^{+0.23}_{-0.25}) \times 10^{-7}$
Powerlaw (unresolved sources)	Γ	1.46
	$norm^{(\ddagger, N/E)}$	$(5.82^{+0.20}_{-0.18}) \times 10^{-7}$
	$norm^{(\ddagger, S)}$	$(5.63^{+0.16}_{-0.15}) \times 10^{-7}$

Notes. (N/E) from CXB used for the Northern or Eastern Filament analysis, (S) from CXB used for the Southern Filament analysis, (\ddagger) (10^{22} atoms cm^{-2}), $(*)$ ($\text{cm}^{-5} \text{ arcmin}^{-2}$), (\ddagger) (photons $\text{keV}^{-1} \text{ cm}^2 \text{ s}^{-1} \text{ arcmin}^{-2}$ at 1 keV).

for cluster outskirts nor filament regions, but more common for the hot and denser ICM gas. The MWH normalization in this case drops by 18%. Therefore, to avoid any source parameters being driven by the CXB components, we restricted the CXB normalizations of the source spectra to the minimum and maximum values obtained from the CXB spectra from the first fit. We note that the resulting gas properties of the outskirts and filaments between freeing and restricting the CXB normalizations are consistent within the 1σ uncertainties, except for the Eastern Filament case described above. In this work, we present only the results from the restricted source CXB normalization fit. The C-statistic (Cash 1979) was adopted. An example of the eROSITA spectrum and its fitted model are shown in Fig. 2.

3. Results

3.1. X-ray surface brightness profiles

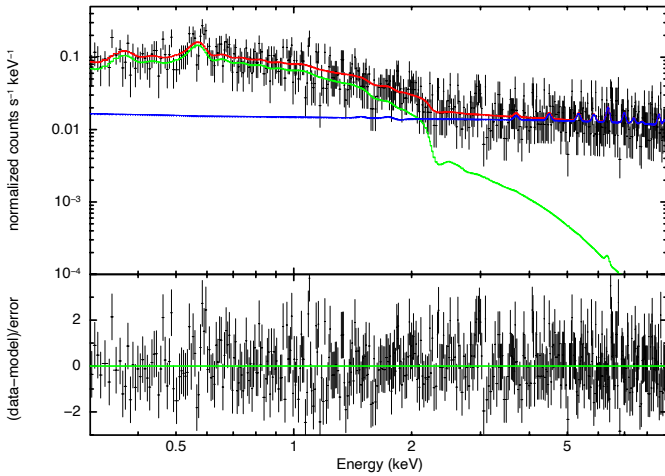
3.1.1. Configuration

We present the configuration of the source region used for the surface brightness analysis around A3391 and A3395S clusters in the left and right panels of Fig. 3, respectively. The corresponding PIB-subtracted surface brightness profiles in the 0.3–2.0 keV band are shown in Figs. 4a and b (top plots). In the bottom plots of Figs. 4a and b, we show the significance of the surface brightness values for $r > R_{200}$ with respect to the CXB level ($S/N_{\text{w.r.t.CXB}}$). The CXB level and its standard deviation (see Sect. 2.1) are shown as magenta dashed lines and the magenta shaded area. The overall significance of the surface brightness excess with respect to the CXB, S/N_{all} , of the different sectors in this regime is listed in the legend. The S/N_{all} was

³ <https://erosita.mpe.mpg.de/edr/eROSITAobservations/EDRFWC/>

Table 4. eROSITA spectral analysis results, the derived electron density (n_e), and the filament gas overdensity (δ_b).

Regions	Fitting	$norm$ ($10^{-6} \text{ cm}^{-5}/\text{arcmin}^2$)	$k_B T$ (keV)	Z (Z_\odot)	n_e (10^{-5} cm^{-3})	δ_b	stat/d.o.f.
NORTH							
A3391-N		$2.47^{+0.24}_{-0.24}$	$2.83^{+1.45}_{-0.63}$	< 0.31			9001.1/9613
NC		$3.68^{+1.10}_{-0.86}$	$0.96^{+0.18}_{-0.19}$	$0.05^{+0.06}_{-0.04}$			6660.5/6630
Box1+2		$1.65^{+0.19}_{-0.18}$	$0.96^{+0.17}_{-0.14}$	< 0.01	$5.93^{+0.34}_{-0.34}$	225^{+13}_{-13}	10855.0/10743
EAST							
A3391-E	fix Z	$2.18^{+0.15}_{-0.15}$	$3.15^{+1.02}_{-0.66}$	0.3			8570.5/9127
Box1+2	fix Z	$0.82^{+0.09}_{-0.09}$	$1.72^{+0.33}_{-0.26}$	0.1	$5.04^{+0.28}_{-0.30}$	191^{+11}_{-11}	11318.2/11078
	fix Z	$0.73^{+0.08}_{-0.08}$	$2.16^{+0.54}_{-0.45}$	0.2	$4.76^{+0.26}_{-0.29}$	180^{+10}_{-11}	11344.9/11078
SOUTH							
A3395		$0.59^{+0.18}_{-0.17}$	$1.68^{+0.31}_{-0.15}$	$0.72^{+0.60}_{-0.33}$			10277.6/10701
Box1+2		$0.74^{+0.13}_{-0.12}$	$1.09^{+0.09}_{-0.06}$	$0.10^{+0.05}_{-0.04}$	$4.37^{+0.36}_{-0.36}$	166^{+14}_{-14}	12756.4/11368
	woLSC	$0.39^{+0.13}_{-0.12}$	$1.16^{+0.19}_{-0.12}$	$0.11^{+0.13}_{-0.07}$	$3.08^{+0.46}_{-0.51}$	117^{+17}_{-19}	12620.0/11363

**Fig. 2.** eROSITA spectrum of the northern outskirts sector of A3391 (A3391-N). The spectra and the corresponding response files of TM3 and TM4 are merged for better visualization. The black points are the spectral data, while the red, green, and blue lines represent the total model, the cluster and CXB model, and the instrumental background model, respectively.

calculated as follows:

$$S/N_{\text{all}} = \frac{SB_{r>R_{200}} - SB_{\text{CXB}}}{\sqrt{\sigma_{r>R_{200}}^2 + \sigma_{\text{CXB}}^2}}, \quad (3)$$

where $SB_{r>R_{200}}$ and $\sigma_{r>R_{200}}$ are the surface brightness value of the entire $r > R_{200}$ region and its statistical standard deviation, and SB_{CXB} and σ_{CXB} are the sky background surface brightness and its standard deviation, which includes a systematic uncertainty (see Sect. 2.1).

In the directions of the Northern and Eastern Filament, we calculated A3391 sectorized surface brightness profiles out to

R_{200} , namely A3391-N and A3391-E (cyan and red sectors in Fig. 3, left). The surface brightness values of the Northern (Eastern) Filament were then calculated from the four cyan (red) boxes of the same size, which were placed outside the R_{200} of the A3391 cluster and the NC. Each Northern Filament box has a size of $7.25' \times 50'$ and is angled at 234.71° from the R_{200} of the A3391 in the NC direction. For the Eastern Filament, each box has the size of $12.5' \times 33.33'$ and is angled at 300° from the R_{200} of the A3391. In the Northern Filament direction, we continued with the surface brightness profile of NC, which was calculated from annuli around the center of the cluster. The data points related to the Northern Filament (filN) and Eastern Filament (filE) are shown respectively as blue upward triangles and red squares in Fig. 4a. To compare with the surface brightness profiles from the filament regions, we also computed surface brightness profiles in the western (green) and eastern (orange) directions out to $57.33'$ ($\sim 2R_{200}$) from the cluster center. The western and eastern sectors have position angles of 316° to 378° and 149° to 209° , respectively. The two apparent extended sources at the edge of the eastern sector are background sources located at $z \sim 0.1$, and therefore we excluded them from our analysis. Due to the influence of the A3395S/N cluster, we did not calculate any surface brightness profiles in the southern direction. The black data points in Fig. 4a are the average surface brightness profile out to the R_{200} of A3391 (excluding the southern area). By comparing the sectorized profiles with this average profile, we checked for any deviations (enhancement or depression) from the spherically symmetric surface brightness profile.

As the A3395S/N cluster comprises two components, a different approach was taken to place the surface brightness regions compared to that used to place those around the A3391 cluster, such that we avoided treating the cluster as a single entity. To minimize the amount of emission from A3395N and to get the coverage of the Southern Filament, we placed five sectors covering the lower half of A3395S (Fig. 3, right). These sectors were

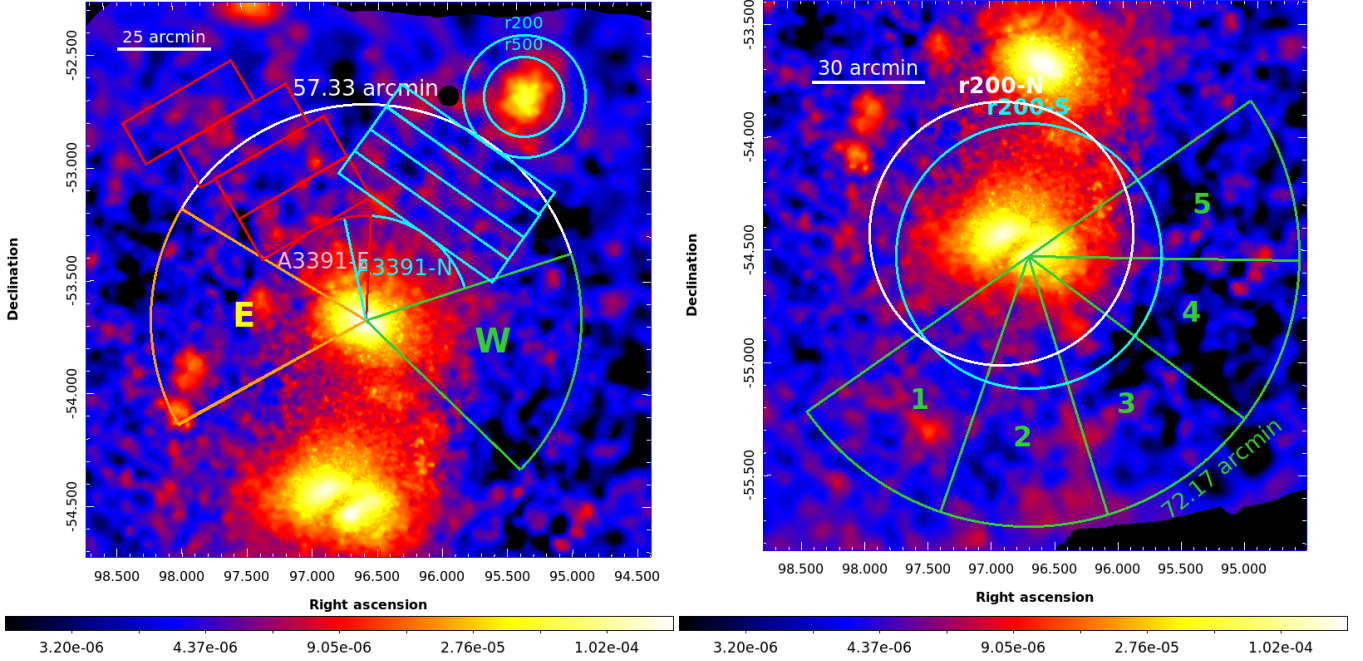


Fig. 3. Configuration of surface brightness profiles related to the A3391 cluster, NC, Northern and Eastern Filament (left), and the A3395 cluster and Southern Filament (right) overlaid on the adaptively-smoothed eROSITA PIB subtracted, exposure corrected, and Galactic absorption corrected image in the 0.3–2.0 keV band.

centered at the A3395S (see Table 2) and have an opening angle of 36° each, with the position angle from Sector 1 to Sector 5 spanning from 215° to 395° . From each sector, we calculated the surface brightness profile out to $72.17'$ ($\sim 2R_{200}$) from the center. The black data points in Fig. 4b are the average surface brightness profile of all sectors.

3.1.2. Inner region ($r \leq R_{500}$)

As seen in Fig. 4a (top plot), within $1\text{--}11'$, the surface brightness values of the A3391-N (blue downward-pointing triangles) are significantly lower than the other directions. In this radial range, compared with the full annuli profile (black data points), the A3391-N surface brightness values are lower, with relative differences ranging $8\% - 36\%$. The lowest surface brightness value in this radial range is located at $6.3'$ with a significance of 11.5σ to the full annulus value. This shows that A3391 has an elliptical morphology, where the minor axis is in the north-south direction while the major axis is in the east-west direction.

Similarly, for A3395S, we observe significantly higher surface brightness in Sector 5 (Fig. 4b, cyan upward-pointing triangles). Within $2.7\text{--}21.6'$, the relative difference values with respect to the average surface brightness profile (black data points) range between 16% and 93% , with the peak located at $7.1'$ with a 13.7σ significance. This bump shows the apparent cluster elongation in this direction. From the center to $\sim 15'$, the profiles of Sector 1 (blue squares) and Sector 2 (red diamonds) drop rapidly, and then flatten outward, denoting the pronounced shorter edge of the cluster in the southern direction.

3.1.3. Outskirts region ($R_{500} < r < R_{200}$)

Within $R_{500} < r < R_{200}$, the enhancement in the western profile of A3391 (Fig. 4a, green diamonds) is apparent. This is not unexpected given that the elongation of the cluster is in this direction. The average enhancement in this radial range with respect to the

annuli profile (black data points) is $14 \pm 2\%$. For the other sectors, the surface brightness profiles are on average lower than the annuli with relative differences of $4 \pm 2\%$ (A3391-N), $3 \pm 2\%$ (A3391-E), and $12 \pm 2\%$ (E), meaning that the A3391-N and A3391-E are still brighter than the E Sector. While ICM emission is still expected in this regime, other sources of emission, for example from the filaments, may contribute to this outskirts excess.

For the A3395 profiles (Fig. 4b) in the $R_{500} < r < R_{200}$ range, an enhancement is observed for Sector 5 (cyan) with $15 \pm 2\%$ average excess with respect to the average profile in the same regime (black points). We attribute this enhancement to the emission from the cluster in this direction. Decrements with an average of $5 \pm 3\%$ and $9 \pm 2\%$ are observed for Sector 3 (green) and Sector 4 (orange). Similar to the case for A3391, insignificant decrements with respect to the average profile of $4 \pm 2\%$ and $2 \pm 3\%$ are seen for Sector 1 (blue) and Sector 2 (red).

3.1.4. Filament region ($r > R_{200}$)

Beyond R_{200} , on average we observe higher surface brightness values in the filN and filE profiles for A3391 (blue upward-pointing triangles and red squares) than in the western (green) and eastern profiles (orange), indicating an enhancement in the intercluster regime. The overall significance values (S/N_{all} ; Eq. (3)) for these $r > R_{200}$ regions show that the Northern and Eastern Filament are $> 3.2\sigma$ away from the CXB level, while the Western and Eastern Sectors are $1.5\text{--}1.7\sigma$ away. We note that the first $r > R_{200}$ bins of all sectors are greater than 3.2σ . In general, the enhancement near R_{200} is expected to originate from the ICM. As can already be observed from the image (e.g., Fig. 3, left), there is an apparent elongation of the cluster to the west. Moreover, the surface brightness elevation of the eastern profile could result from additional residual emission from the excluded background bright galaxies, seen at $\sim 28'$ and $50'$. Removing these first bins in the $r > R_{200}$ regime results in

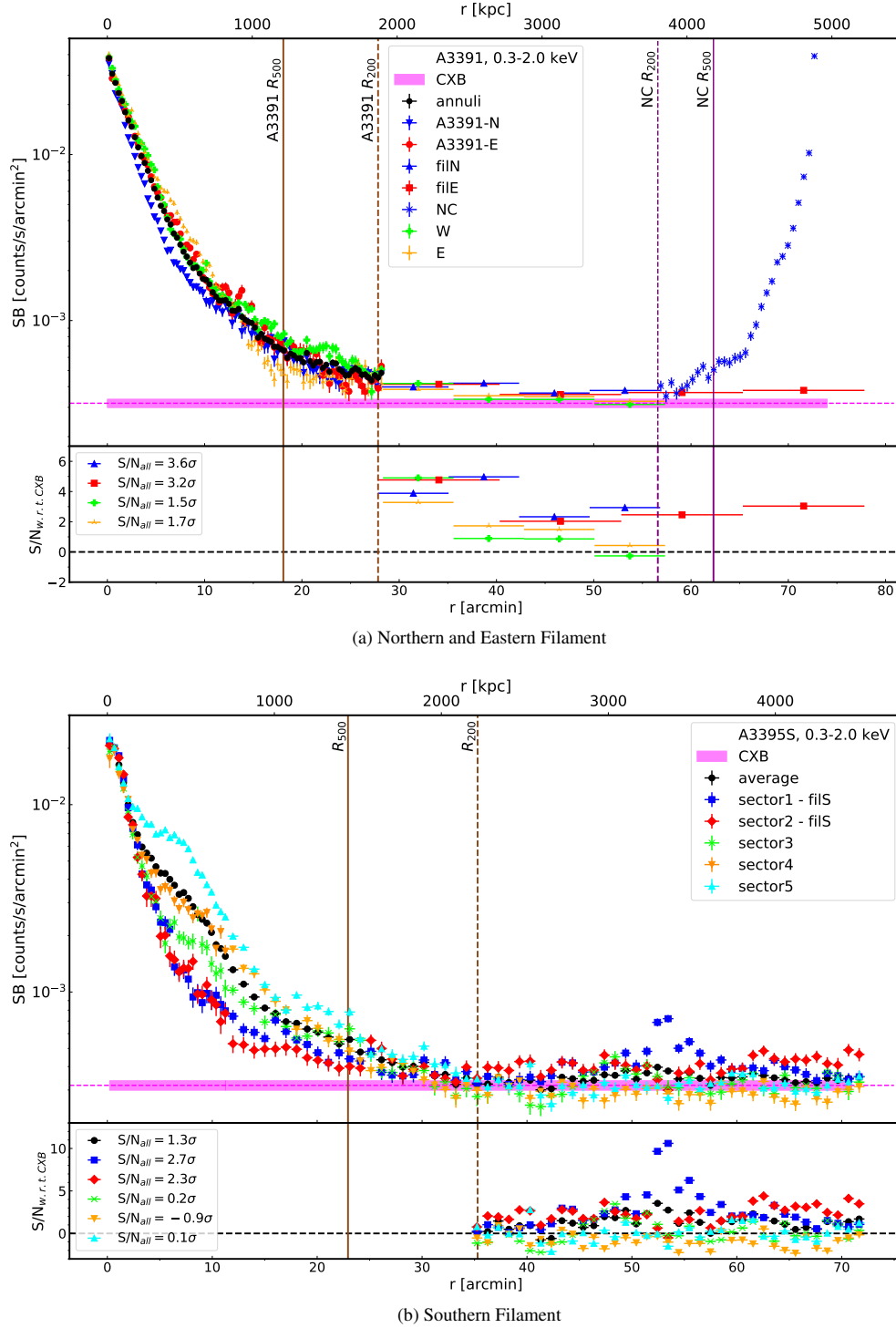


Fig. 4. PIB-subtracted SB profiles in the 0.3–2.0 keV band (top plots) and the significance values with respect to CXB for $r > R_{200}$ data points (bottom plots). The overall significance, S/N_{all} , of the excess emission in this regime is listed in the legends. (a): Profiles from A3391-N, NC, and the Northern Filament in blue; A3391-E and Eastern Filament in red; and west and east of A3391 in green and orange (see Fig. 3, left). (b): Profiles from Sectors 1–5 of A3395S. Sectors 1 (blue) and 2 (red) are related to the Southern Filament (see Fig. 3, right). The CXB level and its 1σ range are plotted as the magenta horizontal dashed-lines and magenta shaded area. The R_{500} (R_{200}) of each cluster is plotted as vertical solid (dashed) lines.

$S/N_{all} = 3.5\sigma$ (filN), 2.5σ (filE), 0.5σ (W), and 1.2σ (E). This shows that there is still significant excess emission in the Northern and Eastern Filament regions in comparison to the other directions.

For A3395S's $r > R_{200}$, a striking surface brightness peak is seen at around $54'$ ($\sim 1.5R_{200}$) of Sector 1. This peak is attributed

to the LSC. For Sector 1 and Sector 2, the S/N_{all} values in this regime are 2.7 and 2.3σ , respectively. Combining Sector 1 and Sector 2, we obtain an excess with an overall significance of 2.5σ . Meanwhile, for Sectors 3–5, the S/N_{all} values are consistent with the CXB level, such that the S/N_{all} values lie around zero (Fig. 4b, bottom plot).

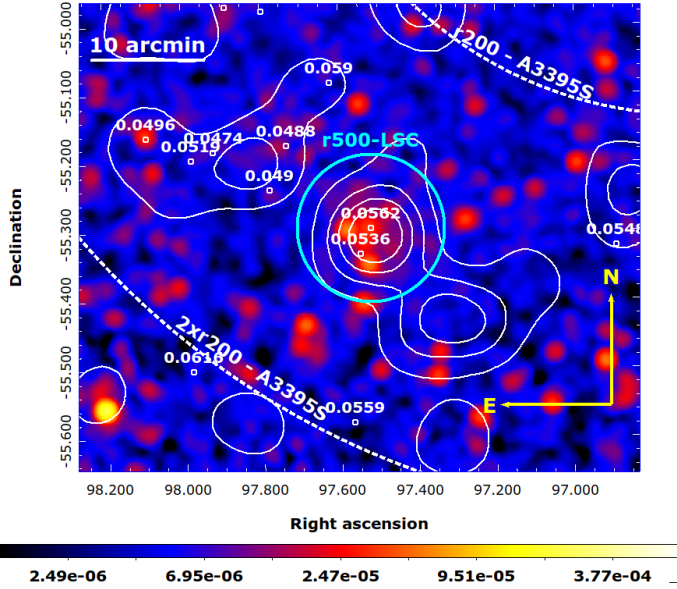


Fig. 5. eROSITA fully corrected count rate image in the 0.3–2.0 keV band (smoothed with a 64'' Gaussian kernel). The cyan circle indicates the R_{500} of the LSC, centered at the coordinates of the WISEA J063004.80-551751.5 galaxy. The small white circles are known galaxies within $0.0424 \leq z \leq 0.0636$ with their redshifts labeled. The overlaid white contours are from the optical DECam/DES galaxy density map. The white dashed lines mark the R_{200} and $2R_{200}$ of the A3395S cluster.

3.2. Spectral analysis

3.2.1. The Little Southern Clump

The LSC is an extended source that resides in the Southern Filament and has completely entered the $2R_{200}$ of the A3395 cluster, as shown in Fig. 1. We show a zoomed-in image around the LSC in Fig. 5. We overlaid the image with the A3391/95 galaxy density map (white contour; also see Sect. 2.2 of Reiprich et al. 2021) obtained from the Dark Energy Camera (DECam, Flaugher et al. 2015) as part of the Dark Energy Survey (DES, Dark Energy Survey Collaboration 2016). The white circles mark the galaxies retrieved from the NED⁴ with known redshifts and further selected with $0.0424 \leq z \leq 0.0636$. We labeled their redshifts on top of each circle. The cyan circle indicates the calculated R_{500} of the LSC and the white dashed lines mark the R_{200} and $2R_{200}$ of the A3395S cluster.

To characterize the LSC and to exclude it during the analysis of the Southern Filament, we need to first determine some characteristic properties of this object. Through spectroscopy, we acquired the $k_B T_{500}$, which was then used to infer the M_{500} and consequently, the R_{500} . The $k_B T_{500}$ was calculated through an iterative procedure, such that we extracted and fit spectra from an annulus centered at the WISEA J063004.80-551751.5 galaxy at $(\alpha, \delta) = (6:30:04.8, -55:17:51.504)$. The inner and outer radii were varied until they correspond roughly to the 0.2 – $0.5 R_{500}$ of the source region, where the R_{500} values are listed in Table 2. Based on this, we obtain $k_B T_{500} = 0.94^{+0.06}_{-0.07}$ keV and $Z_{500} = 0.10^{+0.05}_{-0.04} Z_\odot$ from an annulus with inner and outer radii of $1.3'$ and $3.2'$, respectively. We input this value into the mass–temperature ($M - T$) scaling relation by

Lovisari et al. (2015),

$$\log(M/C1) = a \cdot \log(T/C2) + b, \quad (4)$$

where $a = 1.65 \pm 0.07$, $b = 0.19 \pm 0.02$, $C_1 = 5 \times 10^{13} h_{70}^{-1} M_\odot$, and $C_2 = 2.0$ keV. Assuming spherical symmetry and taking 500 times the critical density of the Universe at the WISEA J063004.80-551751.5 redshift as $\rho_{500}(z = 0.0562) = 4.51 \times 10^{-27} \text{ g cm}^{-3}$, we obtain $M_{500} = (2.33^{+0.31}_{-0.34}) \times 10^{13} M_\odot$ and $R_{500} = (6.44^{+0.29}_{-0.32})' \approx 437.23^{+19.38}_{-21.47}$ kpc. The calculated mass is lower than the one calculated using the eFEDS scaling relation (Chiu et al. 2022), $(4.30 \pm 2.8) \times 10^{13} M_\odot$, but is nevertheless in agreement within their 1σ uncertainties. As the studied group is closer to the cluster population considered in Lovisari et al. (2015), which are average- and low-mass systems at low- z , we use the $M_{500} = (2.33^{+0.31}_{-0.34}) \times 10^{13} M_\odot$ as the default.

Based on the results, we classify the LSC as a small group of galaxies. This is further supported by the DECam/DES galaxy density map (Fig. 5, white contours), where galaxy overdensity was observed within the R_{500} and extending towards the southwest. We also notice an overdensity in the northeast direction that coincides with six known galaxies. As has been discovered in simulations, galaxy groups that are within the vicinity of a cluster can accrete some field galaxies and grow through this process (Vijayaraghavan & Ricker 2013; Kuchner et al. 2022). However, these galaxies, together with the LSC, may also simply be on their way to being accreted towards the A3395 cluster with the filament. Deeper pointed observations, for example by *XMM-Newton* and *Chandra*, will allow us to study the LSC and its surroundings in more detail. With the newly determined R_{500} of the LSC, we performed two analyses of the Southern Filament, namely including and omitting the emission from the LSC within this radius (Sect. 3.2.3).

3.2.2. The outskirts ($R_{500} - R_{200}$)

We list the results of the eROSITA spectral analysis in Table 4. Starting from the northern outskirts of A3391 (A3391-N; Fig. 1, white dashed lines sector), we report an upper limit of the metallicity of $0.31 Z_\odot$. Meanwhile, due to a lack of statistics, we find that it is necessary to fix the metallicity to 0.3 during the fit of the eastern sector (A3391-E; Fig. 1, green sector). This is a typical metallicity value adopted for cluster outskirts (e.g., Reiprich et al. 2013; Urban et al. 2017). Overall, the normalizations and temperatures obtained from A3391-N and A3391-E are in good agreement with each other. The temperature values range between 2.2 and 4.2 keV.

The temperature of the outskirts of the NC (Fig. 1, white dashed lines sector) is $k_B T = 0.96^{+0.18}_{-0.19}$ keV, which is lower than the temperature measured for the outskirts of the NC by Veronica et al. (2022) based on data from *XMM-Newton*, of namely $k_B T = 1.71^{+0.66}_{-0.37}$ keV. Although there is overlap between the definitions of the source regions, they are not identical: the eROSITA region is placed in the south of the cluster at 10.62 – $16.34'$, while the *XMM-Newton* source region is placed at 10.0 – $12.5'$. This temperature difference might also be the product of some other systematic differences, such as background treatment, point source selection, and/or instrumental calibration. Furthermore, the yielded metallicity is $Z = 0.05^{+0.06}_{-0.04} Z_\odot$, whereas for *XMM-Newton* the value has to be frozen at $0.3 Z_\odot$ for statistical reasons. For the A3395 outskirts region (Fig. 1, magenta box), the temperature and metallicity values are $1.68^{+0.31}_{-0.15}$ keV and $0.72^{+0.60}_{-0.33} Z_\odot$, respectively.

Furthermore, we fit eROSITA spectra extracted over 0.2 – $0.5 R_{500}$ of the A3391, A3395S/N, and NC clusters. The

⁴ The NASA/IPAC Extragalactic Database (NED) is funded by the National Aeronautics and Space Administration and operated by the California Institute of Technology.

Table 5. eROSITA X-ray properties of the A3391/95 clusters/groups.

Parameters	A3391	A3395S	A3395N	NC	LSC
$k_B T_{lit}^{(\dagger)}$	$5.40 \pm 0.6^{(a)}$	$5.0 \pm 0.3^{(a)}$	$5.0 \pm 0.3^{(a)}$	$1.99 \pm 0.04^{(b)}$	–
$k_B T_{0.2-0.5R_{500}}^{(\dagger)}$	3.86 ± 0.19	$5.05^{+0.52}_{-0.48}$	3.19 ± 0.21	$1.50^{+0.18}_{-0.17}$	–
$k_B T_{0.2-0.5R_{500,eRO}}^{(\dagger)}$	$3.79^{+0.18}_{-0.18}$	$4.55^{+0.47}_{-0.40}$	$3.76^{+0.30}_{-0.30}$	$1.41^{+0.23}_{-0.09}$	$0.94^{+0.06}_{-0.07}$
$M_{500,eRO}^{(*)}$	$2.54^{+0.33}_{-0.33}$	$3.42^{+0.69}_{-0.62}$	$2.51^{+0.42}_{-0.42}$	$0.45^{+0.12}_{-0.06}$	$0.23^{+0.03}_{-0.03}$
$R_{500,eRO}$ (')	$14.45^{+0.62}_{-0.63}$	$17.06^{+1.15}_{-1.03}$	$15.37^{+0.86}_{-0.86}$	$8.79^{+0.80}_{-0.36}$	$6.44^{+0.29}_{-0.32}$
(kpc)	$978.84^{+42.80}_{-42.93}$	$1071.72^{+72.45}_{-64.66}$	$967.52^{+53.86}_{-54.17}$	$546.14^{+49.98}_{-22.19}$	$437.23^{+19.38}_{-21.47}$

Notes. The first row ($k_B T_{lit}$) shows the literature temperature values. The second row ($k_B T_{0.2-0.5R_{500}}$) lists the eROSITA temperatures over the 0.2–0.5 R_{500} , where the used R_{500} are from Table 2. The third row ($k_B T_{0.2-0.5R_{500,eRO}}$) lists the eROSITA temperatures over the 0.2–0.5 $R_{500,eRO}$, where $R_{500,eRO}$ is the eROSITA radius derived from the eROSITA mass $M_{500,eRO}$ obtained through the $M - T$ scaling relation. ^(a)ASCA temperatures (Reiprich & Böhringer 2002), ^(b)XMM-Newton temperature (Veronica et al. 2022), ^(†)(keV), ^(*)[$10^{14} M_\odot$].

fitted eROSITA temperatures constrained using the R_{500} ($k_B T_{0.2-0.5R_{500}}$) from the literature and the eROSITA newly defined radii ($k_B T_{0.2-0.5R_{500,eRO}}$), as well as other derived quantities ($M_{500,eRO}$ and $R_{500,eRO}$) are presented in Table 5. We report that the eROSITA temperatures for A3391 and A3395N are lower than ASCA values listed in Reiprich & Böhringer (2002), with significances of 2.4σ and 4.9σ , respectively. The eROSITA best-fit temperature for A3395S is higher than that reported for A3391. We argue that since A3395S and A3395N are interacting, this hotter gas could be the result of some merging processes, for instance, shock heating or adiabatic compression. For NC, comparing with the XMM-Newton temperature reported in Veronica et al. (2022), the eROSITA result is 25% lower with 2.7σ significance. We note that this could either originate from some differences in the analyses, such as the source catalog used, or different background treatments or a calibration issue between the two instruments.

To obtain the eROSITA temperatures ($k_B T_{eRO}$) that were calculated within 0.2–0.5 $R_{500,eRO}$, we repeated the $M - T$ scaling relation procedure (see Sect. 3.2.1), starting with the extraction of source spectra from an annulus region. We iterated the steps until the inner and outer radii of the source region corresponded to 0.2 and 0.5 of the calculated $R_{500,eRO}$. We acquire lower $k_B T_{eRO}$ values, which consequently mean smaller eROSITA cluster radii ($R_{500,eRO}$). If we consider these newly calculated eROSITA radii, for example $R_{500} = 1.25R_{500,eRO}$ for A3391 cluster, and take into account our definition of inter-cluster emission, that is, that found at $r > R_{200}$, we find the filaments to be longer. However, for consistency, the characteristic radii used to present the results and discussion throughout this work (and other eROSITA A3391/95 papers) are those listed in Table 2, unless otherwise stated. These eROSITA cluster properties of the A3391/95 clusters are presented in Table 5.

We employed the eROSITA $k_B T$ values constrained from within apertures of 0.2–0.5 R_{500} to compute the universal temperature profile from Reiprich et al. (2013). The profile describes the cluster temperatures within $0.3R_{200} < r < 1.15R_{200}$, such that $k_B T = (1.19 - 0.84r/R_{200})(k_B T)$. We took $\langle k_B T \rangle$ to be the eROSITA temperatures (Table 5, second row). We display the temperature profiles of the outskirts and filament regions related to the Northern, Eastern, and Southern Filaments in the top, middle, and bottom panels of Fig. 6, respectively (data points).

In each plot, the universal temperature profile from the corresponding cluster is plotted as the pink-shaded area. As shown, the acquired temperatures for the outskirts of A3391-N, A3391-E, and NC (Fig. 6, top and middle plots) are higher than the predicted values with a significance of 2.4σ , 2.8σ , and 1.6σ , respectively.

3.2.3. The filaments

We used the obtained apec normalizations to derive the electron densities, n_e , of the filament regions. We assumed a simple geometry for the filament, that is a cylinder with its axis in the plane of the sky. The n_e was calculated by rewriting Eq. (2):

$$n_e = \left[1.52 \times 10^{-10} \text{ cm}^{-3} \times \text{norm} \times (1+z)^2 \times \left(\frac{D_A}{\text{Mpc}} \right)^2 \times \left(\frac{r}{\text{Mpc}} \right)^{-2} \times \left(\frac{h}{\text{Mpc}} \right)^{-1} \right]^{\frac{1}{2}}, \quad (5)$$

where, for instance, $D_A(z = 0.0533) = 222.22$ Mpc. The radius and height of the cylinder are represented by r and h . The values of r and h of the filament boxes were introduced in Sect. 2.2. The hydrogen density is taken to be $n_H \approx n_e/1.17$. Given that the radii of our filament cylinders ranges from 1.07 to 1.62 Mpc, and that the gas in filaments is isothermal up to ~ 1.5 Mpc from their cores, as reported by Galárraga-Espinosa et al. (2021), we deem our assumptions for calculating n_e to be reasonable.

Using n_e , we derived the filament gas density, ρ_{gas} , that is

$$\rho_{\text{gas}} = \mu_e \times n_e \times m_p, \quad (6)$$

where $\mu_e \approx 1.14$ is the mean molecular weight per electron, and $m_p = 1.6726 \times 10^{-24}$ g is the proton mass. Then, we calculated the gas overdensity $\delta_b = \rho_{\text{gas}}/\bar{\rho}_b(z)$, where $\bar{\rho}_b(z) = \Omega_b(z)\rho_{\text{cr}}(z)$ is the mean baryon density at redshift z . With the assumed cosmology used in this work (Planck Collaboration VI 2020), we obtained a baryon density at $z = 0.0533(0.0525)$ of $\Omega_b = 0.0561(0.0560)$, and a corresponding critical density of the Universe of $\rho_{\text{cr}} = 8.9861(8.9790) \times 10^{-30}$ g cm $^{-3}$. We therefore have $\bar{\rho}_b(0.0533) = 5.0455 \times 10^{-31}$ g cm $^{-3}$ and $\bar{\rho}_b(0.0525) = 5.0320 \times 10^{-31}$ g cm $^{-3}$.

To account for the systematic errors introduced by the assumed geometrical shape, we also calculated the n_e and δ_b

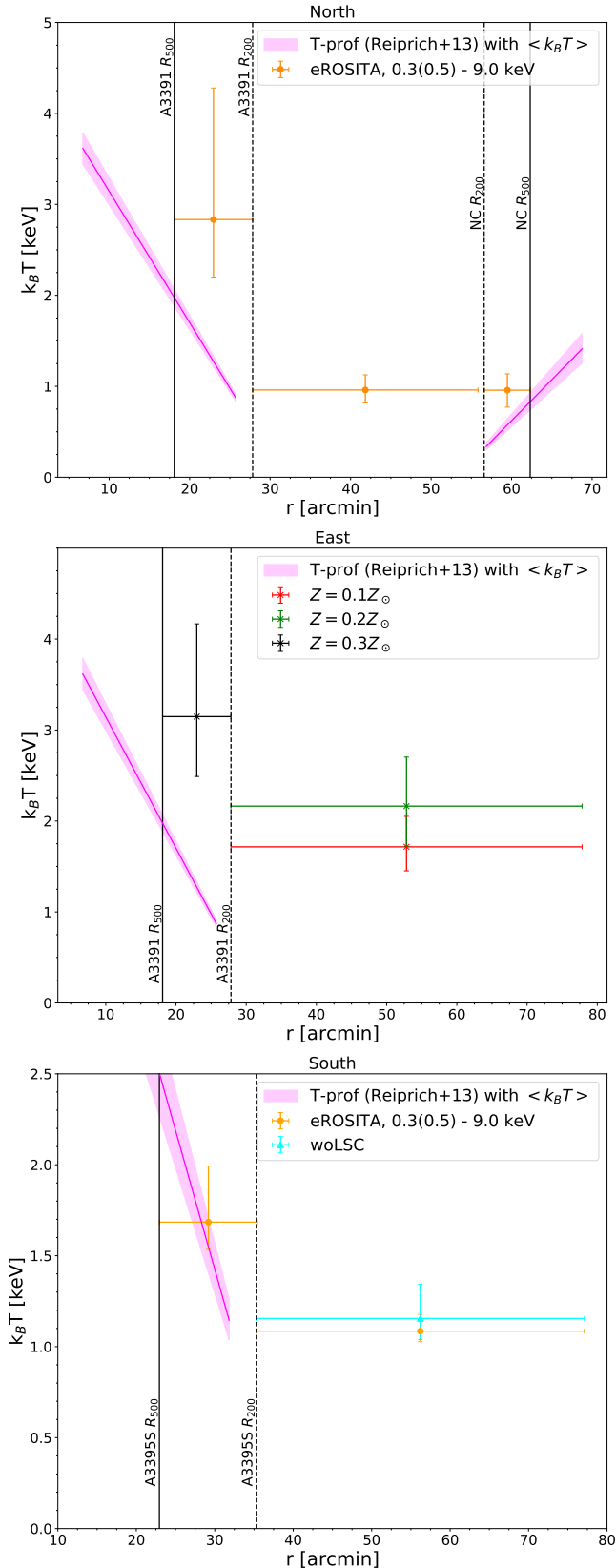


Fig. 6. eROSITA temperature profiles of the outskirts and filaments for the northern (top), eastern (middle), and southern (bottom) regions. The pink shaded areas are the 1σ temperature profiles from Reiprich et al. (2013) using $k_B T_{0.2-0.5 R_{500}}$ as mean temperature of each cluster (see Table 5). The black vertical solid (dotted) lines mark the R_{500} (R_{200}) of the parent clusters.

using two alternative shape assumptions. The first shape is an elliptical cylinder, where the major axis and the height are assumed to be the same as the radius and the height of the previously assumed cylinder, while the minor axis is taken to be half of the radius. The second assumption is a cuboid shape, where we take the width of the base and the height to be the diameter and the height of the cylinder. The density contained in the elliptical cylinder shape is 41% higher than that of the cylinder, while the density of the cuboid shape is 11% lower. Using either of the geometrical shape assumptions does not change the classification of the A3391/95 filaments based on the overdensity criteria stated in Shull et al. (2012), namely that they fall between the WHIM criteria. In Table 4, we therefore only list the n_e and δ_b values calculated whilst assuming the common cylindrical shape.

We compared our results to the WHIM properties predicted by cosmological hydrodynamic simulations (e.g., Davé et al. 2001; Martizzi et al. 2019). For observational constraints of WHIM properties, see, e.g., Shull et al. 2012; Nicastro et al. 2018; Kovács et al. 2019). Here, we adopted temperature cut of $T = 10^5-10^7$ K ($k_B T = 0.009-0.862$ keV) and the gas overdensity $\delta_b = 0.001-316.22$ for the WHIM (Shull et al. 2012). Whereas, gas with $k_B T > 0.862$ keV and any number density n_H was considered as the hot medium (HM), which is the shock-heated gas in and near the most massive dark matter haloes (Martizzi et al. 2019).

We present the results of the spectral analysis of the different filaments in Table 4. Firstly, for the Northern Filament, we obtain a best-fit temperature of ~ 1 keV and an upper metallicity limit of $0.01Z_\odot$. To investigate whether this low metallicity is caused by a bias of some kind, for example, by multi-temperature components, we performed a two-temperature (2T) component fit. We obtain a cool and a warm component of 0.1 and 1.3 keV, respectively. The cool component temperature is well within the range of the expected WHIM temperatures. The temperature of the warm component, on the other hand, agrees well with the 1T fit temperature and gives a higher metallicity upper limit of $0.12Z_\odot$. However, through the Bayesian information criterion (BIC, Schwarz 1978) and the Akaike information criterion (AIC, Akaike 1974) tests, we find that adding a second thermal emission component to the model does not improve the fit. We note that deeper data are required to differentiate between the two models. We list the result of the two-temperature fitting in Table B.1. The derived gas overdensity, δ_b , of the Northern Filament is 225 ± 13 , which is within the predicted WHIM overdensities.

For the Eastern Filament, we needed to fix the metallicity during the fit to typical values found for filaments from observations and simulations (e.g., Tanimura et al. 2020; Biffi et al. 2022), that is 0.1 and $0.2Z_\odot$. The average temperature of both fits is 1.9 keV and the best-fit values of these fits are always within 1σ of one another. We note that fixing the metallicity has an impact on the normalization, such that we observe an anti-correlation between the value fixed for the metallicity and the resulting normalization. The δ_b from both metallicity fits ranges between 169 and 202.

From the Southern Filament boxes, we obtain a 1.1 keV gas with a metallicity value of $\sim 0.10Z_\odot$. The eROSITA data enable us to identify the LSC as a clump within the filament, therefore allowing us to assess the influence of the clump on the Southern Filament (Sect. 3.2.1). We performed spectral fittings excluding the LSC emission within its R_{500} (hereafter, woLSC). The obtained best-fit temperature and metallicity are 1.2 keV and $\sim 0.11Z_\odot$, which means that we observe no significant changes

in these parameters when including or excluding the LSC. However, the normalization per unit area drops by 47%, and the gas overdensity decreases by 30% (from $\delta_b = 166 \pm 14$ to 117_{-19}^{+17}) with a significance of 2.2σ . Through this analysis, we directly demonstrate the extent to which the filament density is overestimated when ignoring the presence of a dense clump (e.g., Nagai & Lau 2011; Eckert et al. 2015b; Mirakhor & Walker 2021).

4. Discussion

4.1. Inner ($r \leq R_{500}$)

Figure 4 shows the surface brightness profiles of the A3391 (top) and A3395S (bottom) clusters from their center out to $\sim 2R_{200}$. From the inner region of the profiles ($r < R_{500}$), we observe that the clusters are not spherically symmetric, but are rather elliptical. The elongation of the A3391 cluster is apparent in the east–west direction, while the A3395S cluster is extended in the northwest direction. A recent study employing galaxy groups and clusters at $z = 0$ from large hydrodynamical simulations shows a correlation between their mass and morphology, as well as a correlation between their morphology and the number of filaments connected (connectivity) to them (Gouin et al. 2021). In these simulations, the unrelaxed groups and clusters of high connectivity, such as the A3391 cluster, are more elliptical than their relaxed and weakly connected counterparts.

4.2. Outskirts ($R_{500} < r < R_{200}$)

For the outskirts regions ($R_{500} < r < R_{200}$), we observe higher surface brightness values in the elongation directions of the clusters (Figs. 3 and 4). Despite this, the filament-facing sectors are still brighter than their non-filament-facing counterparts (see Sect. 3.1.3). For instance, A3391-N and A3391-E of the A3391 cluster are brighter than the E Sector, and Sectors 1 and 2 of the A3395S cluster are brighter than Sectors 3 and 4.

The spectral analysis (Sect. 3.2.2 and Table 4) suggests that the outskirts temperatures of A3391-N, A3391-E, and NC are higher than the universal temperature profile (Reiprich et al. 2013; Fig. 6, pink shaded areas) with a significance of 2.4σ , 2.8σ , and 1.6σ , respectively. A similar comparison to the outskirts of the A3391 and NC clusters reveals a temperature enhancement in the northeastern outskirts of the A1689 cluster (Kawaharada et al. 2010). These latter authors speculated that this is due to the thermalization process induced by the filament in the mentioned direction.

The constrained metallicity values in the outskirts of A3391 and NC (excluding A3391-E, where the metallicity is frozen) range between 0.1 and $0.3Z_{\odot}$. This is in good agreement with other measurements; for example, *Suzaku* measurements of the outskirts of the Perseus cluster (Simionescu et al. 2011), the A3112 cluster (Ezer et al. 2017), and ten other nearby galaxy clusters (Urban et al. 2017), as well as the cosmological hydrodynamical simulations (e.g., Biffi et al. 2018). The metallicity measurements from the observational data reported in the literature are constrained from various radial bins out to R_{200} . In the regime defined as outskirts in our work ($R_{500} < r < R_{200}$), the reported metallicities in the literature are consistent with $\sim 0.3Z_{\odot}$, with large uncertainties ranging between 0.1 and $0.6Z_{\odot}$. The metallicity of the outskirts of A3395 is high ($0.72_{-0.33}^{+0.60}Z_{\odot}$), but is still broadly in agreement with the literature values. The rather high metal content found in the outskirts is supposedly the result of the accretion of already enriched gas together with more pristine gas during the cluster assembly (Ezer et al. 2017; Biffi

et al. 2018). Metal production occurs at higher redshifts ($z \approx 2-3$) through some supernova (SN) events (SN Type II and SN Type Ia) and asymptotic giant branch (AGB) stars (e.g., Werner et al. 2008a; Nomoto et al. 2013) and this material is later mixed and distributed throughout the ICM by various processes, such as AGN feedback, galactic winds, or ram-pressure stripping (e.g., Vazza et al. 2010; Ettori et al. 2013).

4.3. Filaments ($r > R_{200}$)

From the surface brightness analysis (Sect. 3.1.4), we calculated the significance of the emission of all directions in the $r > R_{200}$ regime with respect to the CXB level (S/N_{all} ; Eq. (3)). We confirmed the surface brightness excess of the detected filaments (Reiprich et al. 2021). For the A3391 cluster, we obtain $S/N_{\text{all}} = 3.5\sigma$ and 2.5σ for the Northern and Eastern Filament, respectively, and 0.5σ and 1.2σ for the western and eastern sectors (non-filament-facing directions). For A3395S, excesses with a significance of $S/N_{\text{all}} = 2.7\sigma$ and 2.3σ are acquired from the filament sectors, while the surface brightness of the other sectors is around the CXB level ($S/N_{\text{all}} \approx 0\sigma$). While the significance of the excess emission of the Northern and Eastern Filaments is in good agreement with that reported in Reiprich et al. (2021, see their Table 5), the significance of the excess emission of the Southern Filament is $\sim 1.5\sigma$ lower. As our goal here is to construct surface brightness profiles, we do not have identical surface brightness regions for the filaments as defined in Reiprich et al. (2021) and therefore small differences are expected.

We characterized the properties of the filament gas through spectral analysis (Sect. 3.2.3). While the gas overdensity of our filaments ($98 \leq \delta_b \leq 238$) falls within the predicted WHIM gas overdensity, the temperatures obtained for both the Northern and Southern Filament ($k_B T \approx 1.0$ keV) are more consistent with the HM phase. Nevertheless, these temperatures are close to the upper limit of the WHIM temperature (~ 0.9 keV, as adopted in the simulations of Shull et al. 2012). Our findings for temperature and density are in accordance with the hot gas phase of filaments in the IllustrisTNG simulation (lower right panel of Figs. 6 and 8 of Galárraga-Espinosa et al. 2021). These latter authors found that the profiles of the hot gas phase of the filaments are flat with an average temperature of below 2×10^7 K (~ 1.7 keV), while the density profiles start at $\sim 10^{-4} \text{ cm}^{-3}$ and drop to $\sim 10^{-5} \text{ cm}^{-3}$ at ~ 1 Mpc from the filament spines. We recall that the radial widths of the A3391/95 filaments in this work are $r = 0.45$ Mpc for Northern Filament and 1.33 Mpc for Southern Filament, and their lengths are 1.8 Mpc and 2.7 Mpc, respectively, which means they are considered to be short filaments⁵. The shorter filaments usually trace a denser large-scale environment and are therefore more likely to be associated with the over-dense structures rather than the skeleton of the cosmic web (Galárraga-Espinosa et al. 2020, 2021, 2022; Vurm et al. 2023). Furthermore, they are in deeper potential wells and experience stronger gravitational heating. Our temperatures and gas overdensities are also within the ranges found for gas at $r > R_{200}$ in the EAGLE hydrodynamical simulation (Tuominen et al. 2021). From comparison with other observations, we see that the temperatures of our filaments are consistent with the filament temperatures reported in Tanimura et al. (2020) from the ROSAT stacked analysis of 15 165 filaments ($0.9_{-0.6}^{+1.0}$ keV) and

⁵ Based on the filament populations defined in Galárraga-Espinosa et al. (2021), such as short ($L_f < 9$ Mpc), medium ($9 \leq L_f < 20$ Mpc), and long ($L_f \geq 20$ Mpc).

with those reported in Tanimura et al. (2022) from the eFEDS stacked analysis of 463 filaments ($1.0^{+0.3}_{-0.2}$ keV). Tanimura et al. (2020, 2022) restricted their analyses to a radial range of $r < 2$ Mpc, and the radial widths of the A3391/95 filaments in this work fall within this range.

We find very good agreement between our findings and the gas properties of the simulated A3391/95 analog clusters (outside of their R_{200}) of Biffi et al. (2022). As depicted in their gas phase-space diagram (Fig. 9b), these authors find the bridge gas to be in the warm-hot phase with a typical temperature of ~ 1 keV and a median overdensity of ~ 100 (Biffi et al. 2022).

Furthermore, we find that the Northern and Southern Filaments are poorly enriched by metals; this is expected in these low-density regions as they are further away from any metal production sites, such as star-forming regions (Biffi et al. 2022). While the metallicity values for these filaments are unexpectedly low, these values are not completely excluded by the simulations (e.g., Fig. 9b of Biffi et al. 2022). Deeper data is required to confirm the low metallicity value.

The gas temperature of the Eastern Filament ranges between 1.5 and 2.7 keV. Nevertheless, as reported by Reiprich et al. (2021), the significance of the detection of the Eastern Filament is less than 3σ , which is tentative. We note that the Northern and Southern Filament are confirmed in the *Planck*-SZ and DECam galaxy density maps, as shown in Reiprich et al. (2021). From the spectral modeling, we obtain $3.6\text{--}4.4\sigma$ significance for the Northern and Southern Filament and $< 3\sigma$ significance for the Eastern and Southern Filament without LSC. As the source regions used and the number of the free parameters in the imaging and spectral analyses differ, small differences in the values obtained from both analyses are not unexpected.

We performed additional tests on the outskirts regions of A3391 and A3395, the Northern Filament, and Southern Filaments. These tests involved treating the filament boxes as a possible sky foreground. The results and discussion of these tests can be found in Appendix B.

5. Summary and conclusions

We investigated the outskirts ($R_{500} < r < R_{200}$) and the detected inter-cluster filaments ($r > R_{200}$) of the A3391/95 system using the eROSITA PV data. We focused our analysis on the northern and northeastern directions of A3391, and the southern direction of A3395, which are in the directions of the Northern, Eastern, and Southern Filaments. We created images to generate a PIB-subtracted, exposure-, and Galactic-absorption-corrected image in the soft energy band of 0.3–2.0 keV. Using the final corrected products, we calculated surface brightness profiles out to $\sim 2R_{200}$ of the A3391 and A3395 clusters in various directions. We performed comprehensive spectral analyses in the outskirts and filament regions. We constrained the gas properties, including the normalizations, temperatures, and metallicities. Utilizing the acquired normalizations and assuming a cylinder shape with its axis in the plane of the sky, we derived other quantities, namely the electron densities (n_e) and gas overdensities (δ_b). We compared our results with simulated filament properties. We summarize our findings below:

- The X-ray surface brightness profiles at $r < R_{500}$ in various directions emphasize the morphology of A3391 and A3395S. We notice significant surface brightness decrements below $10'$ in the northern direction of A3391 and higher values below $22'$ in the northwestern profile of A3395S. These show the apparent ellipticity of A3391 in

the east–west direction and the extension of A3395S in the northwestern direction, respectively.

- The temperatures in the filament-facing outskirts of A3391-N, A3391-E, and NC are higher than the temperatures expected for a typical cluster outskirts profile predicted using the universal temperature profile of Reiprich et al. (2013), with significances of 2.4σ , 2.8σ , and 1.6σ , respectively. These enhancements may be related to heating processes induced by the filaments.
- We confirm surface brightness excesses in the profiles of the Northern, Eastern, and Southern Filaments. In the surface brightness profile of the Southern Filament, we observe a peak at $\sim 1.5R_{200}$ due to the LSC.
- We detect hot gas beyond the R_{200} of the cluster (filament regions). The Northern Filament has a best-fit temperature of $0.96^{+0.17}_{-0.14}$ keV, while the Southern Filament has a best-fit temperature of $1.09^{+0.06}_{-0.13}$ keV. The gas overdensities of the Northern and Southern Filaments are found to be within the ranges of $212 < \delta_b < 237$ and $152 < \delta_b < 180$, respectively. The density of these filaments is within the expected range of the simulated WHIM properties. The enhanced temperatures of both filaments may be due to the fact that they are shorter and are located in a denser environment; consequently, they may experience stronger gravitational heating (Galárraga-Espinosa et al. 2020). However, these values are close to the upper limit of WHIM temperatures (~ 0.9 keV, as adopted in the simulations of Shull et al. 2012). More detailed comparisons to the simulated filaments of similar lengths and environments are required, as well as comparisons to other systems in observations.
- An upper metallicity value of $< 0.01Z_\odot$ is obtained for the Northern Filament and $0.10^{+0.05}_{-0.04}Z_\odot$ for the Southern Filament.
- The eROSITA data allowed us to identify the LSC, a clump within a filament. We characterized the properties of the LSC, such that $k_B T_{500} = 0.94^{+0.06}_{-0.07}$ keV, $Z_{500} = 0.10^{+0.05}_{-0.04}Z_\odot$, $M_{500} = (2.33^{+0.31}_{-0.34}) \times 10^{13} M_\odot$, and $R_{500} = (6.44^{+0.29}_{-0.32}) \approx 437.23^{+19.38}_{-21.47}$ kpc. From the optical DECam/DES galaxy density map, we observe some galaxy overdensities around the LSC. These galaxies may be being accreted towards the LSC, or they are simply a part of the filament and are on the way to the A3395 cluster. Deeper observations will enable us to study the LSC and its surroundings.
- In this work, we directly show the extent to which the filament gas density is overestimated when ignoring the presence of a clump. For example, when excluding the LSC from the analysis of the Southern Filament, we observe a decrease of 47% in the normalization per unit area and 30% in the gas overdensity with a significance of 2.2σ . No significant changes to the temperature and metallicity of the gas were observed.

The outskirts of galaxy clusters are of paramount importance not only for locating large-scale structures but also for studying various accretion physics phenomena, such as shocks, mergers, and clumping. However, due to the faint nature and their location, studying the outskirts is most often hindered by a lack of sensitivity in the soft energy band and/or the limited FoV of the instruments. eROSITA, equipped with wide FoV, scan, and survey observation modes, and superior soft energy response, is an outstanding instrument with which to probe these regions. Indeed, through the A3391/95 PV observations, eROSITA has already demonstrated its capability to capturing these nearby clusters beyond their virial radii. Moreover, these observations

reveal the filamentary structure that connects at least five galaxy groups and clusters. Here, we were able to go one step further and characterize the filament properties in terms of density, temperature, and metallicity. With the eROSITA all-sky survey (eRASS), further such systems will be found and this will improve the statistics of observational studies of inter-cluster filaments.

Acknowledgements. The authors would like to thank the anonymous referee for their constructive feedback and suggestions that helped improve the presentation of the manuscript. We thank Gabriele Ponti for the valuable discussion about the eROSITA foreground. Funded by the Deutsche Forschungsgemeinschaft (DFG, German Research Foundation) – 450861021. This research was supported by the Excellence Cluster ORIGINS which is funded by the Deutsche Forschungsgemeinschaft (DFG, German Research Foundation) under Germany's Excellence Strategy – EXC-2094 – 390783311. V.B. acknowledges funding by the Deutsche Forschungsgemeinschaft (DFG, German Research Foundation) — 415510302. A.V. is a member of the Max-Planck International School for Astronomy and Astrophysics (IMPRS) and of the Bonn-Cologne Graduate School for Physics and Astronomy (BCGS), and thanks for their support. K.D. acknowledges support by the COMPLEX project from the European Research Council (ERC) under the European Union's Horizon 2020 research and innovation program grant agreement ERC-2019-AdG 882679 and by the Deutsche Forschungsgemeinschaft (DFG, German Research Foundation) under Germany's Excellence Strategy – EXC-2094 – 390783311. C.S. and T.R. acknowledge support from the German Federal Ministry of Economics and Technology (BMWi) provided through the German Space Agency (DLR) under project 50 OR 2112. This work is based on data from eROSITA, the soft X-ray instrument aboard SRG, a joint Russian-German science mission supported by the Russian Space Agency (Roskosmos), in the interests of the Russian Academy of Sciences represented by its Space Research Institute (IKI), and the Deutsches Zentrum für Luft- und Raumfahrt (DLR). The SRG spacecraft was built by Lavochkin Association (NPOL) and its subcontractors, and is operated by NPOL with support from the Max Planck Institute for Extraterrestrial Physics (MPE). The development and construction of the eROSITA X-ray instrument was led by MPE, with contributions from the Dr. Karl Remeis Observatory Bamberg and ECAP (FAU Erlangen-Nürnberg), the University of Hamburg Observatory, the Leibniz Institute for Astrophysics Potsdam (AIP), and the Institute for Astronomy and Astrophysics of the University of Tübingen, with the support of DLR and the Max Planck Society. The Argelander Institute for Astronomy of the University of Bonn and the Ludwig Maximilians Universität Munich also participated in the science preparation for eROSITA. The eROSITA data shown here were processed using the eSASS software system developed by the German eROSITA consortium. This research has made use of the NASA/IPAC Extragalactic Database (NED), which is funded by the National Aeronautics and Space Administration and operated by the California Institute of Technology.

References

- Akaike, H. 1974, *IEEE Trans. Automatic Control*, **19**, 716
- Akamatsu, H., Fujita, Y., Akahori, T., et al. 2017, *A&A*, **606**, A1
- Alvarez, G. E., Randall, S. W., Bourdin, H., Jones, C., & Holley-Bockelmann, K. 2018, *ApJ*, **858**, 44
- Alvarez, G. E., Randall, S. W., Su, Y., et al. 2022, *ApJ*, **938**, 51
- Arnaud, K. A. 1996, in *ASP Conf. Ser.*, 101, Astronomical Data Analysis Software and Systems V, eds. G. H. Jacoby, & J. Barnes, 17
- Asplund, M., Grevesse, N., Sauval, A. J., & Scott, P. 2009, *ARA&A*, **47**, 481
- Bertin, E., & Arnouts, S. 1996, *A&AS*, **117**, 393
- Biffi, V., Planelles, S., Borgani, S., et al. 2018, *MNRAS*, **476**, 2689
- Biffi, V., Dolag, K., Reiprich, T. H., et al. 2022, *A&A*, **661**, A17
- Bonamente, M., Lieu, R., & Bulbul, E. 2009, *ApJ*, **696**, 1886
- Bonamente, M., Mirakhor, M., Lieu, R., & Walker, S. 2022, *MNRAS*, **514**, 416
- Bond, J. R., Kofman, L., & Pogosyan, D. 1996, *Nature*, **380**, 603
- Bond, N. A., Strauss, M. A., & Cen, R. 2010, *MNRAS*, **409**, 156
- Bonjean, V., Aghanim, N., Salomé, P., Douspis, M., & Beelen, A. 2018, *A&A*, **609**, A49
- Brunner, H., Liu, T., Lamer, G., et al. 2022, *A&A*, **661**, A1
- Bulbul, E., Randall, S. W., Bayliss, M., et al. 2016, *ApJ*, **818**, 131
- Cash, W. 1979, *ApJ*, **228**, 939
- Cen, R., & Ostriker, J. P. 1999, *ApJ*, **514**, 1
- Chiu, I. N., Ghirardini, V., Liu, A., et al. 2022, *A&A*, **661**, A11
- Dark Energy Survey Collaboration (Abbott, T., et al.) 2016, *MNRAS*, **460**, 1270
- Davé, R., Cen, R., Ostriker, J. P., et al. 2001, *ApJ*, **552**, 473
- Eckert, D., Jauzac, M., Shan, H., et al. 2015a, *Nature*, **528**, 105
- Eckert, D., Roncarelli, M., Ettori, S., et al. 2015b, *MNRAS*, **447**, 2198
- Ettori, S., Gastaldello, F., Gitti, M., et al. 2013, *A&A*, **555**, A93
- Ezer, C., Bulbul, E., Ercan, E. N., et al. 2017, *ApJ*, **836**, 110
- Flaugher, B., Diehl, H. T., Honscheid, K., et al. 2015, *AJ*, **150**, 150
- Freyberg, M. J., Müller, T., Perinati, E., et al. 2022, in *Space Telescopes and Instrumentation 2022: Ultraviolet to Gamma Ray*, 12181, eds. J.-W. A. den Herder, S. Nikzad, & K. Nakazawa, International Society for Optics and Photonics (SPIE), 1218155
- Fujita, Y., Tawa, N., Hayashida, K., et al. 2008, *PASJ*, **60**, S343
- Galárraga-Espinosa, D., Aghanim, N., Langer, M., Gouin, C., & Malavasi, N. 2020, *A&A*, **641**, A173
- Galárraga-Espinosa, D., Aghanim, N., Langer, M., & Tanimura, H. 2021, *A&A*, **649**, A117
- Galárraga-Espinosa, D., Langer, M., & Aghanim, N. 2022, *A&A*, **661**, A115
- Gouin, C., Bonnaire, T., & Aghanim, N. 2021, *A&A*, **651**, A56
- Hattori, S., Ota, N., Zhang, Y.-Y., Akamatsu, H., & Finoguenov, A. 2017, *PASJ*, **69**, 39
- HI4PI Collaboration (Ben Bekhti, N., et al.) 2016, *A&A*, **594**, A116
- Kawaharada, M., Okabe, N., Umetsu, K., et al. 2010, *ApJ*, **714**, 423
- Kovács, O. E., Bogdán, Á., Smith, R. K., Kraft, R. P., & Forman, W. R. 2019, *ApJ*, **872**, 83
- Kuchner, U., Haggard, R., Aragón-Salamanca, A., et al. 2022, *MNRAS*, **510**, 581
- Kull, A., & Böhringer, H. 1999, *A&A*, **341**, 23
- Lovisari, L., Reiprich, T. H., & Schellenberger, G. 2015, *A&A*, **573**, A118
- Luo, B., Brandt, W. N., Xue, Y. Q., et al. 2017, *ApJS*, **228**, 2
- Martizzi, D., Vogelsberger, M., Artale, M. C., et al. 2019, *MNRAS*, **486**, 3766
- Mirakhor, M. S., & Walker, S. A. 2021, *MNRAS*, **506**, 139
- Miville-Deschênes, M.-A. & Lagache, G. 2005, *ApJS*, **157**, 302
- Nagai, D., & Lau, E. T. 2011, *ApJ*, **731**, L10
- Nicastro, F., Krongold, Y., Mathur, S., & Elvis, M. 2017, *Astron. Nachr.*, **338**, 281
- Nicastro, F., Kaastra, J., Krongold, Y., et al. 2018, *Nature*, **558**, 406
- Nomoto, K., Kobayashi, C., & Tominaga, N. 2013, *ARA&A*, **51**, 457
- Pacaud, F., Pierre, M., Refregier, A., et al. 2006, *MNRAS*, **372**, 578
- Piffaretti, R., Arnaud, M., Pratt, G. W., Pointecouteau, E., & Melin, J. B. 2011, *A&A*, **534**, A109
- Planck Collaboration VI. 2020, *A&A*, **641**, A6
- Planck Collaboration Int. VIII. 2013, *A&A*, **550**, A134
- Predehl, P., Andritschke, R., Arefiev, V., et al. 2021, *A&A*, **647**, A1
- Ramos-Ceja, M. E., Pacaud, F., Reiprich, T. H., et al. 2019, *A&A*, **626**, A48
- Reiprich, T. H., & Böhringer, H. 2002, *ApJ*, **567**, 716
- Reiprich, T. H., Basu, K., Ettori, S., et al. 2013, *Space Sci. Rev.*, **177**, 195
- Reiprich, T. H., Veronica, A., Pacaud, F., et al. 2021, *A&A*, **647**, A2
- Sarkar, A., Randall, S., Su, Y., et al. 2022, *ApJ*, **935**, L23
- Schwarz, G. 1978, *Ann. Stat.*, **6**, 461
- Shull, J. M., Smith, B. D., & Danforth, C. W. 2012, *ApJ*, **759**, 23
- Simionescu, A., Allen, S. W., Mantz, A., et al. 2011, *Science*, **331**, 1576
- Sugawara, Y., Takizawa, M., Itahana, M., et al. 2017, *PASJ*, **69**, 93
- Tanaka, M., Hoshi, T., Kodama, T., & Kashikawa, N. 2007, *MNRAS*, **379**, 1546
- Tanimura, H., Aghanim, N., Kolodzig, A., Douspis, M., & Malavasi, N. 2020, *A&A*, **643**, A2
- Tanimura, H., Aghanim, N., Douspis, M., & Malavasi, N. 2022, *A&A*, **667**, A161
- Tittley, E. R., & Henriksen, M. 2001, *ApJ*, **563**, 673
- Tuominen, T., Nevalainen, J., Tempel, E., et al. 2021, *A&A*, **646**, A156
- Urban, O., Werner, N., Allen, S. W., Simionescu, A., & Mantz, A. 2017, *MNRAS*, **470**, 4583
- Vazza, F., Gheller, C., & Brunetti, G. 2010, *A&A*, **513**, A32
- Vazza, F., Ettori, S., Roncarelli, M., et al. 2019, *A&A*, **627**, A5
- Veronica, A., Su, Y., Biffi, V., et al. 2022, *A&A*, **661**, A46
- Vijayaraghavan, R., & Ricker, P. M. 2013, *MNRAS*, **435**, 2713
- Vurm, I., Nevalainen, J., Hong, S. E., et al. 2023, *A&A*, **673**, A62
- Werner, N., Durret, F., Ohashi, T., Schindler, S., & Wiersma, R. P. C. 2008a, *Space Sci. Rev.*, **134**, 337
- Werner, N., Finoguenov, A., Kaastra, J. S., et al. 2008b, *A&A*, **482**, L29
- West, M. J., Jones, C., & Forman, W. 1995, *ApJ*, **451**, L5
- Whelan, B., Veronica, A., Pacaud, F., et al. 2022, *A&A*, **663**, A171
- Wilms, J., Allen, A., & McCray, R. 2000, *ApJ*, **542**, 914

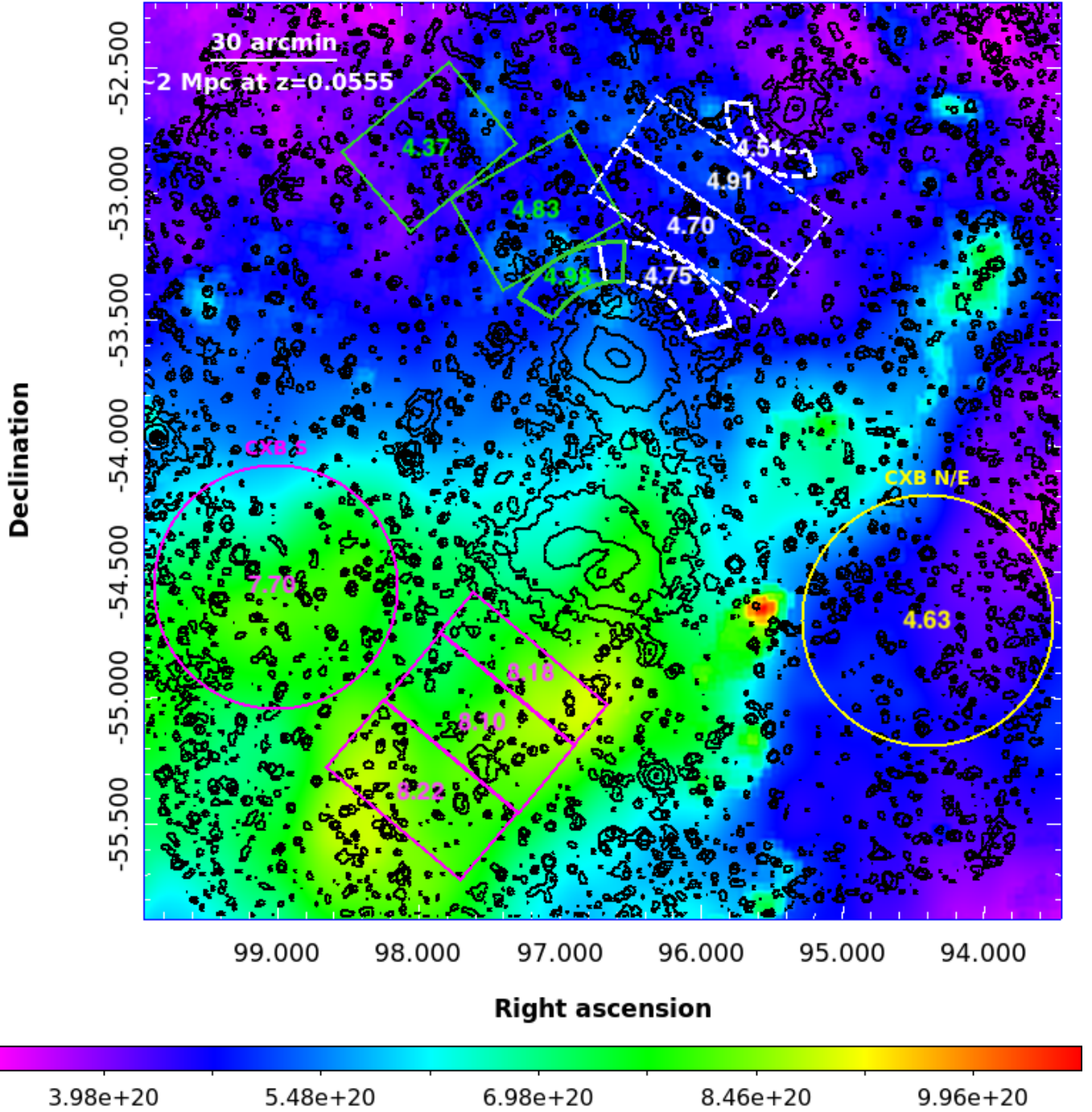
Appendix A: Total N_{H} map of the A3391/95 field

Fig. A.1. The A3391/95 total N_{H} map generated from IRAS 100 μm and HI4PI. We overlaid the source and CXB regions used for the spectral analysis (boxes, sectors, and circles). The numbers in each region are the average values in the units of 10^{20} atoms cm^{-2} . The eROSITA contours are plotted in black. The colorbar is in the units of atoms cm^{-2} .

Appendix B: Additional spectral analysis tests

The first test was to treat the Northern Filament (NF) and Southern Filament without LSC (SFwoLSC) as possible sky background regions. We used these filament regions to estimate the sky background components for the outskirts of the A3391-N and A3395 (A3391-N BGNF and A3395 BGSFwoLSC, respectively), thereby effectively assuming the filament emission as a foreground structure. We find that the normalization of both outskirts regions is reduced by a factor of $\sim 2\text{--}3$. For the A3391-N BGNF, we can only constrain a lower limit temperature of 4.5 keV, while for the A3395 BGSFwoLSC, the temperature is of the same order as the main fit. These results are consistent with removing a ~ 1 keV component from these outskirts regions, i.e., in the case of multi-structure components, leaving a hotter component for the A3391, and a ~ 1 keV component for A3395, because the temperatures found for A3395 and BGSFwoLSC are of this order. The unexpectedly high lower temperature limit for the A3391-N BGNF makes this model seem rather unlikely.

To check whether the filament emission is of Galactic origin, we performed the following three tests for the model in the filament regions; first to fix the redshift of the filament component to 0, second to limit the redshift within $\pm 15\%$ of the average of the cluster redshift, third to limit the redshift between 0 and 1. The normalizations, temperatures, and metallicities of the first and second cases are in good agreement with the main fit. The third case yields unexpectedly high redshifts, that is $z > 0.97$ and $z = 0.19$ for NF and SF, respectively. This would result in an improbably long physical extent of these filaments, namely at least 13.7 Mpc for NF and 8.3 Mpc for SF. As redshift estimation strongly depends on emission lines, these high redshift results could be due to statistical fluctuations. Additionally, we performed a fit where the redshift is fixed at 0 and metallicity to a solar value (while in the above tests, the metallicity is left to vary). The test could only be done to the SF and SFwoLSC, while the NF fit did not converge. This test results in lower temperature limits of 4.6 keV (4.4 keV) for the SF (SFwoLSC). These values are highly unlikely for a region outside R_{200} and are also unlikely temperatures for any extended emission coming from the Galaxy. Thus, this fit cannot physically describe the fitted spectra.

Lastly, we swapped the sky background regions used for the fits in the northern and southern regions. As presented in Table 3, we see in general that the normalizations of the soft components (LHB and MWH) of the CXB-S are higher than those of CXB-N. This is also reflected in the results of this test. The normalization of the NF using CXB-S as the sky background is lower, and the temperature gets higher. On the contrary, as a result of underestimating the soft sky background components, the normalization yielded for the SF (SFwoLSC) using CXB-N as the sky background is higher and the resulting overdensity values indicate that the gas is HM, which is unforeseen for this region. This test illustrates that our default definition of the background regions seems appropriate.

Description of the fitting methods shown in Table B.1: BGNF: Using Northern Filament boxes as sky background. 2T: Two-temperature components. $z = 0$: Redshift is fixed to 0. $z_{\text{free, range} \pm 15\%}$: Redshift is left to vary in a range of $\pm 15\%$ of the starting value. $z_{\text{free, range } 0-1}$: Redshift is left to vary between 0 and 1. CXB-S: Using CXB-S circle as background (Fig. 1 and A.1). BGSFwoLSC: Using Southern Filament boxes (LSC excluded) as sky background. CXB-N: Using the CXB-N circle as background (Fig. 1 and A.1). $z = 0$, $Z = 1$: Redshift is fixed to 0 and metallicity to $1Z_{\odot}$.

Table B.1. eROSITA spectral analysis results from additional tests, the derived electron density (n_e), and the filament gas overdensity (δ_b).

Regions	Fitting	$norm$ [$10^{-6} \text{ cm}^{-5}/\text{arcmin}^2$]	$k_B T$ [keV]	Z [Z_\odot]	n_e [10^{-5} cm^{-3}]	δ_b	stat/dof
NORTH							
A3391-N	BGNF	$1.18^{+0.35}_{-0.21}$	> 4.52	> 0.09			7989.7/9087
NC	BGNF	$1.78^{+0.79}_{-0.84}$	$0.98^{+0.29}_{-0.19}$	$0.14^{+0.14}_{-0.09}$			5682.5/6104
Box1+2	2T	$1.29^{+3.39}_{-1.16}$	$0.14^{+0.03}_{-0.02}$	$0.22^{+0.62}_{-0.17}$	$5.24^{+4.73}_{-3.56}$	199^{+179}_{-135}	10938.4/10740
		$1.05^{+0.27}_{-0.21}$	$1.28^{+0.69}_{-0.23}$	< 0.12	$4.73^{+0.57}_{-0.49}$	179^{+21}_{-19}	
Box1+2	$z = 0$	$1.51^{+0.17}_{-0.16}$	$0.89^{+0.16}_{-0.11}$	< 0.01			10874.7/10743
Box1+2	$z_{\text{free, range} \pm 15\%} = 0.061$	$1.67^{+0.2}_{-0.21}$	$0.97^{+0.16}_{-0.17}$	< 0.01			10854.9/10742
Box1+2	$z_{\text{free, range } 0-1} > 0.967$	$4.06^{+1.04}_{-0.8}$	$1.56^{+0.14}_{-0.19}$	$0.25^{+0.23}_{-0.14}$			10843.0/10742
Box1+2	CXB-S	$0.47^{+0.14}_{-0.11}$	> 1.88	> 0.41	$3.17^{+0.43}_{-0.39}$	120^{+16}_{-15}	10872.3/10790
SOUTH							
A3395	BGSFwoLSC	$0.22^{+0.14}_{-0.05}$	$1.68^{+0.25}_{-0.16}$	> 0.97			10320.1/10701
Box1+2	$z = 0$	$0.71^{+0.13}_{-0.12}$	$0.95^{+0.07}_{-0.08}$	$0.07^{+0.04}_{-0.03}$			12821.9/11368
Box1+2	$z_{\text{free, range} \pm 15\%} > 0.053$	$0.74^{+0.13}_{-0.12}$	$1.09^{+0.11}_{-0.04}$	$0.1^{+0.06}_{-0.04}$			12755.8/11367
Box1+2	$z_{\text{free, range } 0-1} = 0.193^{+0.006}_{-0.020}$	$0.62^{+0.1}_{-0.11}$	$1.91^{+0.23}_{-0.23}$	$0.68^{+0.44}_{-0.40}$			12753.8/11367
Box1+2	$z = 0, Z = 1$	$0.51^{+0.04}_{-0.04}$	> 4.61	1.0			13087.4/11369
Box1+2	CXB-N	$2.80^{+0.32}_{-0.33}$	$0.51^{+0.06}_{-0.04}$	$0.01^{+0.01}_{-0.01}$	$8.52^{+0.48}_{-0.52}$	324^{+18}_{-20}	12882.1/11321
Box1+2, woLSC	$z = 0$	$0.40^{+0.11}_{-0.12}$	$1.05^{+0.19}_{-0.15}$	$0.06^{+0.08}_{-0.05}$			12675.4/11363
Box1+2, woLSC	$z_{\text{free, range} \pm 15\%} = 0.060$	$0.39^{+0.13}_{-0.12}$	$1.19^{+0.18}_{-0.15}$	$0.12^{+0.15}_{-0.08}$			12619.9/11362
Box1+2, woLSC	$z = 0, Z = 1$	$0.29^{+0.04}_{-0.04}$	> 4.38	1.0			12889.0/11364
Box1+2, woLSC	CXB-N	$2.79^{+0.44}_{-0.44}$	$0.38^{+0.06}_{-0.05}$	$0.01^{+0.02}_{-0.01}$	$8.19^{+0.62}_{-0.67}$	311^{+24}_{-25}	12712.7/11316

Appendix C

The SRG/eROSITA All-Sky Survey: Large-scale view of the Centaurus cluster

This work was submitted to the Astronomy & Astrophysics journal and the preprint version is available on <https://arxiv.org/abs/2404.04909>. The submitted version of the manuscript is reproduced below in its original form.

The SRG/eROSITA All-Sky Survey: Large-scale view of the Centaurus cluster

Angie Veronica¹, Thomas H. Reiprich¹, Florian Pacaud¹, Jeremy S. Sanders², Efrain Gattuzz², Michael C. H. Yeung²,
Esra Bulbul², Vittorio Ghirardini², Ang Liu², Caroline Mannes¹, Alexander Morelli¹, and Naomi Ota^{1,3}

¹ Argelander-Institut für Astronomie (AIfA), Universität Bonn, Auf dem Hügel 71, 53121 Bonn, Germany
e-mail: averonica@astro.uni-bonn.de

² Max-Planck-Institut für extraterrestrische Physik, Gießenbachstraße 1, 85748 Garching, Germany

³ Nara Women's University, Kitaouyanishi-machi, Nara, 630-8506, Japan

Received ; accepted

ABSTRACT

Context. The Centaurus cluster is one of the brightest and closest clusters. Previous comprehensive studies were done only in the brightest part ($r < 30'$) where the centers of the main substructures (Cen 30 and Cen 45) are located. Only a small fraction of the outskirts has been studied.

Aims. This work aims to characterize the ICM morphology and properties of the Centaurus cluster out to the radius within which the density is 200 times the critical density of the Universe at the redshift of the cluster, R_{200} ($91'$).

Methods. We utilized the combined five SRG/eROSITA All-Sky Survey data (eRASS:5) to perform X-ray imaging and spectral analyses in various directions out to large radii. We employed some image manipulation methods to enhance small and large-scale features. Surface brightness profiles out to $2R_{200}$ were constructed to quantify the features. We acquired gas temperature, metallicity, and normalization per area profiles out to R_{200} . We compared our results with previous Centaurus studies, cluster outskirts measurements, and simulations. Comprehensive sky background analysis was done across the FoV, in particular, to assess the variation of the eROSITA Bubble emission that partially contaminates the field.

Results. The processed X-ray images show the known sloshing-induced structures in the core, such as cool plume, cold fronts, and ram-pressure-stripped gas. The spectra in the core ($r \leq 11$ kpc) are better described with a two-temperature model than an isothermal model. With this 2T analysis, we measured lower temperature from the cooler component (~ 1.0 keV) and higher metallicity ($\sim 1.6Z_{\odot}$), signifying an iron bias. In the intermediate radial range, the temperature peaks at ~ 3.6 keV, and we observed prominent surface brightness and normalization per area excesses in the eastern sector (Cen 45 location). Temperature enhancements near the location of Cen 45 imply that the gas is shock-heated due to the interaction with the Cen 30. We reveal that the eastern excess emission extends even further out, reaching R_{500} . The peak excess of normalization is located at $\sim 23'$ from the center ($8'$ behind the center of Cen 45) with a 45% and 7.7σ above the full azimuthal value. This might be the tail/ram-pressure-stripped gas from Cen 45. There is a temperature decrease of a factor about 2 – 3 from the peak to the outermost bin at $R_{500} - R_{200}$. We found good agreement between the outer temperatures ($r > R_{2500}$) with the temperature profile from simulations and temperature fit from *Suzaku* cluster outskirts measurements. We detect significant surface brightness emission to the sky background level out to R_{200} with a 3.5σ and followed with 2.9σ at $1.1R_{200}$. The metallicity at $R_{500} - R_{200}$ is low but within the ranges of other outskirts studies.

Conclusions. We present the first measurement of ICM morphology and properties of Centaurus cluster sampling the whole azimuth beyond $\sim 30'$, increasing the probed volume by a factor of almost 30. While the cluster core is rich in features as the result of AGN feedback and sloshing, the cluster outskirts temperature of Centaurus follows the temperature profile of clusters in simulations, as well as temperature fit from other cluster outskirts measurements.

Key words. Galaxies: clusters: individual: Abell 3526, Centaurus – X-rays: galaxies: clusters – Galaxies: clusters: intracluster medium

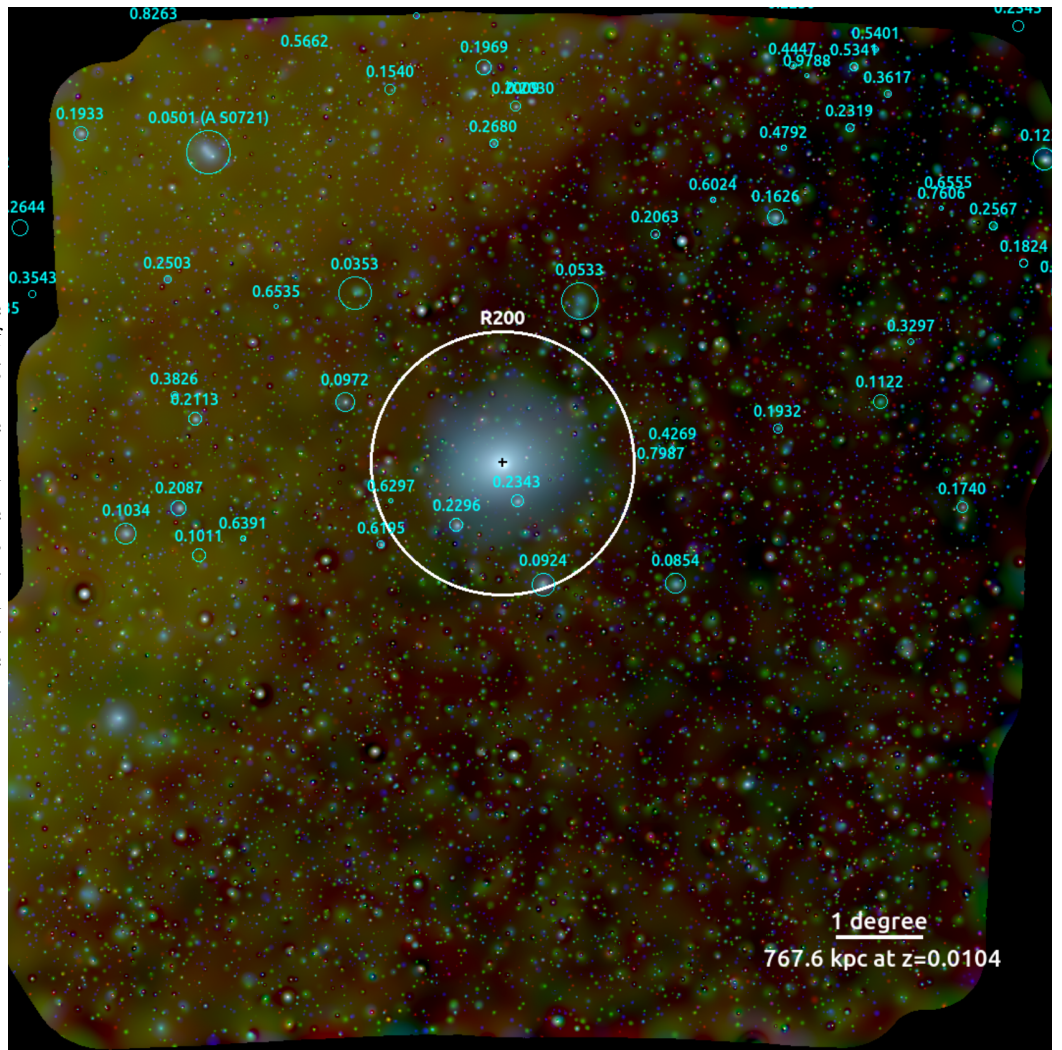
1. Introduction

The Centaurus cluster (Abell 3526) is nearby ($z = 0.0104$) and one of the X-ray brightest clusters with a $0.1 - 2.4$ keV luminosity within the R_{500} of 6.9×10^{43} erg s⁻¹ (Piffaretti et al. 2011). It has been extensively studied by X-ray instruments, for example, *ASCA* (e.g., Churazov et al. 1999; Dupke & Bregman 2001; Furusho et al. 2001), *ROSAT* (e.g., Allen & Fabian 1994; Churazov et al. 1999; Ikebe et al. 1999), *Suzaku* (e.g., Ota et al. 2007; Walker et al. 2013b; Ota & Yoshida 2016), *XMM-Newton* (e.g., Walker et al. 2013a; Fukushima et al. 2022; Gattuzz et al. 2022a, 2023), and *Chandra* (e.g., Sanders & Fabian 2002; Sanders et al. 2016b; Lakhchaura et al. 2019). The X-ray emission of the Centaurus cluster appears smooth with an elliptical

morphology (Allen & Fabian 1994) and it is peaked at its brightest cluster galaxy (BCG), NGC 4696 (Dupke & Bregman 2001).

However, early studies of the line-of-sight velocity distribution of the member galaxies show a bimodality, indicating the presence of two substructures with a velocity difference of $1,500$ km s⁻¹ (Lucy et al. 1986a,b). The main substructure, which sits in the center of the cluster, is called Cen 30 and is centered on the NGC 4696 galaxy. The other substructure, located $\sim 15'$ east of the center, is called Cen 45 and is centered on the NGC 4709 galaxy. Based on the results of $U-V$ color-magnitude relations, luminosity functions, and galactic radius distributions of both substructures, Lucy et al. (1986a) concluded that Cen 30 and Cen 45 belong to the same system, which also indicates

Fig. 1: Composite image of the large scale view of Centaurus (A3526) using eRASS:5 data. Red, green, and blue channels are in the 0.2 – 0.6 keV, 0.6 – 1.0 keV, and 1.0 – 2.3 keV energy bands, respectively. The image in each channel is PIB-subtracted, exposure-corrected, Galactic-absorption corrected, and wavelet-filtered. The cyan circles are the clusters from the eRASS1 cluster catalog (Bulbul et al. 2024; Kluge et al. 2024).



that the Cen 45 is being accreted toward Cen 30. The interaction between the two substructures is further supported by findings of temperature excess near the Cen 45 location, which can be explained by shock heating (Churazov et al. 1999; Walker et al. 2013a).

The central region of the cluster is filled with low-temperature and metal-rich gas (e.g., Ikebe et al. 1999; Sanders & Fabian 2002) and numerous structures (soft filaments, cold fronts, cavities, etc.) that are related to the AGN feedback of the BCG and sloshing motions (e.g., Taylor et al. 2006; Sanders et al. 2016b).

Being nearby, the Centaurus cluster has a relatively large apparent size in the sky ($R_{500} \approx 59'$). Hence, most of the X-ray studies are directed to probe the inner $r < 30'$ region due to the field-of-view (FoV) limitation. An attempt to probe the outskirts of the Centaurus cluster was done in Walker et al. (2013b), with a stripe of six *Suzaku* observations along the north-west direction (avoiding the known cold fronts and bright point sources) up to $0.95R_{200}$. In this work, we present a large-scale view of the Centaurus cluster using the eROSITA All-Sky Survey data (eRASS; Predehl et al. 2021; Merloni et al. 2024; Bulbul et al. 2024). We present the first ICM profiles (surface brightness, temperature, metallicity, and normalization per area) out to R_{200} sampling the full azimuth, as well as four different sectors divided based on the ellipticity of the cluster (semi-major/merger axis versus

semi-minor axis). Therefore, we increase the probed volume of the Centaurus cluster by a factor of almost 30.

The structure of this paper is the following: in Sect. 2, the data reduction steps, as well as the analysis strategy for imaging and spectral analyses are described. In Sect. 3, the results are presented and discussed in Sect. 4. We close with the summary and conclusions in Sect. 5.

Unless stated otherwise, all uncertainties are at the 68.3% confidence interval. The assumed cosmology in this work is a flat Λ CDM cosmology, where the Hubble constant is $H_0 = 70 \text{ km s}^{-1} \text{ Mpc}^{-1}$. At the assumed redshift of the Centaurus cluster, $z = 0.0104$, $1''$ corresponds to 0.213 kpc.

2. Data reduction and analysis

We employed nine sky tiles of the combined first five eROSITA All-Sky Survey data (eRASS:5) to cover the Centaurus cluster out to $3 \times R_{200}$. The data was processed using the c020 configuration. The sky tiles are 188129, 188132, 188135, 191129, 192132, 192135, 195129, 196132, and 197135. The Centaurus cluster is mainly located at sky tile 192132. The data reduction steps were performed utilizing the extended Science Analysis Software (eSASS, Brunner et al. 2022) version eSASSusers_211214 (eSASS4DR1¹). The data reduction started with the removal of

¹ <https://erosita.mpe.mpg.de/dr1/eSASS4DR1/>

Table 1: Information on the Centaurus cluster (Abell 3526) used in the present work.

R.A., Dec. [J2000]	192.200°, −41.308° ^a
Redshift z	0.0104 ^b
R_{500}	0.826 Mpc (3538.50'') ^a
R_{200}	1.271 Mpc (5443.85'') ^c
^a Piffaretti et al. (2011), ^b Lucey et al. (1986a),	
^c $R_{200} \approx R_{500}/0.65 \approx R_{2500}/0.28$ (Reiprich et al. 2013)	

unwanted pixels, such as bad pixels and strongly vignetted corners of the FoV by specifying `flag=0xe00fff30` in the `eSASS` task `evtool`. Afterwards, a light curve was generated for each sky tile by the `flaregti` task. We specified the minimum energy limit for the lightcurve creation of 5 keV (`pimin=5000`). A 3σ threshold was calculated from the lightcurve and supplied to the second run of `flaregti` by the parameter `threshold`. Two additional parameters were supplied, namely, the diameter of source extraction area in arcseconds unit (`source_size=150`) and the number of grid points per dimension (`gridsize=26`). A `FLAREGTI` extension was generated for each sky tile and applied to the event file through `evtool` task by adding the parameter `gti="FLAREGTI"`. In total, 2.1% of the exposure was removed, implying that the sky tiles used were not affected by any flares in all five eRASS passes. The average effective exposure time in the field is around 750 s. We then combined the cleaned and filtered sky tiles and centered them at the cluster center (Table 1). For the image correction, which includes particle-induced background (PIB) subtraction, exposure correction (including vignetting), and Galactic absorption correction across the FoV, we follow the steps described in Reiprich et al. (2021) (see their Sect. 2.1 and 3.3) and Veronica et al. (2024). We summarize the steps below and refer to Reiprich et al. (2021) for more details.

For the imaging analysis, the energy bands of 0.2 – 2.3 keV and 1.0 – 2.3 keV (see Sect. 2.3) were used. The eROSITA Telescope Modules (TMs) consist of five TMs with on-chip filter (TM1, 2, 3, 4, 6; the combination is referred to as TM8) and two without on-chip filter (TM5 and 7; the combination is referred to as TM9). The latter suffer from the optical light leak at the bottom part of their respective CCDs (Predehl et al. 2021). Due to this, different lower energy limits were used for the two types of eROSITA TMs, namely 0.2 keV and 0.8 keV for TM8 and TM9, respectively. It was discovered that the Al-K α at ~ 1.4 keV is higher in the filter-wheel closed (FWC) spectra than in the observations. In order to not overestimate the PIB modelled for the observation, we decided to exclude the 1.35 – 1.6 keV band from the imaging analysis. The correction takes into account the different lower energy limits and the count rates of the final, all-sky tiles combined, and a fully corrected image corresponds to an effective area given by one TM with an on-chip filter in the energy band 0.2 – 2.3 keV excluding the Al-K α line. However, for simplicity, we will refer to this energy band as the 0.2 – 2.3 keV band.

A relative Galactic absorption correction in the FoV was done utilizing the $N_{\text{H,tot}}$ map of the Centaurus field obtained by adding the HI4PI all-sky Galactic neutral atomic hydrogen map (HI4PI Collaboration et al. 2016) with N_{H2} map calculated using the method described in Willingale et al. (2013) through the Swift Galactic column density of Hydrogen tool². The eROSITA

count rates of different column density values, N_{H} , across the FoV were estimated by simulating a typical X-ray fore- and background model that consists of the unabsorbed Local Hot Bubble (LHB), the absorbed Milky Way Halo (MWH), and unresolved sources. For each pixel, the N_{H} correction value was calculated, namely the ratio of the expected eROSITA count rate at the given pixel to the count rate of the median N_{H} across the FoV. The absorption correction factor map was generated for each type of TMs and multiplied by its corresponding exposure map.

To detect and generate the point source catalog, we followed the procedure described in Pacaud et al. (2006) and Ramos-Ceja et al. (2019). The source detection was performed on a wavelet-filtered image by the Source Extractor software (Bertin & Arnouts 1996). The method detects not only point sources, but also extended sources (including small extended background sources) in the FoV. We used the obtained catalog to remove point sources and unwanted or unrelated sources in our imaging and spectral analyses. In order to emphasize low surface brightness and large-scale features, we applied adaptive smoothing to the images. We utilized the Science Analysis Software (SAS; version 20.0.0) task `asmooth` with the parameter `smoothstyle='adaptive'`. A cheese mask was also supplied which allows us to mask out unwanted sources and refill the holes with the surrounding background values. Any adaptively-smoothed images are for visualization purposes only.

2.1. Imaging analysis

We calculated surface brightness profiles of the Centaurus cluster out to $2 \times R_{200}$ using eRASS:5 products (cleaned- and flare-filtered photon map, PIB map, fully-corrected exposure map) in the 0.2 – 2.3 keV and 1.0 – 2.3 keV energy bands (see Sect. 2.3). To assess the morphology of the ICM, surface brightness profiles from four directions were constructed, namely north, west, south, and east. The opening angles of each sector were based on the position angle of the elliptical detection of SExtractor, such that the center of the opening angle of each sector is either the minor or major axis of the ellipse. We show the configurations of the opening angles of all the sectors, the characteristic radii³, and the cosmic X-ray background (CXB) regions used for our analyses in Fig. 2. All of the surface brightness profiles were centered at the center coordinates listed in Table 1.

2.2. Spectral analysis

The source and background spectra, as well as their Ancillary Response Files (ARFs) and the Response Matrix Files (RMFs), were extracted using `eSASS srctool` task. We performed all spectral fitting in XSPEC (Arnaud 1996) version: 12.12.0. The spectral fitting procedure follows closely the steps described in Veronica et al. (2024), except for the additional CXB component to account for the eROSITA Bubble emission (Sect. 2.3) and the used PIB model version. We summarize the spectral fitting procedure below.

The full spectral fitting model is

$$\text{Model} = (\text{apec}_1 + \text{TBabs} \times (\text{apec}_2 + \text{apec}_3 + \text{powerlaw})) + \text{TBabs} \times \text{apec}_4 + \text{PIB},$$

³ We convert the characteristic radii using the relations described in Reiprich et al. (2013), e.g., $R_{500} \approx 0.65R_{200}$, $R_{100} \approx 1.36R_{200}$, and $R_{2500} \approx 0.28R_{200}$.

² <https://www.swift.ac.uk/analysis/nhtot/>

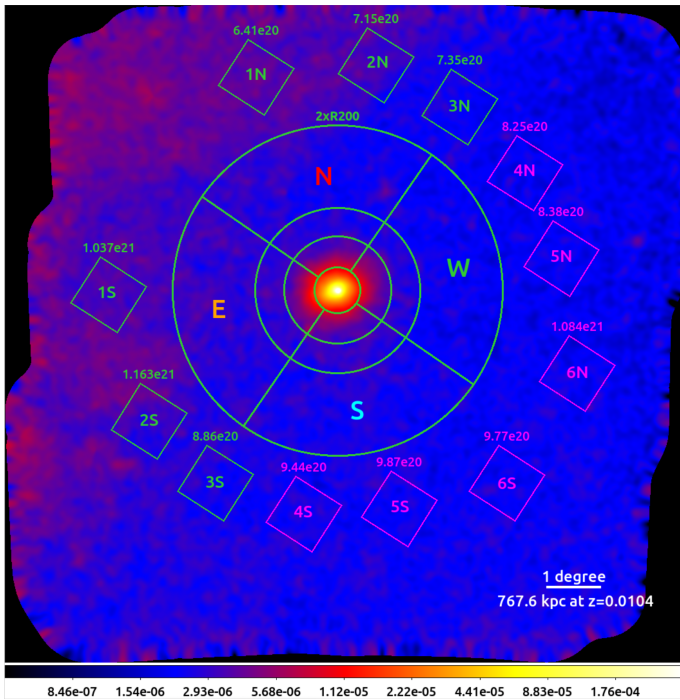


Fig. 2: eRASS:5 fully-corrected image in the 0.2–2.3 keV band. The image has been adaptively smoothed with S/N set to 45 (see Sect. 2.1). The green concentric circles are the characteristic radii of the Centaurus cluster and the four sectors used in the analyses are labelled. The boxes outside $2R_{200}$ are used for the CXB analysis described in Sect. 2.3, as a result we decided to use the magenta boxes for CXB region for our science analyses. The values above the boxes are their median N_H values in atoms cm^{-2} .

(1)

where the first term denotes the CXB components, including the unabsorbed Local Hot Bubble (LHB; apec_1), and the absorbed Milky Way halo (MWH; apec_2), the eROSITA Bubbles (apec_3), and unresolved sources (powerlaw). The apec component is described by five parameters: the plasma temperature ($k_B T$), metal abundances (Z), redshift (z), and normalization ($norm$). The absorption along the line of sight by the Galactic column density is represented by TBabs (Wilms et al. 2000). The N_H values used for the different regions are taken from the $N_{H,\text{tot}}$ map (see Sect. 2). The powerlaw component is described by photon index (Γ) and normalization parameters. For the spectral analysis, we always fixed $\Gamma = 1.46$ (Luo et al. 2017). The absorbed source thermal emission is described by the second term, $\text{TBabs} \times \text{apec}_4$. The PIB is represented by the third term, PIB. The modeling of the PIB in the present work used the results of the analysis of the FWC data processed in configuration c020⁴ (Yeung et al. 2023). The PIB component includes two power laws to account for the detector noise increase at the low energy, a combination of a power law and an exponential cut-off to model the signal above ~ 1 keV, and 21 Gaussian lines to model the fluorescence lines produced through the interaction of high-energy particles with detector components.

The fitting procedure is the following: first, the CXB spectra of all TMs were fitted to constrain the best-fit values of the normalizations of the CXB components. Afterwards, the source and

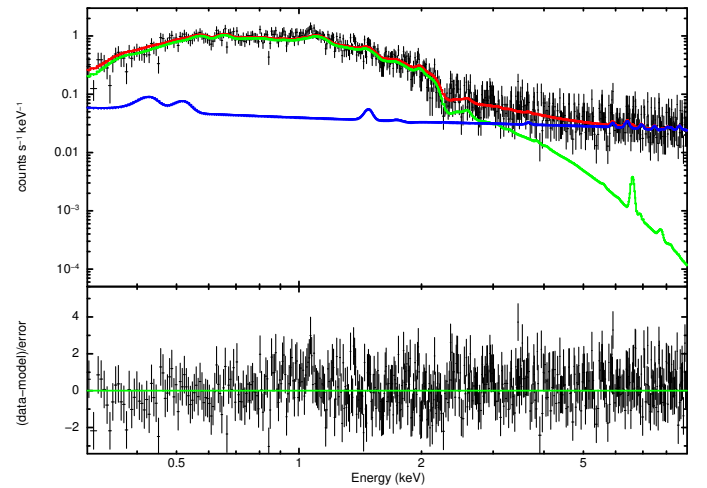


Fig. 3: TM1 spectrum fitted in the 0.3 – 9.0 keV energy band (top plot) and the fit residual (bottom). The black data points are the spectral data points extracted from an annulus of 0.2 – $0.5R_{500}$ around the Centaurus cluster center. The red line is the total model, the green line is the sky component, and the blue line is the PIB component.

CXB spectra were fitted simultaneously. The CXB parameters were linked across the spectra, except for the normalization of the eROSITA Bubble component. The starting parameters of the CXB normalizations were set to be the best-fit values obtained from the first fit. We fixed the eROSITA Bubble normalization of the CXB spectra to the value from the CXB analysis (see Sect. 2.3) and thawed this parameter in the source spectra. All normalizations, including those of the instrumental background components and the CXB components, were freed during the fit. The parameters of the source emission represented by apec_4 , namely $k_B T$, Z , and $norm$, were left to vary. The redshift was fixed to the Cen 30 redshift, $z = 0.0104$ (see Sect. 3.1). The fitting was performed in the energy band of 0.3 – 9.0 keV for TM8 and 0.5 – 9.0 keV for TM9. We adopted the C-statistic (Cash 1979) for estimating the parameters and we used the abundance table from Asplund et al. (2009). The analysis was done in effectively ten bins in full azimuthal configuration (annuli) and each sector out to R_{200} . Additionally, for full azimuthal configuration, we divided the central 0 – $2.50'$ area into three annuli, namely 0 – $0.83'$, 0.83 – $1.67'$, and 1.67 – $2.50'$, and we split the outer $R_{500} - R_{200}$ region into two, namely $R_{500} - 0.8R_{200}$ and $0.8R_{200} - R_{200}$ bins. For the sectors, we kept these two bins as an individual bin to retain good statistics. The configuration of the sectors and the characteristic radii are displayed in Fig. 2. We show an example of the eROSITA spectrum and its fitted model in Fig. 3.

2.3. The eROSITA Bubbles and cosmic X-ray background

ROSAT All-Sky Survey (RASS) discovered a soft X-ray emission that is a part of the North Polar Spur and Loop I (Egger & Aschenbach 1995). The first eROSITA All-Sky Survey (eRASS:1) image further reveals a huge structure in the southern sky analogous to the northern structure (Predehl et al. 2020). These large X-ray structures form a pair of ‘bubbles’ and are dubbed as the ‘eROSITA Bubbles’ (Predehl et al. 2020). The eROSITA Bubbles appear as annuli or shells centered about the Galactic center with extensions of about 80° in longitude and 85° in latitude. Although larger, the eROSITA Bubbles show great

⁴ https://erosita.mpe.mpg.de/dr1/AllSkySurveyData_dr1/FWC_dr1/

Table 2: CXB information for the spectral analysis of the Centaurus cluster.

Component	Parameter	Value
apec ₁ (LHB)	$k_B T^{456}$ [keV]	$0.115^{+0.002}_{-0.002}$
	Z [Z_\odot]	1
	z	0
	$norm^{*,456}$	$(1.42^{+0.09}_{-0.05}) \times 10^{-6}$
apec ₂ (MWH)	$k_B T^{456}$ [keV]	$0.207^{+0.003}_{-0.002}$
	Z [Z_\odot]	1
	z	0
	$norm^{*,456}$	$(1.71 \pm 0.05) \times 10^{-6}$
apec ₃ (eROSITA Bubbles)	$k_B T^1$ [keV]	$0.20^{+0}_{-0.0001}$
	Z [Z_\odot]	1
	z	0
	$norm^{*,456}$	$< 2.80 \times 10^{-8}$
powerlaw (unresolved sources)	Γ	1.46
	$norm^{*,456}$	$(6.66^{+0.13}_{-0.14}) \times 10^{-7}$

⁴⁵⁶ from combined box 4N, 5N, 6N, 4S, 5S, and 6S, ¹ from combined box 1N and 1S
^{*} [10^{22} atoms cm^{-2}], ^{*} [$\text{cm}^{-3}/\text{arcmin}^2$], ^{*} [photons/keV/ $\text{cm}^2/\text{s}/\text{arcmin}^2$ at 1 keV]

similarity in morphology to the Fermi Bubbles (Su et al. 2010) and are therefore thought to originate from the same source, large energy injections from the Galactic center (Predehl et al. 2020).

Our FoV is partially contaminated by the eROSITA Bubble (bright yellowish emission spreading from the center top to bottom left of Fig. 1). As can be seen in Fig. 2, the eROSITA Bubbles emission is also inside the $2R_{200}$ of the Centaurus cluster, mainly in the northern and eastern sectors. Due to this, we performed an exhaustive investigation of various regions before settling on a specific (CXB) region for the science analyses. We distributed six pairs of boxes, spreading from north to west (1 – 6N in Fig. 2) and from east to south (1 – 6S) outside the $2R_{200}$ to minimize the emission from the cluster. Each box has the size of $1^\circ \times 1^\circ$.

First, we performed a spectral fitting in these boxes with a typical CXB model that includes the foreground emission from LHB and the MWH, as well as the emission from the unresolved sources. The LHB and MWH are represented with an apec component each. In this fit, we fixed the temperatures of the LHB to MWH to 0.1 keV and 0.25 keV, whereas their metal abundances and redshift are fixed to $1Z_\odot$ and 0, respectively. Based on this analysis, we observe that the soft band flux ($f_{X,0.5-2 \text{ keV}}$) decreases with a factor of 1.3 – 1.7 outwards and flattens out at box 4N, 5N, 6N, 4S, 5S, and 6S (box 456; magenta boxes). We then used these six boxes to constrain the temperatures of the LHB and MWH and their normalizations, as well as the normalization of the unresolved sources (see Table 2). We found a temperature of 0.115 ± 0.002 keV for LHB, which is in good agreement with the RASS result ($0.097 \pm 0.013 \pm 0.006$ keV; Liu et al. 2016). For the MWH, our estimate ($0.207^{+0.003}_{-0.002}$ keV) agrees within the errors of what was measured from ROSAT spectrum ($0.24^{+0.08}_{-0.03}$ keV; Kuntz & Snowden 2000) and XMM-Newton EPIC spectra (0.204 ± 0.009 keV; Lumb et al. 2002). It is also broadly in agreement with other eROSITA MWH measurements ($0.15 - 0.20$ keV; Ponti et al. 2023; Zheng et al. 2024).

Afterwards, we fit boxes 1N and 1S (box 1) together with an additional absorbed thermal emission that represents the eROSITA Bubbles (apec₃). Similar to the other foreground components, we fixed the metallicity and redshift to $1Z_\odot$ and 0, respectively. In this step, we fixed the parameters related to the LHB, MWH, and unresolved sources to the best-fit values obtained from box 456 and freed the temperature and normaliza-

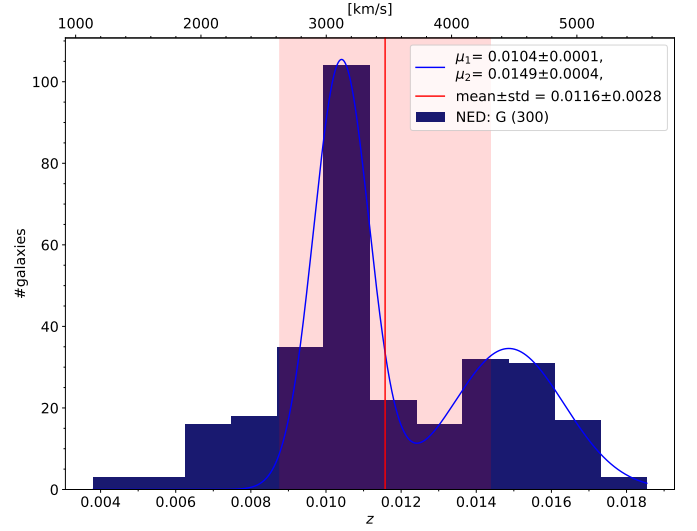


Fig. 4: NED galaxy redshift distribution within R_{200} of the Centaurus cluster. In total, there are 300 galaxies up to $z = 0.02$. The blue line is the double Gaussian fit, the red vertical line and the red shaded area are the mean and the 1σ standard deviation of the whole sample.

tion of the eROSITA Bubbles. We obtained a best-fit temperature of 0.2 keV. A second apec component was added, however, we could not constrain any additional emission from the Bubbles. Comprehensive eROSITA analyses of the LHB, MWH, and eROSITA Bubbles will be reported in the upcoming papers (Yeu et al.; Ponti et al. in prep.). See also recent soft X-ray background investigation using *Suzaku* by Sugiyama et al. (2023), where they report a ~ 0.8 keV component in 56 out of 130 observations. The emission measure of this component is higher toward the Galactic plane, which signifies its Galactic origin. We note that the Centaurus cluster region is outside their studied area.

We listed the results of our local CXB analysis in Table 2. Hence, for the science analyses, we used box 456 as the default CXB region. For instance, in the imaging analysis, the CXB level was calculated to be the average of surface brightness values amongst box 456 (SB_{CXB}) and the standard deviation is the root-mean-square deviation of these values (σ_{CXB}) to take into account the spatial variation of the CXB. For the spectral analysis, we froze the temperatures of the CXB components to the values listed in Table 2.

3. Results

3.1. Galaxy redshift analysis

We compiled a catalog of galaxies with known redshifts within our FoV from NED⁵. To inspect the substructures of the cluster, first, we assessed the galaxy redshift distribution within R_{200} (Fig. 4). Within this perimeter, we found 300 galaxies with $z \leq 0.02$. The mean of the whole sample within the R_{200} is $z = 0.0116 \pm 0.0028$ (red line and red-shaded area in Fig. 4), which is in agreement with the value reported in Piffaretti et al. (2011). In the distribution, a bimodality is apparent, which has

⁵ The NASA/IPAC Extragalactic Database (NED) is funded by the National Aeronautics and Space Administration and operated by the California Institute of Technology.

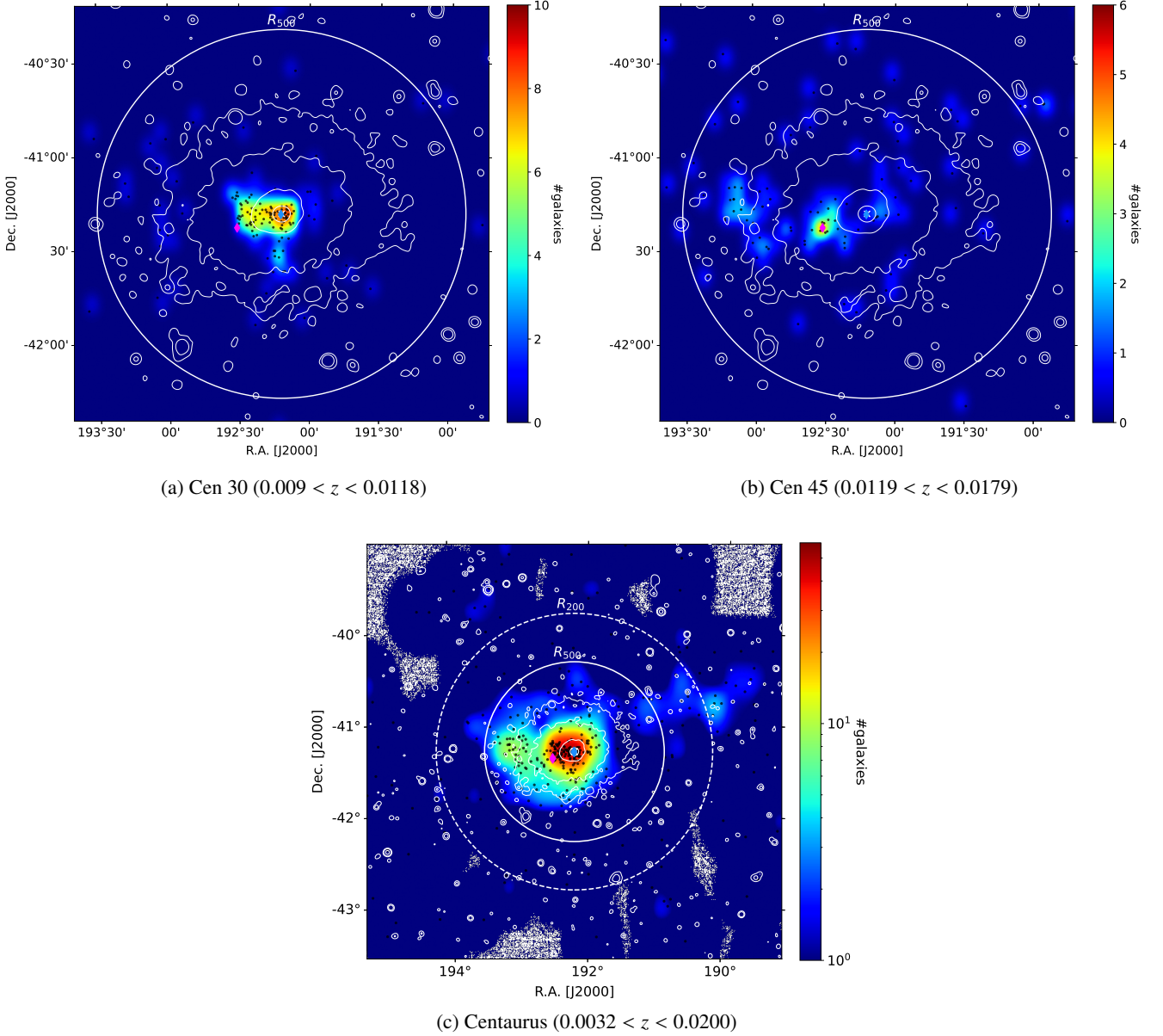


Fig. 5: Galaxy number density maps in different redshift ranges. Blue and magenta diamonds denote the positions of the central galaxies of Cen 30 (NGC 4696) and Cen 45 (NGC 4709). The white contours are the eROSITA X-ray contours.

been known to be contributed by the substructures of the Centaurus cluster, which are Cen 30 and Cen 45 (Lucey et al. 1986a). We fitted a double Gaussian function onto the distribution (shown as blue line in Fig. 4) and found the peaks at $z_{\text{Cen30}} = 0.0104$ ($v = (3117.8 \pm 30.0) \text{ km s}^{-1}$) and $z_{\text{Cen45}} = 0.0149$ ($v = (4466.9 \pm 119.9) \text{ km s}^{-1}$).

In Fig. 5 we display the galaxy number density maps of three redshift slices for Cen 30 (panel 5a; $0.0090 < z_{\text{Cen30}} < 0.0118$), Cen 45 (5b; $0.0119 < z_{\text{Cen45}} < 0.0179$), and Centaurus cluster as a whole (5c; $0.0032 < z < 0.020$). The maps were generated by smoothing the spatial bins of their respective galaxy distributions. From the figures, we see that the distribution of the galaxy members of Cen 30 peaks around its central galaxy, NGC 4696 (blue diamond), which also coincides with the cluster center (white cross). The galaxy number density spreads eastward. Similarly, for Cen 45, the peak galaxy number density is situated

at the central galaxy NGC 4709 (magenta diamond), 14.9' eastward of the cluster center. An excess is also apparent in the east, at the edge of the X-ray contour.

Large-scale filaments can be traced by trails of gas clumps and galaxies (e.g., Malavasi et al. 2020; Tuominen et al. 2021; Angelinelli et al. 2021). Therefore, in Fig. 5c, we expanded the view to $\sim 1.5R_{200}$ and included all galaxies within three times the standard deviation of the mean redshift, which translates to a velocity of 2518.3 km s^{-1} . Within R_{500} , a significant galaxy overdensity is apparent in the east. Outside this boundary, a hint of low significance excess is visible in the west, going slightly northward. This feature was dubbed as the "Western Branch" in Lucey et al. (1986a) and based on their redshifts, it is composed of the supposed galaxy members of the two substructures. The peak overdensity in this feature, slightly outside of the R_{200} , is located at NGC 4603C ($z = 0.0104$; Ogando et al. 2008). We

note that these east and west galaxy overdensities match the apparent elongation directions in the gas distribution of Centaurus cluster.

3.2. X-ray images

We present the composite image of the Centaurus cluster combining nine sky tiles of eRASS:5 data in Fig. 1. The red, green, and blue channels are in the 0.2 – 0.6 keV, 0.6 – 1.0 keV, and 1.0 – 2.3 keV, respectively. Since the lower energy cut of TM9 is 0.8 keV, only TM8 was used to produce the red channel image. The image in each channel was PIB-subtracted, exposure-corrected, and Galactic-absorption corrected following the procedure described in Sec. 2. To enhance large-scale emission, wavelet filtering was also applied using the same scale for each image. With the same purpose, we also generated an adaptively-smoothed image in the 0.2 – 2.3 keV (Fig. 2).

From Fig. 1, the emission from the Centaurus cluster is peaked at the center and smooth going outward. The cluster looks undisturbed with a symmetric elliptical shape. Throughout the FoV, many point sources are noticeable. Some with harder spectra appear in white. Overplotted in cyan are the clusters from the eRASS1 catalog in the Western Galactic Hemisphere (Bulbul et al. 2024; Kluge et al. 2024). The bottom area of the FoV ($b \leq 20^\circ$) is excluded from the eRASS1 cluster detection, hence, the absence of clusters is seen in the image. The sizes of the circles correspond to their R_{500} . Based on their redshifts (labeled on top of each circle), all of the detected clusters are background objects. A distinctive white extended emission at the top left of the FoV is a known background galaxy cluster, Abell S072.

As mentioned in Sec. 2.3, our FoV is partially contaminated by the eROSITA Bubble emission, which is spreading from center top to bottom left corner of the image and apparent in yellowish (reddish) color in Fig. 1 (2). To investigate at which energy the eROSITA Bubbles roughly diminish in the image, we additionally ran the image correction and adaptive-smoothing procedure in three sub-bands. These images are shown in Fig. 6 left (0.8 – 2.3 keV), middle (0.9 – 2.3 keV), and right (1.0 – 2.3 keV) panels. The surface brightness intensity of the eROSITA Bubble emission decreases toward higher low energy bounds. Based on these sub-band images, we therefore also calculated surface brightness profiles using the 1.0 – 2.3 keV energy band to ensure minimum eROSITA Bubble contamination (see Sect. 3.3). An attempt was made to spatially subtract the CXB emission (including the eROSITA Bubbles component) from the image. The details of this effort is described in App. B.

Additionally, we applied Gaussian gradient magnitude (GGM) filtering to the 0.2 – 2.3 keV fully-corrected image. The GGM filtering calculates the magnitude of the surface brightness gradient assuming Gaussian derivatives, which as a result, emphasize features (e.g., edges) in the image (Sanders et al. 2016b). Due to this, the technique is often used to inspect features in clusters, both in simulations and observations (e.g., Sanders et al. 2016b,a; Walker et al. 2016). The GGM filtering is adjusted with the width σ , where a smaller scale is used to amplify features in the regions with more counts (cluster center) and a larger scale is used for regions with fewer counts (outskirts). We performed the GGM filtering using the available implementation from SciPy⁶ (Virtanen et al. 2020). The resulting GGM-filtered images using $\sigma = 2, 4, 8, 32$ are shown in Fig. 7 (left to right). Some features in the central region of the Centaurus cluster are known and well-studied using previous dedicated *Chandra* and *XMM-*

Newton observations (e.g., Sanders & Fabian 2002; Fabian et al. 2005; Sanders et al. 2008; Walker et al. 2013a; Sanders et al. 2016b), for example, the soft filament in the core that extends toward the northeast seen in the 2-pixel GGM-filtered image, as well as the eastern and western edges in the 4-pixel GGM-filtered image ($\sim 2.1'$ and $3.6'$ from the cluster center, respectively). With eRASS:5 data, we are able to examine large-scale features beyond R_{2500} . In the 8 and 32-pixel GGM-filtered images, we observe the east-west ICM emission with longer extension toward the east. This eastern extension coincides with galaxy overdensity (see Sect. 3.1) and the excess will be quantified in Sect. 3.3.

3.3. X-ray surface brightness profiles

We present the surface brightness profiles of the Centaurus cluster out to $2R_{200}$ in the 0.2 – 2.3 keV and 1.0 – 2.3 keV band in the left and right panels of Fig. 8, respectively. In each plot, the full azimuthal (annuli) surface brightness values with the 1σ statistical error are shown as the grey-shaded area. The green, blue, orange, and red data points belong to the western, southern, eastern, and northern sectors, respectively. The configuration of these sectors is shown in Fig. 2. We mark the position of Cen 45, which is located about $15'$ eastward of the center, with a purple vertical line. The CXB level (SB_{CXB}) is shown as magenta horizontal-dashed lines and its standard deviation (σ_{CXB} ; see Sect. 2.3) is as magenta shaded area. Using the full azimuthal surface brightness profile calculated in 0.2 – 2.3 keV band, we also constructed a spherical surface brightness image out to $2R_{200}$, which was subtracted from the fully corrected image in the corresponding band to yield a residual image. The Gaussian-smoothed ($\sigma = 25$ pixels) residual image is displayed in Fig. 9.

3.3.1. Inner ($r \leq R_{500}$)

In Fig. 8a, we show the surface brightness profiles out to R_{500} in the energy band of 0.2 – 2.3 keV (top plot) and the significance deviation profile of each sector with respect to the full azimuthal surface brightness profile ($\sigma_{w.r.t.annuli}$; bottom plot). In the west at around $2 - 3'$, an excess is observed with an average significance of 3.8σ . The significance drops to 1.3σ at the next bin. The location of the western excess matches the location of the western edge that is apparent in the 2 and 4-pixel GGM-filtered images (see Fig. 7).

A striking bump of excess of about $3 - 5\sigma$ is also seen in the eastern sector at $4 - 25'$. This enhancement coincides with the interaction location between Cen 30 and Cen 45, which is shown as the galaxy overdensity in Fig. 5. From the eastern surface brightness profile in the 0.2 – 2.3 keV, the average significance surface brightness excess with respect to the average surface brightness values in different segments are 4.0σ for $0 - 14.8'$, 4.2σ for $14.8 - 25.3'$, and 2.5σ for $25.3 - 35.3'$. Outside the core, the upper limits of these segments correspond to roughly the position of the NGC 4709 galaxy (Cen 45), R_{2500} , and $0.6R_{500}$ from the cluster center, respectively. As a comparison, the significance values in the opposite western sector are -1.4σ , -0.7σ , and -0.2σ for each segment. Moreover, we observe surface brightness deficits of $3 - 5\sigma$ in the southern sector at $5 - 14'$. These features are further emphasized in the residual image (Fig. 9).

We show surface brightness profiles and their significance plot in the 1.0–2.3 keV band in Fig. 8b. Compared to the full soft band profiles, we observe only minor differences, such as lower

⁶ <https://scipy.org/>

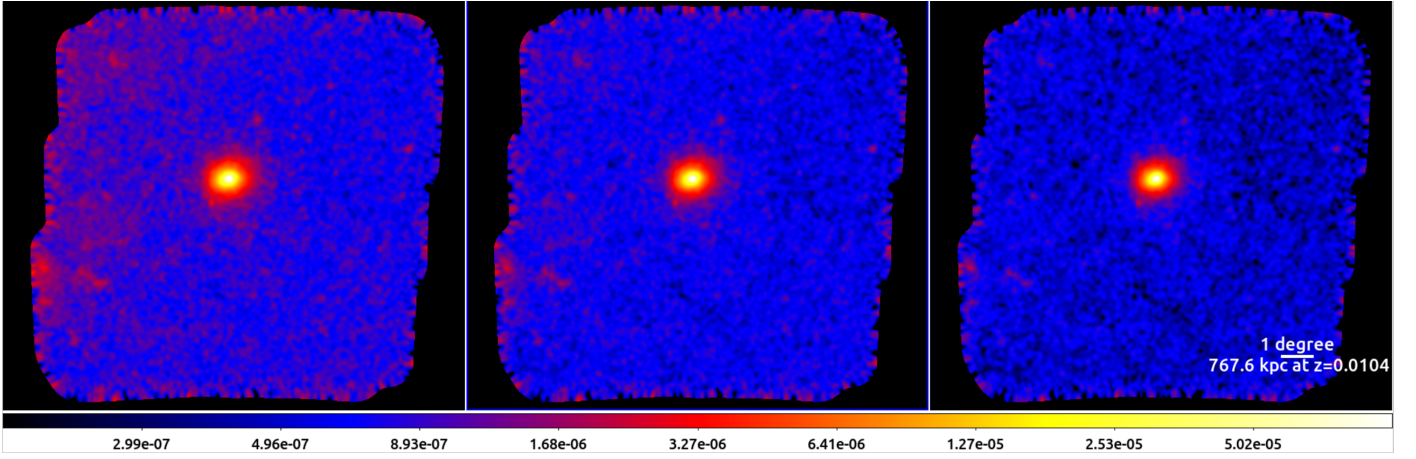


Fig. 6: Same as Fig. 2, but in different energy bands. *Left*: 0.8 – 2.3 keV band. *Middle*: 0.9 – 2.3 keV. *Right*: 1.0 – 2.3 keV.

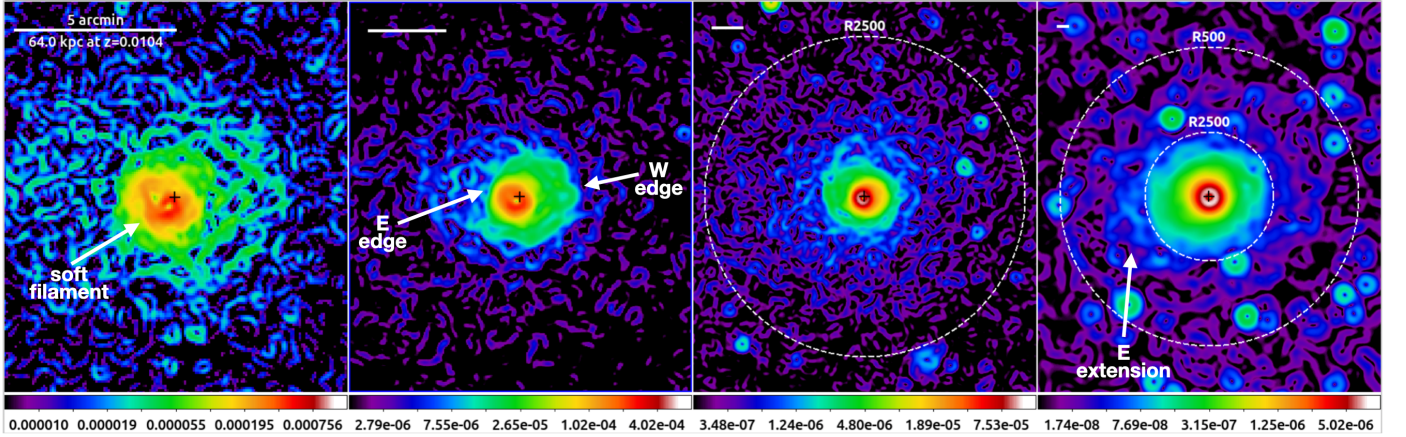


Fig. 7: GGM-filtered images of the fully-corrected image in 0.2 – 2.3 keV using scales $\sigma = 2, 4, 8, 32$ pixels (1 pixel is $4.0''$). The black cross in the center of each panel marks the cluster center. The white line at the top left of each panel indicates a $5'$ (64 kpc) length.

surface brightness amplitudes of the profiles and the CXB level, suggesting that there is little to no impact from the eROSITA Bubbles for inner $r < R_{500}$ regime. We keep the axis scale consistent for both panels 8a and 8b to show the mentioned differences. The western and eastern excesses, as well as the southern depression, are still visible.

3.3.2. Outer ($R_{500} < r < 2R_{200}$)

Similar to Fig. 8a and 8b, the top plots of Fig. 8c and 8d show the surface brightness profiles in the 0.2 – 2.3 keV and 1.0 – 2.3 keV bands, but at radial distance between R_{500} and $2R_{200}$. The bottom plots, instead, show the significance level of the source surface brightness with respect to the CXB level ($S/N_{w.r.t.CXB}$) and is given as:

$$S/N_{w.r.t.CXB} = \frac{SB_{r>R_{500}} - SB_{CXB}}{\sqrt{\sigma_{r>R_{500}}^2 + \sigma_{CXB}^2}}, \quad (2)$$

where SB_r is the surface brightness value of the bin at $r > R_{500}$ regime, σ_r is its statistical uncertainties, while SB_{CXB} and σ_{CXB} are the sky background surface brightness and its standard deviation. In the $R_{500} < r < R_{200}$ regime, we observe significant cluster emission as shown in the 0.2 – 2.3 keV significance pro-

file for the full azimuthal region (grey diamonds) with significance values spreading between 3.3 and 6.7σ . Between R_{200} and $2R_{200}$, the full azimuthal and northern (red) significance profiles show similar trend of steady increase. The significance values at $2R_{200}$ of the full azimuthal and northern profiles are 3.4 and 5.6σ , respectively. The Eastern (orange) significance profile at this regime shows a similar trend but with higher amplitude. The minimum significance is 3.6σ at $110'$ and the maximum is 7.1σ at $190'$. For the southern (blue) profile, excesses are seen, however with less significance in comparison to the northern and eastern sectors. The significance values of the southern sector in $R_{500} < r < R_{200}$ regime are between 1.7 at $160'$ and 5.4σ at $70'$. Unlike the other sectors, at $r > R_{200}$, the surface brightness profile of the green sector stays around the 1σ of the CXB level (magenta-shaded area). The trends seen in the profiles of the various sectors in this 0.2 – 2.3 keV energy band show the levels of eROSITA Bubbles contamination, such that the contamination is the strongest in the east and north, mild in the south, and none in the west. This agrees with the visual inspection (see Fig. 9).

Between R_{500} and R_{200} in the 1.0 – 2.3 keV full azimuthal surface brightness profile (Fig. 8d), we observe similarity in the shape of the profile to those of 0.2 – 2.3 keV profile. For the eastern sector, the average significance value between $60' \leq r \leq 83'$ is 2.6σ . Near the R_{200} mark, the values drop to the CXB level

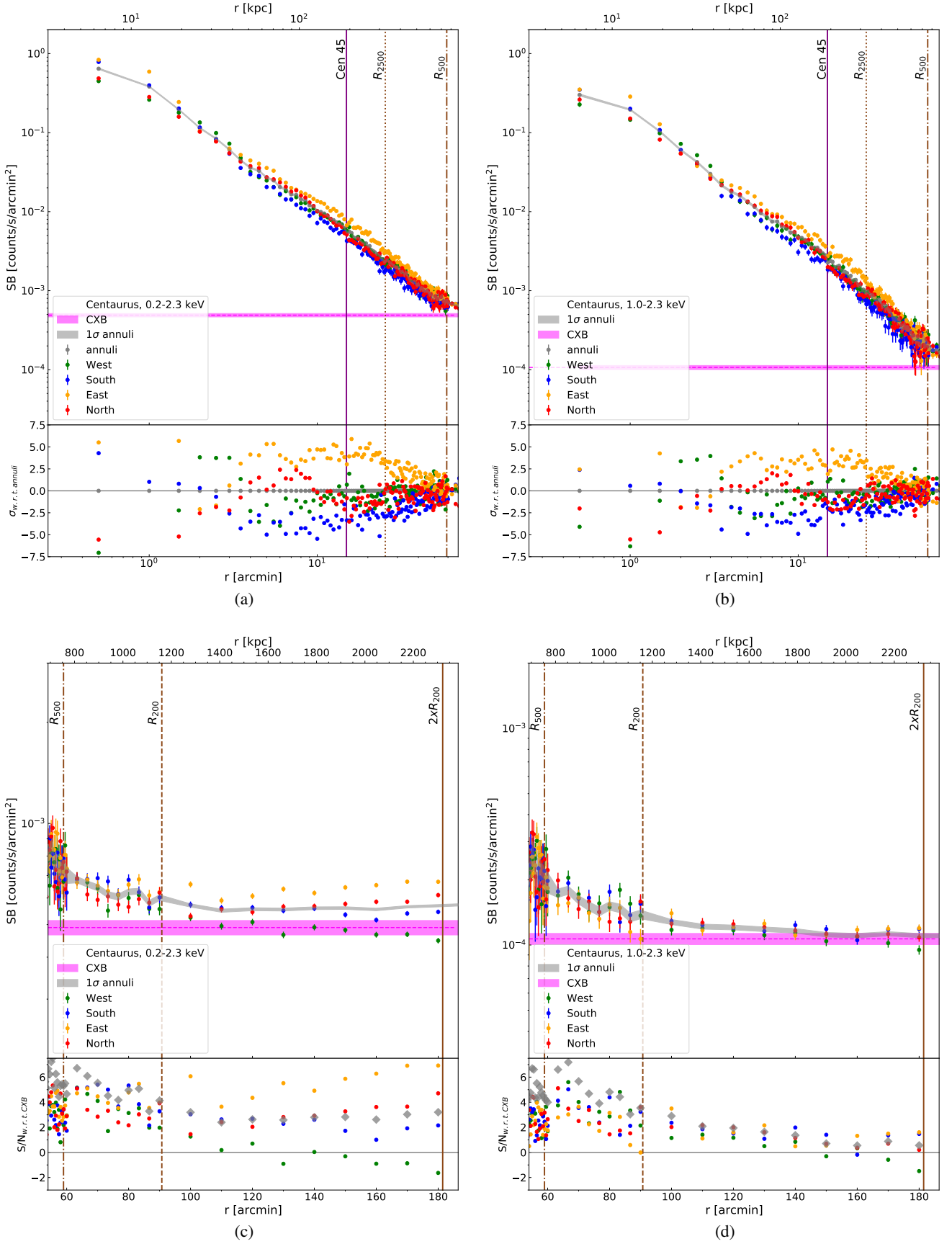


Fig. 8: Surface brightness profiles of the Centaurus cluster are shown in the top panel in each plot. The different sectors are indicated with different colors. The CXB level and its 1σ standard deviation are shown as the magenta dashed line and shaded area. The bottom panels show the significance with respect to the full azimuthal surface brightness profile ($\sigma_{w.r.t.annuli}$) and the CXB level ($S/N_{w.r.t.CXB}$). *Top:* Between 0 – R_{500} . *Bottom:* R_{500} – $2R_{200}$

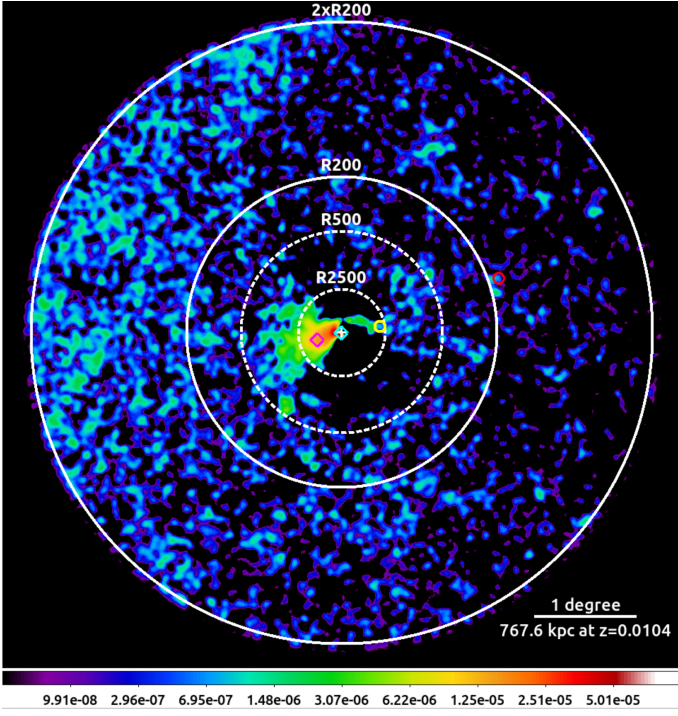


Fig. 9: Residual image out to $2R_{200}$ in the 0.2 – 2.3 keV band. The image is Gaussian-smoothed with $\sigma = 25$ pixels. The cyan and magenta diamonds denote the positions of NGC 4696 and NGC 4709, while the yellow and red circles denote the positions of NGC 4696B and NGC 4603C.

and the bin afterwards jumps to 3.5σ . The significance values of the following eastern bins decrease. As for the other sectors, we see the significance values approach the CXB level between R_{500} and $2R_{200}$. The significance values for the full azimuthal annuli at $R_{500} < r < R_{200}$ regime vary between 3.0σ and 7.2σ . At $90'$ ($\sim R_{200}$), a 3.5σ signal above the CXB was detected, then followed by 2.9σ at $100'$ ($\sim 1.1R_{200}$). The smooth significance decrease hits the 1σ level around $140'$ ($\sim 1.5R_{200}$).

3.4. Spectral analysis

We present the spectral parameter profiles of the Centaurus cluster out to R_{200} obtained from eRASS:5 data in Fig. 10, which are the first detailed profiles of the cluster at $r > 30'$. We display the profiles of the eastern (orange data points) and western (green) sectors in the left panel, and the profiles of the northern (red) and southern (blue) sectors in the right panel of Fig. 10. In each panel, we show the normalization per unit area (top), gas temperature (middle), and metallicity (bottom). In each plot, the full azimuthal profile of each parameter is shown as the grey-shaded area. The purple vertical line is the position of the center of Cen 45 from the X-ray center (only relevant for the eastern sector). The characteristic radii are denoted with the black vertical-dotted (R_{2500}), dashed-dotted (R_{500}), and dashed (R_{200}) lines. We also list these results in Table C.1.

To compare the resulting outskirts temperatures, we plot in Fig. 10 the temperature fit from Reiprich et al. (2013) as a purple-shaded area and the average temperature profile from simulations given in Burns et al. (2010) as a pink-shaded area. The temperature profile from Reiprich et al. (2013) was acquired from fitting 162 *Suzaku* cluster profiles and given as $k_B T(r) = (1.19 - 0.84r/R_{200})\langle k_B T \rangle$ at $0.3R_{200} < r < 1.15R_{200}$.

The profile from Burns et al. (2010) is the average temperature two-dimensional profile of the simulated clusters using the *Enzo* N-body plus hydrodynamics cosmology code (Bryan et al. 2014). The form for the Burns et al. (2010) temperature profile is given in their Eq. 8, which we re-arranged into:

$$k_B T(r) = A \cdot \langle k_B T \rangle \left[1 + B \left(\frac{r}{R_{200}} \right) \right]^\alpha, \quad (3)$$

where $A = 1.74 \pm 0.03$, $B = 0.64 \pm 0.10$, and $\alpha = -3.2 \pm 0.4$. In both temperature functions, $\langle k_B T \rangle$ is given as the eRASS:5 temperature of Centaurus cluster obtained from an annulus of $0.2 - 0.5R_{500}$, that is $2.64^{+0.08}_{-0.07}$ keV.

We also compare the eRASS:5 results with *Chandra* results out to $\sim 13'$ (colored-shaded areas). The *Chandra* information is the adaptation of Fig. 3 or Fig. 6 of Sanders et al. (2016b), which was obtained from *Chandra* spectral fittings in the 0.5 – 7.0 keV band. In order to have a close comparison to the eRASS:5 profiles, the bins in the *Chandra* spectral maps have been split into the sectors defined in this present work. We report the temperatures returned by eROSITA are lower than *Chandra* measurements by about 25% on average, which is on the same order as the reported value in the cross-calibration work by Migkas et al. (2024) (see also Liu et al. 2023, for the eROSITA-*Chandra* temperature comparisons of the SMACS J0723.3–7327 cluster).

To compare with the *Chandra* metallicity profiles, we need to scale up the metallicity values from *Chandra* by a factor of 1.48. The factor is to account for the different abundance tables and is calculated by dividing the solar Fe/H ratio from the abundance table assumed in Sanders et al. (2016b) (Anders & Grevesse 1989, 4.68×10^{-5}) with the Fe/H ratio assumed in this work (Asplund et al. 2009, 3.16×10^{-5}).

Additionally, we fitted the cluster with only atomic hydrogen (N_{H}) absorption. We found systematically higher temperature values in comparison to the spectral fitting results using the $N_{\text{H,tot}}$ values. The same outcome is also reported in Rossetti et al. (2024). In general, we found that the discrepancies for bins with higher temperatures ($k_B T > 2$ keV) are higher ($> 20\%$). We note that the presented spectral analysis are those constrained with the $N_{\text{H,tot}}$ values.

3.4.1. Full azimuthal profiles

We observe a low temperature ($1.43^{+0.03}_{-0.01}$ keV), metal-rich ($0.67 \pm 0.05Z_\odot$) gas in the core of Centaurus cluster, as also seen in other X-ray observatories (e.g., Allen & Fabian 1994; Sanders et al. 2016b; Gatuzz et al. 2022a). Looking at the full azimuthal profile, the temperature increases gradually to ~ 3.0 keV at $6.3'$, then it drops from $22.7'$ ($0.9R_{2500}$) outward. From the peak to the outermost bin, the temperature decreases by a factor of 2.8.

For the metallicity profile, we identified a peak at $1.3'$ of $1.18^{+0.10}_{-0.09}Z_\odot$. From $3.8'$ to $6.3'$, the metallicity drops by a factor of 2 to a sub-solar value of $0.34^{+0.06}_{-0.05}Z_\odot$. Outward, the metallicity decreases smoothly. Near R_{500} , we report a metallicity of $0.12 \pm 0.02Z_\odot$ and a best-fit value of $0.04Z_\odot$ ($R_{500} - 0.8R_{200}$) and $0.09Z_\odot$ ($0.8R_{200} - R_{200}$). We note that for consistency and easier comparison with the other sectors, the combined central ($0 - 2.5'$) and outermost bins ($59.0 - 90.8'$) of the full azimuthal profile are used.

3.4.2. Eastern and western profiles

In agreement with the surface brightness profile and residual image, there is an excess normalization per area with respect to the

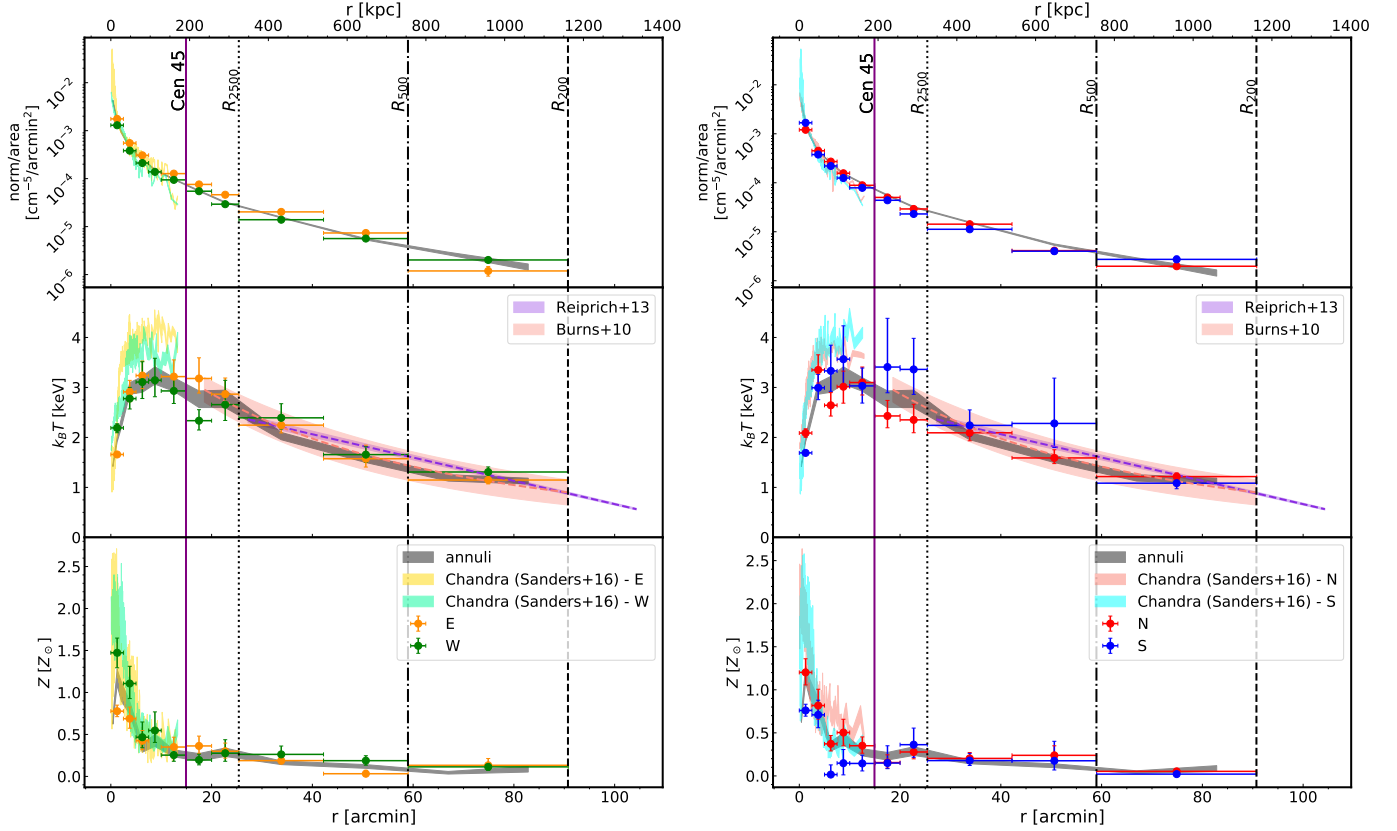


Fig. 10: The spectral parameter profiles of the Centaurus cluster constrained from eRASS:5 data. *Left*: Eastern (orange data points) and western (green) profiles. *Right*: Northern (red) and southern (blue) profiles. In each panel we show the normalization per unit area (top), gas temperature (middle), and metallicity (bottom) plots. The full azimuthal profile of each parameter is shown as the grey-shaded area. In the temperature panels (middle), we plot the *Suzaku* cluster temperature fit (purple-shaded area; Reiprich et al. 2013) and the average two-dimensional cluster profile from simulations (pink-shaded area; Burns et al. 2010).

full azimuthal values in the eastern sector for all bins, except for the outermost one. At the bin before ($10.0 - 15.0'$) and after the center of Cen 45 ($15 - 20.0'$), there is a 31% and 36% excess of 5.4σ in both bins. The normalization excess peaks at $20.0 - 25.4'$ bin with 45% and 7.7σ , then falls to 30% (7.0σ) and 36% (2.6σ) in the following bins. In the last two bins (from $0.7R_{500} - R_{500}$ to $R_{500} - R_{200}$), the normalization per area drops with a factor of ~ 6 , whereas it is only a factor of ~ 3 for the same bins in the west.

The shape of the eastern and western temperature profiles (middle plot of the left panel in Fig. 10) shows a great resemblance to the full azimuthal temperature profile. At the central bin ($0 - 2.5'$), the western sector shows a higher temperature ($2.19^{+0.08}_{-0.10}$ keV) in comparison to the eastern sector (1.66 ± 0.03 keV) with a significance of 5.2σ . In general, except for the first bins, the temperature data points of these sectors are within 1.6σ of the full azimuthal values.

In comparison to the first bin of the eastern best-fit metallicity ($0.78Z_{\odot}$), the value in the west is higher by a factor of 2 ($1.47Z_{\odot}$). The metallicity profiles of both sectors fall after the first bin and flatten outward. At larger radii, for instance, at $59.0 - 90.8'$ ($R_{500} - R_{200}$), the metallicity values are low, that is $Z = 0.07 - 0.16Z_{\odot}$ for the western and $Z = 0.08 - 0.21Z_{\odot}$ for the eastern sectors.

3.4.3. Northern and southern profiles

Similarly, the profiles of the northern and southern sectors exhibit the low-temperature, high-metallicity gas in the core. Temperature and metallicity asymmetry are also observed for the first bins. For instance, the northern sector shows a higher temperature ($2.09^{+0.09}_{-0.09}$ keV) than its counterpart bin ($1.69^{+0.04}_{-0.03}$ keV) with a significance of 4.2σ . The metallicity in the north is $1.2^{+0.16}_{-0.15}Z_{\odot}$, while it is $0.76^{+0.07}_{-0.07}Z_{\odot}$ in the south. The northern metallicity in the core is higher than in the south by a factor of 1.6, with a significance of 2.7σ . Other fluctuation is the southern temperature ($2.28^{+0.91}_{-0.48}$ keV) excess with respect to its northern ($1.59^{+0.16}_{-0.11}$ keV) counterpart at the $42.2 - 59.0'$ bin. However, this temperature excess is only 1.4σ (1.3σ) to the northern (full azimuthal) profile. The large error bars, especially of the southern profiles, can be attributed to the fewer statistics that are evident in the imaging analysis (for example, the residual image in Fig. 9 and surface brightness profiles in these directions in Fig. 8). This is also expected as the north-south direction is the minor-axis direction of the cluster. Between 2.5 and $59'$, the average temperature uncertainty is 0.50 keV for the southern sector and ~ 0.25 keV for the other sectors.

The metallicities in the second bins are high with $0.82Z_{\odot}$ for the northern sector and $0.71Z_{\odot}$ for the southern sector. From the second to the third bin of the southern sector, a dramatic drop of 3.5σ is observed. From this point to R_{500} , the southern metallicity profile appears flat with an average value of $0.19Z_{\odot}$. For the northern sector, the metallicities at the intermediate radial range

of $5.0 - 15.0'$ are relatively high with an average of $0.44Z_{\odot}$ and ranging between 0.29 and $0.66Z_{\odot}$. At $R_{500} - R_{200}$, we report low metallicity ranges of $0.02 - 0.08Z$ in the north and $0.003 - 0.05Z_{\odot}$ in the south.

3.4.4. Two-temperature profile

We performed a two-temperature (2T) fitting to the full azimuthal bins up to $2.5'$ from the center. To reduce the degree of freedom during the fit, we linked the metallicities of the two components. The temperature profile of the hotter component resembles closely the single component temperature profile (grey-shaded area), while the temperatures of the cooler component across the bins are relatively flat, ranging between 0.8 and 1.7 keV. We note that based on the Akaike information criterion (AIC; Akaike 1974) and the Bayesian information criterion (BIC; Schwarz 1978), there is no significant improvement in the fit when adding a second component, except for the first bin ($0 - 0.8'$) where the 2T fit is a more suitable model to describe the spectra. The results of the 2T-fit are listed in Table C.2.

4. Discussion

4.1. Galaxy optical redshift analysis

We performed a galaxy redshift analysis in the eRASS:5 Centaurus field utilizing the available photometric redshift compiled from NED (see Sect. 3.1). We found 300 galaxies within the R_{200} with $z < 0.02$. The distribution shows a bimodality (see Fig. 4), peaked at $z = 0.0104 \pm 0.0001$ ($v = 3117.8 \pm 30.0$ km s $^{-1}$) and $z = 0.0149 \pm 0.0004$ ($v = 4466.9 \pm 119.9$ km s $^{-1}$), which has been known to represent the Cen 30 and Cen 45 substructures (e.g., Lucey et al. 1980, 1986a). The spatial distribution of the galaxy members of each structure is shown in Fig. 5a (Cen 30) and Fig. 5b (Cen 45). In these panels, the peaks of the spatial distributions match well with the position of the brightest galaxies of the components, that is NGC 4696 for Cen 30 (blue diamond) at the very center of the cluster and NGC 4709 for Cen 45 (magenta diamond) at $\sim 14.9'$ eastward of the center. Despite the ~ 1500 km s $^{-1}$ line-of-sight velocity separation, Lucey et al. (1986a) argued that Cen 30 and Cen 45 belong to the same cluster, which was concluded after comparisons of the $U - V$ color-magnitude relations, luminosity functions, and galactic radius distributions of both substructures.

Meanwhile, the redshifts inferred through the ICM velocities using deeper X-ray observations (e.g., *XMM-Newton* and *Suzaku*) at the locations of these substructures suggest that both Cen 30 and Cen 45 are at $z \approx 0.0104$ (Ota & Yoshida 2016; Gatuzz et al. 2022a). The reported radial velocity relative to the optical redshift (line-of-sight bulk velocity) for Cen 45 is < 760 km s $^{-1}$ (90% limit) from *Suzaku* spectra (Ota & Yoshida 2016) and 216 ± 258 km s $^{-1}$ from *XMM-Newton* spectra (Gatuzz et al. 2022a), smaller than the optical estimate of ~ 1500 km s $^{-1}$. Such offset between the ICM mass centroids and the galaxy distribution along the line of sight is a hint of previous subcluster merger (Ota & Yoshida 2016), as has previously been observed in other on-going merging systems, for example, the Bullet cluster, (Markevitch et al. 2004; Clowe et al. 2006) and A2744, (Merten et al. 2011).

In the galaxy distribution map shown with wider FoV (Fig. 5c), we observed a stripe of low significant galaxy overdensity stretching westward. This structure is known as the Western Branch (Lucey et al. 1986a,b) and is composed of the galaxy members of both structures (based on their redshifts). A small

clump in this stripe is seen slightly outside the R_{200} and centered at the NGC 4603C galaxy. However, unlike other galaxy distribution features, we do not observe any correlation of the Western Branch with X-ray emission. Given the separation of the Western Branch from the main location of the distribution of the Cen 45 member galaxies in the east, the galaxies with similar redshifts in the Western Branch are likely background galaxies, decreasing further the significance of this structure.

4.2. X-ray analysis

4.2.1. Nucleus

In the GGM images (Fig. 7), we observed some well-known features in the core and also emphasized large-scale features beyond R_{2500} . For instance, the soft plume-like filament originating from the core that extends toward the northeast can be clearly seen in the 2-pixel GGM-filtered image. This central region has been studied in great detail using *Chandra* observations with better spatial resolution (e.g., Sanders & Fabian 2002; Fabian et al. 2005; Sanders et al. 2016b). As NGC 4696 hosts a low-power radio source, PKS 1246 – 410, radio data were also employed (Taylor et al. 2002, 2006). The multi-wavelength studies using *Chandra* X-ray observations and VLA and VLBA radio observations reveal a wealth of structures in the nucleus of the Centaurus cluster. For example, it was found that the plume is the most prominent below ~ 1 keV and it consists of three soft filaments. The nucleus, where the plume seems to originate, coincides with optical filaments and dust lane from NGC 4696 (Fabian et al. 1982; Sparks et al. 1989; Hamer et al. 2019). On the sides of the nucleus are cavities that anti-correlate with radio lobes. These authors concluded that the plume and other features in the core of the Centaurus cluster (cavities, edges, shocks, bay, etc.), are the result of AGN feedback from the NGC 4696, as well as sloshing motion. We refer to the mentioned previous works for further details of this structure.

The trend shown in the ICM properties (normalization per area, temperature, and metallicity) is similar across the different region configurations (Fig. 10), with some variations that highlight the features which will be discussed in the following subsections.

To investigate the multi-temperature structure effect, we performed a two-temperature spectral fitting to the bins at $r < 2.5'$ (2T; see Sect. 3.4.4). Based on the AIC and BIC statistical tests, we found that a 2T model only statistically improves the fit of the innermost bin ($0 - 0.8'$). The lowest best-fit temperature value decreases from 1.43 keV (1T) to 1.0 keV (2T). Sanders et al. (2016b) attribute the multi-phase nature of the ICM in the core ($r < 10$ kpc) to the plume structure, and not a result of the projection effects from the temperature gradient, which is in accordance with our findings⁷. A similar conclusion was drawn in Ikebe et al. (1999) using *ROSAT* PSPC and ASCA data. Moreover, we acquired a metallicity value of $1.59^{+0.22}_{-0.18}Z_{\odot}$, which is around 2.4 times higher than the 1T value ($0.67^{+0.05}_{-0.05}Z_{\odot}$) with a significance of 4.9σ , removing the central metallicity drop seen in the 1T profile. Buote (2000) investigated the metallicities in the core of 12 bright galaxy groups with ASCA data. The author found that the subsolar metallicity found in previous studies is a fitting artifact caused by assuming an isothermal model. This issue was dubbed the 'iron bias' and was rectified by fitting with a more appropriate mode, namely, the 2T model. The mean metallicity of the sample of Buote (2000) became a factor

⁷ $0.8'$ is ~ 10.7 kpc at $z = 0.0104$

2.6 larger than the value obtained by using the 1T model. On the other hand, the central abundance drop in the Centaurus cluster was previously observed in other studies (e.g., Sanders & Fabian 2002; Matsushita et al. 2007; Sanders et al. 2016b; Lakhchaura et al. 2019; Liu et al. 2019) and was linked to the dust depletion scenario, such that a significant fraction of metals in the hot phase cools down and then get incorporated into the dust grains from the central BCG (Panagoulia et al. 2015; Mernier et al. 2017). Afterwards, the metal-rich dust grains are displaced to larger radii by the AGN feedback (Simionescu et al. 2009; Kirkpatrick et al. 2011). While we confirm the iron bias affecting this first bin, however, due to the limitation from the point spread function (PSF) and statistics, the analyzed bin is larger than previous studies, which may not be ideal for fully resolving the central metallicity drop (Gatuzz et al. 2023).

4.2.2. Eastern and western edges

In the 4-pixel GGM-filtered image, we observed the eastern and western edges that are $\sim 2.1'$ and $3.6'$ from the cluster center. These edges are also evident from the surface brightness profiles (Fig. 8a for $0.2 - 2.3$ keV or 8b for $1.0 - 2.3$ keV). For instance, in the eastern profile of the $0.2 - 2.3$ keV band, the significance surface brightness with respect to the full azimuthal value at $1.5'$ (before the edge) is 5.7σ , then the following bin (centered at $2.0'$), the significance drops to -2.1σ . For the western edge, we noticed a 3.8σ excess at $2 - 3'$. At the following bins centered at 3.5 and $4.0'$, the significance values drop to 1.3 and -2.3σ , respectively. Sanders et al. (2016b) describe these features as cold fronts (Markevitch & Vikhlinin 2007), as they are accompanied by temperature jumps and surface density drops in front of the edges (also see Sanders & Fabian 2002; Fabian et al. 2005). These cold fronts, as well as the east-west asymmetry appearance and metal distributions in the core, are common signatures of sloshing motions that could be triggered by the interaction between Cen 30 and Cen 45 (Fabian et al. 2005; Sanders et al. 2016b). Other sloshing examples seen in observations include the Perseus cluster (Simionescu et al. 2012; Urban et al. 2014), Virgo cluster (Gatuzz et al. 2022b), A2657 (Botteon et al. 2024), A2029 (Paterno-Mahler et al. 2013), A2142 (Markevitch et al. 2000; Liu et al. 2018).

4.2.3. Western filamentary excess

Another feature is the filament-like excess in the west of the cluster center. The feature is only apparent in the residual image (Fig. 9). Note that the eRASS:5 Centaurus residual image is strikingly similar to the ROSAT PSPC relative excess image (right panel of Figure 3 in Churazov et al. 1999) and the XMM-Newton residual image (Figure 7 in Walker et al. 2013a), which were only feasible up to $r < R_{2500}$. This filament-like excess seems to be related to the S0 galaxy NGC 4696B ($z = 0.0104$), which is located in the west, near the boundary of the R_{2500} (yellow circle in Fig. 9). The NGC 4696B galaxy is the third brightest galaxy after NGC 4696 and NGC 4709 in the optical band. As observed in the residual image, the X-ray position of NGC 4696B is slightly offset to its optical position toward the northeast. This excess emission structure was speculated to be ram pressure-stripped gas from NGC 4696B (Churazov et al. 1999). Higher metallicity in the innermost bin in the north (by a factor of 1.6 and a significance of 2.7σ to the south) may also be contributed by the stripped-gas (Walker et al. 2013a).

4.2.4. Eastern excess

The residual image (Fig. 9) reveals a bow-shaped excess in the east of NGC 4696, which is also evident in the ROSAT PSPC relative excess emission (Churazov et al. 1999) and the XMM-Newton residual image (Walker et al. 2013a). Completing the detection view by previous instruments, we show that the eastern excess extends beyond the R_{2500} boundary and diminishes as it approaches the R_{500} . Up to R_{2500} , we acquired an average surface brightness excess with 4.1σ significance in the eastern sector with respect to the average surface brightness values. Between R_{2500} and $0.6R_{500}$, the average eastern significance drops to 2.5σ . The excess beyond R_{2500} in the east is confirmed as the eastern extension in the 32-pixel GGM-filtered image (Fig. 7, right), which also coincides with the location of a galaxy overdensity patch of the Cen 45 member galaxies (Fig. 5b).

From the spectral analysis, excess emission is also observed. We found that the normalizations per area in the east are higher than the full annuli and other sectors, except for the outermost bin ($R_{500} - R_{200}$). With respect to the full azimuthal values, there is a 31% and 36% enhancement of 5.4σ at the bin before ($10.0 - 15.0'$) and after the center of Cen 45 ($15 - 20.0'$), respectively. The excess peaks at $20.0 - 25.4'$ bin with 45% and 7.7σ and continues until the $0.7 - 1.0R_{500}$ bin with a relative difference of 36% and 2.6σ significance, showing that the Cen 45 substructure extends even further out than previously measured. Gatuzz et al. (2022a) found a higher ICM redshift with respect to the Cen 30 optical redshift at a $r > 15'$ bin, east of Cen 45, which signifies that the eastern extension may be a tail of Cen 45 emerging from the merger activity.

At the $15 - 20.0'$ bin, we notice that the temperatures in the east ($3.18^{+0.41}_{-0.29}$ keV) and south ($3.41^{+0.98}_{-0.51}$ keV) are 0.8 keV and 1.0 keV higher to their counterpart bins in the west and north, with a significance of 2.3σ for the east to west and 1.6σ for the south to north comparisons. The temperature values in these bins are consistent with previous temperature enhancement findings in the same directions by other instruments. Using ASCA observations, Churazov et al. (1999) and Furusho et al. (2001) found a temperature value of 4.4 ± 0.2 keV and 4.3 ± 0.2 keV, respectively, while Walker et al. (2013a) reported a hot component of 5.0 ± 0.4 keV from their analysis using XMM-Newton observations. Using the eROSITA-XMM-Newton temperature relation of Migkas et al. (2024), we converted the eastern and southern temperatures at the $15 - 20.0'$ bin. The calculated values (without scatters) are in agreement within $< 1.6\sigma$ with the reported XMM-Newton temperature by Walker et al. (2013a). The temperature enhancement in this location is consistent with shock-heated gas caused by the interaction between Cen 30 and Cen 45.

4.2.5. $R_{2500} < r < R_{500}$

The spectral parameter profiles of the different sectors decrease outward (R_{2500}) with roughly the same shape but with some fluctuations across the different sectors. The most noticeable is the previously mentioned excess normalization per area in the east (see Sect. 4.2.4). Other fluctuation is observed at the southern $0.7 - 1.0R_{500}$ ($42.2 - 59.0'$) bin, where the temperature is higher ($2.28^{+0.91}_{-0.48}$ keV) in comparison to its northern counterpart bin ($1.59^{+0.16}_{-0.11}$ keV), with a 1.4σ significance. The average best-fit temperature in the $R_{2500} - 0.7R_{500}$ ($25.4 - 42.2'$) is 2.2 keV, with a range of $1.9 - 2.4$ keV. For the $0.7 - 1.0R_{500}$ ($42.2 - 59.0'$) bin, the best-fit temperature average is 1.8 keV, ranging from 1.1 to 2.5 keV.

In the temperature profile panels of Fig. 10, we compared the outskirts temperature results with the expected temperature profiles, i.e., temperature profile fitted from *Suzaku* measurements (Reiprich et al. 2013) and the average galaxy cluster temperature profile from *N*-body plus hydrodynamics cosmological simulations (Burns et al. 2010). The temperatures of the Centaurus cluster in $R_{2500} < r < R_{500}$ appear to drop smoothly and the values are in good agreement with the profiles from simulation and fit of *Suzaku* outskirts measurements.

The metallicity values across the sectors in the $R_{2500} - 0.7R_{500}$ ($25.4 - 42.2'$) are in very good agreement with each other with an average value of $0.21Z_{\odot}$. For the $0.7 - 1R_{500}$ ($42.2 - 59.0'$) bin, the metallicity values in the north, south, and west are consistent with each other, with their values lying between $0.07Z_{\odot}$ and $0.40Z_{\odot}$. Meanwhile, we found lower metallicity in the east ($0.03^{+0.04}_{-0.03}Z_{\odot}$) with a 2.3σ significance deviation with respect to the western sector at the same radial bin. Walker et al. (2013b) analyzed *Suzaku* observations of Centaurus cluster along the north-western strip out to $0.95R_{200}$. At $45 - 50'$, they report a metallicity of $0.1Z_{\odot}$, which is broadly in agreement with the value reported in this work. In general, our metallicity values in this regime are in good agreement with other galaxy cluster studies (e.g., Akamatsu et al. 2011; Bulbul et al. 2016; Urban et al. 2017; Ghizzardi et al. 2021), that report a metallicity value of $\sim 0.3Z_{\odot}$ at a similar distance range.

4.2.6. $r > R_{500}$

In the $R_{500} < r < R_{200}$ regime, we measured cluster surface brightness above the CXB level with significance values of the full azimuthal direction spreading between 3.0 and 7.2σ (see bottom plot of Fig. 8c or 8d). At $r > R_{200}$, we observed various levels of eROSITA Bubbles contamination in the different sectors from the $0.2 - 2.3$ keV surface brightness profiles (Fig. 8c), where the strongest is in the east, milder in the north and south, and none in the west. The eROSITA Bubble contamination diminished in the $1.0 - 2.3$ keV profiles (Fig. 8c). In this higher energy band profile, we detected a 3.5σ cluster emission above the CXB at $90'$ ($\sim R_{200}$), and then followed by 2.9σ at $100'$ ($\sim 1.1R_{200}$).

In this regime, the spectral analysis was performed out to R_{200} . There is a temperature drop by a factor of ~ 3 from the peak temperature to this outermost bin. The temperature values in the different sectors at $R_{500} - R_{200}$ are consistent with each other, with an average of 1.2 keV. The outskirts temperatures closely adhere to the predicted temperature profiles derived from simulations and fit from *Suzaku* outskirts measurements. The absence of temperature deviations, such as excess, in the outskirts of the Centaurus cluster corresponds to the lack of large-scale filaments connected to the cluster ("connectivity", e.g., Gouin et al. 2021), which is in agreement with the results of image inspections and optical redshift analysis. As reported in other works (e.g., Kawaharada et al. 2010; Veronica et al. 2024), connectivity with large-scale structures may induce faster thermalization along the connected direction of the cluster outskirts.

The metallicity values acquired in the northern and southern sectors are slightly lower than in the eastern and western sectors. The values range between 0.003 and $0.08Z_{\odot}$ for the former and between 0.07 and $0.21Z_{\odot}$ for the latter. Nevertheless, our findings in this regime are consistent within the measurement ranges of other galaxy clusters; for example *Suzaku* outskirts metallicity of A2204 (Reiprich et al. 2009), A1413 (Hoshino et al. 2010), Perseus cluster (Simionescu et al. 2011; Werner et al. 2013), and ten nearby clusters (Urban et al. 2017), as well as the *XMM*-

Newton measurement of the northern outskirts of the Virgo cluster (Urban et al. 2011).

5. Summary and conclusions

Utilizing the combined five eROSITA All-Sky Survey data (eRASS:5), we performed comprehensive imaging and spectral analyses out to $2R_{200}$ ($\sim 181'$) and R_{200} ($\sim 91'$), respectively, unveiling the first view of Centaurus sampling the whole azimuth beyond $30'$. Our data reduction and image correction steps include flare filtering, Galactic absorption correction, and exposure correction accounting for the different types of eROSITA's telescope modules (see Sect. 2.1). The steps were realized in different energy bands to assess the eROSITA Bubble emission contamination in the field. We applied various image manipulation methods employing the final corrected image products, such as wavelet filtering, adaptive smoothing, and GGM filtering to search for cluster features. We quantified the features by calculating and comparing surface brightness profiles of different energy bands ($0.2 - 2.3$ keV and $1.0 - 2.3$ keV) in full azimuth and four sectors based on the morphology of the cluster. We conducted rigorous sky background spectral analysis to constrain local sky fore- and background components. We developed a technique to spatially subtract the sky background across the FoV from the image. Last but not least, from spectral analysis, we acquired the ICM parameter profiles, namely, normalizations, temperature, and metallicity in various directions. We compared our inner region results ($r < R_{2500}$) with previous studies. In the outskirts ($r > 0.3R_{200}$), we compared the eRASS:5 temperature profile with other cluster measurements and simulations. Additionally, we compiled a galaxy redshift catalog from a public database and carried out galaxy member analysis. We correlated the cluster galaxy member distribution with X-ray emission. We summarized our results below:

- We observed the known bimodality in the distribution of the redshifts of the galaxies within R_{200} of the Centaurus cluster. The peaks of the bimodality are at $z = 0.0104$ that corresponds to the Cen 30 substructure at the cluster center, and at $z = 0.0149$ for the Cen 45 substructure. The peak of galaxy member number density of each substructure is centered at their respective brightest galaxy; NGC 4696 for Cen 30 and NGC 4709 for Cen 45 ($14.9'$ east of the cluster center).
- eRASS:5 images, as well as surface brightness and spectral analyses reveal the previously known features in the cluster inner region ($r < R_{2500} \approx 25.4'$), for instance, the soft filament emission originated from the nucleus (plume), temperatures and metallicities asymmetry in the core, and the eastern and western cold fronts. These features are associated with AGN feedback from NGC 4696 galaxy and the sloshing motion triggered by substructure merger. Additionally, we also observed the western filamentary excess that seems to be the ram-pressure-stripped gas from NGC 4696B (the third optically brightest galaxy in the Centaurus cluster). This feature might be responsible for the higher core metallicity in the north.
- We found that the spectra of the innermost bin of $0.0 - 0.8'$ ($r < 10.7$ kpc) is described better with a multi-temperature model (2T) than an isothermal model (1T). The core temperature drops from 1.4 keV to 1.0 keV. Meanwhile, the metallicity value increases from $0.67^{+0.05}_{-0.05}Z_{\odot}$ to $1.59^{+0.22}_{-0.18}Z_{\odot}$, implying that this bin suffers from an iron bias.
- We traced the X-ray eastern excess emission up to R_{500} , revealing the full extension of the Cen 45 substructure. The

eastern enhancement (normalization per area) peaks at the 20.0 – 25.4' bin ($\sim 5.1 - 10.5'$ behind the Cen 45 center) with a relative difference of 45% and significance of 7.7σ to the full annulus value, then continues until the 42.2 – 59.0' ($0.7 - 1.0R_{500}$) with a 36% and 2.6σ . The excess behind Cen 45 might be the ram-pressure-stripped gas from the substructure. Moreover, we confirmed the previously detected temperature enhancements in the east and south, which are consistent with shock-heated gas resulting from the interaction between Cen 30 and Cen 45.

- We measured significant emission beyond R_{200} , that is surface brightness value of 3.5σ above the CXB level at R_{200} and 2.9σ at $\sim 1.1R_{200}$.
- The cluster temperature profiles in different sectors show a similar trend, namely a drop in the core and a peak in the intermediate radial range. A drop by a factor ~ 3 from the peaks to the outermost bin ($R_{500} - R_{200}$) is seen in various sectors. The measured temperature profiles in the outskirts ($r > 0.3R_{200}$) follow closely the profiles from simulations and fit from *Suzaku* cluster outskirts measurements.
- The metallicity peaks in the center and drops rapidly outwards. In the outskirts ($R_{500} - R_{200}$), a little asymmetry is observed between the east-west (semi-major axis) and north-south (semi-minor axis) measurements, where the first is higher than the latter. The range of outskirts metallicity in the eastern and western sectors is between 0.07 and $0.21Z_{\odot}$, while in the northern and southern sectors is between 0.003 and $0.08Z_{\odot}$. Higher metallicity in the east-west direction might be related to the merger direction. We report that the metallicity estimates of these sectors are in good agreement with the other cluster outskirts measurements.

Acknowledgements. Funded by the Deutsche Forschungsgemeinschaft (DFG, German Research Foundation) – 450861021. A.V. is a member of the Max-Planck International School for Astronomy and Astrophysics (IMPRS) and of the Bonn-Cologne Graduate School for Physics and Astronomy (BCGS), and thanks for their support. T.R. acknowledges support from the German Federal Ministry of Economics and Technology (BMWi) provided through the German Space Agency (DLR) under project 50 OR 2112. M.Y. acknowledges support from the Deutsche Forschungsgemeinschaft through the grant FR 1691/2-1. This work was supported in part by JSPS KAKENHI Grant Number 20K04027 (NO). This work is based on data from eROSITA, the soft X-ray instrument aboard SRG, a joint Russian-German science mission supported by the Russian Space Agency (Roskosmos), in the interests of the Russian Academy of Sciences represented by its Space Research Institute (IKI), and the Deutsches Zentrum für Luft- und Raumfahrt (DLR). The SRG spacecraft was built by Lavochkin Association (NPOL) and its subcontractors, and is operated by NPOL with support from the Max Planck Institute for Extraterrestrial Physics (MPE). The development and construction of the eROSITA X-ray instrument was led by MPE, with contributions from the Dr. Karl Remeis Observatory Bamberg and ECAP (FAU Erlangen-Nürnberg), the University of Hamburg Observatory, the Leibniz Institute for Astrophysics Potsdam (AIP), and the Institute for Astronomy and Astrophysics of the University of Tübingen, with the support of DLR and the Max Planck Society. The Argelander Institute for Astronomy of the University of Bonn and the Ludwig Maximilians Universität Munich also participated in the science preparation for eROSITA. The eROSITA data shown here were processed using the eSASS software system developed by the German eROSITA consortium. This research has made use of the NASA/IPAC Extragalactic Database (NED), which is funded by the National Aeronautics and Space Administration and operated by the California Institute of Technology.

References

Akaike, H. 1974, IEEE Transactions on Automatic Control, 19, 716
Akamatsu, H., Hoshino, A., Ishisaki, Y., et al. 2011, PASJ, 63, S1019
Allen, S. W. & Fabian, A. C. 1994, MNRAS, 269, 409
Anders, E. & Grevesse, N. 1989, Geochim. Cosmochim. Acta, 53, 197
Angelini, M., Etori, S., Vazza, F., & Jones, T. W. 2021, A&A, 653, A171
Arnaud, K. A. 1996, in Astronomical Society of the Pacific Conference Series, Vol. 101, Astronomical Data Analysis Software and Systems V, ed. G. H. Jacoby & J. Barnes, 17

Asplund, M., Grevesse, N., Sauval, A. J., & Scott, P. 2009, ARA&A, 47, 481
Bertin, E. & Arnouts, S. 1996, A&AS, 117, 393
Botteon, A., Gastaldello, F., ZuHone, J. A., et al. 2024, MNRAS, 527, 919
Brunner, H., Liu, T., Lamer, G., et al. 2022, A&A, 661, A1
Bryan, G. L., Norman, M. L., O'Shea, B. W., et al. 2014, The Astrophysical Journal Supplement Series, 211, 19
Bulbul, E., Liu, A., Kluge, M., et al. 2024, arXiv e-prints, arXiv:2402.08452
Bulbul, E., Randall, S. W., Bayliss, M., et al. 2016, ApJ, 818, 131
Buote, D. A. 2000, MNRAS, 311, 176
Burns, J. O., Skillman, S. W., & O'Shea, B. W. 2010, The Astrophysical Journal, 721, 1105
Cash, W. 1979, ApJ, 228, 939
Churazov, E., Gilfanov, M., Forman, W., & Jones, C. 1999, ApJ, 520, 105
Clowe, D., Bradač, M., Gonzalez, A. H., et al. 2006, ApJ, 648, L109
Dupke, R. A. & Bregman, J. N. 2001, ApJ, 562, 266
Egger, R. J. & Aschenbach, B. 1995, A&A, 294, L25
Fabian, A. C., Atherton, P. D., Taylor, K., & Nulsen, P. E. J. 1982, MNRAS, 201, 17P
Fabian, A. C., Sanders, J. S., Taylor, G. B., & Allen, S. W. 2005, MNRAS, 360, L20
Fukushima, K., Kobayashi, S. B., & Matsushita, K. 2022, MNRAS, 514, 4222
Furusho, T., Yamasaki, N. Y., Ohashi, T., et al. 2001, PASJ, 53, 421
Gatuzz, E., Sanders, J. S., Canning, R., et al. 2022a, MNRAS, 513, 1932
Gatuzz, E., Sanders, J. S., Dennerl, K., et al. 2023, MNRAS, 525, 6394
Gatuzz, E., Sanders, J. S., Dennerl, K., et al. 2022b, MNRAS, 511, 4511
Ghizzardi, S., Molendi, S., van der Burg, R., et al. 2021, A&A, 652, C3
Gouin, C., Bonnaire, T., & Aghanim, N. 2021, A&A, 651, A56
Hamer, S. L., Fabian, A. C., Russell, H. R., et al. 2019, MNRAS, 483, 4984
HI4PI Collaboration, Ben Bekhti, N., Flöer, L., et al. 2016, A&A, 594, A116
Hoshino, A., Henry, J. P., Sato, K., et al. 2010, PASJ, 62, 371
Ikebe, Y., Makishima, K., Fukazawa, Y., et al. 1999, ApJ, 525, 58
Kawaharada, M., Okabe, N., Umetsu, K., et al. 2010, ApJ, 714, 423
Kirkpatrick, C. C., McNamara, B. R., & Cavagnolo, K. W. 2011, ApJ, 731, L23
Kluge, M., Comparat, J., Liu, A., et al. 2024, arXiv e-prints, arXiv:2402.08453
Kuntz, K. D. & Snowden, S. L. 2000, ApJ, 543, 195
Lakhchaura, K., Mernier, F., & Werner, N. 2019, A&A, 623, A17
Liu, A., Bulbul, E., Ramos-Ceja, M. E., et al. 2023, A&A, 670, A96
Liu, A., Yu, H., Diaferio, A., et al. 2018, ApJ, 863, 102
Liu, A., Zhai, M., & Tozzi, P. 2019, MNRAS, 485, 1651
Liu, W., Chiao, M., Collier, M. R., et al. 2016, The Astrophysical Journal, 834, 33
Lucey, J. R., Currie, M. J., & Dickens, R. J. 1986a, MNRAS, 221, 453
Lucey, J. R., Currie, M. J., & Dickens, R. J. 1986b, MNRAS, 222, 427
Lucey, J. R., Dickens, R. J., & Dawe, J. A. 1980, Nature, 285, 305
Lumb, D. H., Warwick, R. S., Page, M., & De Luca, A. 2002, A&A, 389, 93
Luo, B., Brandt, W. N., Xue, Y. Q., et al. 2017, ApJS, 228, 2
Malavasi, N., Aghanim, N., Douspis, M., Tanimura, H., & Bonjean, V. 2020, A&A, 642, A19
Markevitch, M., Gonzalez, A. H., Clowe, D., et al. 2004, ApJ, 606, 819
Markevitch, M., Ponman, T. J., Nulsen, P. E. J., et al. 2000, ApJ, 541, 542
Markevitch, M. & Vikhlinin, A. 2007, Phys. Rep., 443, 1
Matsushita, K., Böhringer, H., Takahashi, I., & Ikebe, Y. 2007, A&A, 462, 953
Merloni, A., Lamer, G., Liu, T., et al. 2024, A&A, 682, A34
Mernier, F., de Plaa, J., Kaastra, J. S., et al. 2017, A&A, 603, A80
Merten, J., Coe, D., Dupke, R., et al. 2011, MNRAS, 417, 333
Migkas, K., Kox, D., Schellenberger, G., et al. 2024, arXiv e-prints, arXiv:2401.17297
Ogando, R. L. C., Maia, M. A. G., Pellegrini, P. S., & da Costa, L. N. 2008, AJ, 135, 2424
Ota, N., Fukazawa, Y., Fabian, A. C., et al. 2007, PASJ, 59, 351
Ota, N. & Yoshida, H. 2016, Publications of the Astronomical Society of Japan, 68, S19
Pacaud, F., Pierre, M., Refregier, A., et al. 2006, MNRAS, 372, 578
Panagoulia, E. K., Sanders, J. S., & Fabian, A. C. 2015, MNRAS, 447, 417
Paterno-Mahler, R., Blanton, E. L., Randall, S. W., & Clarke, T. E. 2013, ApJ, 773, 114
Piffaretti, R., Arnaud, M., Pratt, G. W., Pointecouteau, E., & Melin, J. B. 2011, A&A, 534, A109
Ponti, G., Zheng, X., Locatelli, N., et al. 2023, A&A, 674, A195
Predehl, P., Andritschke, R., Arefiev, V., et al. 2021, A&A, 647, A1
Predehl, P., Sunyaev, R. A., Becker, W., et al. 2020, Nature, 588, 227
Ramos-Ceja, M. E., Pacaud, F., Reiprich, T. H., et al. 2019, A&A, 626, A48
Reiprich, T. H., Basu, K., Etori, S., et al. 2013, Space Sci. Rev., 177, 195
Reiprich, T. H., Hudson, D. S., Zhang, Y. Y., et al. 2009, A&A, 501, 899
Reiprich, T. H., Veronica, A., Pacaud, F., et al. 2021, A&A, 647, A2
Rossetti, M., Eckert, D., Gastaldello, F., et al. 2024, arXiv e-prints, arXiv:2402.18653
Sanders, J. S. & Fabian, A. C. 2002, MNRAS, 331, 273
Sanders, J. S., Fabian, A. C., Allen, S. W., et al. 2008, MNRAS, 385, 1186

- Sanders, J. S., Fabian, A. C., Russell, H. R., Walker, S. A., & Blundell, K. M. 2016a, MNRAS, 460, 1898
- Sanders, J. S., Fabian, A. C., Taylor, G. B., et al. 2016b, MNRAS, 457, 82
- Schwarz, G. 1978, The Annals of Statistics, 6, 461
- Simionescu, A., Allen, S. W., Mantz, A., et al. 2011, Science, 331, 1576
- Simionescu, A., Werner, N., Böhringer, H., et al. 2009, A&A, 493, 409
- Simionescu, A., Werner, N., Urban, O., et al. 2012, The Astrophysical Journal, 757, 182
- Sparks, W. B., Macchetto, F., & Golombek, D. 1989, ApJ, 345, 153
- Su, M., Slatyer, T. R., & Finkbeiner, D. P. 2010, ApJ, 724, 1044
- Sugiyama, H., Ueda, M., Fukushima, K., et al. 2023, PASJ, 75, 1324
- Taylor, G. B., Fabian, A. C., & Allen, S. W. 2002, MNRAS, 334, 769
- Taylor, G. B., Sanders, J. S., Fabian, A. C., & Allen, S. W. 2006, MNRAS, 365, 705
- Tuominen, T., Nevalainen, J., Tempel, E., et al. 2021, A&A, 646, A156
- Urban, O., Simionescu, A., Werner, N., et al. 2014, MNRAS, 437, 3939
- Urban, O., Werner, N., Allen, S. W., Simionescu, A., & Mantz, A. 2017, MNRAS, 470, 4583
- Urban, O., Werner, N., Simionescu, A., Allen, S. W., & Böhringer, H. 2011, MNRAS, 414, 2101
- Veronica, A., Reiprich, T. H., Pacaud, F., et al. 2024, A&A, 681, A108
- Virtanen, P., Gommers, R., Oliphant, T. E., et al. 2020, Nature Methods, 17, 261
- Walker, S. A., Fabian, A. C., & Sanders, J. S. 2013a, MNRAS, 435, 3221
- Walker, S. A., Fabian, A. C., Sanders, J. S., Simionescu, A., & Tawara, Y. 2013b, MNRAS, 432, 554
- Walker, S. A., Sanders, J. S., & Fabian, A. C. 2016, MNRAS, 461, 684
- Werner, N., Urban, O., Simionescu, A., & Allen, S. W. 2013, Nature, 502, 656
- Willingale, R., Starling, R. L. C., Beardmore, A. P., Tanvir, N. R., & O'Brien, P. T. 2013, MNRAS, 431, 394
- Wilms, J., Allen, A., & McCray, R. 2000, ApJ, 542, 914
- Yeung, M. C. H., Freyberg, M. J., Ponti, G., et al. 2023, A&A, 676, A3
- Zheng, X., Locatelli, G. P. N., Sanders, J., et al. 2024, arXiv e-prints, arXiv:2401.17310

Appendix A: N_{H} map

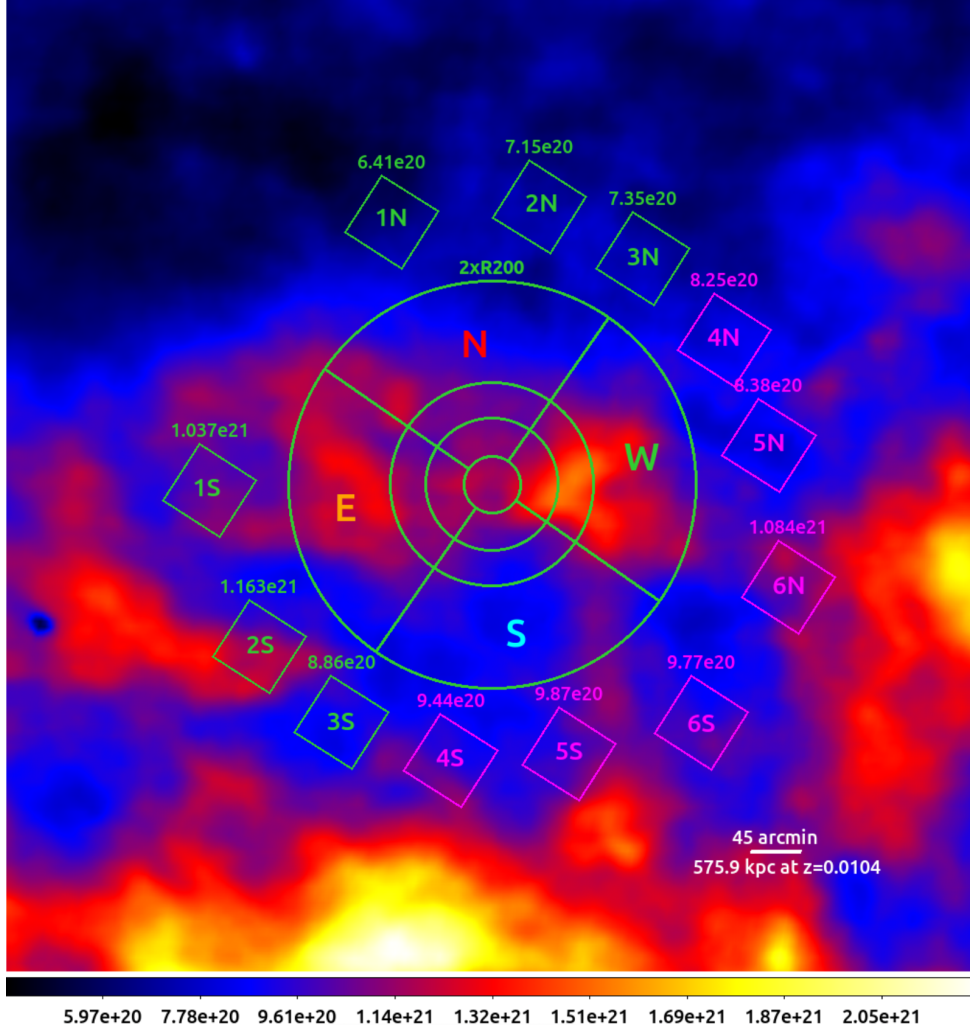


Fig. A.1: The total N_{H} map (combination of HI4PI all-sky Galactic neutral Hydrogen map [HI4PI Collaboration et al. 2016](#) and $N_{\text{H}2}$ map from [Willingale et al. 2013](#)) of the Centaurus cluster field. The configurations of the science and sky background analyses are overlaid on top (see Sect. 2).

Appendix B: CXB map and CXB-subtracted image

In an attempt to spatially remove the sky background emission from the image, particularly the eROSITA Bubble emission, we performed spectral fitting of 409 sky background boxes located $r > R_{200}$. Each box has a size of $0.5^\circ \times 0.5^\circ$. During the fit, we omitted the cluster emission. All sky fore- and background components were frozen to the values listed in Table 2, except for the eROSITA Bubble normalization that shows significant variation across the FoV. From each fitting, we acquired the count-rates value of the on-chip TMs in the energy band of 0.2 – 2.3 keV. We then computed the CXB count rates per pixel by taking the average on-chip TM count-rate value normalized by the corresponding area of the box. The resulting CXB map is displayed in the right panel of Fig. B.1. For the $r < R_{200}$, we computed the average of the values from the immediate surrounding boxes. The CXB-subtracted, fully-corrected image in the 0.2 – 2.3 keV is shown in the middle panel of Fig. B.1. While the fore-/background emission is drastically reduced, making the cluster outskirts more visible, a faint residual from the eROSITA Bubble can be seen in the left part of the image. The residual is likely the hotter phase of the structure, as can be concluded from the yellowish emission (red-soft and green-intermediate channels) in the RGB image (Fig. 1) and apparent emission at higher energy cut image (left panel of Fig. 6). However, we could not constrain this hotter component from the spectra as described in Sect. 2.3. Nevertheless, we present the result of the first attempt and method of spatially removing the CXB contribution from the image, which can be further improved for future large-scale environmental studies.

Appendix C: Spectral Analysis

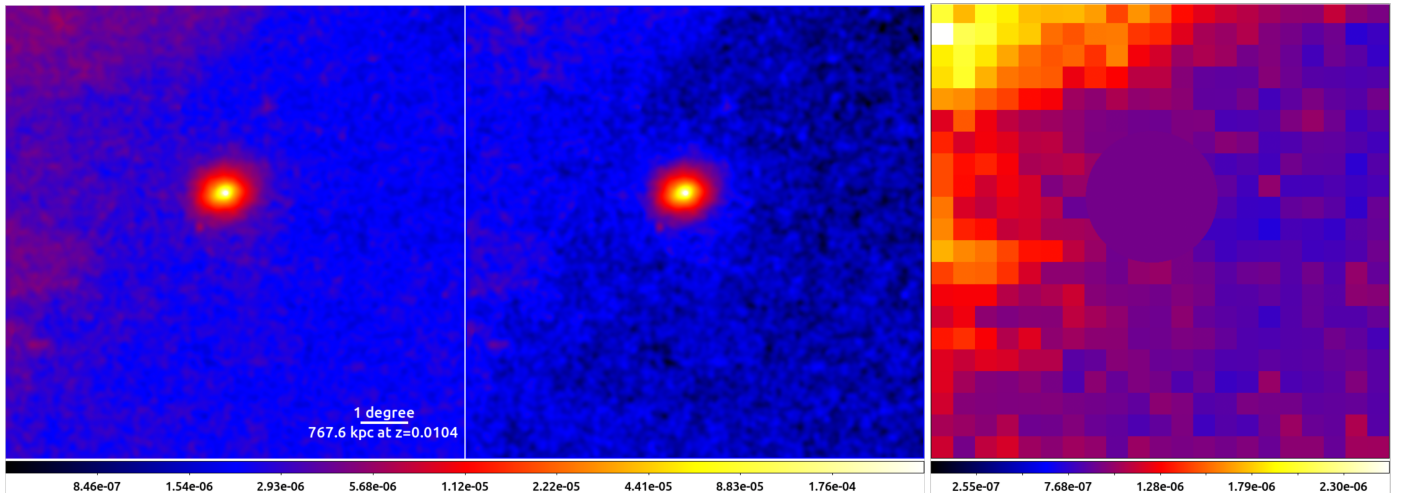


Fig. B.1: CXB subtraction attempt in the Centaurus cluster field. *Left*: Same as Fig. 2. *Middle*: CXB-subtracted, fully-corrected image (*left* minus *right*). The image was then adaptively smoothed with the same S/N as the left image. *Right*: CXB map including the eROSITA Bubble emission in the 0.2 – 2.3 keV. Note that the color bar range of the middle panel is different than the other panels.

Table C.1: The eRASS:5 spectral analysis results (1T fit) of the Centaurus cluster in full azimuthal annuli and various sectors out to R_{200} .

Sector	bin [arcmin]	$norm$ [$10^{-5} \text{ cm}^{-5}/\text{arcmin}^2$]	$k_B T$ [keV]	Z [Z_\odot]	stat/dof	Sector	bin [arcmin]	$norm$ [$10^{-5} \text{ cm}^{-5}/\text{arcmin}^2$]	$k_B T$ [keV]	Z [Z_\odot]	stat/dof
Annuli	0.0 – 0.8	$414.69^{+15.27}_{-13.79}$	$1.43^{+0.03}_{-0.01}$	$0.67^{+0.05}_{-0.05}$	7384.2/7294	Annuli	0.0 – 2.5	$162.77^{+2.99}_{-3.07}$	$1.78^{+0.02}_{-0.02}$	$0.84^{+0.04}_{-0.04}$	8248.9/7974
	0.8 – 1.7	$167.55^{+5.48}_{-5.55}$	$1.97^{+0.05}_{-0.06}$	$1.18^{+0.10}_{-0.09}$	7558.4/7498						
	1.7 – 2.5	$92.66^{+3.10}_{-3.22}$	$2.28^{+0.11}_{-0.08}$	$1.0^{+0.12}_{-0.10}$	7443.1/7433						
	2.5 – 5.0	$43.98^{+0.9}_{-0.9}$	$2.98^{+0.12}_{-0.11}$	$0.81^{+0.08}_{-0.07}$	8072.7/8066						
	5.0 – 7.5	$25.14^{+0.5}_{-0.51}$	$3.04^{+0.18}_{-0.14}$	$0.34^{+0.06}_{-0.05}$	8143.5/8127						
	7.5 – 10.0	$15.29^{+0.41}_{-0.30}$	$3.24^{+0.17}_{-0.17}$	$0.43^{+0.07}_{-0.07}$	8275.2/8188						
	10.0 – 15.0	$9.72^{+0.16}_{-0.16}$	$3.05^{+0.14}_{-0.13}$	$0.27^{+0.04}_{-0.04}$	8736.9/8994						
	15.0 – 20.0	$5.58^{+0.12}_{-0.14}$	$2.76^{+0.17}_{-0.16}$	$0.22^{+0.05}_{-0.04}$	9028.4/9197						
	20.0 – 25.4	$3.19^{+0.07}_{-0.07}$	$2.77^{+0.18}_{-0.17}$	$0.29^{+0.05}_{-0.05}$	9238.9/9550						
	25.4 – 42.2	$1.55^{+0.03}_{-0.03}$	$2.02^{+0.08}_{-0.07}$	$0.16^{+0.02}_{-0.02}$	11805.7/11190						
EAST	42.2 – 59.0	$0.54^{+0.02}_{-0.02}$	$1.57^{+0.07}_{-0.07}$	$0.12^{+0.02}_{-0.01}$	12162.6/11328	NORTH	59.0 – 90.8	$0.21^{+0.02}_{-0.01}$	$1.15^{+0.04}_{-0.06}$	$0.05^{+0.01}_{-0.02}$	12672.2/11375
	59.0 – 74.9	$0.27^{+0.02}_{-0.02}$	$1.19^{+0.06}_{-0.06}$	$0.04^{+0.02}_{-0.01}$	12375.9/11358						
	74.9 – 90.8	$0.14^{+0.03}_{-0.02}$	$1.14^{+0.05}_{-0.07}$	$0.09^{+0.03}_{-0.04}$	12603.0/11365						
	0.0 – 2.5	$175.93^{+6.58}_{-6.73}$	$1.66^{+0.03}_{-0.03}$	$0.78^{+0.07}_{-0.07}$	7326.4/7254		0.0 – 2.5	$120.58^{+5.70}_{-5.63}$	$2.09^{+0.09}_{-0.09}$	$1.2^{+0.16}_{-0.15}$	7026.4/7115
	2.5 – 5.0	$55.04^{+2.01}_{-2.03}$	$2.91^{+0.23}_{-0.20}$	$0.69^{+0.14}_{-0.11}$	7227.7/7289		2.5 – 5.0	$44.92^{+1.85}_{-1.85}$	$3.35^{+0.30}_{-0.26}$	$0.82^{+0.19}_{-0.16}$	7114.3/7214
	5.0 – 7.5	$30.66^{+1.13}_{-1.10}$	$3.24^{+0.29}_{-0.26}$	$0.42^{+0.12}_{-0.11}$	7183.9/7238		5.0 – 7.5	$27.06^{+1.04}_{-1.0}$	$2.64^{+0.25}_{-0.22}$	$0.37^{+0.10}_{-0.08}$	7157.7/7158
	7.5 – 10.0	-	-	-	-		7.5 – 10.0	$15.64^{+1.01}_{-0.71}$	$3.01^{+0.31}_{-0.33}$	$0.50^{+0.15}_{-0.15}$	6970.3/7127
	10.0 – 15.0	$12.73^{+0.40}_{-0.25}$	$3.22^{+0.33}_{-0.25}$	$0.35^{+0.12}_{-0.08}$	7749.6/7743		10.0 – 15.0	$8.88^{+0.30}_{-0.30}$	$3.10^{+0.31}_{-0.25}$	$0.35^{+0.10}_{-0.09}$	7526.0/7630
	15.0 – 20.0	$7.57^{+0.25}_{-0.35}$	$3.18^{+0.41}_{-0.29}$	$0.36^{+0.12}_{-0.09}$	7642.4/7814		15.0 – 20.0	$5.02^{+0.26}_{-0.30}$	$2.43^{+0.31}_{-0.24}$	$0.16^{+0.09}_{-0.06}$	7495.6/7586
	20.0 – 25.4	$4.62^{+0.17}_{-0.17}$	$2.87^{+0.32}_{-0.26}$	$0.30^{+0.10}_{-0.08}$	7785.2/7840		20.0 – 25.4	$2.92^{+0.15}_{-0.16}$	$2.35^{+0.31}_{-0.26}$	$0.28^{+0.11}_{-0.08}$	7552.5/7736
WEST	25.4 – 42.2	$2.03^{+0.06}_{-0.06}$	$2.25^{+0.18}_{-0.16}$	$0.19^{+0.05}_{-0.04}$	9244.7/9544		25.4 – 42.2	$1.43^{+0.07}_{-0.07}$	$2.09^{+0.21}_{-0.16}$	$0.20^{+0.07}_{-0.05}$	9038.9/9508
	42.2 – 59.0	$0.74^{+0.06}_{-0.07}$	$1.57^{+0.27}_{-0.17}$	$0.03^{+0.04}_{-0.03}$	9336.8/9906		42.2 – 59.0	$0.41^{+0.04}_{-0.04}$	$1.59^{+0.16}_{-0.11}$	$0.24^{+0.11}_{-0.08}$	9452.5/9995
	59.0 – 90.8	$0.12^{+0.03}_{-0.03}$	$1.15^{+0.06}_{-0.06}$	$0.13^{+0.08}_{-0.06}$	11774.3/11145		59.0 – 90.8	$0.20^{+0.03}_{-0.02}$	$1.22^{+0.07}_{-0.11}$	$0.05^{+0.03}_{-0.03}$	11870.2/11164
	0.0 – 2.5	$129.66^{+5.85}_{-5.81}$	$2.19^{+0.08}_{-0.10}$	$1.47^{+0.17}_{-0.18}$	7262.4/7234	SOUTH	0.0 – 2.5	$167.64^{+6.23}_{-6.33}$	$1.69^{+0.04}_{-0.03}$	$0.76^{+0.07}_{-0.07}$	7257.7/7216
	2.5 – 5.0	$38.27^{+1.79}_{-1.73}$	$2.78^{+0.22}_{-0.21}$	$1.11^{+0.20}_{-0.18}$	7104.9/7164		2.5 – 5.0	$37.66^{+1.90}_{-1.66}$	$2.99^{+0.27}_{-0.24}$	$0.71^{+0.17}_{-0.15}$	7000.4/7077
	5.0 – 7.5	$21.17^{+0.96}_{-1.15}$	$3.11^{+0.41}_{-0.33}$	$0.47^{+0.18}_{-0.13}$	7000.1/7090		5.0 – 7.5	$22.05^{+0.79}_{-1.08}$	$3.33^{+0.51}_{-0.41}$	$0.02^{+0.11}_{-0.02}$	6874.6/6993
	7.5 – 10.0	$13.84^{+0.67}_{-0.88}$	$3.14^{+0.44}_{-0.33}$	$0.55^{+0.22}_{-0.14}$	7028.4/7050		7.5 – 10.0	$12.48^{+0.85}_{-0.61}$	$3.57^{+0.67}_{-0.52}$	$0.15^{+0.16}_{-0.14}$	6897.2/6933
	10.0 – 15.0	$9.42^{+0.32}_{-0.32}$	$2.93^{+0.29}_{-0.25}$	$0.25^{+0.08}_{-0.07}$	7605.9/7646		10.0 – 15.0	$7.87^{+0.42}_{-0.37}$	$3.03^{+0.36}_{-0.34}$	$0.14^{+0.10}_{-0.09}$	7410.4/7493
	15.0 – 20.0	$5.47^{+0.22}_{-0.22}$	$2.33^{+0.22}_{-0.19}$	$0.2^{+0.07}_{-0.06}$	7504.7/7558		15.0 – 20.0	$4.39^{+0.24}_{-0.32}$	$3.41^{+0.98}_{-0.51}$	$0.15^{+0.20}_{-0.07}$	7510.2/7540
	20.0 – 25.4	$2.93^{+0.18}_{-0.21}$	$2.66^{+0.49}_{-0.32}$	$0.28^{+0.16}_{-0.10}$	7575.9/7764		20.0 – 25.4	$2.31^{+0.13}_{-0.12}$	$3.36^{+0.62}_{-0.5}$	$0.36^{+0.19}_{-0.15}$	7378.6/7586
	25.4 – 42.2	$1.39^{+0.08}_{-0.08}$	$2.39^{+0.28}_{-0.22}$	$0.26^{+0.10}_{-0.07}$	9170.7/9576		25.4 – 42.2	$1.12^{+0.05}_{-0.07}$	$2.24^{+0.31}_{-0.22}$	$0.18^{+0.08}_{-0.06}$	8949.5/9309
	42.2 – 59.0	$0.56^{+0.04}_{-0.03}$	$1.66^{+0.16}_{-0.16}$	$0.19^{+0.06}_{-0.05}$	9537.2/10045		42.2 – 59.0	$0.40^{+0.05}_{-0.05}$	$2.28^{+0.91}_{-0.48}$	$0.18^{+0.23}_{-0.11}$	9410.9/9826
	59.0 – 90.8	$0.20^{+0.02}_{-0.02}$	$1.31^{+0.10}_{-0.12}$	$0.11^{+0.04}_{-0.04}$	11961.9/11166		59.0 – 90.8	$0.27^{+0.05}_{-0.04}$	$1.08^{+0.12}_{-0.11}$	$0.02^{+0.03}_{-0.02}$	11606.6/11109

 Table C.2: Spectral analysis results (2T fit) of Centaurus cluster using eRASS:5. Subscript h and c are for hotter and cooler components, respectively. The metallicity, Z , is linked across both components.

bin [arcmin]	$norm_h$ [$10^{-5} \text{ cm}^{-5}/\text{arcmin}^2$]	$k_B T_h$ [keV]	$norm_c$ [$10^{-5} \text{ cm}^{-5}/\text{arcmin}^2$]	$k_B T_c$ [keV]	Z [Z_\odot]	$norm_h/norm_c$	stat/dof
0.0 – 0.8	$249.44^{+16.87}_{-16.51}$	$1.89^{+0.08}_{-0.11}$	$34.8^{+7.71}_{-6.73}$	$1.0^{+0.05}_{-0.06}$	$1.59^{+0.22}_{-0.18}$	7.2	7300.9/7292
0.8 – 1.7	$101.77^{+22.30}_{-32.10}$	$3.51^{+1.75}_{-0.39}$	$50.09^{+38.44}_{-27.65}$	$1.56^{+0.14}_{-0.18}$	$1.64^{+0.29}_{-0.21}$	2.0	7523.9/7496
1.7 – 2.5	$87.17^{+3.85}_{-4.75}$	$2.39^{+0.16}_{-0.11}$	$0.95^{+1.35}_{-0.53}$	$0.95^{+0.30}_{-0.20}$	$1.15^{+0.19}_{-0.13}$	91.9	7439.7/7431

List of Figures

1.1	Composite image of the Abell 1689 cluster	5
1.2	Distribution of galaxies in two slices of the Universe extending outward from the Milky Way Galaxy	6
1.3	Illustration of gravitational lensing of a background galaxy by a galaxy cluster.	7
1.4	The undistorted and distorted CMB spectrum by the Sunyaev-Zel'dovich effect	8
1.5	Radio images of merging and relaxed clusters	9
1.6	Composite image of the galaxy cluster MS0735.6+7421	10
1.7	The simulated X-ray spectra of the ICM	11
1.8	The effective photoelectric absorption cross-section as a function of energy, scaled by E^3	12
1.9	Measured surface brightness profile of A1795 fitted with β -model	14
1.10	The on-axis effective areas as a function of energy	17
1.11	An illustration of eRASS sky tile division	18
1.12	Annotated composite image of eRASS1	19
1.13	Average eROSITA PIB spectrum	20
1.14	Cosmic web from Illustris simulation taken at $z = 0$	22
1.15	Multiple <i>XMM-Newton</i> and <i>Suzaku</i> pointings on the A3391/95 cluster system and the Centaurus cluster	23
3.1	The eROSITA data reduction and science analysis workflow	33
3.2	Photon images of the A3391/95 PV observations in the 0.2 – 10.0 keV energy band	35
3.3	Sky tile footprint of the Centaurus cluster field	36
3.4	Lightcurve in the 5.0 – 10.0 keV band from an eRASS:5 sky tile (195129)	38
3.5	Fully-cleaned photon images of Centaurus field before and after PIB subtraction	40
3.6	N_{Htot} map for Galactic absorption correction in the A3391/95 field	41
3.7	N_{Htot} maps for Galactic absorption correction in the Centaurus field	42
3.8	Simulated eROSITA spectra using the sky background model of different N_{H} values	43
3.9	Fully-cleaned photon images of Centaurus field before and after corrections	44
3.10	Wavelet image and cheese mask of the Centaurus cluster field	45
3.11	Image processing techniques applied to the Centaurus cluster field	46
3.12	RGB images of the Centaurus cluster	47
3.13	Demonstration of surface brightness profile calculation of the Centaurus cluster	48
3.14	Centaurus cluster's TM1 spectrum and the fitted model	50
4.1	eROSITA and <i>XMM-Newton</i> images of the Northern Clump	55
4.2	Instrument independent surface brightness profiles (<i>Chandra</i> , <i>XMM-Newton</i> , and eROSITA) of the Northern Clump	57
4.3	Profiles of gas properties of the Northern Clump in the intermediate regime	58

5.1	Configurations for surface brightness profiles of the A3391/95 clusters and filaments . .	63
5.2	Configurations for spectral analysis of the A3391/95 cluster outskirts and filaments . . .	64
5.3	The surface brightness profiles and their significance to the CXB level	66
5.4	Temperature measurements of the outskirts and filaments	68
6.1	Composite image of the large-scale view of the Centaurus cluster	74
6.2	Soft band flux ($f_{X,0.5-2 \text{ keV}}$) of the CXB boxes	75
6.3	The galaxy redshift histogram of the Centaurus cluster	76
6.4	Galaxy number density maps in different redshift ranges	77
6.5	GGM-filtered images of the fully-corrected images	78
6.6	Surface brightness profiles of the Centaurus cluster	80
6.7	The residual image within $2R_{200}$ in the 0.2 – 2.3 keV energy band	81
6.8	The ICM property profiles of the Centaurus cluster	82

List of Tables

1.1	Λ CDM parameters from Planck Collaboration et al. (2020b)	24
3.1	The information of eROSITA A3391/95 PV observations	34
3.2	Information on the eROSITA data and software version used in each project, as well as the energy range for the imaging analysis.	39
3.3	Summary of the relative Galactic absorption correction	43
4.1	First results of eROSITA spectral analysis of the Northern Filament	59
5.1	Information on the A3391/95 cluster parameters	67
5.2	eROSITA spectral analysis results of the filaments and the derived quantities	70

Acknowledgements

I would like to express my sincerest gratitude to my supervisor, Prof. Dr. Thomas Reiprich, for the opportunity to continue with my Ph.D. in his group right after my Master's and for providing me with his invaluable guidance and encouragement throughout this journey. I felt trusted to have the independence in shaping my projects and I always have the support whenever I need it. Thank you to Dr. Florian Pacaud who has been an excellent daily supervisor. His many insightful comments, discussions (scientific and non-scientific), and help have been instrumental in this thesis. To PD. Dr. Jürgen Kerp, thank you for agreeing to be on my TAC committee and readily be my second supervisor. I am deeply grateful for your advice and encouragement from my Master's to my Ph.D. I would like to thank Prof. Dr. Naomi Ota, who gave me a great opportunity to learn from her. Visiting her working group at Nara Women's University is a wonderful experience. I am also grateful to Prof. Dr. Helmut Meusinger, who helped me find this path.

I am profoundly thankful to Georgios Giakoustidis for his unwavering support, constructive input, and understanding. Your hard work and dedication are truly inspiring. Many thanks to Caroline Mannes, Kateryna Vynokurova, Simon Dannhauer, and Jann Aschersleben for your friendship, moral support, and encouragement. I would also like to thank the past and current members of the Dark Energy team, especially, Dr. Konstantinos Migkas, Jakob Dietl, and Vardan Nazaretyan, and my AIfA colleagues, Christos Karoumpis, Maude Charmetant, and Tsan-Ming Wang. Thanks to the AIfA's secretaries and IT team for their assistance in administrative work and IT help.

I am grateful to the eROSITA-DE consortium and the ASKAP/EMU team for their support and collaboration. I acknowledge the support of the International Max Planck Research School (IMPRS) for Astronomy and Astrophysics at the Universities of Bonn and Cologne, and by the Bonn-Cologne Graduate School for Physics and Astronomy (BCGS) that enabled me to showcase my works and allowed me to interact with other scientists in local and international conferences. I am thankful to the Humboldt-Gesellschaft Japan (HGJ) that financed the eROSITA-XRISM feasibility project and my stay at Nara Women's University.

To Mom and Dad, thank you for your boundless love, support, and trust. To Devi Sabella Sentosa, Yonardhi Sutanto, Refnita Zhuo, Evan Matheus, Evi Lin, Tesa Naibaho, Diva Agrita, and Meutia Yuniningsih, thank you for always being there.